Development of a Large-Dose, High-Resolution Dosimetry Technique for Microbeam Radiation Therapy using Samarium-Doped Glasses and Glass-Ceramics

A Thesis Submitted to the
College of Graduate Studies and Research
in Partial Fulfillment of the Requirements
for the degree of Doctor of Philosophy
in the Department of Electrical and Computer Engineering
University of Saskatchewan
Saskatoon

By
Go Okada

Permission to Use

In presenting this thesis in partial fulfillment of the requirements for a Postgraduate degree from the University of Saskatchewan, I agree that the Libraries of this University may make it freely available for inspection. I further agree that permission for copying of this thesis in any manner, in whole or in part, for scholarly purposes may be granted by the professor or professors who supervised my thesis work or, in their absence, by the Head of the Department or the Dean of the College in which my thesis work was done. It is understood that any copying or publication or use of this thesis or parts thereof for financial gain shall not be allowed without my written permission. It is also understood that due recognition shall be given to me and to the University of Saskatchewan in any scholarly use which may be made of any material in my thesis.

Requests for permission to copy or to make other use of material in this thesis in whole or part should be addressed to:

Head of the Department of Electrical and Computer Engineering
University of Saskatchewan
Saskatoon, Saskatchewan
Canada
S7N 5A9

Abstract

Microbeam radiation therapy (MRT) is a potential cancer therapy technique that uses an intense X-ray beam produced by a synchrotron. In MRT, an array of microplanar beams, called a *microbeam*, is delivered to a tumour. The dose at each centre of planar beams is extremely large (several hundred grays) while dose level in the valley between the peaks is below several tens of gray. Moreover, the width of each planar beam is typically 20 – 50 μm, and the distance from a centre of planar-beam to that of adjacent beam is 200 – 400 μm. For the latter reasons, the fundamental requirements for the dosimetry technique in MRT are (1) a micrometer-scale spatial resolution and (2) detection sensitivity at large doses (5 – 1000 Gy). *No existing detectors can satisfy those two requirements together.*

The objective of the Ph.D. research is to develop a prototype dosimetry technique which fulfils the requirements for measuring the dose profile in the microbeam. The currently used approach relies on the indirect detection of X-rays; in which the X-ray dose is recorded on a detector plate, and then the recorded signals are digitized using a reader. Our proposed approach utilizes Sm^{3+}-doped polycrystallites, glasses, and/or suitable glass-ceramics (though our approach is not limited to the use of Sm ion) for the detector plate, in which a valence reduction of Sm^{3+}, that is the conversion of Sm^{3+} to Sm^{2+}, takes place upon irradiation of X-rays. The extent of reduction is further read out using confocal fluorescence microscopy via the photoluminescence (PL) signals of Sm^{3+} and Sm^{2+}.

The work carried out throughout the course of the research includes the construction of confocal fluorescence microscopy, synthesis and characterizations of dosimeter materials, as well as application tests of our approach for measuring the dose profile of a microbeam used at synchrotron facilities – Canadian Light Source (CLS), Saskatoon, Canada, European Synchrotron Radiation Facility (ESRF), Grenoble, France, and SPring-8, Hyogo, Japan. Further, the research has shown that 1 % Sm-doped fluoroaluminate glass is one of the best candidates for the type of dosimetric application. It has the dynamic range of ~1 to over 1000 Gy which covers the dose

range used in MRT, excellent signal-to-noise ratio (large extent of $\mathrm{Sm}^{3+} \rightarrow \mathrm{Sm}^{2+}$ change), and excellent stability of recorded signal over time. The recorded signal in the detector is erasable by heating or exposing to light such as UV. Furthermore, with a use of confocal microscope, it has ability to measure the distribution pattern of dose over the cross-section of microbeam. Therefore, we believe that our approach is one of the most promising techniques available.

ACKNOWLEDGEMENTS

I would like to express my sincerest gratitude to my supervisor, Dr. Safa Kasap, professor at the Department of Electrical and Computer Engineering, University of Saskatchewan, for his guidance and assistance both professionally and personally to make my work and life experience in Saskatoon richer and successful. He showed me various valuable and priceless experiences that I could not have even imagined I would have . I place on record, my sincere gratitude to Dr. George Belev, Canadian Light Source, Saskatoon, who was always my first point of contact for discussions and questions, and through his knowledgeable advice it always solved the problems and pushed my work forward towards the goal. Also, my experimental work at the Canadian Light Source would not have been successful without his tireless support. I am also very grateful to Dr. Andy Edgar and Mr. Chris Varoy, School of Chemical and Physical Sciences, Victoria University of Wellington, New Zealand, and also to Dr. Setsuhisa Tanabe and Dr. Jumpei Ueda, Graduate School of Human and Environmental Studies, Kyoto University, Japan, for providing us with detector samples as well as for allowing me to be in the laboratories for experimental work with generous assistance and productive discussions throughout our collaborative research. Many thanks to Dr. Cyril Koughia, Electrical and Computer Engineering, University of Saskatchewan, due to his knowledgeable and educational advice and discussions, from which I learned not only science but also data analysis and organizational skills, Dr. Dancho Tonchev, Electrical and Computer Engineering, University of Saskatchewan, for assistance in sample preparation and advice from the chemistry point of view, Dr. Tomasz Wysokinski, Canadian Light Source, Saskatoon, and Dr. Dean Chapman, Department of Anatomy and Cell Biology, University of Saskatchewan, for the productive discussions and advice, and my colleagues for the productive discussions and friendship. Last, but not least, I am grateful for the financial support provided by my supervisor, Dr. Safa Kasap, the Department of Electrical and Computer Engineering, the College of Engineering, and the College of Graduate Studies and Research, University of Saskatchewan.

Contents

List of Tables

List of Figures

List of Abbreviations

BMIT	Bio-Medical Imaging and Therapy
CCD	Charge-Coupled Device
CLS	Canadian Light Source
CMOS	Complementary Metal-Oxide Semiconductor
CT	Computed Tommography
DPSS	Diode Pumped Solid State
DAC	Data Acquisition Controller
ESRF	European Synchrotron Radiation Facility
FA	Fluoroaluminate
FCZ	Fluorochlorozirconate
FNTD	Fluorescent Nuclear Track Detector
FOV	Field Of View
FP	Fluorophosphate
FWHM	Full-Width at Half-Maximum
IR	Infra-Red
LD	Laser Diode
LED	Light Emitting Diode
MOSFET	Metal-Oxide-Semiconductor Field-Effect Transistor
MRI	Magnetic Resonance Imaging
MRT	Microbeam Radiation Therapy
MSC	Multi-Slit Collimator
MTF	Modulation Transfer Function
NA	Numerical Aperture
ND filter	Neutral Density Filter
NIR	Near Infra-Red
OD	Optical Density
OSL	Optically-Stimulated Luminescence
PID	Proportional-Integral-Derivative
PL	Photoluminescence
PMT	Photomultiplier Tube
POHC	Phosphorus-Oxide Hole Centre
PSF	Point Spread Function
PSL	Photo-Stimulated Luminescence
PVDR	Peak-to-Valley Dose Ratio
RE	Rare Earth
S/N ratio	Signal-to-Noise ratio
SEM	Scanning Electron Microscope
SSD	Silicon Strip Detector
SW	Solid Water
TFT	Thin-Film Transistor
TLD	Thermally-stimulable Luminescence Detector

TSL, TL	Thermally-Stimulable Luminescence
USB	Universal Serial Bus
UV	Ultraviolet
XL	X-ray-stimulated Luminescence
XRD	X-Ray Diffraction

CHAPTER 1

INTRODUCTION

Microbeam radiation therapy (MRT) is a pre-clinical cancer therapy technique. It may cure many types of cancers with a very unique approach. The most distinguished features of MRT are that it utilizes a very intense X-ray beam, which is spatially modulated on the micrometer scale with very high gradients of dose distribution. Here, such X-ray beam is a so-called *microbeam*. Typically, the X-ray doses delivered to the patient are over several hundreds of gray for the large-dose regions and a few grays to several tens of grays for the low-dose regions. These two levels (high and low) of dose are distributed over tens to several hundred micrometers. The dose rate of a microbeam in the high-dose regions is typically over thousands of grays per second, which ensures the microbeam is delivered to the live-patient with the structures of dose distribution designed for the therapy.

Measurement of a microbeam is a highly challenging task. The measurements fundamentally require a detector that has two essential features:

1. It requires detection of extremely large doses. For instance, conventional radiotherapies utilize doses up to 50 Gy, whereas the dose range in MRT is far beyond (up to thousands of grays).

2. It requires detection of X-rays with the resolving power on the micrometer scale. *To date, no existing detector can satisfy these two fundamental requirements at the same time.*

Towards the goal of developing a novel dosimetry technique for MRT, we have first proposed our original dosimetry approach for an NSERC strategic project grant 2009-2013 [1], and the work presented in this thesis is a part of the project, which is to develop a prototype dosimetry technique for MRT. Hence, the objective of the Ph.D. work presented in this thesis focuses on the development of a prototype dosimetry technique that can be used to measure high doses with high resolution for use in MRT.

The following chapter covers the essential fundamental and engineering science required to understand the contents of work presented in the thesis. It includes the production and detection of X-rays. Rare earth ions for use in luminescent materials are discussed in relation to X-ray detector and dosimetry applications.

Chapter 3 reviews MRT and dosimetric detectors that have been tested for the purpose of measuring microbeam characteristics. Moreover, our novel approach towards the detection of microbeams is described in detail.

Chapter 4 provides experimental techniques used throughout the course of this work. It includes the synthesis procedures of dosimetric detector materials, and describes several measurement techniques used to characterize the dosimetric materials. The techniques used characterize the optical, thermal, and structural properties of solid-state materials. Furthermore, experimental set-ups used to characterize the practical applications of dosimetric materials for measurement of microbeam dose profile are also described. It includes the confocal fluorescence microscopy constructed, optical scanners used to digitize a conventional radiochromic film detector, as well as the production of microbeam and the irradiation geometries performed at three synchrotron facilities; Canadian Light Source (CLS; Saskatoon, Canada), European Synchrotron Radiation Facility (ESRF; Grenoble, France), and Spring-8 (Hyogo, Japan).

We have started the project with a search of detector materials, which is described in Chapter 5. The successful detector material, essentially, needs to show valence reduction of Sm^{3+} ($Sm^{3+} \rightarrow Sm^{2+}$) doped in the material by X-ray irradiation. The reduction effect, or response, should continuously last over the dose range used in MRT, which is $\sim$5 to 1000 Gy. Moreover, the material should be homogeneous over the detector plate. Towards the search of successful detector materials, several different types of Sm^{3+}-doped materials have been tested.

Chapter 6 describes the work done with Sm^{3+}-doped fluorophosphate (FP) and fluoroaluminate (FA) glasses. These are, in fact, the most successful dosimeter materials discovered in our approach. The contents include dose-response curves examined with varying concentrations of Sm^{3+} added. Furthermore, measurements of microbeam dose profile are demonstrated.

A new glass-ceramic material was synthesized and studied for use as a dosimetric detector, which is discussed in Chapter 7. The detector plate includes CaF_2:Sm^{3+} nanocrystals uniformly distributed in an oxyfluoride glass matrix. The contents in this chapter include characterizations of thermal properties and structure, which were carried out in order to identify the temperature to heat the material in order to nucleate and grow the nanocrystals and also to identify which nanocrystals have been grown and the size. Furthermore, the valence reduction of Sm^{3+} is tested, and attempts to use the device for measurement of microbeam dose and dose profile are described.

In Chapter 8, measurements of microbeam carried out at three different synchrotron facilities (CLS, ESRF, and SPring-8) are discussed. The X-ray beams at these facilities have different properties such as mean energy and intensity; moreover, they produce microbeam in different ways. The microbeams in these facilities are characterized using our approach (with 1 % Sm^{3+}-doped FA glass) as well as using one of the conventional techniques (with a GafChromic® film (HD-810)). Further, our dosimetry approach is characterized in comparison with the conventional method based on GafChromic® film.

At last, Chapter 9, concludes the thesis with summary of the work, contributions, as well as suggestions of future work for further advance of research.

Chapter 2

Background and Principles of Related Physics

2.1 Introduction

X-rays are characterized as high energy photons. These were first discovered by Wilhelm C Röntgen in 1895, for which the first Nobel Prize in Physics was awarded in 1901. Immediately after the discovery, for its excellent transparency to human tissue while being strongly interrupted by bones, X-rays soon found their application in medical diagnosis. It became possible to use X-rays to image inner parts of a body and differentiate between bones and soft tissue. Further, the unique properties extended its applications in non-destructive inspection, crystallography, radio surgery, and so on. Whenever X-rays are used, production as well as detection of X-rays are of fundamental importance.

Microbeam radiation therapy (MRT) is not an exception. MRT is a pre-clinical stage cancer therapy technique. In this application, the X-ray source should be powerful enough to deliver hundreds to over a thousand grays of X-ray dose at one instant of time and the X-ray beam should be highly collimated. For the latter reason, MRT is often carried out at a 3rd generation synchrotron facility. Further, the spatial variation of X-ray dose must be measured for system alignment, to monitor the X-ray beam delivered to the patient, to assure the quality of therapy, etc. In this particular application, the detector requires high spatial resolution over a few micrometer scale and dose detection over wide range. Put differently, the detector must have a very large dynamic range, up to a thousand grays, and be able to capture the dose variation with high resolution.

The aim of this chapter is to provide sufficient background knowledge to understand the contents of thesis. This chapter covers principles of related background physics, which are involved in the production and detection of X-rays. X-rays are typically produced by an X-ray tube or free electron laser such as a synchrotron. Moreover, X-rays are detected by different ways, depending on the application. One of the common methods is to use luminescent materials, which converts X-ray photons to low energy photons such as visible light. Therefore, the X-rays can be detected indirectly using conventional photodetection techniques.

2.2 Production of X-rays

X-rays are typically produced by two different methods. The most common technique is to use a so-called X-ray tube. Another method is to use a large-scale accelerator such as a synchrotron. This section discusses how X-rays are produced by these two methods.

An X-ray tube is the most commonly used tool to generate X-rays. In fact, the present principle is the same as at the time of discovery by Röntgen. X-ray tubes are widely used in X-ray applications such as medical diagnosis, non-destructive security and inspection, spectroscopy, and elsewhere.

Figure 2.1 (a) is an illustration of an X-ray tube. It mainly consists of a cathode electron source and an anode metal target which are located in a vacuum glass tube. Under its operation, a high voltage is applied across the two electrodes, and the electrons generated by the cathode element are accelerated and then strike on to the anode target. The anode material is usually tungsten, molybdenum or copper. The highly accelerated electrons are forced to stop inside the anode material and lose their energy; some of the lost energy is converted into photons, which is in fact X-rays.

A typical X-ray spectrum produced by this regime is shown in Figure 2.1 (b). There are two components of the spectrum as indicated in the figure − *characteristic*

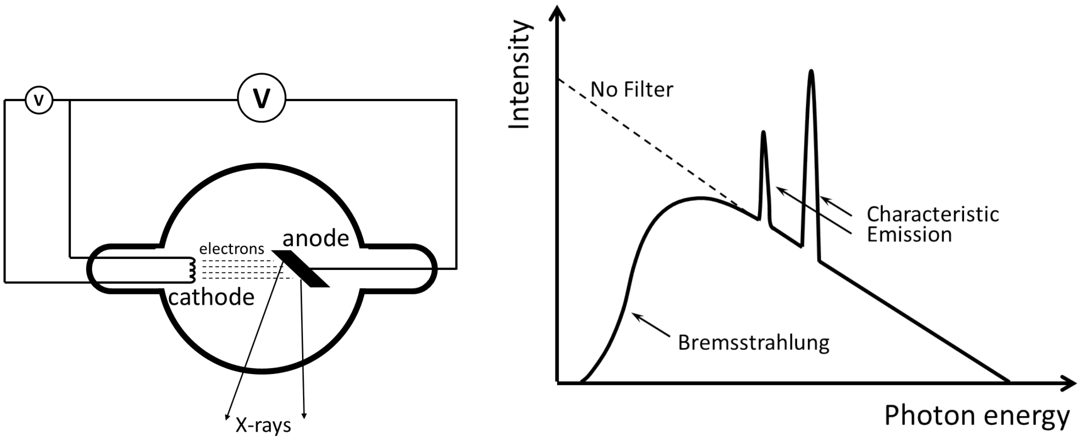

(a) (b)

Figure 2.1: Illustration of (a) X-ray tube and (b) typical spectrum of X-rays generated by an X-ray tube.

and *Bremsstrahlung* X-rays, which have two different origins. Inside the X-ray tube, electrons emitted from the cathode electrode are accelerated by the electrical field, carry high energy and then collide on to the anode material. During the interaction of the electrons with the anode material two different processes take place, which gives rise to two different X-ray emissions. Figure 2.2 illustrates the origins of the two different types of X-rays. In Figure 2.2 (a), an incident electron carries enough energy to remove an electron from the K-shell of an atom in the anode material. As a result, the created vacancy in the K-shell will be filled by an electron from the outer shell (L) orbit, which results in a radiative emission. The energy of this radiation is the difference of binding energies of K- and L- shells, which are well-defined by the material itself. Thus, the X-rays produced by such a mechanism are so-called characteristic X-rays. Further, if the incident electron has sufficient large energy to remove an L-shell electron, then the vacancy is filled from the M-shell electrons, which results in the X-ray emission with a binding energy difference between L- and M-shells, and so on.

The accelerated incident electrons do not always strikes out the orbital electrons, but they may interact with the nuclei by coulomb interactions. As illustrated in Figure 2.2 (b), the trajectory of incident electrons is, then, bent, and as a result the X-ray photons are produced in the trajectory direction, which is called Bremsstrahlung X-rays. The X-ray energy depends on the loss of the electron momentum by bending, which in turn depends on the extent of coulomb interaction. For this reason, the Bremsstrahlung X-ray spectrum has the continuous broad structure. Further, the maximum photon energy of Bremsstrahlung X-rays is defined by the acceleration energy since the maximum possible energy that can be lost by such an interaction is the maximum energy that the incident electron possesses.

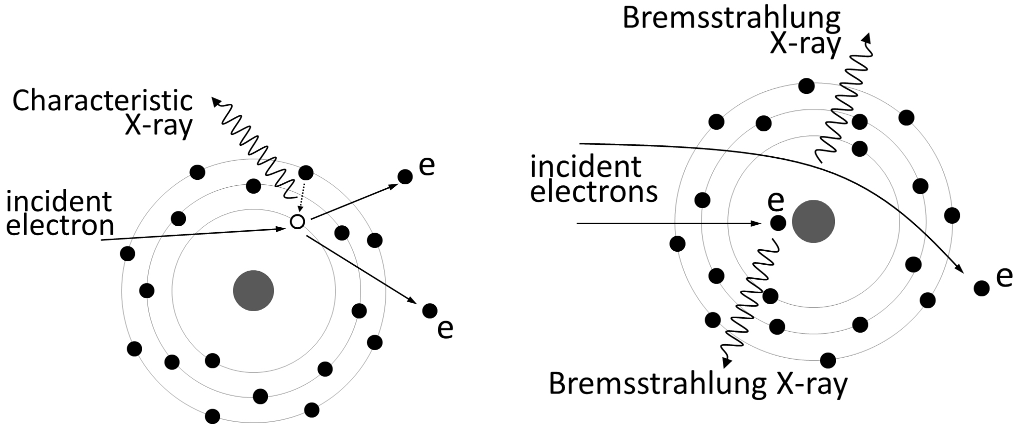

(a) (b)

Figure 2.2: Origins of (a) characteristic and (b) Bremsstrahlung X-ray emissions by an X-ray tube.

A synchrotron facility allows generation of X-rays that might not be obtained from an X-ray tube. Such X-rays are extremely intense in a wide range spectrum. Further, the beam is coherent, and the origin of the source size is very small. For their unique properties which cannot be achieved by a conventional X-ray tube, synchrotron generated X-rays provide highly specialized features in a wide range of applications such as crystallography, spectroscopy, micro-fabrication by lithography, medical imaging, and radiation cancer therapy.

At a synchrotron, charged particles such as electrons are accelerated to speeds close to the speed of light. The orbit of the accelerated electrons is then bent by a strong magnetic field, which results in Bremsstrahlung X-ray radiation. Figure 2.3 illustrates an example of a typical synchrotron facility. First, electrons are injected

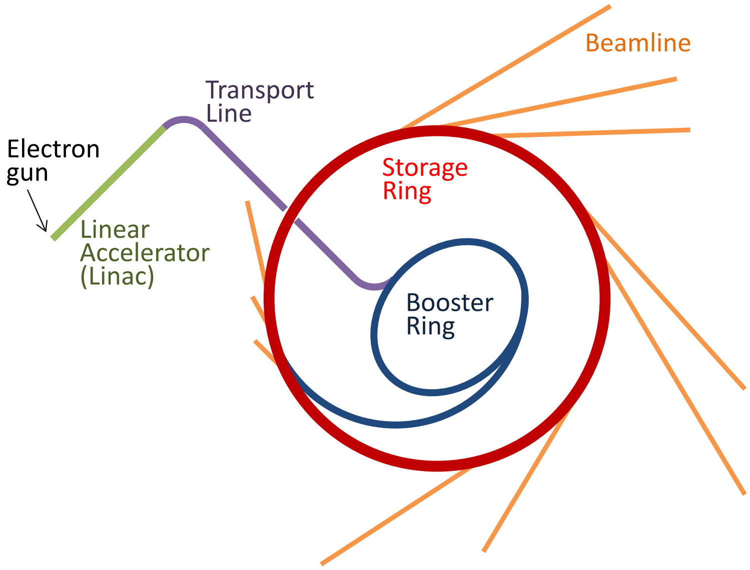

Figure 2.3: General sketch of a synchrotron facility.

into an evacuated ring chamber by the electron gun and accelerated by a linear particle accelerator, or linac. Next, the accelerated electrons are transferred to a booster ring where the electrons are further accelerated to relativistic speeds. These electrons are delivered to the outer ring called the storage ring, in which the speed of electrons are kept at relativistic speeds and stored. The electrons in the storage ring are subject to ”bending” in order to generate Bremsstrahlung X-rays, and they are used for experiments at each beamline. Common techniques of ”bending” are discussed below. These electron paths take place in vacuum in order to avoid the interaction of electrons with air molecules, which would prevent the acceleration.

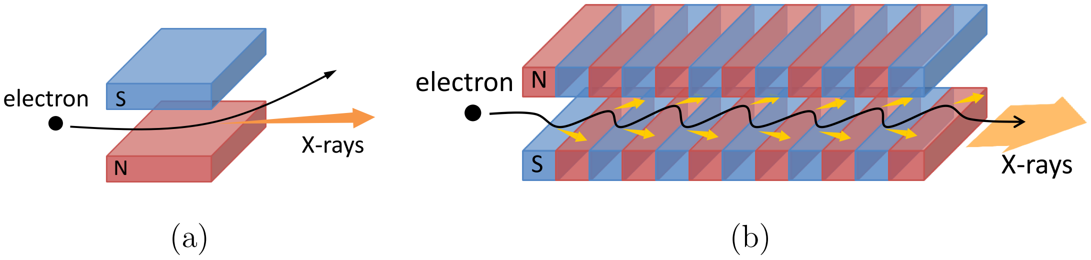

(a) (b)

Figure 2.4: Illustrations of X-ray generations at a synchrotron by (a) bending magnet and (b) insertion device.

The electrons in the storage ring are subject to bending. The most common way is to bend by a pair of superconductive electro-magnetic coils as illustrated in

Figure 2.4 (a). As a result of bending the electron path, Bremsstrahlung X-rays are generated in the trajectory direction. The X-rays have continuous and broad spectrum (as illustrated in Figure 2.5), therefore specific photon energy can only be selected by using an X-ray monochromator. The brilliance at the centre of the X-ray beam generated by a bending magnet source is given by [2]:

$$\left.\frac{d^2\mathscr{F}_B}{d\theta d\psi}\right|_{\psi=0} = 1.327 \times 10^{13} E_R^2[\mathrm{GeV}] I[\mathrm{A}] H_2(y) \quad [\mathrm{ph} \cdot \mathrm{s}^{-1} \cdot \mathrm{mr}^{-2} \cdot 0.1\%\mathrm{bw}^{-1}] \quad (2.1)$$

where $H_2(y) = y^2 K_{2/3}^2 \left(\frac{1}{2}y\right)$, $\mathscr{F}_B$ is photon flux, θ is observation angle in the horizontal plane, ψ is observation angle in the vertical plane, I is storage beam current, and E is electron beam energy. Further, H_2 is a function which includes a modified Bessel function of the second kind $K_{2/3}$ and a look-up table or graph is available for practical use elsewhere [2], y is the fraction of photon energy with respect to the critical energy ($\varepsilon_c = 0.665 E^2[\mathrm{GeV}] B[\mathrm{T}]$), that is $y = \varepsilon/\varepsilon_c$, and B is the magnetic field strength of the bending magnet source.

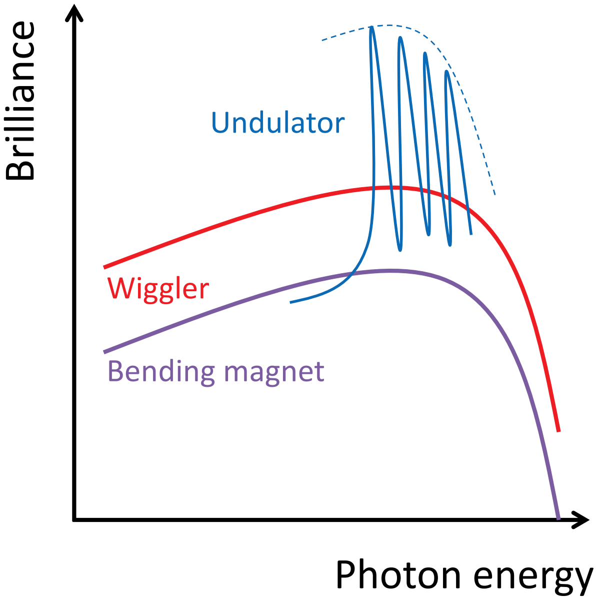

Figure 2.5: Illustration of spectral shapes generated by bending-magnet, undulator, and wiggler sources.

An array of dipole magnets which is oriented periodically as shown in Figure 2.4

(b) can also be used to generate X-rays at a synchrotron facility. In this device, electrons travel between the magnet arrays and are bent multiple times periodically, and each of the bendings produces Bremsstrahlung X-ray photons. Since this type of device is ”inserted” in the storage ring, it is referred as an *insertion device*. With the insertion device, X-rays can be generated with two different characteristics depending upon the device design, and characterized by the following equation:

$$K = \frac{eB\lambda_u}{2\pi\beta m_e c} \tag{2.2}$$

where e is the electron charge, B is the magnetic field, λ_u is the period of dipole magnets, β is the speed of the electron relative to that of light ($\beta = v/c$), m_e is the electron rest mass, and c is the speed of light. When $K << 1$, the oscillation of travelling electrons is small, so the resulting X-rays are distributed in a small area with a very high brightness. Moreover, in this condition, the radiation generated from different bendings interfere with each other, thus the spectrum shows several sharp peaks, caused by the interferences, as shown in Figure 2.5. This type of insertion device is called an *undulator*. When $K >> 1$, radiation generated from each section of curves adds up incoherently, and its energy spectrum is broad as shown in Figure 2.5. This type of insertion device is called a *wiggler*. The X-rays that are generated by an undulator or wiggler device are more intense and harder than those generated by a bending magnet.

2.3 Interaction of X-rays with Matter

In order to detect X-rays, one must use an interaction with matter. Any resulting effect by this interaction should be considered as a ”measure” of the X-rays. For example, an X-ray scintillator converts incident X-ray photons into low energy photons. The converted photons can be used as a measure of X-rays; and one can use a conventional photodetector to detect X-rays indirectly. In this particular case, a good scintillator should have strong interaction with X-rays into such a way that the incident X-ray photons are stopped in the scintillator material as much as possible, so that more photon energy will be converted to light.

As X-ray photons interact with matter, the intensity of incident X-ray intensity decreases exponentially with the travelling distance in the medium. The exponential decay is expressed by the following equation:

$$I(t) = I_o \exp\left\{-\left(\frac{\mu}{\rho}\right)\rho t\right\} \tag{2.3}$$

where I_o is the incident X-ray intensity at a surface of material, μ/ρ is mass attenuation coefficient, ρ is density of material, and t is distance from the surface. The extent of attenuation depends not only on the type of material, but also on the photon energy. Figure 2.6 shows, as an example, the mass attenuation coefficient (μ/ρ) of air as a function of X-ray energy. Mass attenuation coefficient is a form of attenuation coefficient that is independent of the density of material.

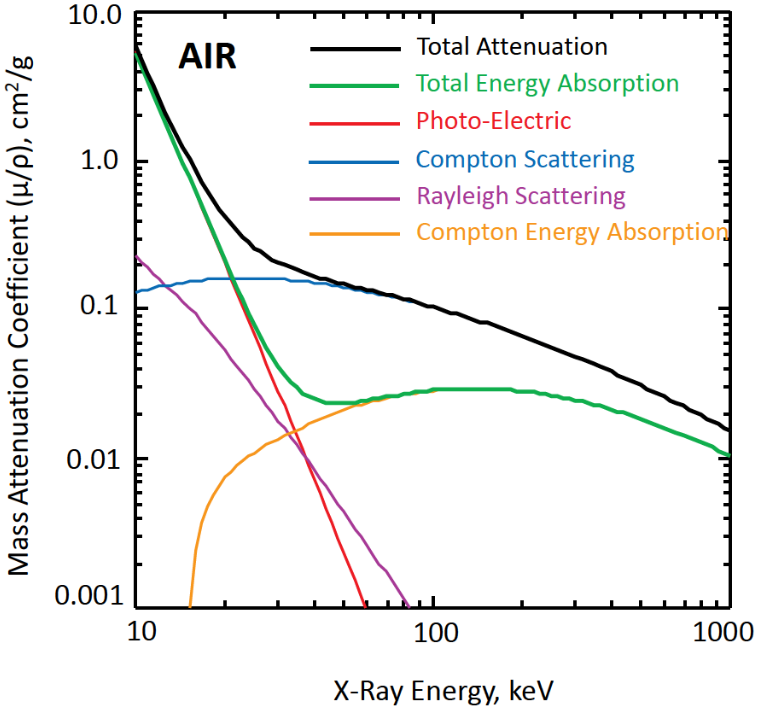

Figure 2.6: Mass attenuation coefficient of air as a function of X-ray energy. Courtesy of Professor Dean Chapman, University of Saskatchewan.

The attenuation is governed by multiple interaction processes. At low energies, *photoelectric* interaction (τ) and elastic (*Rayleigh*) interaction (ω) are dominant. As the energy increases, inelastic interaction (*Compton scattering*) (σ) becomes dominant, which is followed by *pair production* (κ) and *photodisintegration* (π). The total attenuation coefficient (μ) is normally written as a linear sum of all these effects as:

$$\mu = \tau + \omega + \sigma + \kappa + \pi \tag{2.4}$$

Since the energy range of our interest is a few hundred keV at maximum, only τ, ω, and σ are subject to our consideration.

Figure 2.7 illustrates three different interaction processes of X-rays with an atom − photoelectric, elastic, and inelastic interactions. As sketched in the upper-left of figure, when X-ray energy is absorbed and transferred to an atom, the energy is so large (larger than binding energy of an orbital electron) that an orbital electron is ejected, hence the atom is said to be ionized. This process is called photoelectric interaction. Subsequently, the vacancy is filled by an outside electron, resulting in the emission of characteristic X-rays (or secondary X-ray emission). When an incident X-ray photon interacts with the whole atom or electron elastically (upper-right), the photon may be deflected from its original path without losing its energy. Hence, the photon energies of incident and scattered X-rays are the same. This type of interaction is referred as inelastic interaction, or Rayleigh scattering. The incoming X-ray photon may interact with an atom inelastically (lower figure). In this case, the incident X-ray photon ejects an electron from its orbit, and then the electron gains sufficient energy to give rise to secondary ionization effects; on the other hand, after the interaction, the incident X-ray photon loses its energy and keeps travelling in a deflected direction. This type of interaction is called Compton scattering.

Mass attenuation coefficient of each chemical element is available in the literature [3]. From the database, one can simulate the coefficient of an arbitrary compound (μ/ρ_{comp}) from the following relationship:

$$\frac{\mu}{\rho}_{\text{comp}} = \sum_i w_i \left(\frac{\mu}{\rho}\right)_i \tag{2.5}$$

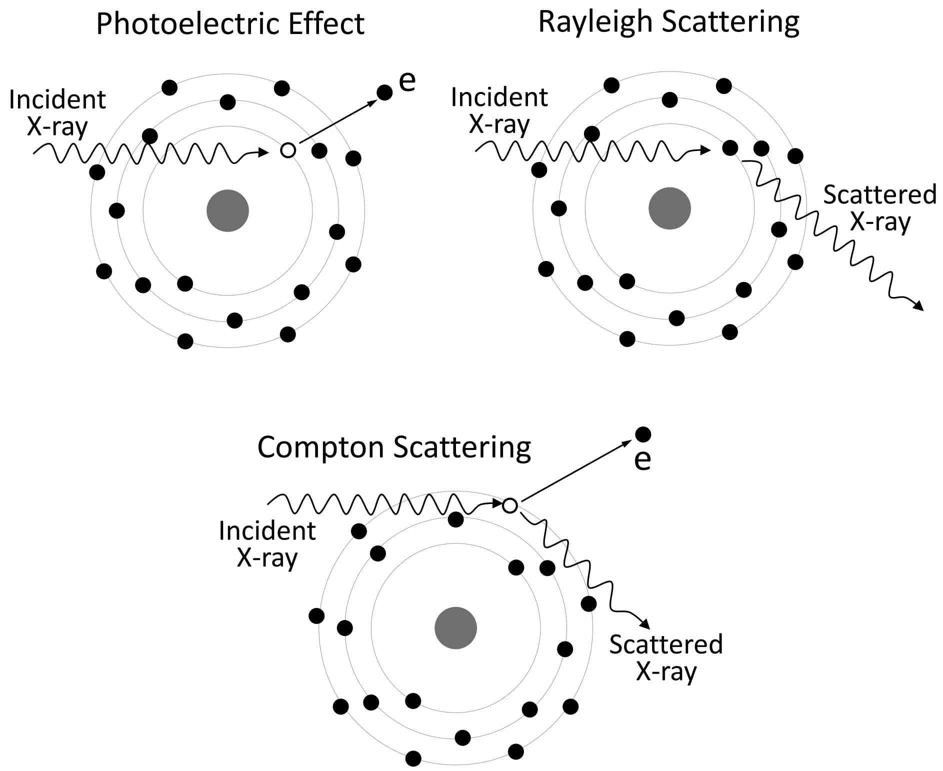

Figure 2.7: Schematic views of several X-ray interaction mechanisms with matter.

where w_i and $(\mu/\rho)_i$ are the weight fraction and mass attenuation coefficient of element i, respectively.

2.4 Dose

The "amount" of X-rays absorbed is usually quantified by dose. Dose is radiation energy absorbed in an object, and it is represented by an SI unit in *gray* (Gy). A dose of 1 Gy is equivalent to 1 joule of radiation energy absorbed per unit mass (kg). An absorbed dose, $D(E_{ph})$, at a monochromatic energy, E_{ph}, is given by:

$$D(E_{ph}) = \frac{N_{abs}E_{ph}}{M} \tag{2.6}$$

where N_{abs} is the number of absorbed photons, E_{ph} is photon energy, and M is mass of the absorber material. Further, the number of absorbed photons (N_{abs}) which deposits its energy to the material is given by:

$$\begin{aligned} N_{abs} &= N_o \frac{\mu_{EA}}{\mu_{total}} \{1 - \exp(-\mu_{total} t)\} && (2.7) \\ &= N_o \frac{(\mu/\rho)_{EA}}{(\mu/\rho)_{total}} \left[1 - \exp\left\{-\left(\frac{\mu}{\rho}\right)_{total} \rho t\right\}\right] && (2.8) \end{aligned}$$

where N_o is the number of total photons deposited to incident on the material, and t is the thickness of material, $(\mu/\rho)_{EA}$ is the energy absorption mass attenuation coefficient which accounts for X-rays absorbed and resulting in energy deposition to the material. $(\mu/\rho)_{total}$ is the total mass attenuation coefficients which is a measure of X-ray attenuation due to photoelectric absorption, Rayleigh scattering, and Compton scattering. These coefficients are specific to the material composition and independent on the state, such as gas, liquid, or solid, or in other words its density.

2.5 X-ray Detection Methods

X-rays are invisible to the human eye. The detection of X-rays depends on using one of the effects of X-rays when they interact with a medium. Table 2.1 summarises X-ray detection techniques with the associated physical effects used to detect X-rays.

Table 2.1: X-ray Detection Methods

Effects	Detectors
Ionization	Ionization chamber, Geiger counter, Semiconductor detector etc.
Fluorescence	Scintillation counter etc.
Photoconductivity	PbO vidicon
Photostimulable luminescence (PSL)	Imaging plate
Photographic	Photographic film

An ionization chamber is one of the detectors most commonly used to measure the radiation dose. Figure 2.8 shows an illustration of an ionization chamber. In principle, an ionization chamber contains gas inside the chamber where two electrodes are located. Here, high DC voltage is applied to the electrodes such that electric field is created across the electrodes. When ionizing radiation such as X-rays passes across the region between the electrodes, the confined gas on the track of X-rays is ionized (electron-hole pairs are generated). The electrons and positive ions that are generated by the ionization process are guided towards the anode and cathode electrodes, respectively. The consequent electric current produced by these events is detected by the ammeter. The detected electric current and number of incident X-ray photons have the following relationship:

$$i = N_o e \frac{E_{ph}}{\varepsilon_{e-ion}} \frac{\mu_{EA}}{\mu_{total}} \left(1 - e^{-\mu_{total} L}\right) \tag{2.9}$$

where N_o is the number of incident X-ray photons, e is electron charge, E_{ph} is X-ray photon energy, ε_{e-ion} is the efficiency of ionization chamber as a function of photon energy, μ_{EA} is energy absorption coefficient, μ_{total} is total attenuation coefficient, and L is the length of the X-ray path where the gas is ionized and the charges are collected by electrodes.

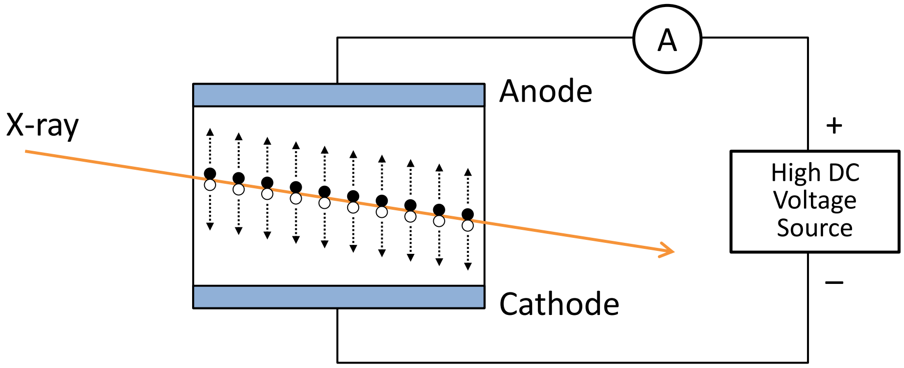

Figure 2.8: Illustration of ionization chamber. Filled in circles are electrons whereas empty circles are positive ions.

Similarly, semiconductor-based detector utilizes the ionization effect by X-rays in the solid state semiconductor layer. One of the well known detectors is a flat-panel digital X-ray detector where amorphous selenium (a-Se) is used as an X-ray sensing material. Figure 2.9 illustrates a cross-section of the detector. The layer of a-Se is coated on a thin film transistor (TFT) array and the selenium layer is biased by a high voltage. Just as in the ionization chamber, the a-Se layer is ionized upon the deposition of X-ray photons, and consequently generated electrons and holes are drifted by the electric field across the a-Se layer. The generated charges are collected locally and read out through the TFT array. Each pixel on this flat panel X-ray image detector detects X-rays incident on it and generates an electrical signal proportional to the delivered dose. The signals from these pixels then constitute the X-ray image. The resolution in a-Se detectors is limited by the pixel size, which currently is around 50-100 μm.

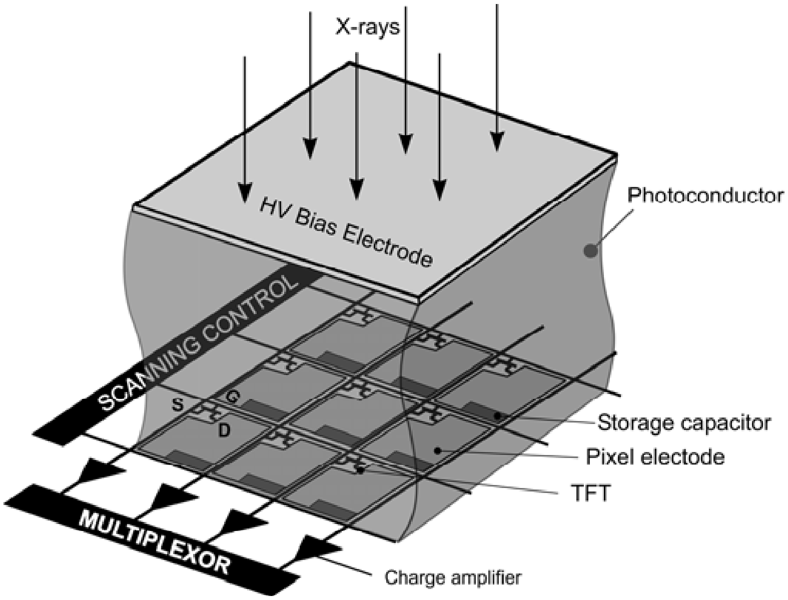

Figure 2.9: Illustration of a-Se direct flat panel X-ray detector. From [4].

X-ray detection using fluorescence (XL) as well as photostimulable luminescence (PSL) effects can be accomplished by using phosphors. A phosphor is a class of material which converts high energy photons or radiations, e.g. X-rays, to low energy photons, e.g. visible light. Therefore, it is basically used in such a way that radiation is detected indirectly using conventional photodetectors. X-ray detection using a phosphor is one of the key topics in this work; hence, it is discussed in more detail in the following sections.

Photographic film is one of the most traditional techniques for X-ray detection. Just as it works with optical light, photographic film senses X-rays as well. However, the sensitivity of film to X-rays is very low compared to optical light; therefore, it is commonly used with an intensifier screen. An intensifier screen is also a phosphor, which emits light upon absorption of X-rays. So, the screen attached closely with a photographic film intensifies the X-ray signal detected by the film.

2.6 Phosphors using Rare Earths

Phosphor is generally a material which emits light upon photoexcitation. A phosphor material often contains impurity ions which play an important role in controlling the luminescent properties of the phosphor material. Such impurity ions absorb energy from an external source such as light, heat, or radiation, and the electronic state is excited. The excitation is followed by the return to the original, or ground, state which results in an emission of different form of energy such as photon and heat. Very often, rare earth ions are included in a host material of phosphor as the impurity (as an activator) to activate such luminescent properties.

Rare earth ions in luminescent materials refer to the chemical elements with the atomic number of 57 (La) through 71 (Lu). These elements have the especially unique feature that the $4f$ orbital is incompletely filled by electrons, whereas the outer $5s^2$ and $5p^6$ orbital shells are filled. The state of electron is commonly expressed using a term symbol as ${}^{(2S+1)}L_J$, where L, S, and J are quantum numbers of the electron's total angular momentum, total electron spin, and the total angular momentum, respectively. For convenience, total angular momentum L is expressed using alphabets as $(S, P, D, F, G, H, I, \ldots) = (0, 1, 2, 3, 4, 5, 6, \ldots)$. The multiplicity of spin is given by $(2S{+}1)$. The total angular momentum J is the vector sum of overall angular momentum and overall spin ($J = L + S$).

The energy levels that the $4f^n$ electrons can take are determined by various interactions: coulomb interaction between the electrons, spin-orbit coupling, and the surrounding crystalline field. The energy level splitting of $4f^5$ electrons in trivalent

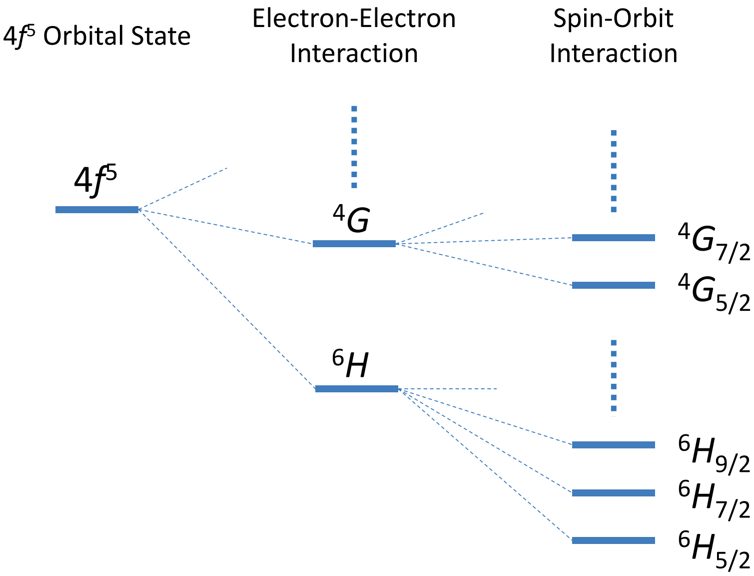

Figure 2.10: Low-lying energy levels of $4f^5$ electrons in Sm^{3+} ion by various effects.

samarium (Sm^{3+}) ion by these effects is illustrated in Figure 2.10 as an example. The electrons in the $4f$ orbital interact with each other by coulomb interaction, resulting in the splitting into different energy levels (^6H, ^4G, ^4F etc.). These levels are further split by spin-orbit interaction. Since the spin multiplicity of ^6H level is 6, it is split into 6 energy levels $^6H_{5/2}$, $^6H_{7/2}$, $^6H_{9/2}$, and so on. Moreover, these levels, split by spin-orbit interaction, can be further split by surrounding crystal field with the multiplicity given by $(2J + 1)$. Therefore, the ground level ($^6H_{5/2}$), for example, can be split into $(2 \times 5/2 + 1) = 6$ levels. It should be instructive to note here that the number of split levels depends on the crystal-field strength in practice. The energy levels of trivalent rare earth ions as the result of these splitting effects are summarised in Figure 2.11, which is often referred as a *Dieke diagram*. The illustrated energy levels are determined in LaCl_3, but in fact effectively consistent among different host materials with slight shifts since these $4f$ electrons are shielded by the outer $5s^2$ and $5p^6$ electrons.

When these atoms interact with photons, the electrons are, upon the absorption of photon energy, excited to higher energy levels. Further, an excited electron will return back to its ground state by emitting a photon or phonons (heat). The

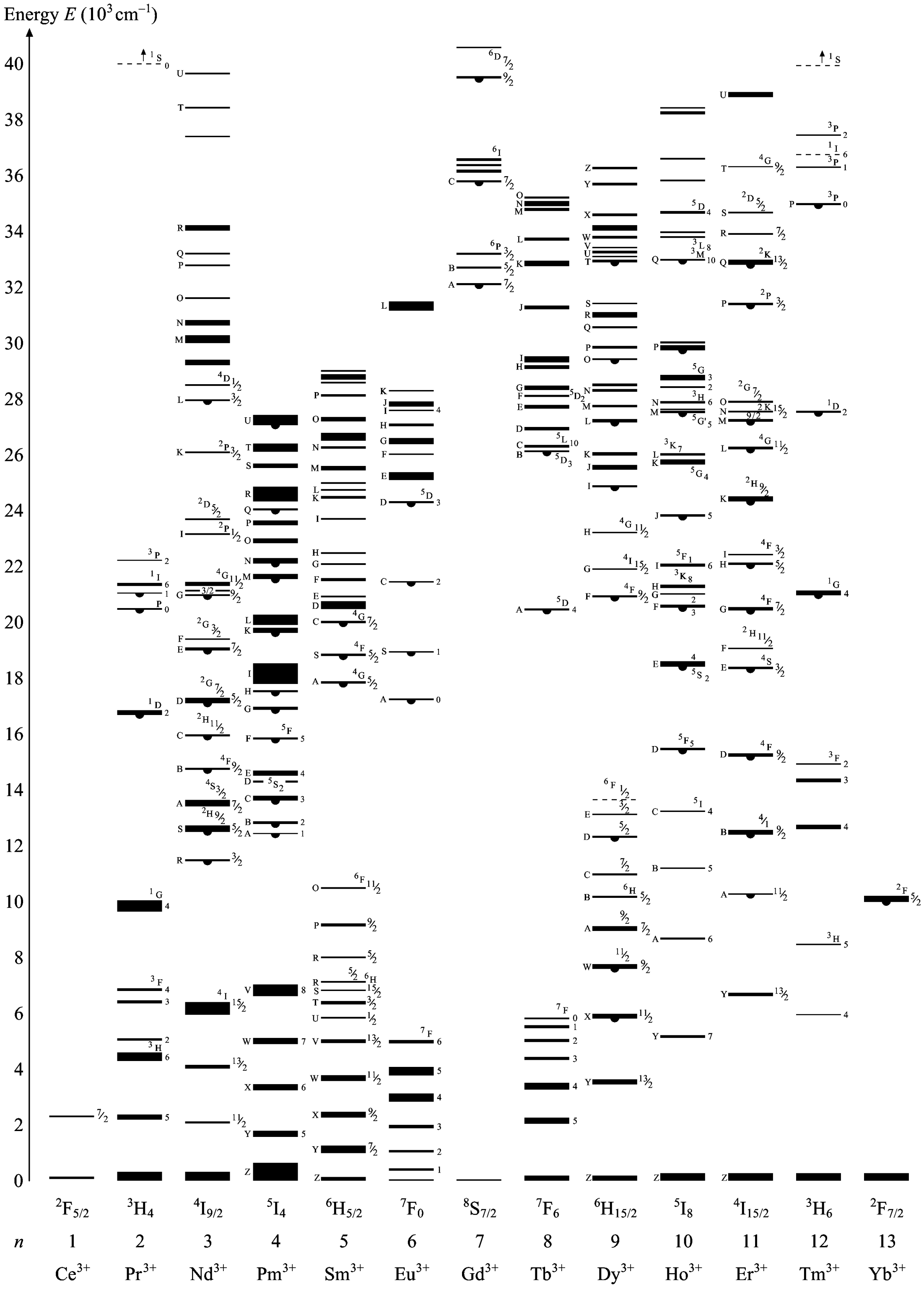

Figure 2.11: Dieke diagram. Energy levels of $4f^n$ electrons of trivalent rare earth ions doped in $LaCl_3$. After [5].

photoemission upon optical excitation is referred as *photoluminescence* (PL). These transitions between electronic states are normally governed by the *selection rules.* The selection rules suggest that optical transitions that are *allowed* are those in which the electric dipole parity must change, whereas the magnetic dipole is unaffected. This means that, since all the $4f^n$ configurations have the same parity, all the electric dipole transitions within the $4f^n$ configurations are *forbidden.* Nonetheless, optical emission is still possible by magnetic dipole transitions. Magnetic dipole transitions are governed by the following selection rules:

$$\begin{cases} \Delta L = 0, \pm 1 \\ \Delta S = 0 \\ \Delta J = 0, \pm 1 \quad (J = 0 \rightarrow J = 0 \text{ is forbidden.}) \end{cases} \tag{2.10}$$

The magnitude of magnetic dipole transition is typically weaker by five orders of magnitude than that of electric dipole transitions. For example, allowed $5d \rightarrow 4f$ transitions of Eu^{2+} are often used for radiation detection applications as such emission is very strong and the emission spectrum (usually blue) is in excellent agreement with a spectral response of photomultiplier tube (PMT) detector. On the other hand, weak but sharp $4f \rightarrow 4f$ forbidden transitions in Sm^{2+} have the advantage that they can be used as a probe of the localized environment in a glass ceramic [6]. Further, the lifetime of allowed transitions is fast (ns – μs), while that of forbidden transitions is long (μs – ms).

2.7 Phosphors for X-ray Imaging

X-rays are invisible to eye. Therefore, in order for us to ”see”, or detect, X-rays, we must use a physical phenomenon caused by X-rays. One of the common methods is to use a phosphor material. Phosphor material converts X-rays to low energy photons (e.g. visible light) such that the converted photons can be indirectly detected by a conventional photodetector.

There are several types of phosphors that are used in the detection of X-rays.

A scintillator is one of the phosphor types, where light is emitted upon excitation by X-rays. This process is called *X-ray-induced luminescence* (XL). Another class of phosphors is based on using a plate to locally store the information of deposited X-rays. Upon stimulation by light, such a phosphor emits light with the intensity proportional to that of the original deposited X-ray. This process is called *photo-stimulable luminescence* (PSL).

Scintillator and PSL materials are those phosphors that are commonly used in X-ray radiography applications. Such applications require the detection of X-rays in two-dimensional space. In this section, the use of these phosphors in X-ray imaging applications is discussed.

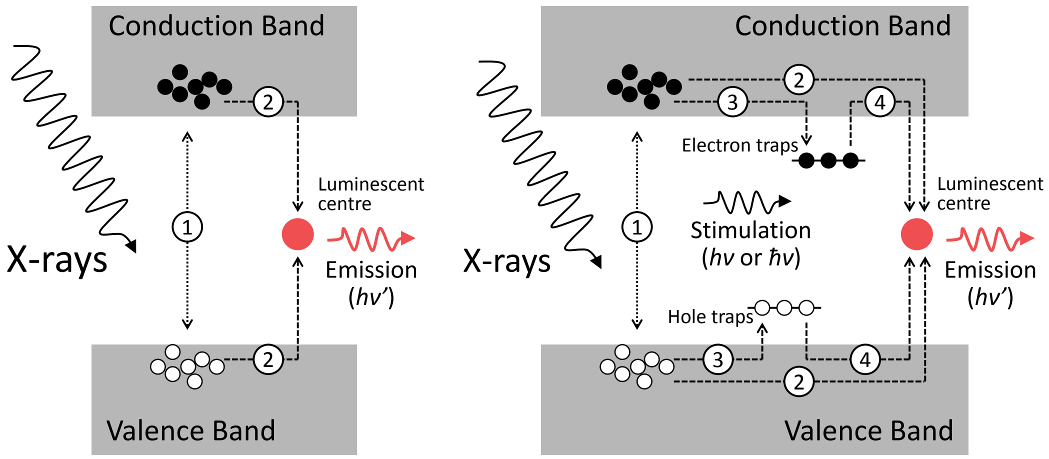

(a) (b)

Figure 2.12: Illustrations of luminescent mechanisms in phosphor materials using energy band diagrams for (a) X-ray induced luminescence and (b) thermally- or optically-stimulated luminescence.

A scintillator material is used to convert X-rays to light. For example, upon X-ray excitation, $Gd_2O_2S{:}Tb^{3+}$ emits green light. The scintillation mechanisms can be very complex depending upon the type of material. However, in general, X-rays are absorbed in the material, and then electrons and holes are generated. (This process is indicated as ① in a band diagram in Figure 2.12 (a)). Next, the generated electrons and holes will recombine (②) at localized luminescent centres such as rare earth impurities. Further, the energy released by recombination excites the luminescent centres, and then light is emitted. This light emission is then detected by conventional photodetectors such as a photographic film, PMT, CCD etc. Figure 2.13 illustrates the application in digital X-ray radiography, where a scintillator plate is placed on an array of photodetectors gated by thin-film transistors. The light emission properties depend on the type of luminescent centre and localized environment. A good scintillator material should have the following characteristics [7]:

1. high emission efficiency
2. strong X-ray absorption
3. emission spectrum matched to the spectral sensitivity of photodetectors
4. short emission decay time
5. durability
6. dispersion

First, in order to obtain strong light yield, as many X-ray photons as possible should be absorbed in the material and the absorbed energy should be transferred to luminescent centres efficiently. Particularly, the scintillator material should consist of heavy elements with large density to gain a high stopping power for X-rays. Spectral matching of emission light with photodetector is of particular importance. A typical radiographic film is sensitive with near UV to green light. A PMT is typically sensitive to blue. A Si-based detector such as a CCD is sensitive to red light. In radiography, efficient detection reduces the exposure dose to the patient. The phosphorescence afterglow occurring after the cessation of X-ray exposure is unacceptable for real-time detection. Particularly, when used for radiography, significant after-glow, or phosphorescence, will result in a low contrast image. Moreover, when a scintillator is used in computed tomography (CT) applications, the decay time especially has to be short enough such that it does not affect the scanning speed. The material should be durable for multiple uses. Last, the phosphor material needs to be dispersed homogeneously over the detection area for X-ray imaging applications.

One of the most successful applications of PSL would be digital X-ray radiography. The detector plate making a use of PSL effect used in X-ray radiography

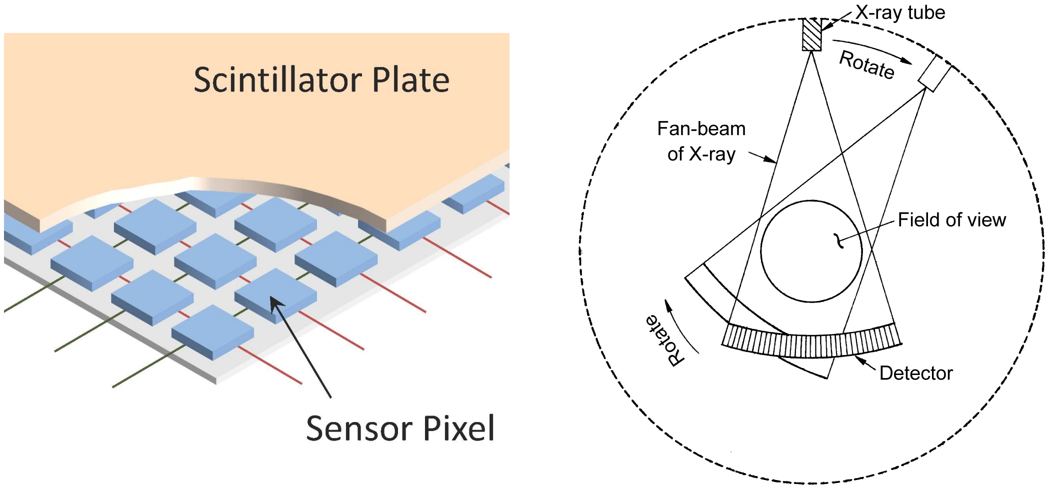

(a) (b)

Figure 2.13: Examples of scintillator applications for X-ray detection. (a) Indirect flat panel radiographic detector. A scintillator plate is placed on an array of photo detectors. (b) Computed Tomography (CT). A scintillator plate is coupled with the detector array.

is often referred as an imaging plate. Figure 2.12 (b) illustrates the mechanism of PSL. An interaction with X-rays results in the generation of electrons and holes in the phosphor matrix (①). Next, the free charges either recombine at the local luminescent centres immediately (②), giving rise to XL, or become captured by local trapping centres (③). These trapping centres are metastable, therefore the trapped charges can be detrapped by stimulating optically ($h\nu$) (④), and then the charges will recombine at local luminescent centres, which results in light emission. Rare earth ions are often used as the luminescent centre. In the PSL processes, the trap depth must be deep enough to be stable over a long time, meaning that trapped charges do not become detrapped by ambient temperature or light exposure. Meanwhile, the trapping depth should not be too deep, so that stimulation is possible with low energy photon. The ability of low energy photon stimulation makes it possible to detect signals only from the PSL process without exciting the luminescent centre directly. A radiographic system using PSL in BaFX:Eu^{2+} (X = Cl, Br, or I) has been developed by FUJIFILM in 1978, which was the first commercial radiographic system after the first discovery of the PSL effect in a chalcogenide material in 1947

[8]. An imaging plate where powderized phosphor is homogeneously distributed over the film is used to detect X-rays, and then the recorded information is digitized using a reader system as illustrated in Figure 2.14 as an example. The stimulation laser beam (red) is guided to the imaging plate using a scanning mirror through a focusing lens. The resulting PSL signal (blue) is guided to a suitable photodetector such as a PMT. The image resolution strongly depends on the focus size of stimulation light and the scattering of light in the imaging plate.

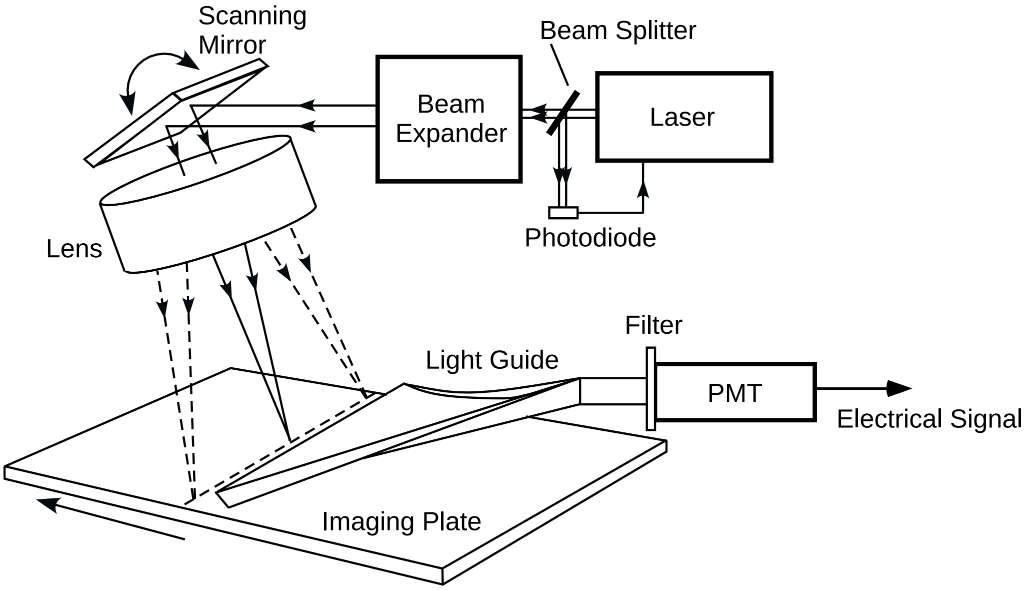

Figure 2.14: Schematic of radiographic imaging plate reader. Reproduced after [9].

2.8 Phosphors for Dosimetry

Rare earth doped materials are also used in dosimetry applications. In such applications, rare earth ions are doped in a suitable material to act as luminescent centres. *Thermally-stimulated luminescent* (TSL) dosimetry is one of the kinds that have been most widely used in dosimetry practice. Details of luminescent mechanism vary depending on the detector material types, but the mechanism is briefly described here. As shown in Figure 2.12 (b), the TSL material is ionized by absorbing the deposited X-ray energy. A fraction of generated electrons and holes will recombine immediately at the luminescent centres (indicated as ②) as seen in a scintillator material, but just as in PSL phosphor material the remainder of charges are captured by metastable trapping centres and locally stored (indicated as ③). The number of captured charges is supposed to be proportional to the irradiation dose. In the TSL material, the captured charges can be detrapped back to the transport band by thermal stimulation ($h\nu$ equivalent of thermal energy), and then the freed charges will recombine at local luminescent centres resulting in light emission ($h\nu'$) (indicated as ④). The detector is heated at a constant rate over a certain temperature range. The integrated light intensity is proportional to the number of trapped charges, which in turn is proportional to the deposited dose. Instead of thermal stimulation in TSL, optical stimulation just like PSL-based imaging plate has been also used. Such a method is referred as *optically stimulated luminescence* (OSL) dosimetry [10].

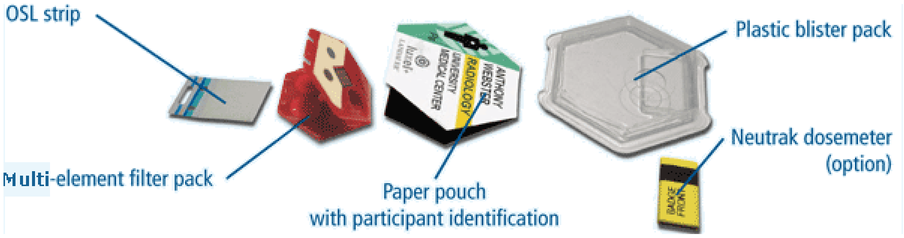

Figure 2.15: A commercial dosimeter capable with TL and OSL readout. From [11].

An example of commercially available dosimeter is manufactured by Landauer Inc., USA. The sensing material is Al_2O_3:C crystalline and distributed as a badge to wear, as shown in Figure 2.15, and to monitor radiation dose. After a certain time period of use, the badge will be returned to a lab and the accumulated dose over the time is measured using a setup illustrated in Figure 2.16 as an example. The reader setup is capable of measurement by both thermal- and optical-stimulation. For TL, a heating element is placed underneath the sample, and the consequent luminescence is measured by the PMT through an optical filter as the temperature is elevated. For OSL, blue or IR stimulation is guided onto the sample, and then the luminescence is detected by the PMT.

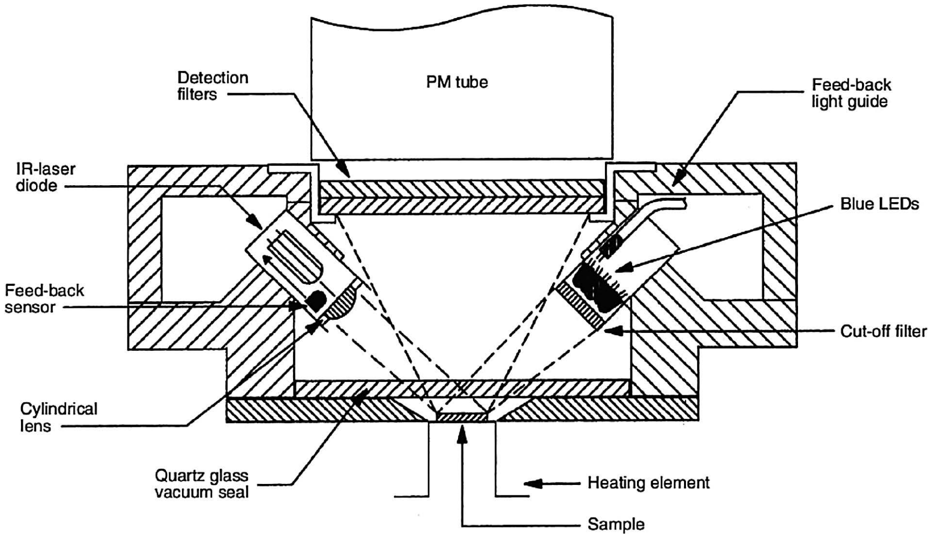

Figure 2.16: Example of TL/OSL reader setup. Reprinted from [12].

Important characteristics to consider for dosimetry include:

1. response linearity
2. emission spectrum
3. stability
4. energy dependence
5. tissue equivalence
6. reusability

Detector response such as light intensity increases as the deposited X-ray dose increases. When the response is linearly proportional to the deposited radiation dose in the dose range of interest, it has a large advantage that the dose calibration process needed after the signal readout is straightforward, and the errors on dose calibration fitting is minimized.

As for phosphor materials in X-ray imaging applications, the luminescent spectrum should match the spectral sensitivity of photodetector. The material should be transparent to the PL light.

A reliable dosimetric material should store the dose information without fading until readout. Fading may occur by unexpected stimulation by the ambient temperature or by ambient light exposure in which the detector is stored post-exposure.

This may occur especially when the trap depth from the transport band is shallow. Risk of fading is reduced when the charges are trapped at deeper centres.

It is of importance for dosimetric detector that the sensitivity is independent to the radiation energy. An energy dependent detector requires calibration, which always includes a certain degree of error.

Tissue equivalent materials are those that have X-ray absorption and scattering properties equivalent to tissue. When a dosimetry detector is used in applications such as radiosurgery, the detector material should be tissue equivalent otherwise the detector material would block the majority of radiation at upstream of patient. Also, tissue equivalent material can be used to simulate the radiation behaviour in human tissue.

A reusable detector material would, of course, be economically and environmentally friendly. A reusable detector is one that has an ability that the recorded information can be, somewhat, erased intentionally, and the dose-response behaviour must be consistent regardless of erasure history.

Chapter 3

Microbeam Radiation Therapy and its Dosimetry

3.1 Introduction

This thesis focuses on development of new X-ray dosimetry techniques. The techniques are designed to be used particularly in microbeam radiation therapy (MRT) and its research. Such radiosurgery uses an X-ray beam which is spatially modulated on a micrometer scale; and the dose contrast between large-dose and low-dose regions is extremely high. Due to the very unique properties of MRT, none of existing dosimetry satisfactorily meets the stringent requirements – high-spatial-resolution and large-dynamic-range in the large dose range. The work reported in this thesis is based on developing a dose detection technology with high-resolution and large-dynamic-range.

The next section describes how MRT is carried out and its special characteristics. The following section (3.3) discusses dosimetry approaches and contrasts between computational and experimental techniques. Further, Section 3.4 describes dosimetric detectors tested for MRT in earlier studies in the literature. Finally, our novel dosimetry technique is proposed in Section 3.5. In addition to basic concepts, discussions from materials to instruments are made.

3.2 Microbeam Radiation Therapy

Radiosurgery is a form of medical procedure in which radiation is delivered to a local area of a patient to kill malignant cells, or tumour. In contrast to the conventional surgery, radiosurgery is a non-invasive treatment. In general, radiations such as X-rays, γ-rays, proton, or neutron are directed to the tumour to destroy the tumour during irradiation, and invariably healthy tissue is also somewhat damaged, hopefully for minimal extent.

Microbeam radiation therapy (MRT) is a type of radiosurgery where X-rays are used. MRT has been first reported by Slatkin et al. in 1992 [13]. Figure 3.1 illustrates the way that MRT is typically carried out. It utilizes an X-ray beam which is spatially fractionated and consists of a bundle of micro-scale planar rays travelling parallel to each other. This type of specialized X-ray beam is a so-called microbeam. A typical distribution of X-rays over the cross-sectional area of microbeam is illustrated in Figure 3.2. The microbeam is typically produced by inserting a multi-slit collimator (MSC) in the path of a broad and well-collimated X-ray beam. The MSC is often made of a tungsten block where a number of micro-scale slits are cut in parallel to each other; hence the microbeam is produced as the X-rays are transmitted through the slits.

Some of the terminologies commonly used in MRT research slightly differ between various disciplines; here we attempt to clarify and define the terminologies used in this thesis. As mentioned above, a *microbeam* is considered as an array of microplanar beams each with the thickness of $20 - 100$ μm. Some works in the literature use this term to refer to an individual narrow beam, however it seems like that the term in this manner is commonly used in the dosimetry side of MRT research. The separation of individual beams is described by using a *centre-to-centre distance*, which is the shortest distance from the centre of one beam to the centre of an adjacent beam. It should also be pointed out that, when we discuss the design of MSC, the centre-to-centre distance refers to the shortest distance from the centre of one slit to the centre of an adjacent slit, which is theoretically the same as the centre-to-centre distance

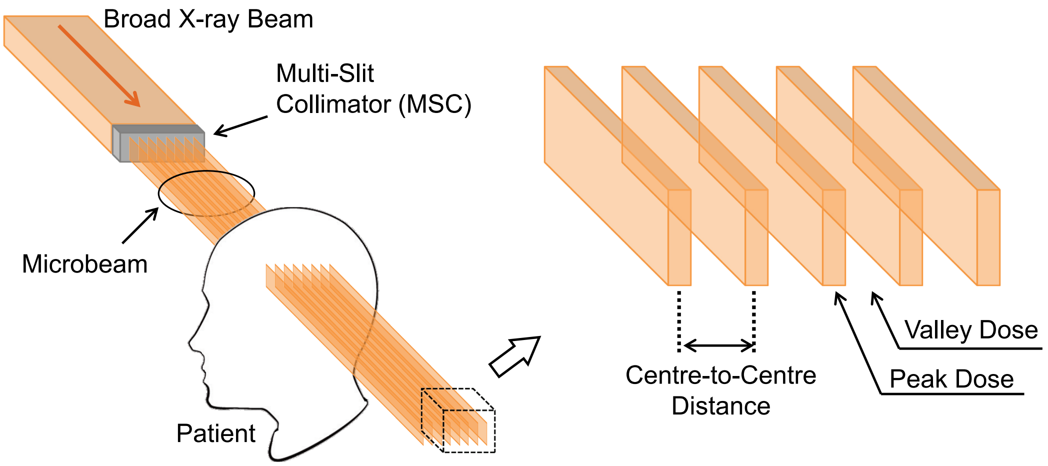

Figure 3.1: Illustration of microbeam radiation therapy (MRT). (Left) Microbeam is created by inserting a multi-slit collimator in a collimated broad X-ray beam path such as a synchrotron radiation, and then delivered to the patient. (Right) A microbeam, in general, consists of a number of microplanar beams oriented parallel to each other. The beam width, centre-to-centre distance, peak dose, and valley dose are important parameters to determine the quality of therapy.

between the neighbouring maxima in the radiation pattern. The largest X-ray dose in the microbeam is located at the centre of each individual beam, and this is called *peak dose*; whereas the dose value between two adjacent beams is called the *valley dose*.

One of the key advantages of using a microbeam is for its superior sparing effect. When the patient is treated with a microbeam, human tissue experiences very large dose at the peak (hundreds of grays) while the valley dose is maintained below the threshold. After the treatment, under such conditions, evidence shows that partially damaged healthy tissue located in the beam path, on one hand, will recover with the help of adjacent healthy cells, which would have been exposed to radiation in the valley and hence only minimally damaged. On the other hand, the cancer cells do not show such an ability to recover (whether irradiated or not), hence the entire tumour will necrosis. To date, the physical and biological mechanisms of this sparing effect are not fully understood. Nevertheless, the experimental evidence shows that, for a successful treatment, the peak dose and the valley dose have to be well controlled and the ratio of peak dose to the valley dose is a key parameter for a successful

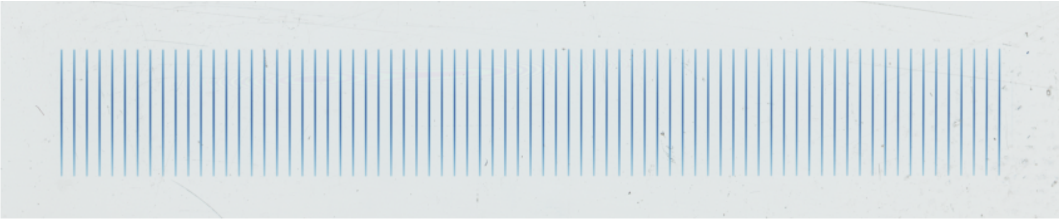

Figure 3.2: An example of a microbeam pattern. It was measured using a GafChromic$^{\textregistered}$ film detector at Bio-Medical Imaging and Therapy (BMIT) beamline, Canadian Light Source, Saskatoon. The each planar beam has 50 μm width separated by 400 μm from centre to centre. Total number of planar beams is 75.

treatment. This dose ratio is called the *peak-to-valley dose ratio* (PVDR). The peak dose is understood to be strongly dependent on the dose given by the broad beam (as shown in Figure 3.1). However, the X-rays in the valley is a contribution of scatterings and X-ray divergence, thus the valley dose, in turn PVDR, depends on a number of parameters including the width of micro planar beam, centre-to-centre distance, density of patient cells, distance from the MSC etc. Optimized treatment conditions are currently under investigation. With this sparing effect, MRT has a great advantage over conventional radiosurgeries for being able to apply a large dose to the patient.

Since the first report in 1993, MRT experiments have been carried out at synchrotron facilities. This is because synchrotron X-ray radiation has important characteristics which are essential for MRT. The key characteristics are:

1. minimum beam divergence,
2. high fluence rate, and
3. large photon energy ($<$ 150 keV).

and the reasons are as follows. When the divergence of beam is minimum (1), the microbeam includes minimum scattering of X-rays by MSC, which is made of materials with a large atomic number. Therefore, the minimum divergence of beam ensures a high contrast of peak and valley doses, thus large PVDR. (2) Bright X-ray source enables us to deliver large dose over a very short duration of time. A movement of patient during the treatment would result in a distortion of absorbed microbeam dose-profile where the peak dose value drops and the valley dose increases. Consequently, effective sparing effect as well as tumoricidal effect are not expected due to the low PVDR. Using a high flux microbeam would avoid the development of a low contrast of absorbed dose caused by an unwanted movement of the subject. (3) While the majority of low energy X-ray photons are absorbed at the surface of the target object due to the predominant photoelectric interaction, high energy photons (hard X-rays) have the ability to penetrate inside the body and make it to the affected area. Figure 3.3 shows an image of the brain of a piglet after a microbeam irradiation with an entrance skin dose of 300 Gy. It can be seen that the microbeam has penetrated to the inner brain.

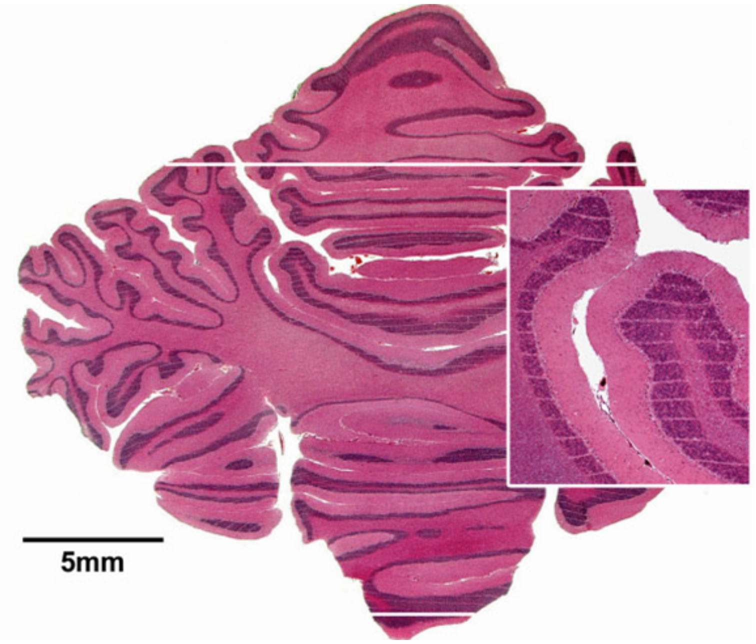

Figure 3.3: A cross-sectional image of the brain of a piglet after a microbeam irradiation. The skin entrance dose was 300 Gy. The tracks of microbeam are represented as lighter coloured lines. Each of the microplanar beams is about 25 μm wide and separated by about 200 μm. After [14].

The geometry of irradiation in MRT illustrated in Figure 3.1 has been the most common method and most intensively studied, but this has not been the only approach. This method is sometimes refereed as a *unidirectional* MRT in contrast to the method which delivers a microbeam from multiple directions (*multi-directional*). In the latter approach, the necessary damage of healthy tissue can be minimized without lowering the destructive impact to the tumour. In terms of the microbeam design, instead of using an array of planar beams, using an array of cylindrical beams is another optional approach [15]. In radiosurgeries, the use of radiosensitizer has been widely studied and clinically accepted, in practice, in order to enhance the effect of treatment; however, only a few studies have used in microbeam radiation therapy [16].

3.3 Dosimetry in Microbeam Radiation Therapy

MRT utilizes a highly specialized X-ray beam, a microbeam. The width of each individual beam is typically 10 to 100 μm, and the centre-to-centre distance is 100 to 400 μm. These parameters vary depending upon the design and the settings of MSC. MRT employs higher dose than ordinary radiosurgery at the centre of the microplanar beams (hundreds of grey) while the valley dose is controlled below the threshold of critical tissue damage. In order for MRT to advance into the clinical stage, it is essential for us to accurately understand the distribution of dose delivered over the patient. The dosimetry in MRT has been done mainly by two types of approach — computer simulation or experimental measurement.

Dosimetry by computer simulation has been extensively studied by using Monte Carlo codes which include EGS4 [17], PSI-GEANT [18], GEANT4 [19] and PENELOPE [15, 20]. These codes use different physical models and algorithms, which are beyond the scope of this research, in order to simulate the scatterings and divergence of X-rays, which in turn predicts the distribution of dose in the microbeam deposited to the patient. A simulated microbeam dose distribution profile is illustrated in Figure 3.4 as an example. The simulation of the microbeam profile is an inexpensive approach and allows invaluable estimation, which may not be easy to achieve experimentally.

In contrast to computational dosimetry, experimental dosimetry allows the measurement of the actual dose-profile which is delivered to the patient. Consequently, experimental dosimetry finds applications that include:

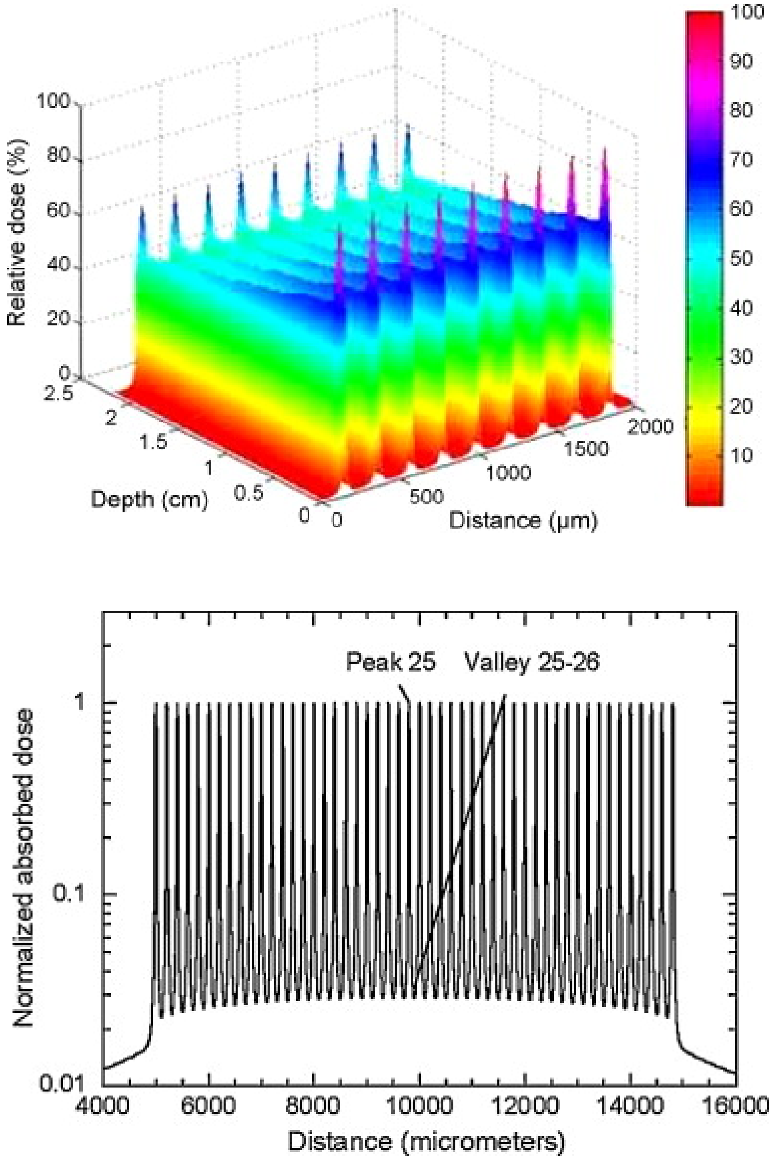

Figure 3.4: A microbeam X-ray dose distribution profile predicted by a Monte Carlo simulation. The microplanar beams have 25 μm width, and the centre-to-centre distance is 200 μm. [21]

1. Quality assurance,
2. Optimization of treatment conditions,
3. Study of physical mechanism, and
4. Legal record of patient file

(1) Quality assurance cannot be done without an experimental dosimetry. In particular, the alignment of the MSC requires highly precise positioning by a goniometer. In order to ensure the MSC has been properly aligned, the microbeam dose distribution pattern needs to be measured as a practical matter. (2) Successful MRT parameters need to be optimized, and experimental dosimetry would also have an important role in this regard. The MRT parameters to be optimized include peak dose and valley dose, PVDR, individual beam dimensions (width and height), centre-to-centre distance, number of microplanar beams etc. These parameters perhaps can be predicted by computer simulation; however, the actual measurement could interpolate the data caused by the unpredictable numerical parameters in the simulation such as imperfections in the collimator fabrication and alignment. (3) The microbeam shaped by the MSC is guided to the patient with a minimum change of beam parameters during the propagation. The X-ray beam suffers considerable scattering at the MSC and the beam divergence becomes significant as it propagates in the patient's body. These physical interactions of X-rays with matters would especially cause an increase of the valley dose and also the peak dose drops by the latter interaction, hence leading to a reduced PVDR. The actual measurement of the microbeam dose profile would help the researchers to study and understand the mechanism of the factors causing a low PVDR. (4) Information of microbeam parameters delivered to the patient should be recorded and filed as a legal record. The actual microbeam profiles can only be found by an actual measurement, thus experimental dosimetry is an indispensable asset.

As discussed above, dosimetry in MRT is both essential and indispensable for researchers to develop a successful treatment. Both the approaches by computer simulation and experimental measurement have their advantages, thus researchers need to utilize the two different approaches jointly in order to advance MRT. However, the scope of this thesis is on the experimental side of dosimetry, so we will discuss the experimental techniques in the following sections.

3.4 Potential Dosimetric Detectors

3.4.1 Fundamental Requirements

As mentioned previously, a search for an appropriate dosimetric detector is a primary and essential task. A successful dosimetry technique for MRT requires mainly two tasks - *spatial resolution* and *dynamic range*. As the dose distribution of microbeam is on a micrometer scale (each of microplanar beams in microbeam has the width of 20 to 100 μm and these are separated by 100 to 400 μm), the dosimetric detector needs to possess the resolving power of a few micrometers in order to accurately measure the dose distribution caused by the divergence and scattering of the X-ray beam. Moreover, the microbeam carries a very large dose at the centre of the microplanar beam (hundreds of grays) whereas the valley dose has to be kept lower than the threshold of normal tissue damage. Therefore, the detectable dose range of the required dosimeter must cover both the peak and valley doses, which is in a range of 5 to 1000 Gy.

Since the evolution of MRT, many dosimetric techniques have been tested and also specially developed. Bräuer-Krisch et al. [22] have reviewed the potential dosimetries for MRT, and the different approaches are introduced in the following sections. Table 3.1 summarises the potential dosimetries in terms of the dynamic range and spatial resolution.

3.4.2 MOSFET

The Metal-Oxide-Semiconductor Field-Effect Transistor (MOSFET) consists of a gate-oxide layer (SiO_2) deposited on a silicon crystal. Upon X-ray irradiation, electrons and holes are generated in the silicon oxide layer, and then the charges are collected through the gate. Since the device is oriented in such a way that the cross-

Table 3.1: Potential Dosimetries for MRT. Data taken from [22]

Dosimetry	Dose Detection Range	Spatial Resolution	Remarks
Flash Memory MOSFET	1 – 1000 Gy	0.2 μm	One dimensional
Polymer Gel Dosimetry	0.01 – 100 Gy	> 100 μm	Three dimensional
Fluorescent Nuclear Track Detector (FNTD)	0.005 – 50 Gy	0.6 μm	Confocal readout capability
High-Resolution Thermo-Luminescence Detector	0.01 – 500 Gy	~ 0.5 μm	
GafChromic® Film Dosimetry	10 – 400 Gy	12.5 μm	Commercially available
Optical Computed Tomography	10 – 500 Gy	20 μm	Three dimensional
Silicon Strip Detector	10 – 50000 Gy	10 μm	Real time, One/two dimension

section of the layer is perpendicular the X-ray beam direction (so-called edge-on orientation), the flash memory MOSFET has a lateral resolution as much as the thickness of the sensitive oxide layer (< 1 μm). This technique has been developed to especially monitor the peak and valley doses of microbeam online during the therapy [23, 24, 25, 26]. The detection range is sufficiently large; however, the spatial resolution is insufficient to resolve the beam pattern. Moreover, two dimensional mapping is preferred for MRT dosimetry.

3.4.3 Polymer Gel Dosimetry

Polymer gel dosimetry [27, 28] utilizes the polymerization of monomers dissolved in polymer gel matrix by interaction with X-rays. The polymers after the reaction can be detected by using a magnetic resonant imaging (MRI) technique. Since the polymer gel is characterized as tissue equivalent, the microbeam dose distribution as a function of the depth in the tissue can be continuously measured, with a use of MRI readout in the three-dimensional space. However, the detection at large dose as well as the spatial resolution needs to be improved for practical applications.

3.4.4 Fluorescent Nuclear Track Detector (FNTD)

Fluorescent Nuclear Track Detector (FNTD), shown in Figure 3.5, is an aluminium oxide single crystal doped with carbon and magnesium (Al_2O_3:C,Mg) [29]. Electron and hole charges are created by the X-ray irradiation and the free electrons are trapped by F_2^{2+} color centres, giving rise to F_2^{+}, which emits in the near infrared range upon UV excitation. The fluorescent signal is read out by confocal fluorescent microscopy with high resolution. This technique has been developed for detecting tracks of heavy charged particles and neutrons. In order to apply it for dosimetry in MRT, the detection of high dose needs to be demonstrated.

Figure 3.5: Photograph of fluorescent nuclear track detector (Al_2O_3:C,Mg). After [30].

3.4.5 Thermally-stimulated Luminescence Dosimeter (TLD)

Thermally stimulated luminescence is often used for radiation measurement. Typically, the electrons and holes generated in the detector material by ionizing radiation are captured by local trapping centres and stored. The trapped charges are released back by thermal stimulation which is followed by recombination of electrons and holes giving rise to light emission. Ptaszkiewicz et al. [31] have developed LiF:Mg,Cu,P-based TL foils and a reader, shown in Figure 3.6, equipped with a CCD camera and heater. The image resolution is typically limited by the pixel size of camera and the thickness of the detector material. The thinner the thickness of detector matrix, the better the image resolution, because the resolution is strongly limited by the scattering of light emission inside the detector matrix. On the other hand, the light yield is lower, which results in a decrease of signal-to-noise (S/N) ratio, as the detector volume decreases with decreasing the thickness. The TLD measurement technique needs to be improved for detection at high dose as well as in terms of the spatial resolution to apply in MRT.

3.4.6 GafChromic® Film Dosimetry

GafChromic® (HD-810) film (Figure 3.7) is a self developing dosimetry film specifically created for radiotherapy applications, and it is commercially available world-

Figure 3.6: A prototype of readout set-up for two-dimensional thermally stimulated dosimetry. After [32].

wide. It turns dark (reddish) as it is exposed to radiation. Therefore, the deposited dose is read as light transmission (or absorption); and signal readout may be done by a micro-densitometer or ordinary optical scanner. Although it does not fully satisfy the requirements for MRT dosimetry, it has been nonetheless used to characterize microbeam in MRT research for its easiness of handling and for its availability in the commercial market. Crosbie et al. [33] have attempted to measure both peak and valley doses together by combining two different films that have different dose detection ranges; one is for measuring the peak dose and the other one is for valley dose detection. The response seems to be insignificantly dependent on the X-ray photon energy (30 % of decrease when the energy drops from 1.7 MeV to 28 keV [34]. Further, the response is unstable within $1 - 2$ days after the irradiation (approximately 10 % increase).

3.4.7 Optical CT

Optical computed tomography approach proposed by Doran et al. [35] use a radiochromic plastic called PRESAGE$^{\text{TM}}$ as a detector material. The PRESAGE$^{\text{TM}}$ is a colourless and transparent material, but it turns dark by X-ray irradiation and the change in optical density is used as a probe of X-ray dose. The detector is a cylindrical bulk material, and irradiation is made from one side of face. The optical

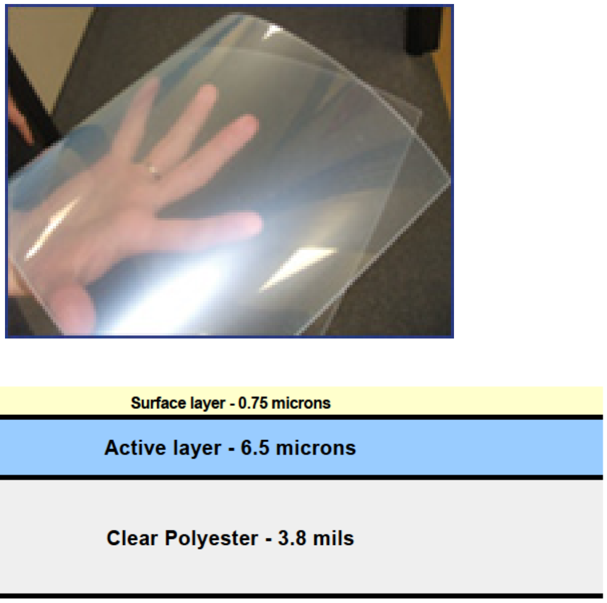

Figure 3.7: Photograph (top) and a layer configuration (bottom) of GafChromic® film (HD-810). The images are after the manual.

density is read out by the same manner as X-ray CT but using the transmission of visible light instead of X-rays. The PRESAGE^{TM} is tissue equivalent, thus the distribution of microbeam as a function of depth in the tissue can be easily studied.

3.4.8 Silicon Strip Detector (SSD)

A silicon strip detector (SSD) is often used in the studies of high energy particles as a sensing technique to detect the position of a high energy particle. Typically, an n-type silicon bulk is sandwiched by an array of p-type silicon semiconductor strips deposited and a plane of electrode or another set of silicon strip array aligned perpendicular with respect to the other set. Upon interaction with a high energy particle, electron and hole charges are generated in the silicon bulk and then collected by the strip channels. For its simple architecture, the strips can be densely fabricated thus small can be achieved. A single silicon strip detector chip (Figure 3.8) has been tested for microbeam detection by Lerch et al. [36] and Petasecca et al. [26]. The dose detection is excellent in the high dose range, but spatial resolution needs to be improved. In addition to the capability for a real time measurement, as in the case of a MOSFET detector, the SSD is essentially capable for two-dimensional detection.

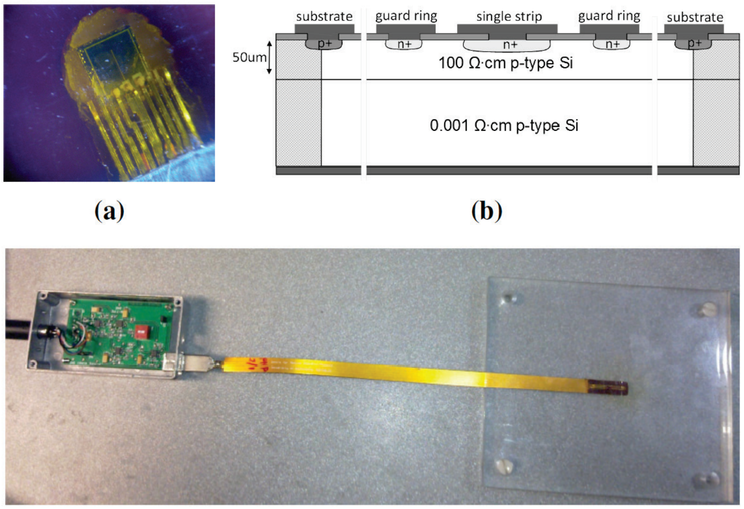

(a)

(b)

(c)

Figure 3.8: An example of silicon strip based detector prototype for microbeam radiation therapy dosimetry. After [26]

3.5 Proposed Approach

In Microbeam Radiation Therapy (MRT), a spatially fractionated X-ray beam, or microbeam, is deposited to the patient to cure a tumour such as brain cancer. In order to resolve such an extremely high gradient of X-ray dose at a micrometer scale, a specialized dosimetry technique needs to be developed. As mentioned before in Section 3.4.1 a successful dosimetry should, essentially, have a few micrometer of image resolving power with a high dose detection range, for example 5 – 1000 Gy.

Throughout the course of the research we have developed a new dosimetry technique towards the goal to fulfil the requirements. The technique is based on an *indirect X-ray detection* in which X-rays are, first, detected and stored on a dosimetric detector plate, and then the stored information is read and digitized using a special read technique based on confocal microscopy.

This chapter proposes and describes, in detail, our technique, and provides further scientific and technical discussions and analysis.

3.5.1 Basic Concept

This section briefly introduces our proposed approach to measure the X-ray dose distribution of microbeam used in MRT. Our approach mainly consists of two parts. One part is the *detection and recording* of X-ray dose distribution using a dosimetric detector plate. The second part is *readout and digitization* of the stored information on the detector plate. Figure 3.9 gives an overall illustration of our technique. Note here that, although only samarium (Sm) ion is sketched in the figure, our approach is not necessarily limited to using Sm ions embedded in a host material. Other ions that show valence change under X-ray radiation can also be used but the two valence states should have distinguishable PL characteristics. However, since only Sm^{3+}-doped materials have been mainly used in the research so far, the discussions below will refer to Sm ions for convenience. (Section 3.5.2 compares different rare earth ions as dopants that may possibly be used in the research.)

As the basic principle, we have intended to utilize a *valence reduction* process of Sm^{3+}. It is commonly understood that Sm^{3+} ions doped in a selected material show the reduction of valence state to the divalent state (Sm^{2+}) upon interaction with ionizing radiations such as X-rays or high energy particles. Therefore, as sketched in Figure 3.9 (left), when an X-ray beam is incident on the detector material, which is originally doped with Sm^{3+} ions, a fraction of Sm^{3+} ions only in the irradiated region is reduced to Sm^{2+}. Since both Sm^{3+} and Sm^{2+} ions are typically understood to show fluorescence in defined spectral ranges, the presence of reduction should be observable by PL measurement, which is shown on the lower left part of Figure 3.9. Here, we simply assume that the intensity of the PL signal by Sm^{2+} is proportional to the number of reduced Sm^{2+} ions, which is, further, proportional to the deposited X-ray dose. Therefore, the dosimetry technique utilizes the extent of $Sm^{3+} \rightarrow Sm^{2+}$ observed as a PL signal as a measure of the X-ray dose deposited.

The right side of Figure 3.9 is a simplified illustration of signal readout setup based on a *confocal fluorescence microscopy* technique. The confocal microscopy is a widely-used technique in various disciplines, such as biology and medicine. It

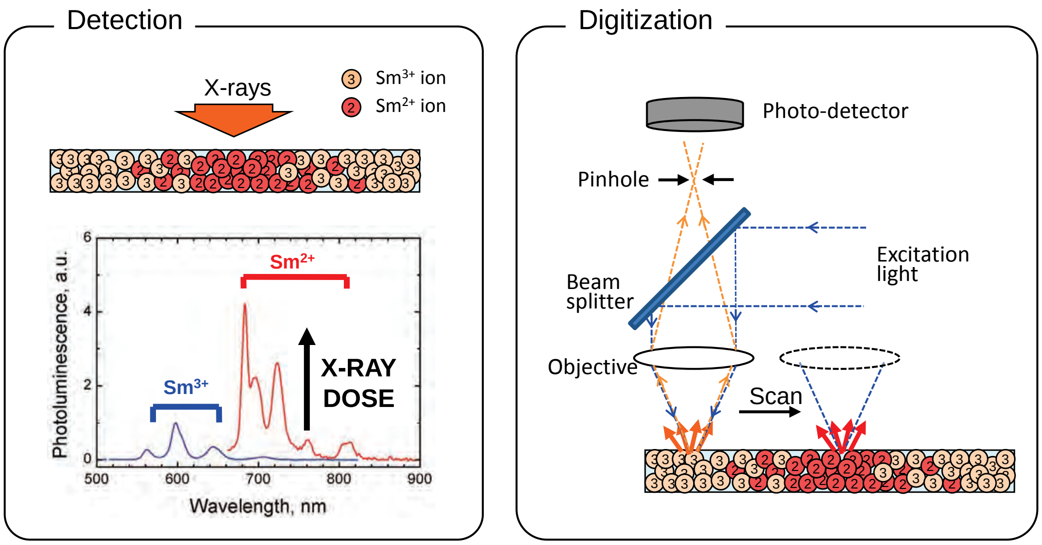

Figure 3.9: Illustration of the proposed dosimetry approach for microbeam radiation therapy. Sm^{3+} ions in the detector material are reduced to the Sm^{2+} by interacting with absorbed X-rays, and this reduction is used as a sign of the X-ray dose deposited and measured as PL signal (left). Confocal fluorescent microscopy is used in order to map the PL signals of both Sm^{3+} and Sm^{2+} over the detector plate, in turn X-ray dose distribution (right).

optically collects and measures fluorescence signals from a horizontal plane near the surface of a sample and maps the signals to visualize the fluorescence emission distribution on the detector plate. So, it is often used in biological applications such that a biological sample of interest is stained by a fluorescent ink and then scanned by the microscopy. Typically, confocal microscopy technique allows submicrometer spatial resolution. In our dosimetry approach, it is used to digitize the distribution of PL signals by Sm^{3+} and Sm^{2+} on the sample and to store the information on a computer for processing and analysis. The PL signal data are then calibrated to the dose values in the incident radiation. A principle of confocal microscopy will be discussed in Section 3.5.5 in this chapter, and the readout system we have developed throughout the course of research is introduced in detail in 4.5.

3.5.2 Valence Change of Rare Earth Ions

In our dosimetry approach, a valence change of rare earth ion caused by ionizing radiation is utilized as a probe of delivered dose. This section discusses the mechanism of valence change of this rare earth ion in detail.

Rare earth ions often display different properties in their different valence states. Therefore, a change of valence state in a rare earth embedded in a medium is often studied and discussed for a variety of applications. One of the most common methods to reduce the valence state is to synthesize the material under a reducing atmosphere such as hydrogen. Hydrogen donates its electron to the rare earth ion, for example trivalent (3+) state, and the reaction results in the divalent (2+) rare earth ion. Another approach is to include an additional chemical compound, or so-called reducing agent, during the synthesis. During the synthesis, or chemical reaction, the reducing agent donates electrons to the rare earths without affecting the properties of the host material [37]. Rare earths with a particular valence state prefer to locate at a particular cation site of a given crystal structure. For example, when an europium ion is forced to be included at strontium site in SrF_2, the valence state of europium is preferred to be divalent for charge compensation (two of negatively charged chlorine ions F^- is compensated with one divalent cation) [38]. A change of valence state of a rare earth ion cannot only perform during the synthesis but also after the synthesis as reported in the literature. The technique to reduce rare earth ions after synthesis includes the photoionization of host material by γ-rays [39, 40, 41, 42], X-rays [43, 44, 45, 46, 47, 48], β-rays [41, 49, 50], and focused infrared light from a femto-second laser [51, 52, 53, 54]. The reduction by ionizing radiation is, in fact, used in our dosimetry approach and is further discussed below.

The mechanism of valence change by photoionization is not fully understood and the interpretation may vary depending upon the host material. However, in general, it is commonly explained that ionized charges (electrons and holes) generated by the photoelectric interaction are captured by trapping centres. Here, the rare earth ions may act as either electron traps or hole traps (under certain conditions). As a result, the valence state may be reduced by capturing an electron; or the oxidation state may be increased by capturing a hole. To discuss the oxidation process of rare earths, one may use the so-called Dorenbos model [55]. Dorenbos has systematically studied the location of a series of rare earth ions doped in chemical compounds. As an example, Figure 3.10 illustrates energy band diagram of CaF_2 crystal with the locations of divalent and trivalent rare earth ions indicated. His systematic research over a numerous number of materials has revealed that the relative location between trivalent rare earth ions as well as between divalent ions are consistent regardless of the host material. However, what differs in different materials is the relative location of ground level of divalent rare earth ions with respect to the bottom of conduction band; also, the relative location of ground level of trivalent rare earth ions with respect to the top of valence band differs. As it turns out, the ground level of Eu^{2+} ion locates at the lowest energy among the rare earth ions always, and Sm^{2+} locates at the next lowest energy, regardless of host matrix.

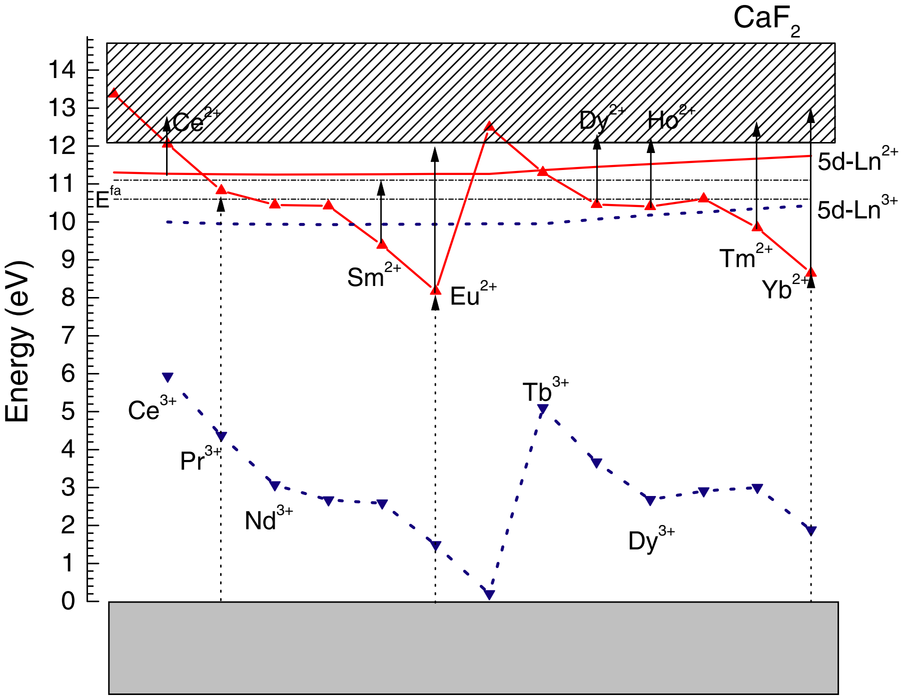

Figure 3.10: Location of trivalent and divalent rare earth ions in the energy band diagram of CaF_2 crystal. The relative positions over the different rare earth ions are consistent regardless of the type of host material. The position of ground state of divalent ions relative to the bottom of conduction band and the ground state of trivalent ions relative to the top of valence band may vary depending on the host material. After [55].

When the energy levels of the rare earth ion is located within the forbidden band, then the rare earth ion may act as a trapping centre. For example, Eu^{2+}, Ce^{3+}, Pr^{3+}, and Tb^{3+} often act as a hole trapping centre [56, 57]. They capture free hole charges from the valence band and then, as a result, become Eu^{3+}, Ce^{4+}, Pr^{4+}, and Tb^{4+}, respectively. Such a reaction may be expressed as:

$$\mathrm{Eu^{2+} + h^{+} \longrightarrow Eu^{3+}} \tag{3.1}$$

$$\mathrm{Ce^{3+} + h^{+} \longrightarrow Ce^{4+}} \tag{3.2}$$

$$\mathrm{Pr^{3+} + h^{+} \longrightarrow Pr^{4+}} \tag{3.3}$$

$$\mathrm{Tb^{3+} + h^{+} \longrightarrow Tb^{4+}} \tag{3.4}$$

Here, it should be instructive to note that these ions may act as a ”stable” trapping centre only when the ground level of consequent valence state still remains within the forbidden band, and also locates far from the top of valence band. If Eu^{3+} and Ce^{4+} take their positions in the valence band, the captured hole will be immediately released back to the valence band. Moreover, if the location of Eu^{3+} and Ce^{4+} are still in the forbidden band but very close to the top of valence band, then the captured charge will be most likely released back to the valence band due to phonon excitation etc.; therefore the trapping centre is not stable.

Now, consider electron trapping: Sm^{3+}, Eu^{3+}, and Yb^{3+} would be good candidates as a stable trapping centre for the same reasons discussed for hole traps. The divalent forms of these ions locate at low energy levels among other ions based on the Dorenbos model. It means that there is a good chance that, after capturing electrons, the ground energy level of resultant divalent state would still position below the bottom edge of conduction band in such a way that the captured electron will not easily escape. In this case, these ions act as stable electron traps. By the same manner as hole trapping, such trapping process may be expressed as:

$$\mathrm{Sm^{3+} + e^{-} \quad \longrightarrow \quad Sm^{2+}} \tag{3.5}$$

$$\mathrm{Eu^{3+} + e^{-} \quad \longrightarrow \quad Eu^{2+}} \tag{3.6}$$

$$\mathrm{Yb}^{3+} + \mathrm{e}^{-} \quad \longrightarrow \quad \mathrm{Yb}^{2+} \tag{3.7}$$

3.5.3 Host Material for Rare Earth Ions

Our dosimetry detector medium embeds rare earth ions. As discussed earlier, the extent of valence reduction of a rare earth ion ($\mathrm{RE}^{3+} \rightarrow \mathrm{RE}^{2+}$) due to X-ray irradiation is to be used as a probe of X-ray dose; and it is read out as a PL signal using a confocal microscope at high resolution. This section discusses a variety of potential host materials in which rare earth ions are included and to be used as a dosimetric detector plate in our research.

From the physics point of view, the host matrix must be such that the embedded rare earth ion can change its valence state upon X-ray irradiation. In principle, as discussed in Section 3.5.2, in order for the ions to change the valence state, they need to act as a stable electron trapping centre. Moreover, the stable electron trapping centre is such that the location of, for example, RE^{3+} must be within the forbidden band (above the top of valence band), and the location of the ion after capturing an electron (RE^{2+}) is well below the bottom of conduction band. According to the Dorenbos model, the energy gap between RE^{3+} and RE^{2+} varies depending on the host material; however, there is a better chance for a rare earth to be a stable electron trapping centre when the band gap between the bottom of conduction band and top of valence band is wide. For example, fluoroaluminate and fluorophosphate glasses, which seem to allow the valence change, have the band gap energies of 8.25 and 7.8 eV, respectively [58]. Further, most of trivalent rare earths doped in CaF_2 can be reduced by X- or γ-ray irradiation at 77 K [59] where the band gap of CaF_2 is very large, 12 eV [55]. As far as we are aware, the valence change of rare earths embedded in a material with small band gap energy has not been reported.

Usually, a phosphor material for X-ray imaging applications is preferred to be transparent to light. A scintillator plate converts X-rays to visible light in general, therefore the plate is placed on an imaging sensor to indirectly measure X-ray intensities distributed over the field of view. If the scintillator material is not transparent to light, the converted light is scattered as it travels in the material. As a result, the image resolution is lost. The same idea applies to an X-ray storage phosphor, or imaging plate. X-ray information is stored as charges trapped at localized centres. A focused laser beam is raster-scanned over the plate, which stimulates the trapped charges to be free, and then the charges are recombined at luminescent centres followed by a light emission. The emitted light is digitized through a photodetector to construct the X-ray image detected. Here, the storage phosphor material needs to be transparent to both the stimulation and emission light. Otherwise the light scattering would reduce the image resolution. Figure 3.11 shows an X-ray image of an integrated circuit detected by a transparent CsBr:Eu^{2+} imaging plate.

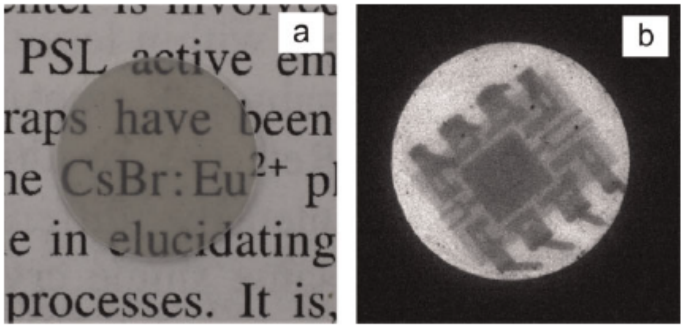

Figure 3.11: Example of a transparent X-ray phosphor. (a) Transparent CsBr:Eu^{2+} imaging plate. (b) X-ray image of an integrated circuit chip detected by a transparent imaging plate. After [60]

The rare earth may be included in the detector medium which can be different structures of materials. A crystal is a form of atoms, molecules or ions arranged periodically in a three dimensional periodic lattice. In a crystal, the number of neighbours and their orientations are well defined. Further, the chemical bonding length as well as the angle are also well defined in the presence of long-range order. When such crystal properties are extended over a certain area or volume, the material is referred as a single crystal. With its well-defined structural properties, numerical approaches have been widely undertaken to design and optimize the material. Further, in general, single crystal structures, compared with polycrystalline or amorphous counterparts, provide superior optical and electrical properties for most applications. For example, the solar cells that give the highest energy conversion to date is made of multiple layers of III-V based single crystal semiconductor [61].

Moreover, from the literature, it seems that most of reported RE host materials that allow the $RE^{3+} \rightarrow RE^{2+}$ change are crystals. Despite the excellence of material properties, it is a big challenge to grow a single crystal without (or with less) inclusion of unwanted impurities and defects over a large area or volume. It is important that the detector material is homogeneous over the area of interest.

Since it is not an easy task to fabricate a single crystal over a large area or volume, one may create fine crystal powder and then distribute it on a substrate. This technique allows the fabrication of a detector film over a large area while taking advantages of good optical properties of the crystal. This technique is commonly used for X-ray imaging plates. For example, computed radiography invented and commercialized for the first time by FUJIFILM is based on europium doped barium fluorobromide ($BaFBr_2$:Eu^{2+}) powder [62, 63]. During the digitization, the imaging plate is raster scanned by a red laser beam, and then the consequent blue photostimulated luminescence is detected. Since the readout of the imaging plate relies on an optical method, a severe light scattering of stimulation and emission light by the powder dramatically reduces the resolution. In addition, the larger powder size, the poorer resolution; and uniformly distributing the powder over the imaging plate is also a challenge.

A phosphor material can be mechanically shaped in order to improve the spatial resolution, which is limited by light scattering at the detector medium. Figure 3.12 shows an example of such a phosphor. The crystals (often NaI, CsI or CsBr with impurities as a luminescent centre such as rare earths) are grown in such a way that they forms a bundle of columnar-like structure, so each fibre acts like an optical fibre. When this is used as an X-ray imaging scintillator, it is placed on an imaging sensor. Upon X-ray exposure, scintillation luminescence is guided along columns, hence the light spread is minimal. When this type of device is used as a storage phosphor, a spread of the photostimulation beam as well as consequent luminescence is also controlled.

In contrast to crystals, glass (or amorphous solid) is characterized by the absence of long-range order. There is only short range order in the sense that only nearest

Figure 3.12: SEM micrograph of X-ray imaging plate based on CsBr:Eu grown as a bundle of columnar crystals. After [64].

neighbours are well defined. Typical structural defects that exist in the crystalline state are normally absent in the glassy state or have no meaning. For example, there are no dislocations or grain boundaries in the glass state. Point defects such as vacancies have no meaning. There are many possible configurational arrangements to the structure, which means that the glassy state has higher entropy. Unlike crystals, the fabrication of glass does not require a challenging task to eliminate the defects; as a result, it can be fabricated over a large area easily. For example, a most successful direct conversion X-ray imaging detector (shown in Figure 3.13) is based on amorphous selenium (a-Se) X-ray sensitive layer, which converts X-rays to charges and then the charges are read out by thin-film transistor (TFT) electronics. In this detector, a-Se is deposited on the TFT array uniformly, which allows the detector area size large enough to image a chest. Valence reduction of rare earth ions in a glass has been "first" reported by Qiu et al. [51] with a Sm^{3+}-doped sodium aluminoborate glass. The Sm^{3+} is reduced to Sm^{2+} when irradiated by an intense infrared femtosecond laser. Since then, a number of glass materials have been reported as a host of rare earth ions which can be reduced by irradiation of X-rays [43, 44, 45, 46, 47, 48], γ-rays [39, 40, 41, 42], β-rays [41, 49, 50] and infrared femtosecond laser [51, 52, 53, 54].

Glass-ceramics may combine the advantages of crystals and glasses. It is a type of material that has a glass matrix which contains nano-sized crystallites distributed

Figure 3.13: Direct conversion flat panel X-ray detector. Amorphous selenium sensitive layer is coated over the thin-film transistor array. Amorphous material has advantage to be easily fabricated over a large area homogeneously. After [65].

over the volume. It is often fabricated as a form of glass first, and then it is thermally treated in order to nucleate and grow nanocrystals inside the glass matrix. Therefore, the fabrication process is as easy as that of glass, and it is also easily made over a large volume or area. In addition, the included nanocrystals provide the distinct advantages of the crystalline state such as strong scintillation yield [6, 66], X-ray storage [67, 68, 69, 70, 71, 72, 73], up-conversion [74, 75, 76] etc. The crystalline size can be controlled by adjusting the heat-treatment conditions such as temperature and time. The transparency of glass ceramic is proportional to the size of crystallites; however it is possible to produce a glass ceramic as transparent as glass when the diameter of crystallites is maintained less than 50 nm [77] to maintain the transparency. Such glass ceramic (fluorochlorozirconate glass-ceramic) has been shown the improved image resolution by a factor of 5 compared to a $BaFBr_2$:Eu^{2+} powder based film [72, 78] when used as an X-ray storage phosphor.

3.5.4 Potential Materials

There have been a large number of materials reported to show the reduction of trivalent rare earth ($RE^{3+} \rightarrow RE^{2+}$) by various methods. This section introduces such materials as an example of potential dosimeter materials to be considered for use in this research.

There have been a numerous number of materials reported to be a host to give the reduction effect under ionizing radiation. However, the majority of the reports are in crystalline hosts. These materials include those showing the $Sm^{3+} \rightarrow Sm^{2+}$ change by X-ray irradiation in, for example, CaF_2 [79], $CaSO_4$ [80], $BaBPO_5$ [81], BaFCl [82], SrB_4O_7 [83], SrB_6O_{10} [83], $Mg_{0.5}Sr_{0.5}FCl_{0.5}Br_{0.5}$ [84], $LiBaB_9O_{15}$ [85], $Ba_3BP_3O_{12}$ [48], Ba_2SiO_4 [86].

Table 3.2 shows a list of glass materials as potential detector materials to be considered. The $RE^{3+} \rightarrow RE^{2+}$ change has been commonly observed in crystals, and such phenomena have been intensively studied especially for TSL dosimetric detector applications. In contrast, the valence change in glasses is a relatively new field of study. In 1999, Qiu et al. [51] has reported a $Sm^{3+} \rightarrow Sm^{2+}$ reduction in a B_2O_3-Al_2O_3-Na_2O glass by an intense infrared femtosecond laser irradiation. This is probably the first report or one of the first reports, as far as we are aware, of a reduction of trivalent rare earth doped in glass by photoionization. Since then such a reduction has been reported in borate, silicate, and fluoride glasses due to femtosecond laser [51, 52, 53, 54], γ-ray [39, 40, 41, 42], beta-ray [41, 49, 50], and X-ray [43, 44, 45, 46, 47] irradiations. One may notice that the majority of reported glasses are doped with the Sm^{3+} ion. One of the reasons is that, in the 1990s and early 2000s, Hirao's research group at Kyoto University, Japan, has intensively studied the use of such $Sm^{3+} \rightarrow Sm^{2+}$ transitions induced by femto-second laser irradiation or $Sm^{2+} \rightarrow Sm^{3+}$ by red laser irradiation for three dimensional optical memory applications based on spectral hole burning.

There are a number of samples in which the conversion has only been confirmed by melting the glass in a reduced atmosphere (denoted as H_2). Since a glass like SiO_2-Al_2O_3 has shown the conversion by both the methods (photoionization and reduction by H_2), it is worth testing conversion of these samples under X-rays, as well.

In addition to the materials in the tables, pure silica (SiO_2) glass may be an interesting material for its excellent transparency and because the band gap energy is large (8.2 eV [58]), however its high melting temperature (1600 °C) makes it difficult to synthesize by a conventional melt-quenching method using an ordinary electric furnace (the melting point can be lowered by the addition of compound(s) with a decrease in the band gap energy). Further, one may try to fabricate a high purity SiO_2 glass as a phase separation of an alkali borosilicate glass (such as SiO_2-B_2O_3-Na_2O) followed by acid leaching [87]. The obtained glass is heat treated to separate into two phases: high purity silica and alkali-rich borate phases. Since silica has a very low solubility in an acid medium, only the latter phase is extracted from the glass bulk. The result is a glass which includes pores in nanometer to microscale size; but, they can be removed by heat-treatment at the glass transition temperature at $\sim$1400 °C.

The idea of our dosimetry technique relies on the dosimeter device to show the valence reduction of rare earth ion ($RE^{3+} \rightarrow RE^{2+}$) doped in a dosimeter material. Perhaps, among the series of rare earth ions, Sm would be a reasonable choice with which we can develop our prototype and to show the proof of principle because:

1. earlier studies have already reported a notable valence reduction of Sm^{3+} doped in a number of materials (particularly glasses), and
2. PL and excitation spectra of both Sm^{3+} and Sm^{2+} are well defined regardless of the host material.

A search for a good host material for our applications would be one of the tasks to begin within the research project; thus it is of primary interest to test the existing materials first. Further, the transitions of Sm^{3+} and Sm^{2+} may tend to occur within the $4f$ orbitals, which is shielded by the surrounding $5s^2$ and $5p^6$ orbitals. Therefore, the influence by the host is small, which implies that the PL and excitation spectra do not vary significantly over different hosts. This would help us to design and develop a single readout set-up that works for multiple types of detector samples.

Sm-doped materials have, in recent years, been widely studied in a variety of optoelectronic applications such as X-ray imaging phosphors [88, 89, 90, 6], optical waveguides [91, 92], three dimensional optical memories [93, 94, 95], pressure sensors [96, 97], white LEDs [98, 99, 100, 101] and solar cells [98, 102, 103].

Table 3.2: List of glasses reported to show valence reduction of rare earth ion.

#	Host	Rare Earth Dopant	Preparation Method	Reduction Method	Reference
1	SiO_2-Al_2O_3	Sm	Sol-Gel	X-rays, IR, or H_2	[44, 53, 84]
2	SiO_2-Al_2O_3-TiO_2	Sm	Sol-Gel	IR	[54]
3	SiO_2-Al_2O_3-Na_2O	Sm	Melt-Quenching	H_2	[104]
4	SiO_2-Al_2O_3-B_2O_3-Na_2O	Sm	Melt-Quenching	H_2	[104]
5	SiO_2-Al_2O_3-TiO_2-ZrO_2	Sm	Sol-Gel	X-rays	[105]
6	SiO_2-Al_2O_3-B_2O_3-Na_2O-ZrO_2	Sm or Gd	Melt-Quenching	β- or γ-rays	[41, 49, 50]
7	SiO_2-$Al(PO_3)_3$-NaPO-$AgNO_3$	Eu	Melt-Quenching	γ-rays	[42]
8	B_2O_3-Na_2O	Sm	Melt-Quenching	H_2	[93, 106]
9	B_2O_3-Li_2O	Sm	Melt-Quenching	H_2	[107]
10	B_2O_3-K_2O	Sm	Melt-Quenching	H_2	[107]
11	B_2O_3-Al_2O_3-Na_2O	Sm, Eu	Melt-Quenching	IR, X-rays, or γ-rays	[51, 43, 40]
12	Li_2O-SrO-B_2O_3	Sm	Melt-Quenching	X-rays	[45]
13	Li_2O-BaO-B_2O_3	Sm	Melt-Quenching	X-rays	[46]
14	SrO-BaO-P_2O_5-B_2O_3	Sm	Melt-Quenching	X-rays	[47]
15	MgF_2-AlF_3-CaF_2-SrF_2-$Sr(PO_3)$ (Fluorophosphate)	Sm	Melt-Quenching	IR	[58]
16	MgF_2-AlF_3-CaF_2-SrF_2-YF_3-BaF_2 (Fluoroaluminate)	Sm	Melt-Quenching	X-rays	[108]

3.5.5 Confocal Fluorescence Microscopy

Confocal microscopy has been first invented by Marvin Minsky in 1955, and then patented in 1957 [109]. Figure 3.14 shows one of the schematic designs of confocal microscopy introduced in the patent file. Since the discovery, there has been numerous attempts made to improve the performance of the confocal microscope; however, in fact, the basic principle has remained the same to date. This section discusses the principle of confocal microscopy.

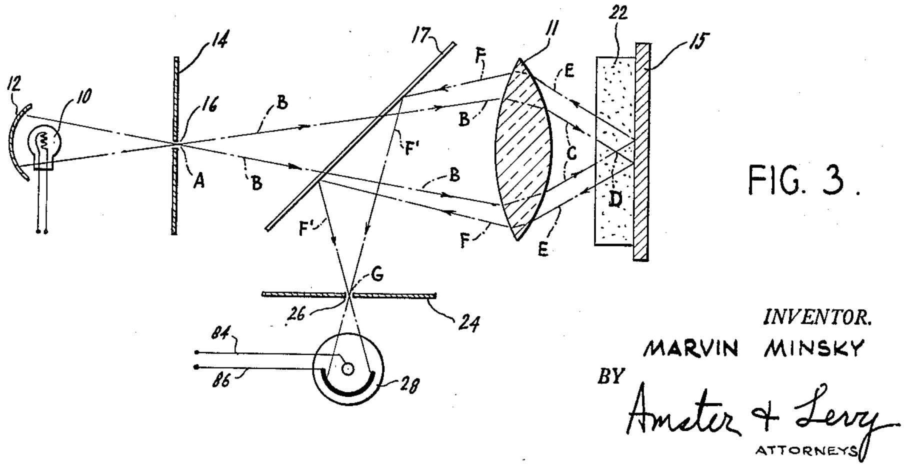

Figure 3.14: A schematic design of confocal microscopy. The diagram was reproduced after the patent filed by Minsky in 1957 [109].

The basic optical design of confocal microscope in Figure 3.14 enhances the image resolution over a conventional wide-field optical microscope. The proposed technique here is, in fact, to observe the transmission signal of light through a specimen; however, it is also applied for fluorescence imaging, which is what is used in the present work. In the figure, optical light emerging from the light source (denoted as 10) passes through a pinhole plate (14) and a beam-splitter (17) and is focused on to a specimen (22) by an optical lens (11). The focused spot is denoted as D. Further, the light transmitted through the focus point (D) reflects at the mirror (15) back towards the lens (11) and then focused at the point G on a pinhole plate (24), after reflection at the beam-splitter (17). Behind the pinhole plate (24), a photodetector is located, which digitizes the optical signal to be processed further. Here, by the use of pinhole apertures, light signals arising off the focus point (D) or scattering of light are diminished; hence the image resolution is enhanced. In the case of measuring fluorescence light instead of transmitted light, the mirror (15) in Figure 3.14 is no longer needed. A simplified illustration is shown on the right side of Figure 3.9. Since the specimen is a fluorescent material, the incident light wavelength is selected for an efficient excitation. The excitation beam is focused on the specimen to obtain fluorescence light at a local "imperceptible" volume. The resultant fluorescence light is collected through the lens and pinhole by the same manner as in Figure 3.14. Here, the role of pinhole is to eliminate the detection of the out-of-focus signal as well as scattered light at the specimen.

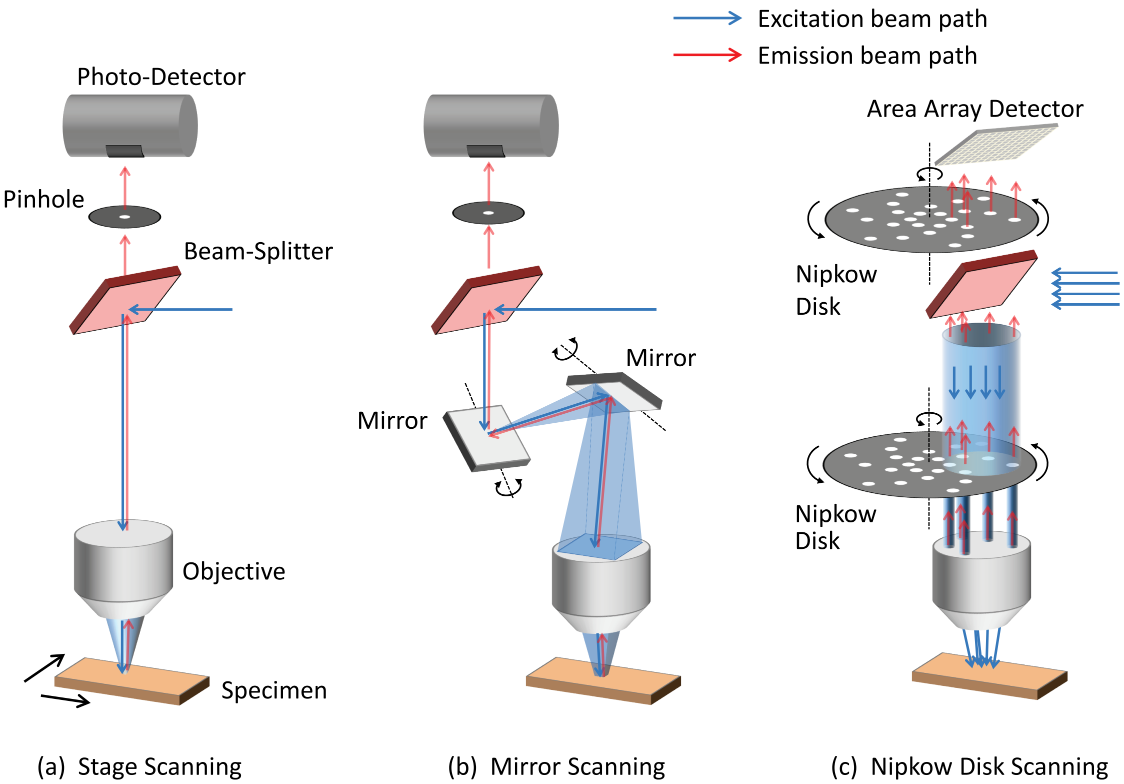

Figure 3.15: Illustration of various scanning methods used in confocal microscopy. (a) Stage scanning technique relies on the translation of the position of specimen. (b) A pair of mirrors is used to guide the excitation beam at a desired angle. Each mirror rotates around a single axis, and the two axes are perpendicular each other. (c) Nipkow disk acts to produce multiple planar beams exciting multiple spots on the specimen and also acts as a pinhole.

In order to obtain a complete two- or three-dimensional image, the measurement technique, discussed above, needs to be done at the every point of the area of interest in the specimen. Figure 3.15 illustrates three different scanning techniques used in confocal microscopy. The simplest technique would be to translate the specimen position while measuring the signal (Figure 3.15 (a)). Since this technique does not require mechanical movements of optics parts, the system can be relatively easily constructed and it does not require much maintenance. Further, the scanning area, or the field of view (FOV) is limited not by the FOV of objective lens but by the travel distance of the translating actuator, which is typically much larger than the FOV of objective lens. An alternative technique of scanning is to use a couple of rotating mirrors as shown in Figure 3.15 (b). Each mirror rotates around a single axis, and these two axes are oriented perpendicular each other. In this construction, it is possible to guide an excitation beam at a desired position in the two-dimensional space. However, the scanning area is limited by the FOV of the objective lens. Compared to the stage scanning technique, the scanning time is faster. The scanning using a Nipkow disk (Figure 3.15 (c)) might be the latest scanning technique for confocal microscopy. The Nipkow disk is a disk plate in which small pin holes are arranged in an Archimedean spiral at a constant pitch. In general, two disks are installed in the system (these are oriented just to sandwich the beam splitter and synchronized each other). Therefore, multiple parallel beams are created by passing a broad beam through the lower Nipkow disk; and further the upper disk works as pinhole assembly to enhance the image resolution. The greatest advantage of Nipkow disk scanning is the superior speed of scanning. It allows the excitation of multiple points on the specimen, and then the fluorescence signals from the each point may be detected separately by using photodetectors such as an area array detector, e.g. CCD, CMOS etc.

With a use of an objective lens, a light beam is focused having a beam shape of two cones as illustrated in Figure 3.16 (left). The interception region of these cones carries the highest light intensity and is used to excite an infinitesimal volume of sample. Further, upon excitation light scattering as well as out-of-focus signals are prevented by a pinhole from being detected; therefore, the image resolution achiev-

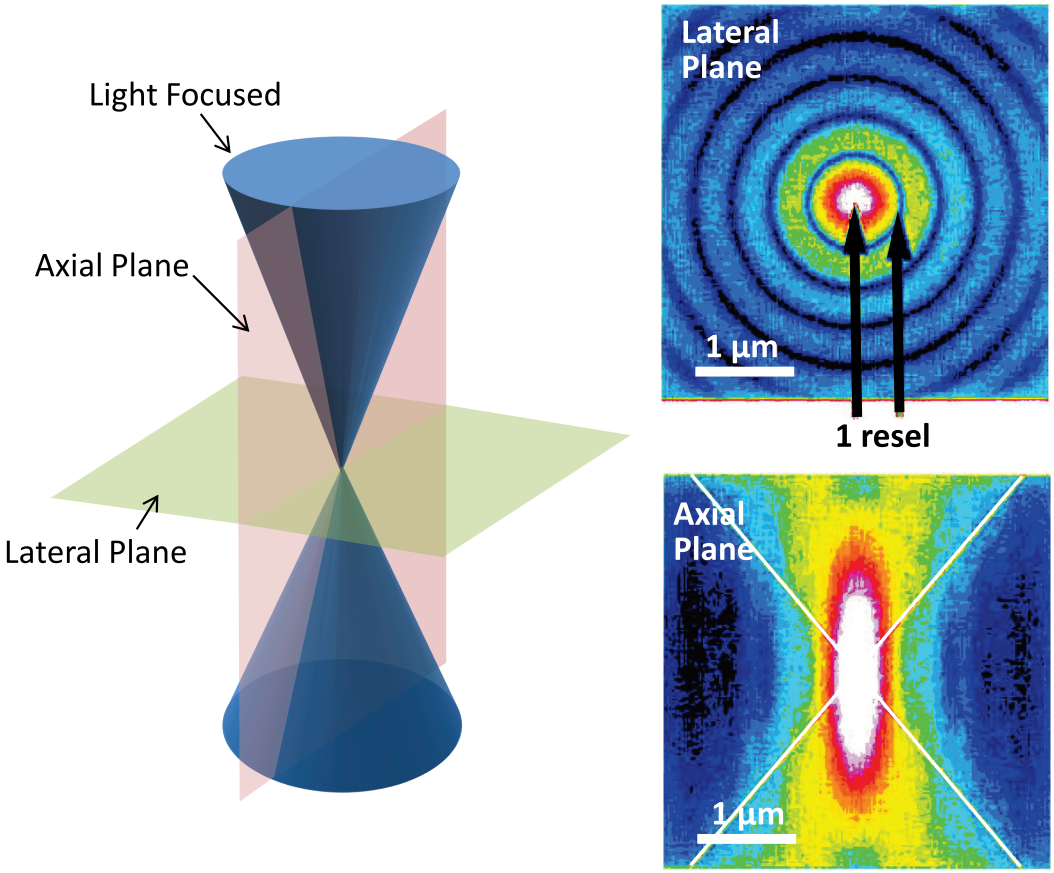

Figure 3.16: Example images of light diffraction when the light is focused by an objective lens. The left image is the lateral diffraction pattern in the focal plane, while the right image is the axial diffraction pattern. The image was obtained using an objective lens with the numerical aperture (NA) of 0.65 in a water environment ($n = 1.33$). The pixel intensity values are in logarithmic scale. The images were reproduced after [110].

able is theoretically limited by the diffraction of light. Adjacent light waves interfere constructively and destructively. The resultant intensity distribution pattern forms over a sub-micrometer scale of space. Figure 3.16 (right) shows example images of light diffraction patterns when a light beam is focused by an objective lens. It is often referred as a point spread function (PSF). The numerical aperture (NA) of lens is 0.65, and the light is travelling in water, in which the refractive index (n) is 1.33. The top-right image is a distribution of light intensities created by diffraction of light in the lateral focal plane, whereas the bottom-right image is those in the plane perpendicular to the lateral plane, or axial focal plane. Apparently, the focused light intensity is largest at the centre of the focal plane, and the intensity drops sharply with distance from the center; this creates a ring shaped centre at a focal point. Additional rings are observed with further distance from the centre. The centre part of this diffraction pattern is termed as an *Airy disk*. Since the highest intensity of light lies at the centre of the disk, the diameter of the inner ring is a theoretical measure of lateral image resolution of a confocal microscope. The axial image resolution, by the same manner, is given by the height of the focal spot at the half maximum intensity. Apparently, the axial resolution is larger than lateral resolution. These theoretical measures of resolution ($d_{x,y}$ for the lateral plane and d_z for the axial plane) are given by the following equations:

$$\begin{aligned} d_{x,y} &= 0.61\frac{\lambda}{NA} && (3.8) \\ d_z &= \frac{2\lambda}{NA^2} && (3.9) \end{aligned}$$

where λ is the wavelength of light and NA is the numerical aperture of objective lens. Usually, upon excitation of a sample, the consequent fluorescence light signal is weak (meaning that results in low S/N of image). Therefore, larger pinhole is used to detect more photons at a cost of spatial resolution.

CHAPTER 4

EXPERIMENTAL TECHNIQUES

4.1 Introduction

This chapter discusses the experimental procedure and techniques carried out throughout the course of the present study. The chapter starts with a description of synthesis techniques of our dosimeter materials in Section 4.2. The following section (4.3) covers various measurement techniques to characterize the prepared samples. These characterizations are based on measurements and observations by steady-state photoluminescence (PL) emission/excitation, PL life-time, optical transmittance, differential scanning calorimetry (DSC), X-ray diffraction (XRD), thermally-stimulated luminescence (TSL), and scanning electron microscopy. Section 4.4 discusses, in detail, the X-ray irradiation of the samples. The X-rays were produced either by an X-ray tube or synchrotron facilities at the Canadian Light Source (CLS), European Synchrotron Radiation Facility (ESRF), and SPring-8. Section 4.5 provides specifications of the confocal fluorescence microscopy readout set-up, which was used to digitize the response from the sample upon the X-ray dose deposited particularly for the measurement of microbeam dose profile. Conventional film dosimeters, irradiated together with our samples, were digitized using a scanner, which is discussed in Section 4.6.

Table 4.1: List of Major Samples Studied in the Research

Chemical Composition	Material Structure	Place of Synthesis
$BaBPO_5:Sm^{3+}$	Polycrystalline and Glass	Saskatoon
$SrBPO_5:Sm^{3+}$	Polycrystalline and Glass	Saskatoon
$SrB_4O_7:Sm^{3+}$	Polycrystalline	Sofia, Bulgaria
MgF_2-AlF_3-CaF_2-SrF_2-$Sr(PO_3)$-SmF_3 (Fluorophosphate)	Glass	Wellington, NZ
MgF_2-AlF_3-CaF_2-SrF_2-YF_3-BaF_2-SmF_3 (Fluoroaluminate)	Glass	Wellington, NZ
SiO_2-Al_2O_3-CaF_2-CaO-SmF_3 (Oxyfluoride)	Glass and Glass-Ceramic	Saskatoon

4.2 Sample Preparation

4.2.1 Introduction

We have tested several Sm^{3+}-doped samples towards the use of these samples in MRT dosimetry. These samples are either polycrystalline or glass, which has been doped with Sm^{3+} ions. Some samples were synthesized in our lab, while others were provided by other research groups. The materials that we have extensively studied in the research are listed in Table 4.1. The fluoride glass samples (FP and FA) were synthesized by our research partner Dr. Andy Edgar's group at the Victoria University of Wellington(Wellington, New Zealand). Other samples ($BaBPO_5$, $SrBPO_5$, and oxyfluoride) were made in our laboratory in Saskatoon. Throughout the search of potential dosimeter materials, these turned out to be of our particular interest and highly promising for MRT applications. Therefore, this section describes sample preparation methods used at this university and at the Victoria University of Wellington.

4.2.2 Sample Preparation in Saskatoon

In our laboratory, several different Sm-doped materials were synthesized. These samples include $BaBPO_5:Sm^{3+}$ and $SrBPO_5:Sm^{3+}$ polycrystallites and glasses, and oxyfluoride glass and glass-ceramic which contains $CaF_2:Sm^{3+}$ nano particles. The material syntheses were based on solid-state reaction, which is basically performed by heating a mixture of chemical compounds. The furnaces used to heat and fuse a mixture of compounds are illustrated in Figure 4.1. The ISOTEMP furnace (left) was used for our initial experiments to synthesize $BaBPO_5:Sm^{3+}$ and $SrBPO_5:Sm^{3+}$ polycrystalline samples, which require temperatures up to 1000 °C. The HOT SPOT 110 (middle) was used for syntheses which require higher temperature especially for producing glass materials. This furnace allows samples to be heated up to 1600 °C. The CMF1100 (right) was primarily used for annealing materials. Super-cooled glass products contain strong internal stresses that can lead to fracture and/or adversely affect PL properties. Therefore, the quenched glass sample is often heat-treated around or below the glass-transition temperature for a short time just to relieve the stress.

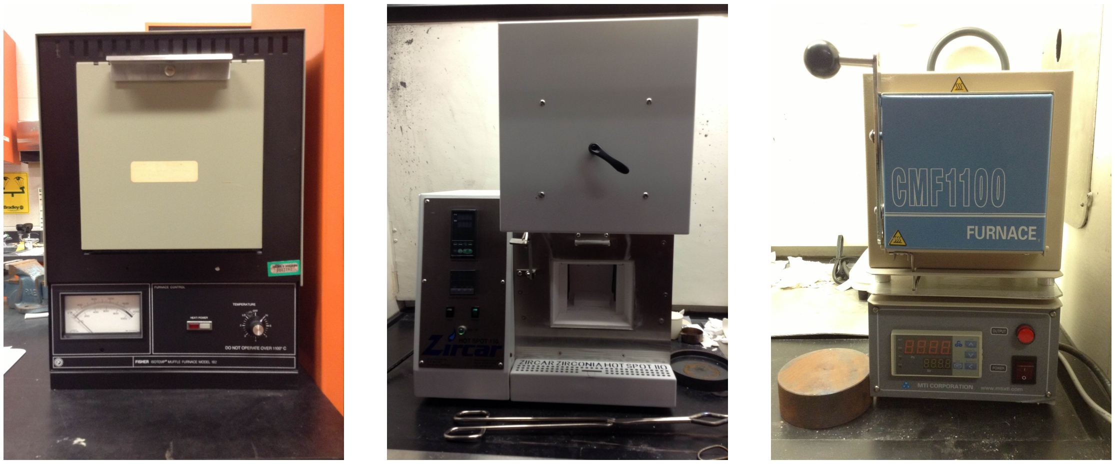

Figure 4.1: Electric Furnaces. (left) ISOTEMP Muffle Furnace Model 182, FISHER, which was used to synthesize $BaBPO_5:Sm^{3+}$ and $SrBPO_5:Sm^{3+}$ polycrystalline samples. (middle) HOT SPOT 110, Zircar Zirconia, Inc., which was used to synthesize glass samples. (right) CMF1100, MTI Corporation, which was used for the purpose of annealing.

$BaBPO_5:Sm^{3+}$ and $SrBPO_5:Sm^{3+}$ polycrystalline and glass samples were prepared by solid-state reactions. The compositions of starting compounds were:

- $BaCO_3$, H_3BO_3, and $(NH_4)_2HPO_4$ for $BaBPO_5$:Sm^{3+}, and
- $SrCO_3$, H_3BO_3, and $(NH_4)_2HPO_4$ for $SrBPO_5$:Sm^{3+}.

The compounds were mixed, ground and then loaded in an alumina crucible, to heat in an electric furnace (ISOTEMP Muffle Furnace Model 182, FISHER) at 500 °C for 5 hours, and then cooled down to room temperature. Next, the obtained product was crushed to form powder and, then, mixed with Sm_2O_3. The mixture was then loaded in an alumina crucible to heat at 950 °C for 6 hours in the furnace, followed by slow cooling to the room temperature to synthesize polycrystalline samples. Moreover, to synthesized polycrystalline material loaded in an Al crucible was heated in the furnace at 1200 – 1300 °C to melt and then quickly quenched on a preheated plate around 250 – 300 °C. The entire synthesis processes were performed in air atmosphere.

Oxyfluoride glass-ceramic which contains CaF_2:Sm nanocrystals was prepared as follows. The composition of starting materials in molar percentage is:

- 45 % SiO_2, 20 % Al_2O_3, 22 % CaF_2, 10 % $CaCO_3$, and 3 % SmF_3.

Each compound was in the powder form and the weight was precisely measured using precise electronic scales (DI-100, Denver Instruments) First, starting compounds of reagent grade were mixed, ground and loaded in an alumina crucible. Next, the mixture in the crucible covered by a lid was heated at 1400 °C for 1 hour and then quenched on a pre-heated stainless plate at 200 °C. The obtained glass was then annealed at 500 °C for 1 h to relieve the internal stresses. This synthesis was performed in air atmosphere.

4.2.3 Sample Preparation in Wellington, New Zealand

Sm^{3+}-doped FP and FA glasses were synthesized by a conventional melt-quenching method by Dr. Andy Edgar's group in Wellington, New Zealand.

The starting materials were mixed in a glove box in a dry nitrogen atmosphere, and loaded in a glassy carbon crucible. The mixture was, then, melted in an RF furnace at 1000 °C for 120 min, and then the melt was quenched on a temperature-controlled titanium plate at 380 °C in argon atmosphere. The furnace is equipped with a glove box, thus the entire chemical reaction processes were made in the inert atmosphere. The compositions in molar percentage were:

- 10 % MgF_2, $(34.4 - x)$ % AlF_2, 30.4 % CaF_2, 15.2 % SrF_2, 10 % $Sr(PO_3)_2$, and x % SmF_3 (for Sm^{3+}-doped FP glass), and

- 10 % MgF_2, 35 % AlF_2, 20 % CaF_2, 10 % SrF_2, $(15 - x)$ YF_3, 10 % BaF_2, and x % SmF_3 (for Sm^{3+}-doped FA glass).

Here, the variable x is a doping concentration of SmF_3, which varies from 0.1 to 10 %. The quenched glass samples were annealed 380 °C for 8 hours to relieve internal strain.

4.3 Sample Characterization

4.3.1 Introduction

After the synthesis, the prepared samples were characterized by studying the optical, thermal, and structural properties. The characterization study involves steady-state photoluminescence (PL) (Section 4.3.2), PL excitation spectrum (Section 4.3.3), PL lifetime measurement (Section 4.3.4), optical transmittance measurement (Section 4.3.5), thermally stimulated luminescence (TSL) measurement (Section 4.3.6), differential scanning calorimetry (DSC) measurement (Section 4.3.7), powdered X-ray diffraction (XRD) measurement (Section 4.3.8), and scanning electron microscopy (SEM) measurement (Section 4.3.9). This section will discuss procedures and techniques used for those measurements in detail.

4.3.2 Steady-State Photoluminescence (PL)

PL is the most important property of detector materials in our dosimetry approach. We expect a change of PL spectrum as X-rays are delivered to the sample. We use this change in PL signal as a response of the detector, and this signal is read out and digitized by a confocal fluorescence microscope. The detail of the PL mechanism of rare earth doped materials was discussed earlier in this thesis (2.6), and the dosimetry approach was discussed in 3.5.

The PL spectrum of prepared samples have been measured using different set-ups (lab-constructed set-up or commercial set-up). Despite the differences in the instruments, the principles of the measurement are the same. Typical PL measurement set-up configuration is illustrated in Figure 4.2.

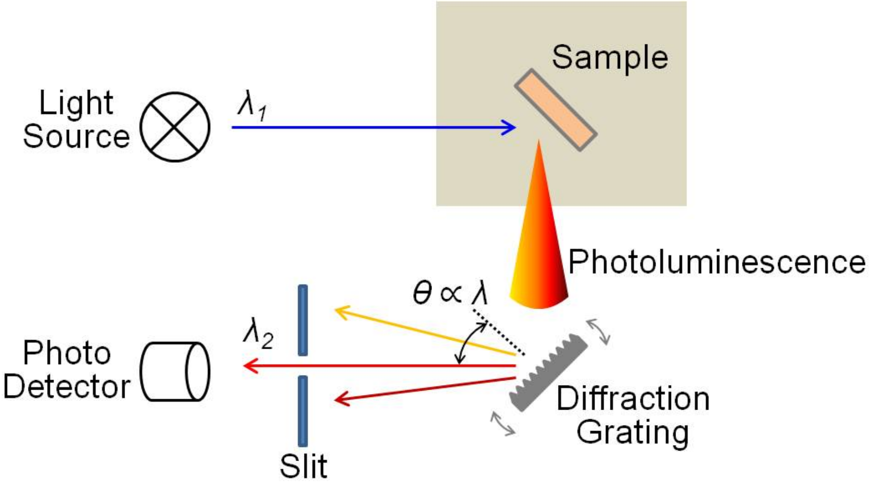

Figure 4.2: Typical configuration of photoluminescence measurement set-up.

A light beam from the source is delivered to the sample of interest to excite the Sm-ions. Upon an appropriate excitation, the sample is excited and emits photons with a variety of wavelengths as a PL signal. The PL signal is then guided to the diffraction grating, in which the incident photons reflects on the surface of the grating at the reflection angle which varies as a function of wavelength, $\theta = \sin^{-1} \frac{m\lambda}{d}$. Here, m is the order of diffraction (integer value), d is the spatial period of grating, and λ is the wavelength of light. The signal at a particular wavelength is selected by inserting a slit at a particular angle θ. Therefore, the diffraction grating allows us to decompose the input light signal into the wavelength components by corresponding diffraction angles. The selected light is eventually detected by the photodetector. Consequently, this set-up allows us to obtain the spectrum of PL, when the sample has been excited at λ_1, by recording signals for varying wavelength λ_2 while rotating the diffraction grating, or changing the position of the slit.

In our research the PL measurements may have been performed using different set-ups. Most of samples were tested using LEDs or laser diodes (LD) as an excitation source, and then the consequent PL spectra were measured using a commercial spectrometer, EPP2000, Stellar Net Inc. This is a class of spectrometer that uses a linear CCD array sensor to measure the diffracted light at once, instead of using a slit and photodetector together. Another set-up used in the research is a commercial integrated system (RF5000, Shimadzu). One may refer to Figure 4.3 to represent a simplified configuration of the PL set-up. This type of system allows you to choose the excitation light at a desired wavelength, and the use of PMT high-sensitivity photon detection. Moreover, the excitation bandwidth and the spectral resolution of measurement can be readily adjusted by adjusting the slit size; the spectral resolution can be improved by making the slit width smaller while the S/N ratio decreases.

The light source was selected depending on the characteristic of sample since an excitation at a particular wavelength may be suitable for one sample, but may not for others. This can be studied by measuring the *excitation spectrum* (which is discussed in the next section. In order to excite the embedded samarium ions in the trivalent and divalent states, we have used several different light sources: 405-nm laser diode for $BaBPO_5:Sm^{3+}$ and $SrBPO_5:Sm^{3+}$ polycrystalline samples as well as FP and FA glass samples and 633-nm He-Ne laser for exciting particularly Sm^{2+} in oxyfluoride glass-ceramic samples (Sm^{3+} ion in this sample was excited at a different wavelength, e.g. 460 nm (LED)).

4.3.3 Photoluminescence (PL) Excitation

A PL signal is emitted when the sample is excited optically. The intensity, and perhaps spectrum, of emission light may depend on the wavelength of excitation, and the PL mechanism may be different from one sample to another. It is important for us to know the optional wavelength to be used for exciting the samples and for the confocal fluorescence microscopy readout.

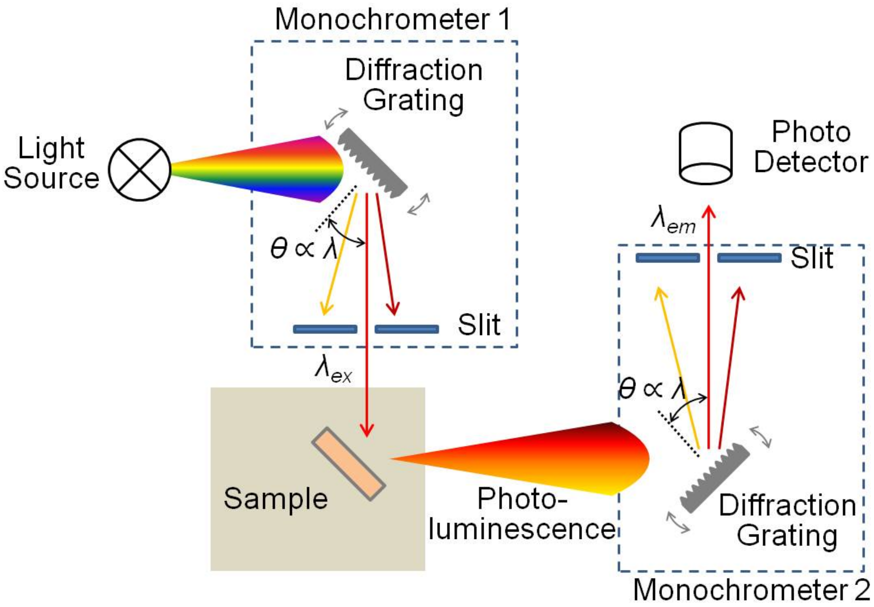

Figure 4.3: Typical configuration of photoluminescence excitation measurement set-up. The set-up may also be used as an integrated PL measurement system, which allows one to choose the excitation light at a desired wavelength.

While PL measurement detects the emission spectrum during the excitation at a fixed wavelength, excitation spectrum measurement detects emission light at a fixed wavelength as a function of excitation wavelength. Configuration of excitation spectrum measurement is illustrated in Figure 4.3. A white light source is taken and the wavelength used to excite the sample, λ_{ex} is selected by monochrometer 1 and guided to the sample. The consequent photoluminescence emission from the sample is next guided to monochrometer 2 which is set to a particular wavelength of interest, and it is then detected by the photodetector. Therefore, the excitation spectrum is obtained by detecting a PL signal at a wavelength of interest, λ_{em}, which is selected by a monochrometer 2 while changing the excitation wavelength, λ_{ex}, by the monochrometer 1.

Excitation spectra were measured at two different laboratories; our own laboratory and professor Tanabe's laboratory at Kyoto University. Most of our samples were measured by our own lab-constructed set-up. The important specifications of our lab-constructed set-up are listed in Table 4.2. Only the spectra of oxyfluoride glass and glass-ceramic samples were measured at Kyoto University, during a visit on a collaborate work, using a commercial spectrometer (RF5000, Shimadzu).

Table 4.2: Specification of Excitation Spectrum Measurement Set-up

	Specifications
Light source	150 Watt Xenon UV Enhanced Arc Lamp (Model 6253, Newport)
Monochrometer 1	Mini Monochromator (Model 78024, Newport)
Monochrometer 2	Monochromator (Cornerstone$^{\mathrm{TM}}$~130 1/8 m, Oriel)
photodetector	Photomultiplier tube (C7950, Hamamatsu)

4.3.4 Photoluminescence (PL) Lifetime

The photoluminescence lifetime is a property of a fluorescent material, which characterizes the rate of PL intensity decay. This is often measured and studied to understand the physics of PL mechanisms, while it is also of particular interest for the application side of the MRT dosimetry detector project. Our dosimetry approach was described in Chapter 3.5 and the details of confocal fluorescence microscopy readout set-up are described in Section 4.5. As described earlier, our approach uses a confocal fluorescence microscope to read out the PL signal over the surface of the sample. The scan by the microscope is based on raster scanning by laser, and the signal from the target sample is measured point-by-point. During this process, the PL afterglow limits the interval time to measure one pixel point to another because the afterglow signal from the adjacent pixel may overlap the signal from the next pixel area.

Lifetime of PL was measured for FA glass and oxyfluoride glass and glass-ceramic samples using a commercial spectrometer (Quantaurus-Tau C11367, Hamamatsu) at Kyoto University. This system is capable of measuring the lifetime from sub-nanoseconds to millisecond range. Specifications of the spectrometer are listed in

Table 4.3.

Table 4.3: Specification of Hamamatsu Quantaurus-Tau C11367

	Specifications
Excitation light source	LED light source (280, 340, 365, 405, 470, 590, and 630 nm)
Detection wavelength range	300 nm to 800 nm
Measurement time range	2.5 ns to 50 ms
Total time resolution	$<$ 1.0 ns FWHM

4.3.5 Optical Transmittance/Absorbance

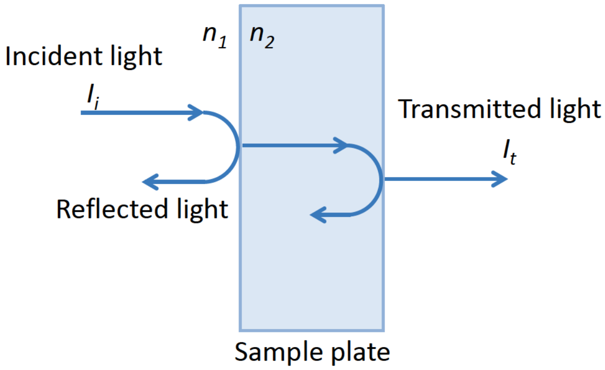

Figure 4.4: Components of optical light involved as it is transmitted through an arbitrary medium at a normal angle of incidence.

Optical transmission measurement was carried out to experimentally derive the absorbance of the sample. Considered the system in Figure 4.4, the absorbance $A(\lambda)$ can be expressed as:

$$A(\lambda) = -\ln\left(\frac{I_t}{I_i}\right) + \ln(T^2(\lambda)) \tag{4.1}$$

where $T(\lambda)$ is the transmittance at a boundary of ambient/sample at normal incidence of light, $T = 4n_1n_2/(n_1+n_2)^2$. In Equation 4.1, the multiple reflections have been neglected for simplicity. The transmittance of a plate with multiple reflections can be found elsewhere, e.g. [111]. In many materials such as glasses, it is commonly known that the optical transmission (or absorption) characteristics change with high

X-ray dose deposition. After the effect, the material typically turns darker due to additional optical absorption induced by X-rays. With the optical transmission measurement data before and after X-irradiation, one can derive a so-called *X-ray induced absorbance* as:

$$\begin{aligned} A(\lambda, D) &= A(\lambda, D) - A(\lambda, D = 0) \\ &= -\ln\left(\frac{I_t}{I_i}\right)_D + \ln\left(\frac{I_t}{I_i}\right)_{D=0} \end{aligned} \tag{4.2}$$

where $A(\lambda, D)$ is the X-ray induced absorbance at a delivered X-ray dose of D. Here, the change in refractive index of subject is assumed to be negligibly small.

Transmittance spectra throughout the research were measured using Perkin Elmer Lambda 900 spectrometer (Figure 4.5). The important specifications are summarised in Table 4.4. For the transmittance measurement, the sample surface was polished flat and the polishing was performed such that the two surfaces were maintained parallel each other.

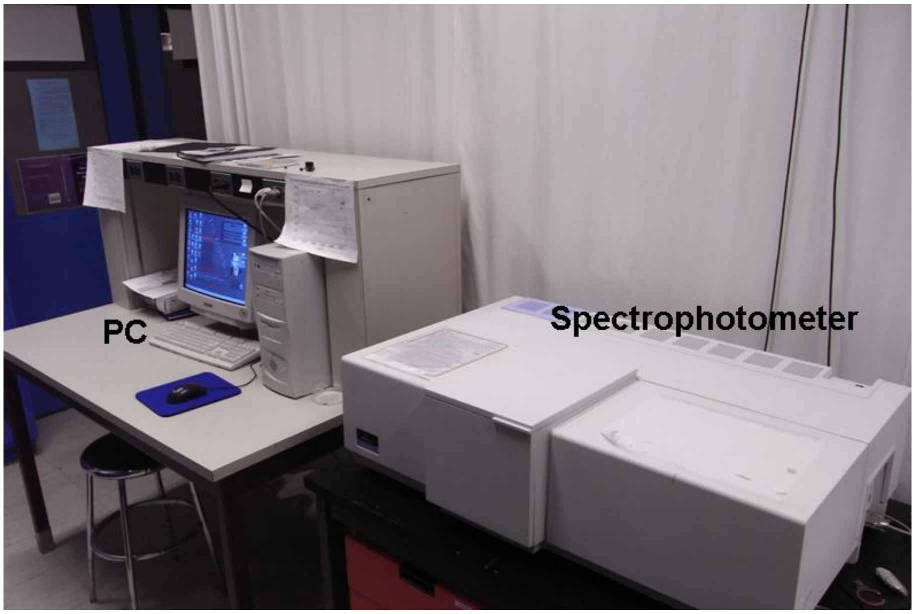

Figure 4.5: The workstation for optical transmission measurement.

Table 4.4: Specifications of Perkin Elmer Lambda 900

	Specifications
Beam cross-section	Width: 0.04, 0.09, 0.45, 0.89, 1.00, 4.44 mm Height: 11.7 mm at a wavelength of 500 nm
Monochromator	Holographic grating with 1449 lines/mm (UV/Vis) and 360 lines/mm (NIR)
Light source	Deuterium (UV) and halogen (Vis/NIR) lamps
Wavelength range	180 to 3300 nm
Wavelength accuracy	0.8 nm (UV/Vis) and 0.32 nm (NIR)

4.3.6 Thermally Stimulated Luminescence (TSL)

Thermally stimulated luminescence (TSL) was studied for FP and FA glass samples to investigate localized charged carriers which were ionized by X-ray exposure and then captured at localized trapping centres. The trapped charges may be released by heat stimulation and may be relaxed to the ground energy level by emitting photons. The principle of the TSL mechanism was discussed earlier in Section 2.8.

The experimental set-up was built in the laboratory. The block diagram of the set-up is illustrated in Figure 4.6. A pair of platinum (Pt) resistors (PT100; F3101, Omega) act as a heating element and also as a temperature sensor, sketched at the top and bottom in the figure, respectively. These Pt resistors were attached to each other by high thermal-conduction cement (OMEGABOND® 600, Omega). The power supply to the heating side of the Pt element is controlled by pulse width modulation (PWM) control, in which the PWM signal is sent by the data acquisition controller unit (DAC; USB-2009, National Instruments) upon the command control from the PC. As it is heated, the temperature is monitored by the other Pt resistor, which is attached below the heating element. The resistance of the Pt element increases with increasing the temperature. The constant current (1 mA) is supplied from an external circuit and the voltage drop across the Pt resistor is monitored as the measure of temperature. The voltage values are digitized by the DAC and stored on the PC. Here, a piece of sample is attached on the temperature sensing side (below the Pt assembly). The light emission as a TSL signal is collected by an objective lens (10x/0.30NA, Meopta) and guided towards the photodetector. The spectral region for detection is selected by a band pass filter placed between the lens and photomultiplier tube detector (R1477-06, Hamamatsu). The temperature control and data acquisition are instrumented by a custom-built Labview® program on PC. The temperature control is based on a PID scheme and the parameters are selected on an empirical basis.

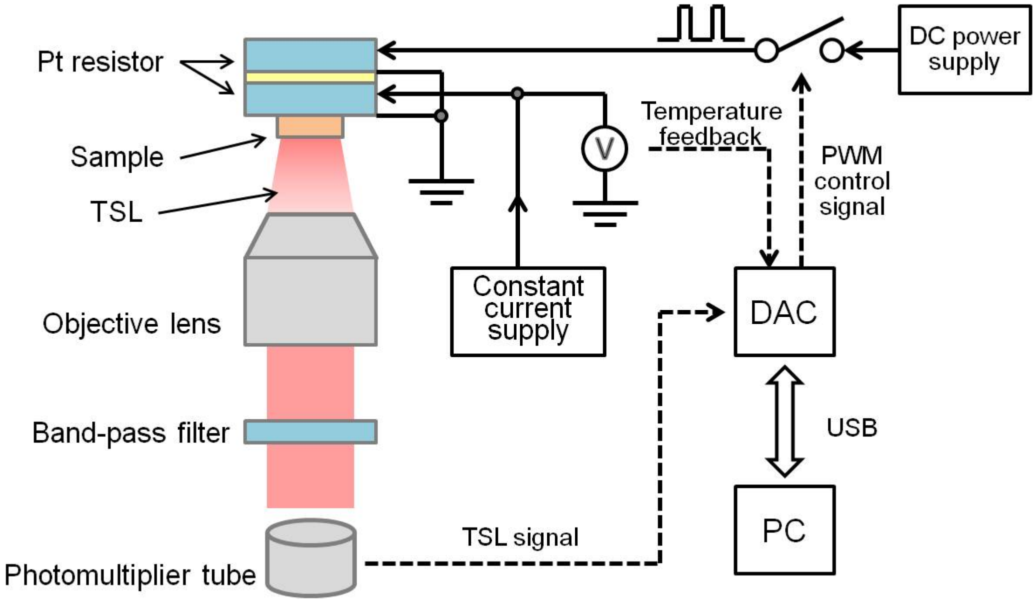

Figure 4.6: Block diagram of thermally stimulated luminescence measurement set-up.

Figure 4.7 shows the temperature control profiles of the TSL reader set-up as a reference for the instrument performance. The temperature was controlled at the rates of 0.1, 0.5, and 1.0 °C per second. The upper figure illustrates that the set-up allows linear increase of temperature at a constant heating rate over the temperature range from 30 to 450 °C. The lower graph indicates that the accuracy of temperature control is within ±2 °C. Here, the error is defined as $(T(t) - Rt)$, in which $T(t)$ is the temperature at time t, and R is the rate of temperature increase; therefore, Rt is the target control temperature.

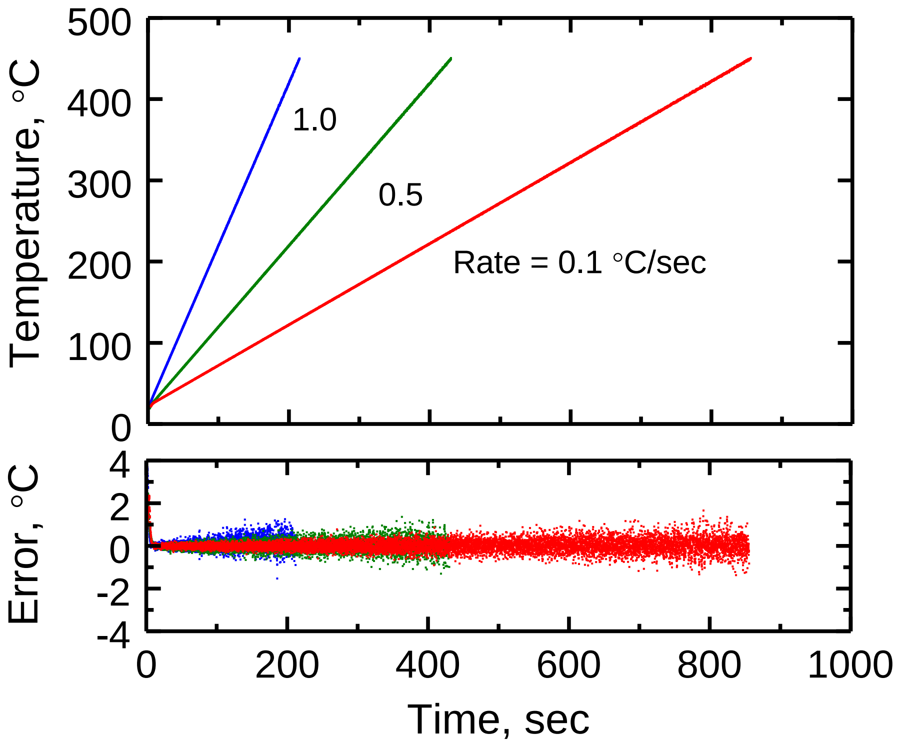

Figure 4.7: Temperature control profiles of TSL reader set-up with varying heating rates, 0.1, 0.5, and 1.0 °C per second.

4.3.7 Differential Scanning Calorimetry (DSC)

Differential scanning calorimetry (DSC) was studied especially on glass-ceramic sample to characterize the glass transition (T_g) and crystallization (T_p) temperatures of particularly oxyfluoride glass sample. The measurement was carried out at Kyoto University using DSC8270, Rigaku. The glass sample was powdered, and then loaded into a platinum container for DSC measurements. Alumina powder was used as a reference material. The sample was heated at a rate of 10 °C per minute.

4.3.8 Powdered X-ray Diffraction (XRD)

Powered X-ray diffraction (XRD) measurement was carried out on oxyfluoride glass and glass-ceramic samples in order to study the size and structure of nanocrystals which are embedded in a glass matrix environment. The measurement was carried out at Kyoto University using Shimadzu XRD-6000, which uses CuK$_{\alpha 1}$ X-ray characteristic line. The scanning rate was 2.0 ° per minute.

4.3.9 Scanning Electron Microscopy (SEM)

Together with XRD measurements, oxyfluoride glass and glass-ceramic samples were examined by a scanning electron microscope (SEM) in order to study the nanocrystals embedded in the glass matrix. A piece of sample was first cracked, and the cracked sharp surface was observed. Since the sample itself is electrically an insulator, the sample surface was coated by a thin gold film and sample was held on a substrate with a carbon tape from the gold film surface and to the substrate. The experiment was performed using a JSM-890 (JEOL) at Kyoto University.

4.4 X-ray Irradiation

4.4.1 Introduction

In the course of research, the dosimetric detector samples were irradiated either under a conventional X-ray tube available in our laboratory or at synchrotron facilities. The X-ray tube was used, at a preliminary stage of characterizations, especially to investigate whether or not the Sm^{3+}-to-Sm^{2+} change by X-ray irradiation is present in a newly synthesized sample. Promising samples were further investigated with high-flux, high-dose irradiations as well as for microbeam irradiations, which were produced at synchrotron facilities: Canadian Light Source (CLS; Saskatoon, Canada), European Synchrotron Radiation Facility (ESRF; Grenoble, France), and SPring-8 (Hyogo, Japan).

In this section, experimental details of X-ray irradiation carried out in the research are provided. Descriptions for conventional X-ray tube irradiation can be found in Section 4.4.2, and X-ray irradiations carried out at the CLS, ESRF, and SPring-8 are discussed in Sections 4.4.3, 4.4.4, and 4.4.5, respectively.

4.4.2 X-ray Tube

At a preliminary stage of sample characterization and especially for investigation whether or not a newly synthesized sample exhibits the $\mathrm{Sm}^{3+} \rightarrow \mathrm{Sm}^{2+}$ valence reduction upon X-irradiation, the sample was irradiated, in a laboratory, under a conventional X-ray tube instead of synchrotron radiation for reasons of accessibility.

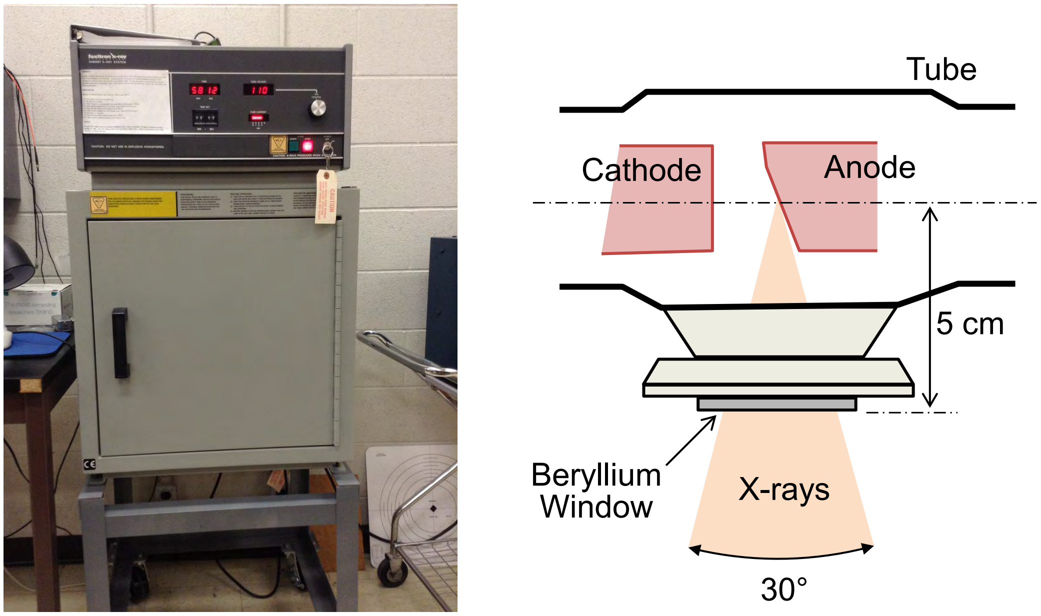

Figure 4.8: Faxitron (43855D) X-ray cabinet unit (left) and a sketch of X-ray tube installed therein (right).

The X-ray source unit used in this research (43855D, Faxitron X-Ray LLC) is shown in Figure 4.8. The X-ray tube installed in this unit uses tungsten as the anode target material. For all the irradiations in the research, the power supply was fixed at 110 kVp with approximately 3 mA of filament current. The produced X-rays are guided to the sample through the beryllium window with a thickness of 0.76 mm, which is located approximately 5 cm down from the centre of anode target. The sample was placed at 1 cm below the window to irradiate it. The generated X-rays have the spectrum shown in Figure 4.9. The spectrum is, in fact, a result of computer simulation available on the SIEMENS' website [112]. The simulation method is well described in the literature [113, 114, 115].

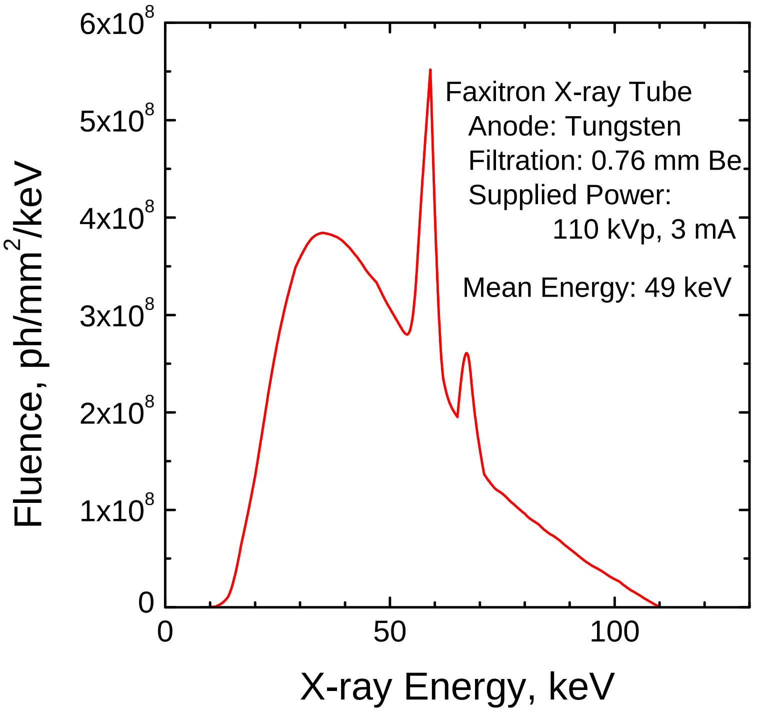

Figure 4.9: Simulation result of X-ray spectrum with 0.72-mm Be filtration and the applied field of 110 kVp at 3 mA.

4.4.3 The Canadian Light Source (CLS)

Dosimeter materials synthesized in the research were tested towards their practical use in MRT at synchrotron facilities. Biomedical imaging and therapy (BMIT) beamline at the Canadian Light Source (CLS) is one of the groups engaged in MRT research among other synchrotron facilities around the world.

The X-ray source used in this facility was the bending magnet (05B1-1). The bending radius is 7.144 m and the magnetic field strength is 1.354 T. With the storage ring energy of 2.9 GeV, the generated X-ray has a continuous and broad spectrum with a critical energy of 7.57 keV as shown in Figure 4.10. After a copper filtration with an effective thickness of 0.94 mm, the X-ray spectrum is such that the peak energy is ∼50 keV, and we used this X-ray beam for all the irradiation experiments at the CLS. The reason for choosing this particular X-ray spectrum is because the energy is in the spectrum range used for MRT research, which is from 50 to 120 keV. Low energy X-rays are avoided in MRT since they are significantly absorbed at

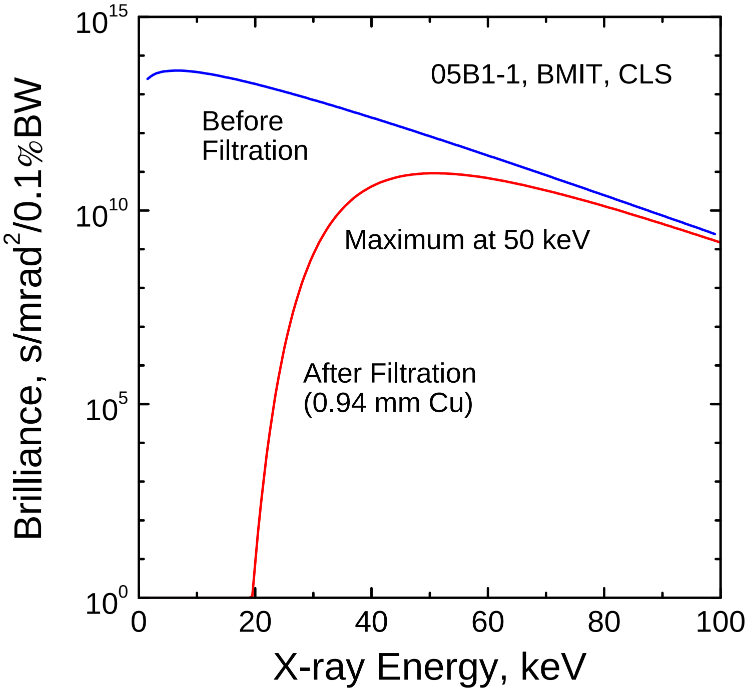

Figure 4.10: X-ray spectrum used for irradiations at the CLS. The peak energy is 50 keV after the copper filtration with the effective thickness of 0.94 mm.

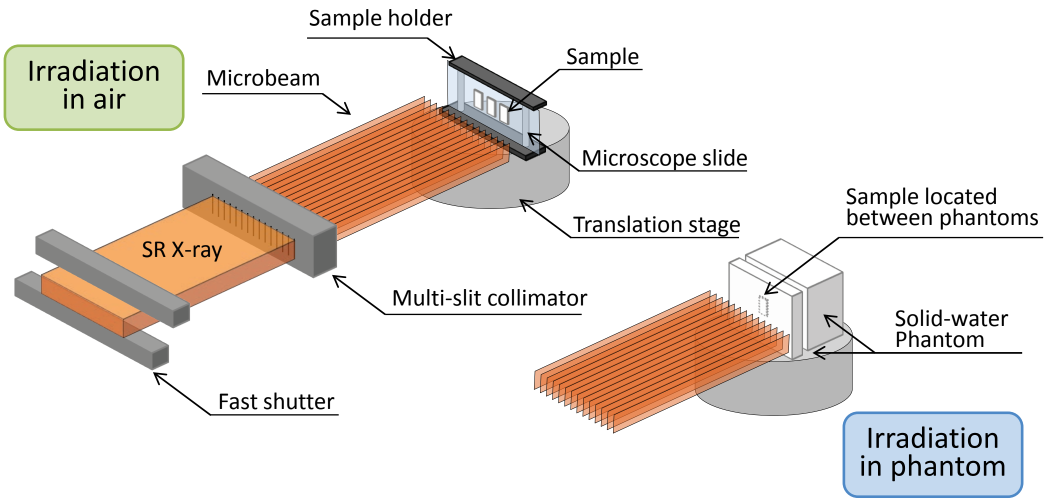

Figure 4.11: Illustration of experimental set-up carried out at biomedical imaging and therapy (BMIT) beamline, Canadian Light Source (CLS).

the surface of the skin and they do not penetrate inside the body. The dose rate in air was experimentally obtained, by Anderson et al. [116], as 7.2 (± 0.4) mGy s^{-1} mA^{-1}. Therefore, under the normal operation, the dose rate is 1.8 mGy s^{-1} with the storage ring current (I_R) = 250 mA. The achievable cross-sectional beam size is 240 mm × 7 mm (horizontal × vertical) at the experimental hatch, which is where the samples were irradiated.

The schematic of the experimental set-up is illustrated in Figure 4.11. The X-ray dose is controlled by the fast shutter. The multi slit collimator (MSC) (Usinage et Nouvelles Technologies, Morbier, France), shown in Figure 4.12, is placed on a motorized goniometer stage and inserted in the beam to create the microbeam (the MSC was moved off the beam when the sample was irradiated with a broad beam). The sample is placed on another motorized translation stage located downstream of the MSC. The motorized stages were controlled from a computer in the control room (outside of the experimental hatch). A video camera was used to monitor the sample during the irradiation and to ensure that the sample is properly aligned in the beam. The distance between the collimator and the sample was fixed to 1 m.

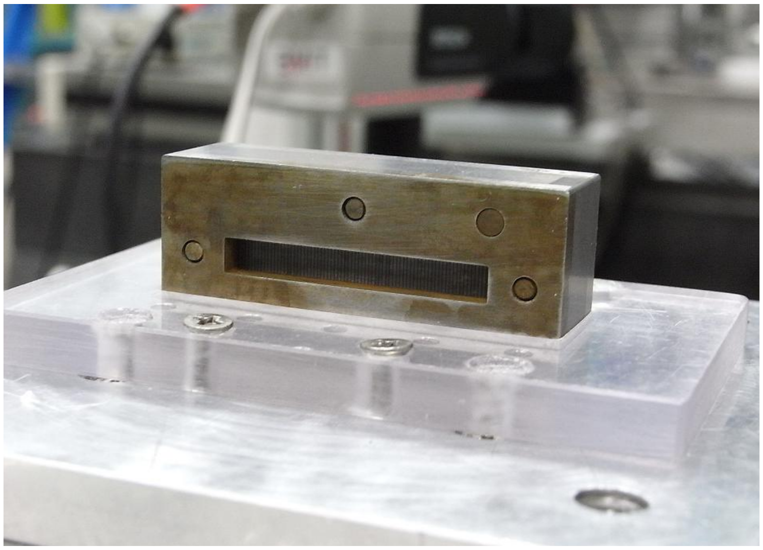

Figure 4.12: Photograph of multi slit collimator installed on a motorized translation stage in the experimental hatch of BMIT beamline at the CLS.

The samples were irradiated either in air or in solid-water (SW) phantom (EMP 5001-499, IMRT-Phantom EASY CUBE, Euromechanics Medical) environment as shown in Figure 4.11. Samples were also irradiated inside a SW phantom. SW is a material that consists of light chemical elements and the relative density is close to 1. Therefore, it is equivalent to water or human tissue in terms of interaction with radiation; hence it is often used to experimentally simulate radiation inside the human body. For the irradiation in air, one or multiple pieces of sample were attached onto a microscope slide. The sample slide was firmly mounted to a holder, which is installed on the sample stage. For the irradiation in SW phantom, a piece of detector samples was closely attached to a phantom plate and then loaded inside into box to irradiate. The box of SW phantom consists of an outer cubic shell and a number of phantom plates with varying thickness (1 – 10 mm) which fit in the box. Therefore, irradiation can be made at a desired depth inside the phantom. For a record and perhaps for comparison purposes a GafChromic® film was also irradiated together with our samples. The orientation was such that the film and sample were closely sandwiched by SW plates with the film at the upstream side.

All the irradiations were carried out in the dark at room temperature. Further, after the irradiation, the samples were wrapped with an aluminium foil to protect them from photoexposure until they were read out.

4.4.4 European Synchrotron Radiation Facility (ESRF)

Our samples were also tested at the European Synchrotron Radiation Facility (ESRF) which is located in Grenoble, France. The experiments were carried out at the Biomedical beamline (ID17). Unlike the BMIT beamline, ID17 beamline is equipped with a wiggler source. With the 1.4 T of the peak magnetic field B_{max} and the deflection parameter $K_{max} = 19.6$, it produces high-fluence, high-energy, and broad spectrum of X-rays. A series of filtrations (1 mm Cu, 1.25 mm Al, 0.5 mm Ce, and 0.5 mm Be) were inserted in the beam in order to remove low-energy X-rays, which results in an X-ray spectrum [24] with a maximum intensity at 83 keV as illustrated in Figure 4.13.

The irradiation experiment at the ESRF was done by the beamline scientists from BMIT, CLS, Dr. Tomasz Wysokinski and Dr. George Belev, during their visit

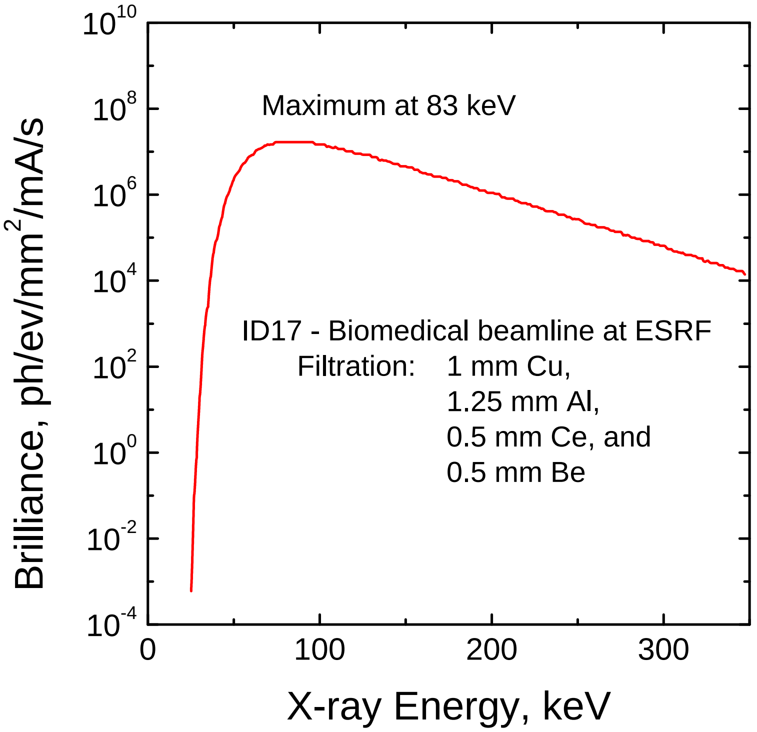

Figure 4.13: The X-ray spectrum used for irradiations at ID17 - Bio-medical beamline at the ESRF. After [24].

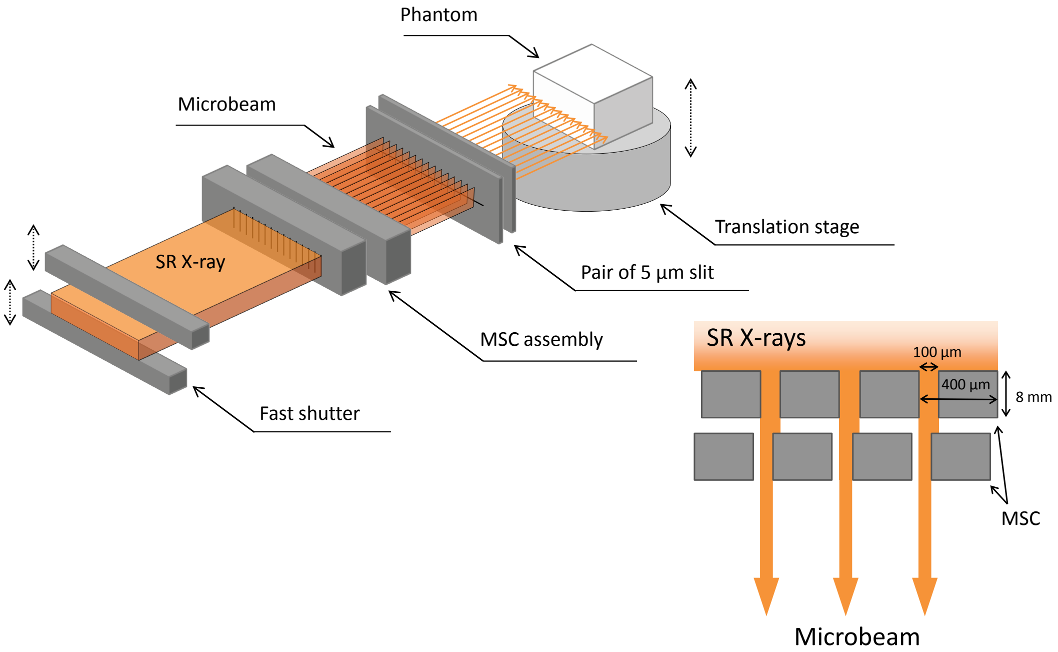

Figure 4.14: Schematics of (upper left) the experimental set-up and (lower right) multi slit collimator (MSC) for irradiations at ID17 - Bio-medical beamline at the ESRF.

in July, 2012, with the support of a beamline scientist, Dr. Elke Brëuer-Krisch. The experimental set-up is illustrated in Figure 4.14. The X-ray dose deposited from the wiggler source to the sample is controlled by a fast shutter. The broad beam passed through the shutter is delivered to the MSC in order to create microbeam. A schematic of the MSC used at the ESRF is illustrated in Figure 4.14. Detailed characteristics of the collimator are found elsewhere [20], but the important properties are as follows. The MSC is an 8-mm thick tungsten block in which 125 narrow slits are structured. Each of the slits is 100-μm in width and these are separated by 400 μm from one centre of the slit to that of adjacent slit. The MSC is manufactured by Tecomet (Massachusetts, USA). Two blocks of identical MSCs are assembled adjacent to each other, and installed in alignment such that the paths of the slits are parallel to the beam direction to allow the X-rays to pass through. The MSC positioned at the downstream side is mounted on a precise translation stage in such a way that the width of microplanar beams can be adjusted by translating the MSC block in the perpendicular direction with respect to the beam path while the MSC at the upstream side is fixed. The microbeam dimension we used in our study is 50-μm wide and 400-μm center-to-center. Moreover, at the downstream of the MSC assembly, a pair of 5-μm tungsten slits was inserted in the centre of the beam path horizontally to adjust the vertical size of the beam. This "narrow" microbeam is delivered to the sample as the sample stage is translated vertically at a constant speed. This configuration allows the delivery of homogeneous dose over a large area (the vertical size is limited by the travelling distance of the sample stage). The accuracy of dose delivery is better than 95 %.

1 % Sm-doped FA glass sample was irradiated together with a GafChromic® film inside a SW phantom. These were closely attached to each other as well as to the adjacent SW phantom inside the phantom box. The GafChromic® film was located upstream of the glass sample. The detector samples were located at a depth of 2 cm from the beam entrance of phantom entrance.

4.4.5 SPring-8

Irradiation experiments were also carried out at SPring-8, Hyogo, Japan. The X-ray source we used was a bending-magnet at BL28B2 beamline. After the filtration by a 3-mm Cu, the beam spectrum becomes as illustrated in Figure 4.15 where the peak energy is around 90 keV and the dose rate is 150 Gy/s [117].

The experiment was carried out by the beamline scientists from BMIT, CLS, Dr. George Belev and Dr. Tomasz Wysokinski during their visit in October, 2012, with a support from a beamline scientist, Dr. Keiji Umetani, at SPring-8. The experimental set-up is illustrated in Figure 4.16. The dose deposition was controlled by the fast shutter, which is made of tantalum. After the shutter, the broad beam passes through a pair of tungsten blocks in order to create a microplanar beam with a thickness of 50 μm. Only, a single planar beam can be created and delivered to the sample at a time; therefore, delivery of multiple microplanar beams (i.e. a microbeam) was realized by repeating the delivery of single planar beam multiple times while translating the sample stage vertically by a distance of 400 μm for each irradiation. Consequently, the delivered beam, overall, consists of 50-μm wide beams which are separated by 400 μm from centre-to-centre. For uniform deposition of X-rays, which is used for dose calibration, 200-μm wide beams were delivered to the detector sample at every 200 μm. Our dosimetric detector sample irradiated at SPring-8 was 1 % Sm^{3+}-doped FA glass. For comparison purposes, the microbeam was also measured by a GafChromic® film together with our test samples. In fact, our glass detector was placed on a piece of GafChromic® film during the irradiations. The irradiations at SPring-8 were only carried out in air.

4.4.6 Summary

Throughout the research, we have used four different X-ray production sources to irradiate and test our dosimeter samples. Although MRT is designed and performed at high-flux and high-energy X-ray synchrotron source, we have also used an X-ray tube, for its convenience and accessibility, in order to characterize the dosimeter

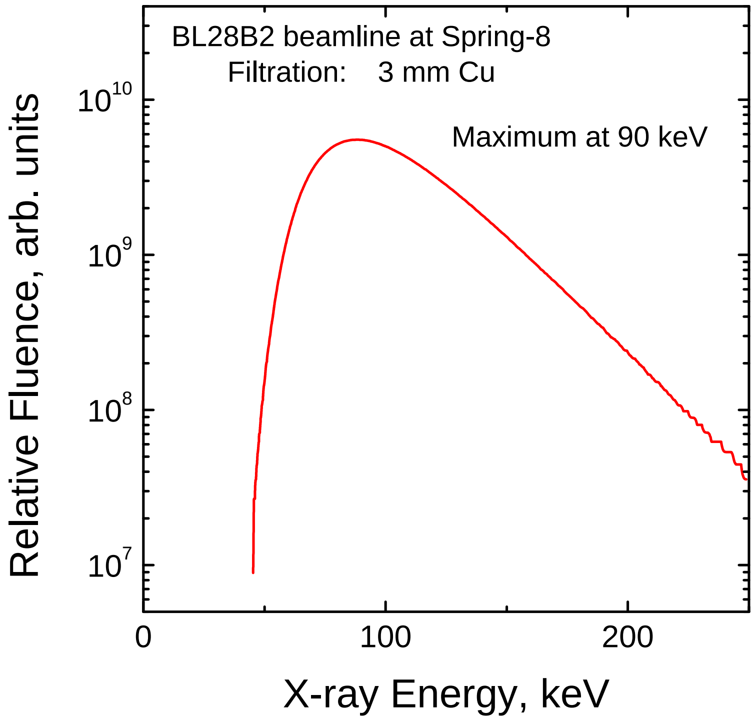

Figure 4.15: X-ray spectrum used for irradiations at SPring-8. The X-rays from the bending-magnet source was filtered by 3-mm Cu. The spectrum was calculated with SPECTRA code. After [118].

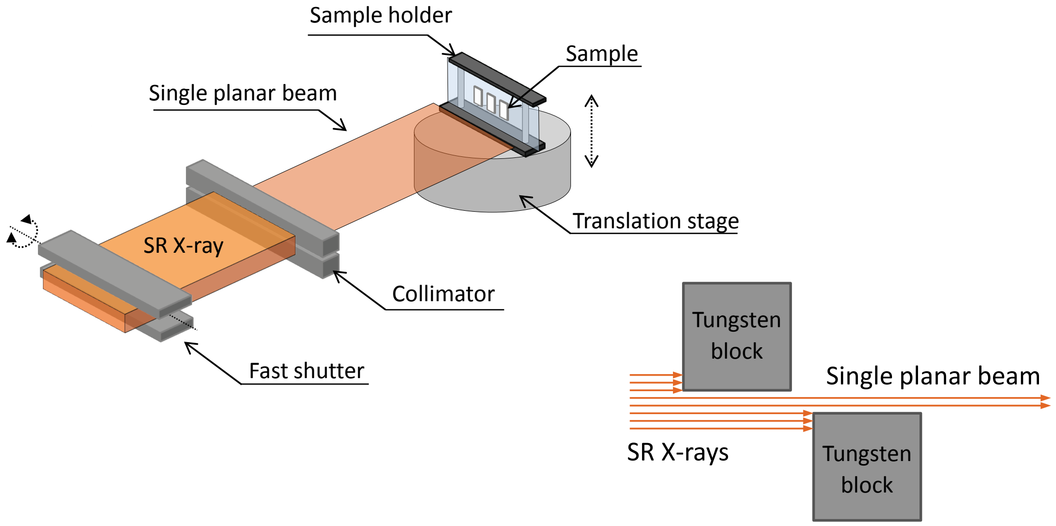

Figure 4.16: Illustrations of (upper left) the experimental set-up carried out at SPring-8 and (lower right) the collimator used.

Table 4.5: Comparison of experimental conditions at synchrotron facilities

Synchrotron Facilities	CLS Bio-Medical Imaging and Therapy (05B1-1)	ESRF Bio-Medical Beamline (ID17)	SPring-8 (BL28B2)
Radiation Source	Bending-Magnet	Wiggler	Bending-Magnet
Dose Rate	6.4 mGy s^{-1} mA^{-1}	16,000 Gy s^{-1} [119]	150 Gy s^{-1} [117]
Peak Energy	50 keV	83 keV [119]	90 keV [117]
Absorber	Air / Solid-Water (2cm)	Solid-Water (2cm)	Air
Number of Micro-Planar Beams	75	49	10
Length of Micro-Planar Beams	4.5 mm	20 mm	14 mm
Broadbeam Irradiation Method	Delivery of single broad beam with a vertical dimension of about 7 mm. (The sample was precisely aligned at the centre of the beam.)	Delivery of single microplanar beam while vertically translating sample at a constant speed.	Delivery of 200 μm microplanar beams at every 200 μm of vertical translation of sample.
Microbeam Irradiation Method	Single multi slit collimator (Dimensions not adjustable.)	Pair of multi slit collimators (Dimensions are adjustable as translating one of the collimators horizontally with respect to the other.)	Pair of tungsten block slit producing a single microplanar plane of beam (thickness 50 μm), which is delivered every 400 μm as the sample is moved vertically.
Expected Dimensions of Microbeam	50 μm wide beams, which are separated by 400 μm at centres.		

materials such as examining the presence of any $Sm^{3+} \rightarrow Sm^{2+}$ conversion and reusability of the detector.

Microbeam irradiations were carried out at three different synchrotron facilities, CLS, ESRF, and SPring-8. We have used 1 % Sm^{3+}-doped fluoroaluminate glass detector to characterize the microbeams produced at these different facilities. The production as well as delivery method of the microbeam are different from one facility to another, so it would be of particular interest to conduct a comparison of these microbeams. It should be emphasized that there has been no such comparison work of microbeams to date as far as we are aware. Table 4.5 summarises the experimental conditions at those three facilities.

4.5 Confocal Fluorescence Microscopy Readout

4.5.1 Introduction

Confocal microscopy is a key technique in this research. As discussed earlier in Section 3.5, dose information is recorded and stored on Sm-doped dosimeter materials. The information is stored as the extent of reduction of Sm^{3+} ($Sm^{3+} \rightarrow Sm^{2+}$) and can be read out via the PL signals of the Sm-ions. With the use of confocal fluorescence microscopy, the stored dose information and its distribution may be read and digitized at a micrometer-scale resolution.

Throughout the course of this research, a readout set-up based on confocal fluorescence microscopy was constructed and used to measure the dose information stored in suitable dosimeter materials. This section provides the detailed descriptions and specifications of the readout set-up developed and used in this research.

4.5.2 Optics Design

Figure 4.17 illustrates the confocal fluorescence microscopy set-up. Table 4.6 provides a list of the optical parts used in this system. The system was refurbished and modified from a used system (MultiProbe 2001 TM CLSM, Molecular Dynamics).

The optics line configuration was kept as it is (the way it was built by Molecular Dynamics), but the excitation source unit and the optical parts were re-configured as described below.

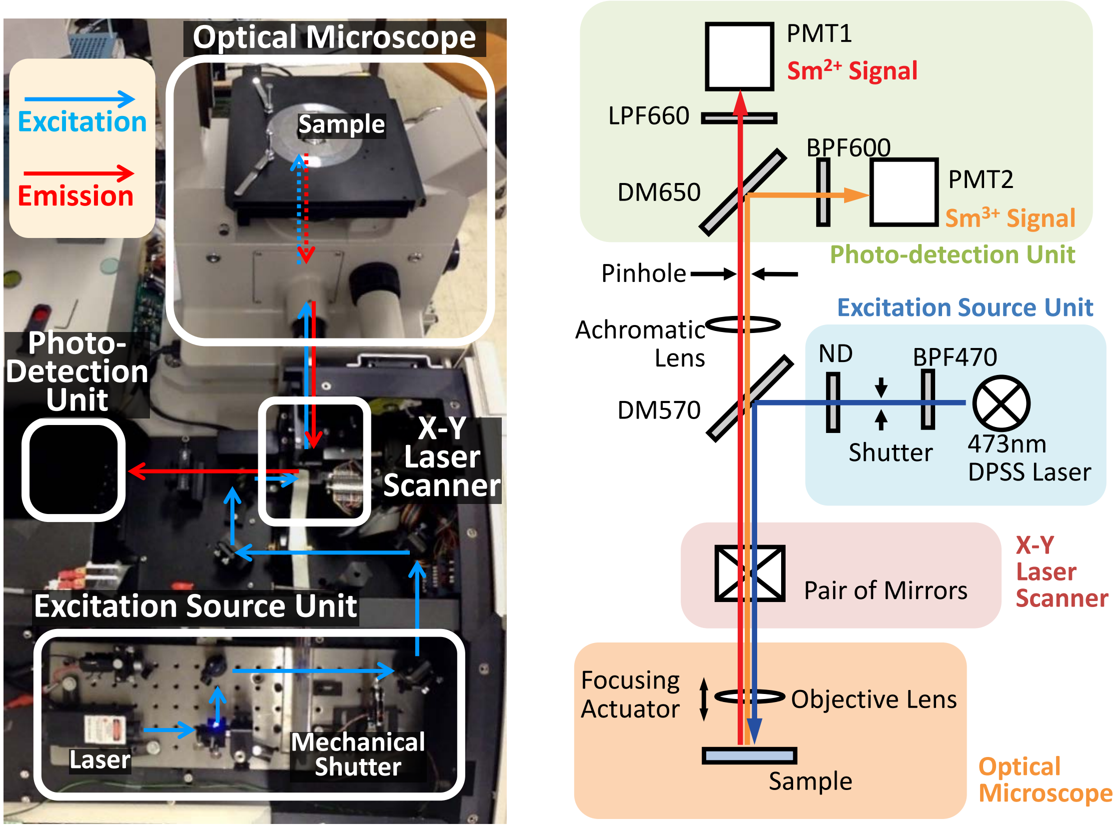

Figure 4.17: Illustrations of confocal fluorescence microscopy set-up used in the research.

We used a 473-nm laser (DHOM-L-473-50, Ultralasers Inc.) as the excitation source. The spectrum of the excitation laser is illustrated in Figure 4.18. Such a wavelength spectrum is suitable to optically excite both the divalent and trivalent samarium ions together [88]. The excitation beam is guided towards the sample through several parts. The bandpass filter (BPF470) was placed in order to subtract the near infrared emission (946 nm) from the laser, which was used to pump the laser-gain medium to double up the energy, which hence produces the 473-nm emission. The mechanical shutter allows the beam to pass or be blocked, and the neutral density filter (ND) adjust the beam intensity. The dichroic mirror (DM570) reflects light of wavelengths shorter than 570 nm, whereas light with longer wavelength is

Table 4.6: List of optical parts used in the readout system (alphabetical order).

Label	Description
AL	Apochromatic lens
BPF470	Band-pass filter
BPF600	Band-pass filter
DM570	Dichroic mirror
DM650	Dichroic mirror
LPF660	Long-pass filter
ND	Neutral density filter
Obj	Objective lens (20×/0.75NA PlanApo, Nikon, or 10×/0.3NA, Meopta)
PH	Pinhole with a diameter of 200 μm
PMT1 and PMT2	Photomultiplier tubes
Sample	Dosimetry detector sample
Shutter	Mechanical shutter

transmitted through (hence the blue excitation beam is guided down as in Figure 4.17 (right)). In the laser scanner unit, a pair of mirrors is oriented perpendicularly. The angle of the mirrors is controlled externally as one mirror is attached to a stepper motor while the other is attached to a galvanometer. The former is used to guide the beam in the vertical direction, while the latter is for the horizontal position, thus the rotation of the pair of mirrors allows two-dimensional (horizontal and vertical) laser scanning. Further, the beam is focused by the objective lens to excite a very small volume of the sample. For the 20× objective lens (PlanApo 20×/0.75NA, Nikon), the field of view (FOV) is about 1 mm in full diameter, the working distance is 1 mm, and the focal diameter is 4 μm. On the other hand, for the 10× objective lens (10×/0.3NA, Meopta), the FOV is about 2 mm, the working distance is 5 mm, and the focal diameter is 5 μm. The sample is raster scanned at a certain depth (adjusted by the focusing actuator) over the field of view of the objective lenses. The focal diameters were experimentally estimated.

Upon the excitation, Sm^{3+} and Sm^{2+} ions emit their respective PL signals. The typical PL emission spectra of the Sm ions (due to $4f$-$4f$ transitions) are shown in

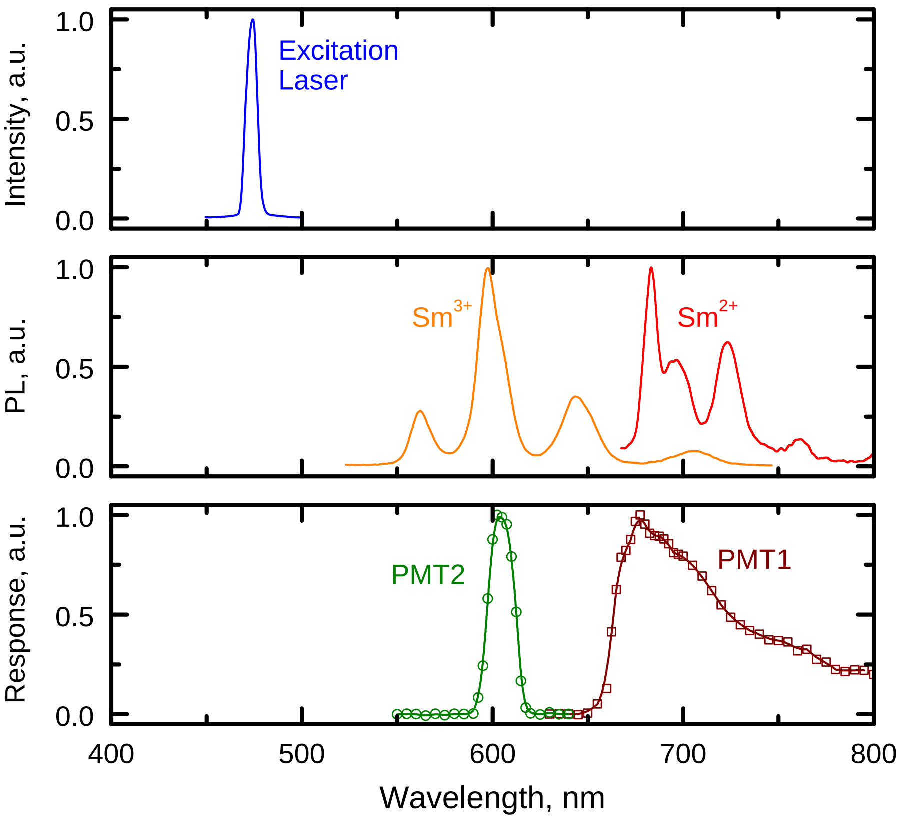

Figure 4.18: Spectral response spectra of photodetection in the confocal fluorescence microscopy readout. The response was experimentally measured.

Figure 4.18 (middle). The PL signals of Sm^{3+} and Sm^{2+} ions are detected by the confocal microscope as follows. The signal is collected back to the objective lens and then guided towards the photodetection unit. As the PL emission by Sm ions is in the red to near-infrared range, DM570 passes the PL signal and then focused to the pinhole (PH) by the achromatic lens (AL). Here, the alignment is done in such a way that the focal point at the sample side corresponds to the focal point at the pinhole side; hence, only the signal at the focal point is allowed to pass through the pinhole to be detected and the out-of-focus signal as well as scattered light in the sample medium are eliminated. The dichroic mirror (DM650) passes the incident light of wavelength longer than 650 nm and reflects light with shorter wavelengths. So, it separates the PL signals from Sm^{3+} and Sm^{2+}. Eventually, the PL signal from the Sm^{2+}-ion is detected by the photomultiplier tube (PMT1) through the long-pass filter (LPF660); while, the Sm^{3+} signal is detected by the other photomultiplier

(PMT2) through the band-pass filter (BPF600). The spectral detection response of the system was experimentally measured and shown in Figure 4.18 (bottom). Note that the response spectra of PMT1 and PMT2 match to the PL spectra of Sm^{2+} and Sm^{3+}, respectively.

Here, using the confocal microscopy set-up, the detector response (R) is defined as:

$$R = \left.\frac{I_{\mathrm{PMT1}}}{I_{\mathrm{PMT2}}}\right|_{\mathrm{IRR}} - \left.\frac{I_{\mathrm{PMT1}}}{I_{\mathrm{PMT2}}}\right|_{\mathrm{NIRR}} \tag{4.3}$$

where I_{PMT1} and I_{PMT2} are measured signal intensities by PMT1 and PMT2, respectively. As indicated in the equation, the first term takes into account the signals from irradiated samples; whereas, the second term is for non-irradiated samples, which subtracts the contribution of typical ${}^4G_{5/2} \rightarrow {}^6H_{11/2}$ emission peak of Sm^{3+} overlapping the ${}^5D_0 \rightarrow {}^7F_{0,1}$ emissions by Sm^{2+}. As a result, the value of R without irradiation is, indeed, zero.

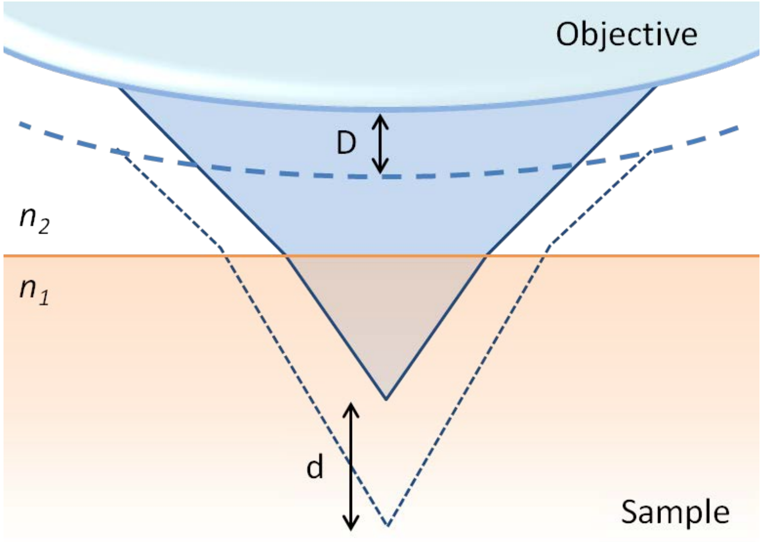

Figure 4.19: Cross-sectional illustration of objective lens, excitation light, and sample when the focal plane of excitation light is in the sample matrix.

An axial position of the objective lens may be adjusted during the measurement as needed. Especially, light reflection from the sample surface may be used as a measure of the relative position between the sample surface and focal plane of the objective lens. Moreover, the excitation beam is guided inside the sample volume to obtain a fluorescence signal from the position of interest. Figure 4.19 is a cross-sectional illustration of objective lens, excitation light, and sample. The distance between the objective lens and the sample surface may be adjusted in order to vary the axial position of the focal plane. However, the travel distance of the objective lens for adjustment (D) is not always the same as the relative change of the focal position (d), particularly when the refractive indices of the ambient medium and sample are different. The relationship between D and d can be derived by ray optics and Snell's law, and the result is simply,

$$\frac{d}{D} = \frac{n_2}{n_1} \tag{4.4}$$

where, n_1 and n_2 are refractive indices of the sample and medium filled between objective lens and sample, respectively. Here, n_2/n_1 is termed as a correction factor. Refractive indices for FP and FA glasses and oxyfluoride glass are approximately 1.5 [58, 120].

4.5.3 Data Acquisition and Control

The detected signal by PMTs is digitized and recorded on a computer, and also the actuators in the readout system are controlled from the computer. Figure 4.20 shows a block diagram of the interface system between the readout system and computer. The computer (PC) is equipped with a suitable data acquisition board (DAC; USB-6009, National Instruments) and these instruments communicate through a USB cable. The PMT signals are smoothen by the simple RC low-pass filter (LPF) and then measured. The analogue voltage signal was digitized by the DAC at a quantum resolution of 14 bit over the range from 0 to 10 V. The galvanometer (Galvo) preamp is an analogue closed-loop feedback circuit which controls the angle of X-scanning mirror, which in turn controls the scanning position in the horizontal direction within the FOV of the objective lens upon receiving the control signal sent by DAC. The minimum interval distance in the horizontal direction is 0.50 μm for the 10× and

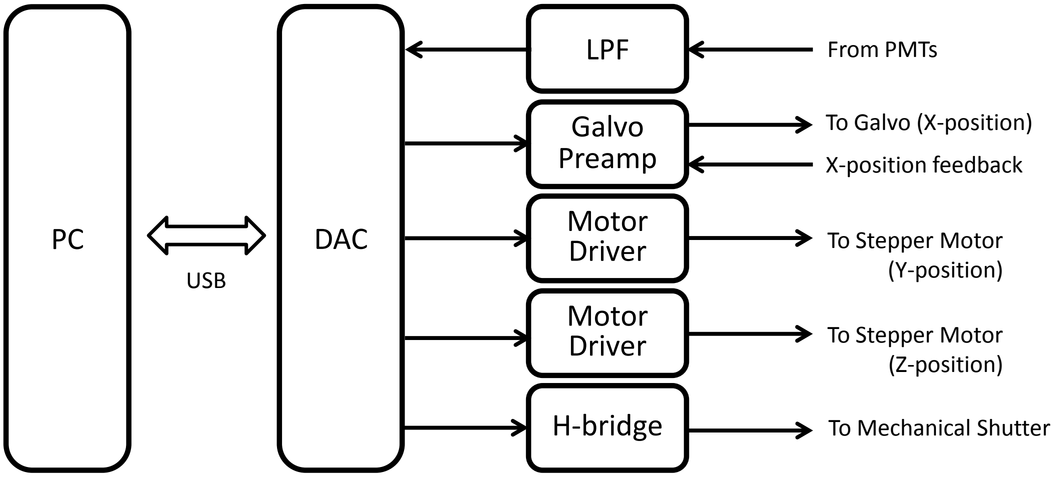

Figure 4.20: Block diagram of the interface (data acquisition and control) system.

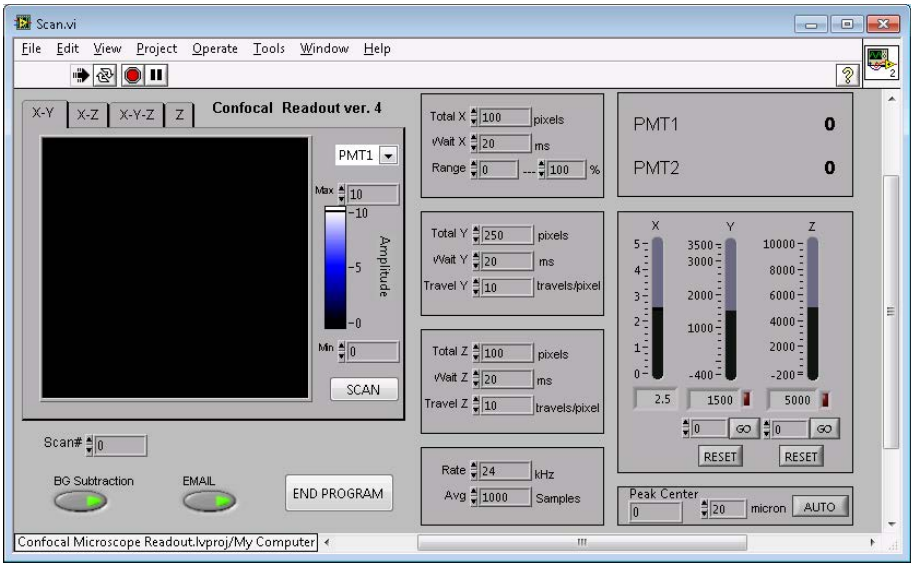

Max 10
Min 0
Scan# 0
Total X 100 pixels
Wait X 20 ms
Range 0 --- 100 %
Total Y 250 pixels
Wait Y 20 ms
Travel Y 10 travels/pixel
Total Z 100 pixels
Wait Z 20 ms
Travel Z 10 travels/pixel
Rate 24 kHz
Avg 1000 Samples
PMT1 0
PMT2 0
X 2.5
Y 1500
Z 5000
Peak Center 0
20 micron

Figure 4.21: Front panel of the Labview® program which controls the confocal microscopy readout set-up.

0.25 μm for the 20× objective lenses, and that for the vertical direction is better than these values. Two 5-phase micro-stepper motors (VRDM 564/50, BERGER LAHR) are controlled by the motor drivers (D631, BERGER LAHR) for the vertical (Y) and axial (Z) movements. The minimum travel distance in the Y direction is 0.70 μm for the 10× and 0.35 μm for the 20× objective lenses; while the 0.1 μm in the axial direction for both the objective lenses. The mechanical shutter is actuated with a magnetic solenoid and driven by the H-bridge circuit. The system allows less than 10 ms to switch from open to close and vice versa.

Figure 4.21 shows the front panel of the Labview® program which controls the reader set-up. The program offers the following functions:

- Four different types of scanning: X-Y, X-Z, X-Y-Z, and Z.
- Image size and resolution.
- Target area to measure.
- Dwelling time between pixels.
- Adjustment of Y and Z position.
- PMT signal sampling rate and number of averaging for noise reduction.
- Automatic dark noise subtraction.
- Email notification at the end of scan.

4.5.4 Summary

The confocal fluorescence microscopy readout was used in the research project to digitize and map the PL signals of Sm^{3+} and Sm^{2+} ions near the surface of a dosimeter sample. Table 4.7 summarises the important specifications of the readout system. Further, Figure 4.22 demonstrates the image resolving power of the system with the 20× objective. The system resolution is sufficiently high to resolve a 4-μm fluorescent sphere (MultiSpeck™ Multispectral Fluorescence Microscopy Standard, Molecular Probes).

Table 4.7: Specifications of the confocal fluorescence microscopy readout system.

Parameters	Description
Photodetection range (PMT1)	660 to 720 nm (FWHM)
Photodetection range (PMT2)	595 to 615 nm (FWHM)
PMT signal acquisition mode	Integration
Objective lens	10×/0.3NA (Meopta), 20×/0.75NA (Nikon)
Pinhole diameter	200 μm
Minimum increment of X position	0.50 μm (10× obj.), 0.25 μm (20× obj.)
Minimum increment of Y position	0.70 μm (10× obj.), 0.35 μm (20× obj.)
Minimum increment of Z position	0.1 μm
Excitation wavelength	473 nm
Focused excitation beam diameter	5 μm (10× obj.), 4 μm (20× obj.)
Scanning speed	600 pixels/min (typical)

4.6 Radiochromic Film Readout

During X-ray irradiations at three synchrotron facilities, our dosimetric samples were irradiated together with a commercial radiochromic film (HD-810, GafChromic®; ISP Technologies, NJ, USA). It is a self-developing film in which the optical density (OD) increases as a function of deposited radiation dose, and the OD is stably stored over a long time. Therefore, the OD is essentially digitized in the form of optical transmission or absorption. While GafChromic® film is widely used in various types of radiation therapy applications, it has also been studied for use in MRT. Therefore, despite the fact that GafChromic® film does not fulfil the requirements for use in MRT, as described in the previous chapter, we have used it as an experimental record and reference.

In the present research, the film was digitized by two different instruments. One is a flat-bed optical scanner (Perfection V700, EPSON), and the other is a wide-field optical microscope (Diaphot-TMD, Nikon) which is equipped with a digital camera.

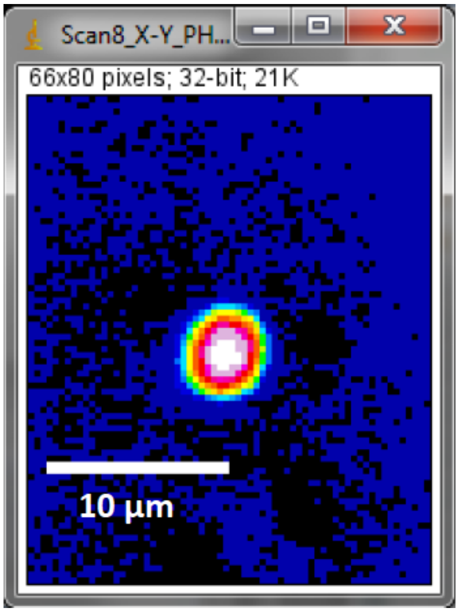

Figure 4.22: An image of 4-μm fluorescent microsphere which was acquired using the confocal fluorescence microscopy readout system with the 20× objective.

Technical details of these readers are provided in next section.

4.6.1 Flat-Bed Optical Scanner

A flat-bed optical scanner (EPSON scanner) was used to digitize the optical density recorded on a GafChromic® (HD-810) film. Figure 4.23 shows a photograph of the scanner. A tube fluorescent lamp is equipped on the lid of the scanner which travels vertically along the longer sides, while a line-array detector is equipped in the bottom side of the scanner, which also travels together with the light source. For measurements, a film is placed on the flat glass bed in such a way that it is sandwiched by the lamp and detector. In this orientation, transmitted light through the film from the source is detected to obtain a light transmission image.

The measurement settings were as follows. The sampling distance of image was 12,800 dpi (1.98 μm/pixel), the colour depth was 24 bit, and the image was saved as TIFF. The acquired image may be separated into three different colour channels (blue, green, and red) using a public-domain image processing program, ImageJ, and then the individual images were used for analyses.

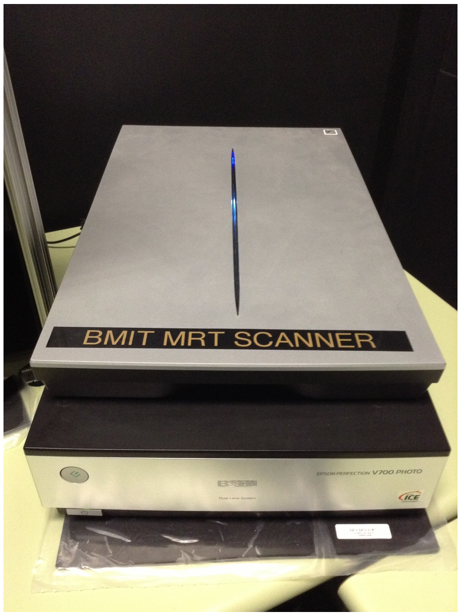

Figure 4.23: EPSON scanner used to digitize the response of GafChromic® film.

Figure 4.24 (left) is an example image of resolution test chart (1951 USAF Glass Slide Resolution Target, Edmund Optics) obtained by the scanner. It is a transparent glass plate which is coated by a mirror surface. The mirror coating is supposed to prevent light from passing through the plate. So the regions in the image seen black correspond to the mirror coating, and light image region is without the mirror coating. It is instructive to note here that the image is represented such that the pixel value is proportional to the transmitted light detected; and, higher the pixel value, the brighter the image. The MTF obtained from the image is shown in Figure 4.24 (right). It is seen that it has a better resolving power along the horizontal direction (along the line array detector) than the vertical direction (along the direction of scan). This may be due to the mechanical vibration caused as the lamp and detector travel for scanning. For this reason, the film irradiated with a microbeam was placed such that the microplanar beams of microbeam recorded on the film are parallel to the horizontal direction.

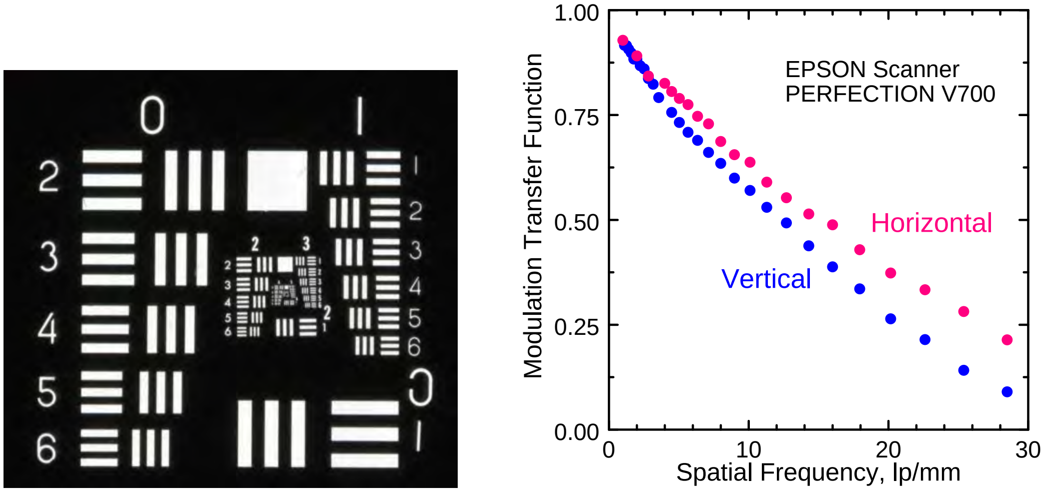

Figure 4.24: Image resolution of EPSON scanner. An image of resolution test chart (1951 USAF) (left), and MTF obtained from the scanned chart (right).

4.6.2 Wide Field Optical Microscope

GafChromic® film may be scanned using a conventional optical microscopy technique. The microscopy set-up we have used in the present research is illustrated in Figure 4.25. In fact, the set-up is more or less given as the original commercial product (Diaphot-TMD, Nikon) besides the objective lens and digital camera. The light emitted from the halogen lamp transmits through the diffuser and is guided to the film detector via the condenser lens. The optical diffuser was used to ensure homogeneous illumination over the film, and the condenser lens focuses the light on to the film. The film is sandwiched by two glass plates as shown on the right side of the figure. It ensures that the film is placed firmly flat and perpendicular to the optical axis. The position of the objective lens is set such that the focal plane is within the sensitive layer of GafChromic® film. The light transmitted through the region of the film focused by the objective lens is guided to the digital colour camera (D3200, Nikon) to detect. The camera is equipped with a 24.2 megapixel CMOS imaging sensor, which allows, in this configuration, approximately 157,000 dpi (0.16 μm/pixel). The image was acquired as the RAW (.NEF) format, and decoded using an open source code (DCRaw; `http://www.cybercom.net/~dcoffin/dcraw/`) for image processing. ImageJ was used for image processing for splitting the colour channels (red, green, and blue) and to obtain the pixel values.

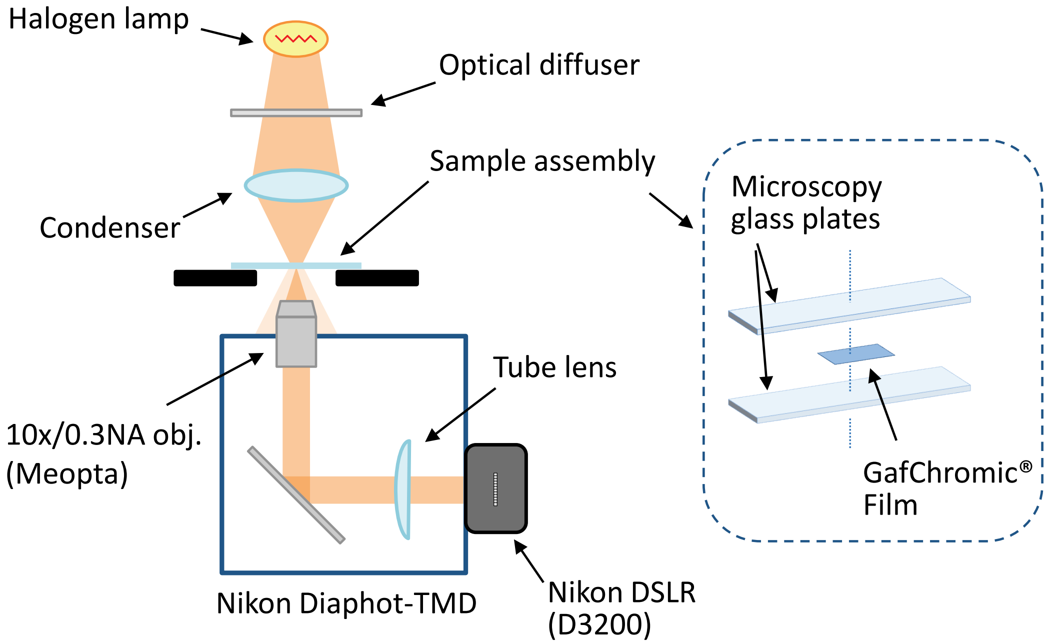

Figure 4.25: A microscopy set-up used to digitize the response of GafChromic® film.

Figure 4.26 shows the way the set-up works from the spectral point of view. The top image is the spectrum of the halogen lamp, middle is the transmittance spectra of GafChromic® films irradiated by different X-ray doses, and the bottom is the spectral responses of red, green, and blue channels of the digital camera (D3200, Nikon). These spectra were experimentally obtained by us. The light emitted from the halogen lamp has broad and continuous spectra over the visible range. The GafChromic® films (HD-810) has two main absorption peaks centred around 610 and 670 nm. It means that red light emitted from the lamp is more strongly absorbed than green or blue, meaning less red photons are transmitted with increasing radiation dose. However, especially for those irradiated by larger doses, the tail of absorption lies over the green and blue regions. The transmitted light is next collected by the image sensor of the digital camera. The image sensor detects light in the visible range. With the use of a color sensor, it can detect light distinguished by the spectral regions (red, green, and blue).

Figure 4.27 provides a representation of the image resolution that can be achieved

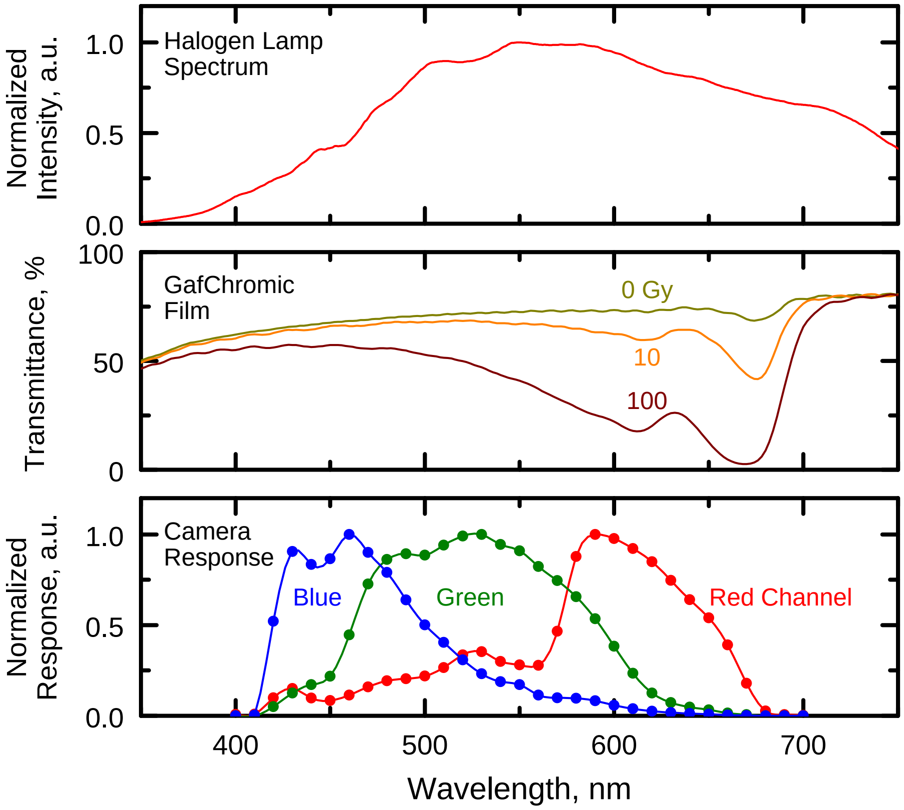

Figure 4.26: Spectra of components involved in the optical microscopy set-up: (top) halogen lamp, (middle) transmission of GafChromic® film, and (bottom) camera response for each channel.

using the microscopy set-up. Note here that the image of bar patterns (left) is in much higher magnification than that shown in Figure 4.24 (left). For example, the width of one bar for the element 4-2 (at the left top) is 27.86 μm; on the other hand, the bar width of the element 0-2 at the left top image of Figure 4.24 (left) is 446.43 μm. Both images are obtained from the same test chart. With the use of higher magnification as well as larger pixel density (157,000 dpi), the microscopy set-up has much higher resolving power than the flat-bed scanner. The right side of Figure 4.27 shows the MTF obtained by the wide field microscopy in comparison with that from the EPSON scanner. It is obviously seen that the microscope has a much higher contrast (resolving power) than EPSON scanner. Particularly, comparing the contrast at the line width of 50 μm (top axis), which is the width of each microplanar beam of the microbeam used in this study, the microscope has nearly full contrast while the contrast of the EPSON scanner is approximately 60 %. This indicates that the microscopy set-up is able to measure the response value which corresponds to the peak dose without the signal loss by contrast.

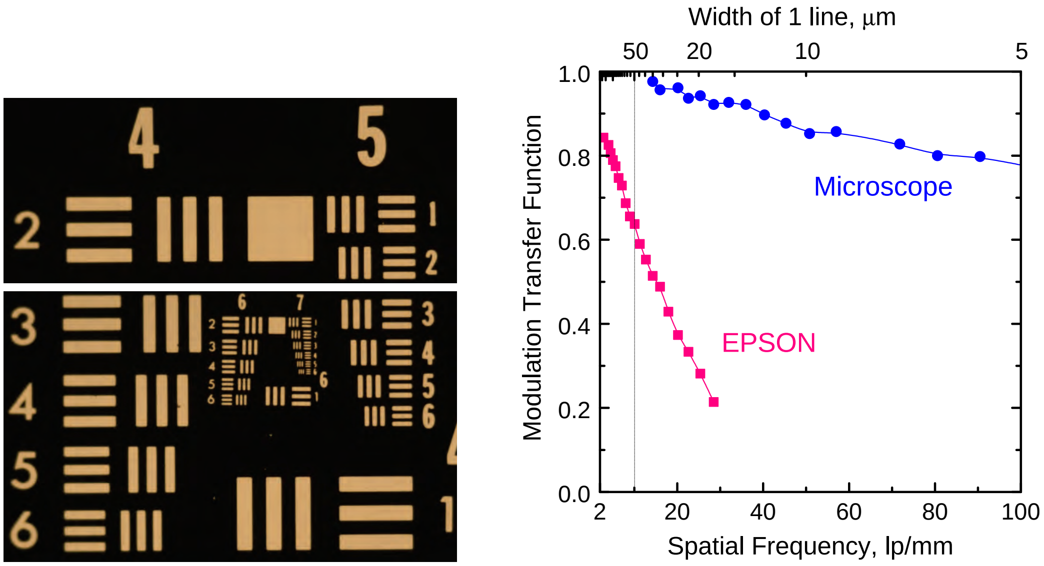

Figure 4.27: Image resolution with a microscope setup. An image of resolution test chart (1951 USAF) (left), and MTF obtained from the scanned chart (right).

Chapter 5

A Search for Detector Materials

5.1 Introduction

The research project had started with a search of an appropriate detector material for MRT. Such a material fundamentally should be those that show $Sm^{3+} \rightarrow Sm^{2+}$ conversion by X-ray irradiation, and this was, in fact, our immediate goal of the project. Detailed discussions on the potential dosimeter materials in our project were made in an earlier chapter (Section 3.5). An investigation of such the reduction of Sm in various host media is appropriate for choosing the dosimetric detector material. As a host material for Sm-ions, it seems to be easier for Sm^{3+} to be reduced in crystals than glasses; however, it is well known, in general, that it is a challenging task to grow a certain area size of crystal-based detector plate which has a homogeneous feature over the area range of interest and at a submicron scale. In contrast, this issue may be fairly easily overcome by using a glass or glass-ceramic material, both of which can be readily prepared in large areas. However, the number of reported glass materials with the $Sm^{3+} \rightarrow Sm^{2+}$ conversion is limited, and, as far as we are aware, no relevant report has been found for glass-ceramics. For these reasons, our initial task in the project had been to find a material, preferably a glass for reasons mentioned in Chapter 3, showing a valence reduction of Sm^{3+} under X-ray irradiation.

This chapter focuses on our initial work done to find a Sm^{3+}-doped materials showing the $Sm^{3+} \rightarrow Sm^{2+}$ change by X-ray. Moreover, we will discuss possible improvements of such material, if we find any, for use as a practical device for high-resolution and large-dynamic-range dosimetry in MRT.

The dosimetric materials that were finally used, fluorphosphate and fluoroaluminate glasses, and oxyfluoride glass-ceramics will be described in Chapter 6 and 7. This chapter only addresses our initial search for a host medium in which we can observe the Sm^{3+} to Sm^{2+} conversion, and some of the unusual and unexpected observations noted during this search.

5.2 Methodology

We have tested the X-ray induced $Sm^{3+} \rightarrow Sm^{2+}$ conversion in a number of different materials. The materials had been obtained by not only synthesizing in our laboratory but also collected from other research groups. In addition, Sm-doped materials from our previous research were also tested. All the materials tested in our initial investigation of the project are listed in Table 5.1. The valence reduction of Sm^{3+} by X-ray irradiation in $BaBPO_5$:Sm^{3+} [121] polycrystaline materials had been reported earlier, and the synthesis procedure was reproducible in our laboratory. Also, for the similarity, an isostructural material ($SrBPO_5$:Sm^{3+}) was synthesized by the same manner. Moreover, these polycrystal samples were melted and quenched to produce glasses, which were also tested. SrB_4O_7 polycrystalline sample was provided by Professor Gospodinov's group at the Bulgarian Academy of Science. In this material, the concentration of Sm was quite high (about 10 %), and there was a large fraction of excess Sm ions in the divalent state (Sm^{2+}) included already in the as-prepared sample. Li_2O-SrO-B_2O_3 [45] and SrO-BaO-P_2O_5-B_2O_3 [47] glasses were selected since these glasses were reported earlier to show the valence reduction of Sm^{3+} under X-ray irradiation. These materials were reproduced in our laboratory followed by the preparation procedures described in the literature. ZrF_4-NaF-AlF_3-LaF_3-SmF_3-BaF_2-$BaCl_2$ was synthesized and provided by Dr. Edgar's group at the Victoria University of Wellington, New Zealand. This glass composition is often refereed as fluorochlorozirconate (or FCZ) glass; and it was used in a previous project on transparent X-ray scintillator applications [37]. The FCZ glass can be made into a glass-ceramic, which includes $BaCl_2$ nanocrystals, by a heat-treatment procesure in a particular temperature range (225 – 270 °C). Both SiO_2-NaO-Al_2O_3-LaF_3-PbF_2-SmO_3 and LaO_3-B_2O_3-GeO_2-SmO_3 were synthesized and provided by Dr. Jha's group at the University of Leeds, UK.

Table 5.1: List of Sm-doped materials tested for initial investigation of project. SK, BG, NZ, and UK indicate our group, Professor Gospodinov's group at Bulgarian Academy of Science, Dr. Edgar's group at Victoria University of Wellington, New Zealand, and Dr. Jha's group at the University of Leeds, UK, respectively.

#	Composition	Material Structure	Place of Synthesis
1	$BaBPO_5:Sm^{3+}$	Polycrystal and Glass	SK
2	$SrBPO_5:Sm^{3+}$	Polycrystal and Glass	SK
3	$SrB_4O_7:Sm^{3+,2+}$	Polycrystal	BG
4	Li_2O-SrO-B_2O_3-Sm_2O_3	Glass	SK
5	SrO-BaO-P_2O_5-B_2O_3-Sm_2O_3	Glass	SK
6	ZrF_4-NaF-AlF_3-LaF_3-SmF_3-BaF_2-$BaCl_2$ (fluorochlorozirconate (FCZ))	Glass and Glass-ceramic	NZ
7	SiO_2-Na_2O-Al_2O_3-LaF_3-PbF_2-SmO_3	Glass	UK
8	LaO_3-B_2O_3-GeO_2-SmO_3	Glass	UK

In order to investigate the valence change of Sm, all the samples listed in Table 5.1 were irradiated under an intense X-ray beam at the biomedical imaging and therapy beamline (BMIT; 05B1-1), Canadian Light Source, Saskatoon. The facility specifications are described in Section 4.4.3 in detail. Further, PL spectra of each sample were measured before and after the irradiation. The samples were excited using a 405-nm laser diode, and a CCD-based spectrometer (EPP2000, StellarNet Inc.) was used to detect the resulting PL spectrum through a 550-nm long-pass filter to prevent the measurement of the scattered portion of excitation light beam. The resolution of spectrometer is about 8 nm as given by the manufacturer. For the purpose testing the reusability of the detector material, irradiations were done under an X-ray tube (43855D, Faxitron X-Ray LLC), and 460-nm LED was used for PL measurements. The dose values used here are air kerma (kinetic energy released per unit mass) and represented in Gy.

In order to detect the dose distribution of the microbeam, the detector material needs to be homogeneous on the micrometer scale. Therefore, the surface of the polycrystalline and glass samples were observed by a confocal fluorescent microscope described in 4.5.

5.3 Photoluminescence spectra

Almost all the samples before the irradiation showed typical PL spectrum of only Sm^{3+} ions, which is due to the $4f$-$4f$ transitions. The only exception was the SrB_4O_7 polycrystalline sample in which both Sm^{3+} and Sm^{2+} ions coexisted as prepared. Figure 5.1 compares the PL spectrum of an as-prepared SrB_4O_7:$Sm^{3+,2+}$ sample with that of $BaBPO_5$:Sm^{3+} as a reference. The valence change of Sm was also tested for the glass and glass-ceramic samples.

After X-ray irradiation, valence reduction ($Sm^{3+} \rightarrow Sm^{2+}$) by X-ray irradiation was observed as the appearance of an Sm^{2+} signal in PL spectra in all the polycrystalline samples we tested. Although Sm^{2+} was already present from the beginning, even further increase of Sm^{2+} signal was observed in SrB_4O_7. Figure 5.2 illustrates the difference in the PL spectra of $SrBPO_5$:Sm^{3+} before and after X-ray irradiation as an example. After the irradiation at approximately 90 Gy, the PL spectrum is dominated by Sm^{2+} ions generated by the X-rays. Moreover, the appearance of Sm^{2+} signature in the spectrum was clearly detectable after irradiation at $\sim$ 16 mGy. Figure 5.2 clearly convinces the capability of X-ray sensing using the appearance of PL by Sm^{2+} after X-ray irradiation. Further discussion will be presented in the next section.

To our disappointment, none of the glass and glass-ceramic samples we tested have shown any measurable $Sm^{3+} \rightarrow Sm^{2+}$ conversion even after X-ray irradiation with very high dose (over 5000 Gy). Figure 5.3 shows PL spectra of $BaBPO_5$:Sm^{3+} glass before and after X-ray irradiation as an example. It was surprising that we

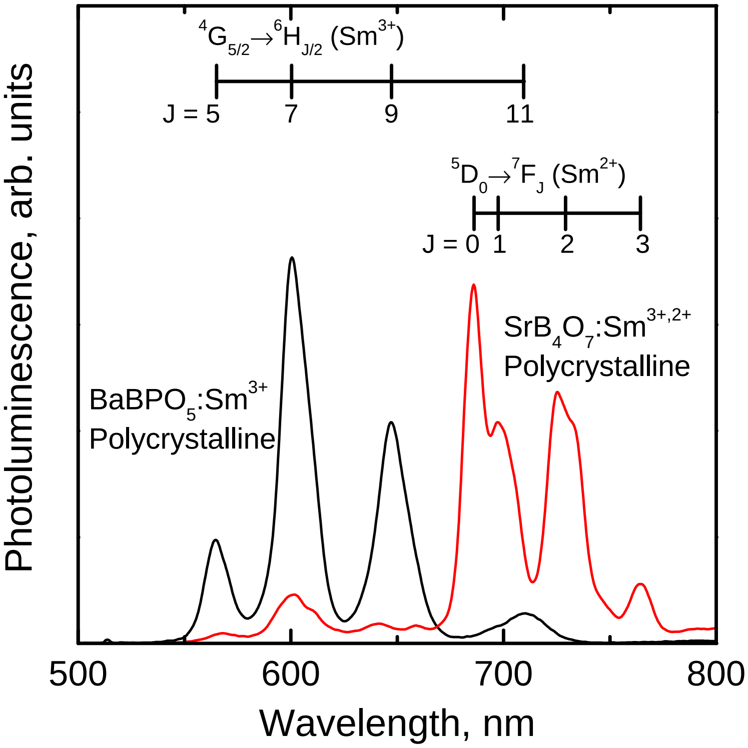

Figure 5.1: PL spectra of Sm-doped BaBPO$_5$ and SrB$_4$O$_7$ polycrystalline samples before irradiation.

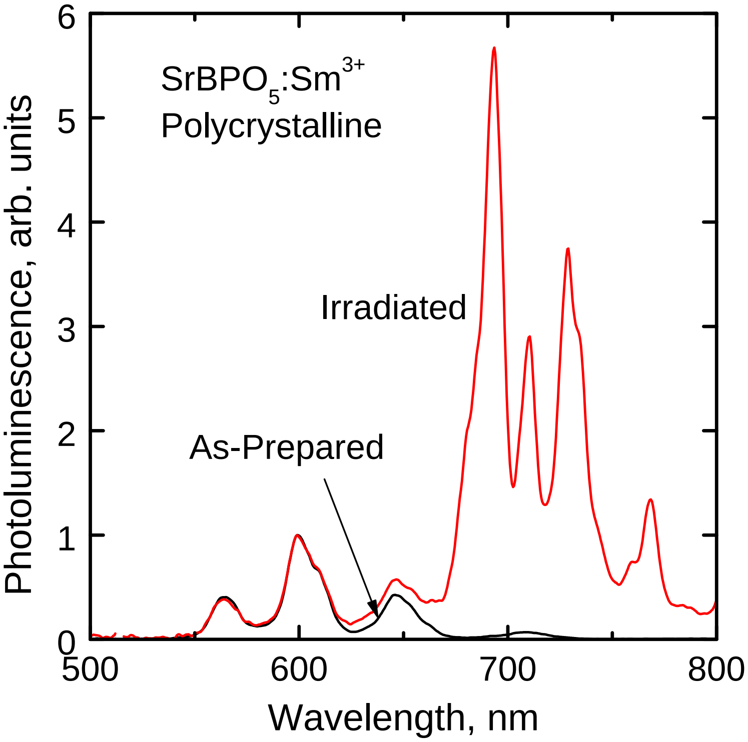

Figure 5.2: PL spectra SrBPO$_5$:Sm^{3+} polycrystalline with different X-ray irradiation doses delivered.

could not observe any reduction of Sm^{3+} in Li_2O-SrO-B_2O_3 and SrO-BaO-P_2O_5-B_2O_3 glasses despite the evidence by earlier studies [45, 47]. Despite the the absence of any detectable Sm^{2+} signal, the colour of the materials became darkened, and the shape of PL spectra were distorted as illustrated in the figure. Moreover, the relative PL yield is reduced dramatically. This should have been caused by the darkening of the host matrix by X-ray irradiation. The darkening of a material is a common phenomenon associated with the absorption of X-rays. The X-ray irradiation generates electron-hole pairs in the host material, and these are, next, trapped by localized centres (electron or hole traps), which cause strong optical absorption, typically in the UV-blue region. As a result, the blue excitation light cannot penetrate the sample and cannot excite the whole volume of sample, which results in a low PL yield. Further, the side-band of the X-ray induced absorption may overlap to the Sm^{3+} emission range, so the PL emission by Sm^{3+} is self-absorbed which causes the distortion of the spectral shape.

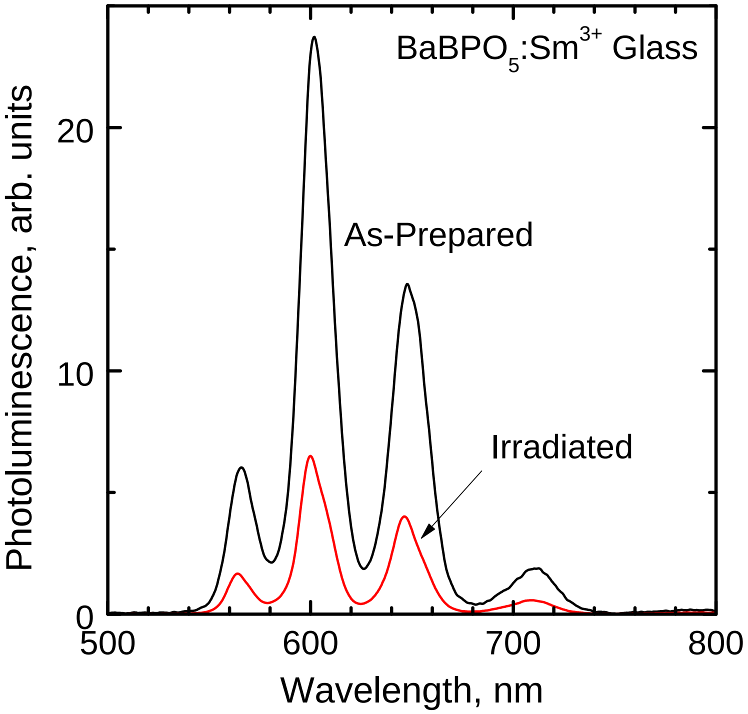

Figure 5.3: PL spectra of Sm-doped $BaBPO_5$ glass sample before and after irradiation.

5.4 Dose-response for dose calibration

Since we would like to use the extent of change in the PL spectrum due to Sm^{3+} → Sm^{2+} as a measure of X-ray dose delivered, we have to be aware of the correspondence between the degree of signal change and the delivered X-ray dose. For this purpose, dose-response curve, which is a *detector response* as a function of X-ray dose delivered, is often presented used for dose calibration. Also, the dose-response provides information on the detectable dose range that the detector can handle. The dose-response curves of Sm-doped $BaBPO_5$, $SrBPO_5$, and SrB_4O_7 are illustrated in Figure 5.4. Here, the detector response is defined as a non-dimensional variable:

$$Response(Dose) = \frac{PL^{670-830nm}(Dose)}{PL^{550-660nm}(Dose)} - \frac{PL^{670-830nm}(0)}{PL^{550-660nm}(0)} \tag{5.1}$$

where the first term is a ratio of the integrated PL intensity over the range of 670 – 830 nm to that of 550 – 660 nm for a given X-ray dose value (*Dose*). The former range corresponds to the PL emission range of Sm^{3+} and the latter is for Sm^{2+}. The second term in the above equation is the value without X-ray irradiation. Here, instead of using absolute intensities, the PL ratio is used as a response so that the response value is independent of the excitation intensity and we can maintain the measurements with high degree reproducibility. The subtraction by the second term is to remove the interference of the ${}^4G_{5/2} \rightarrow {}^6H_{11/2}$ emission by Sm^{3+}, which overlaps to the spectrum of Sm^{2+}. From Figure 5.4, it is clear that the dose-response varies depending on the host material. Particularly, the response change in $SrBPO_5{:}Sm^{3+}$ extends over a large dose range up to approximately 500 Gy. Although it is desirable to have an ability of detection at higher doses, some MRT researches have used the doses that may be covered by this material. For the SrB_4O_7 polycrystalline material, we were unable to observe saturation in the dose-response curve even over 5500 Gy which shows that the $SrB_4O_7{:}Sm^{3+}$ should be a highly potential detector material in terms of the dynamic range.

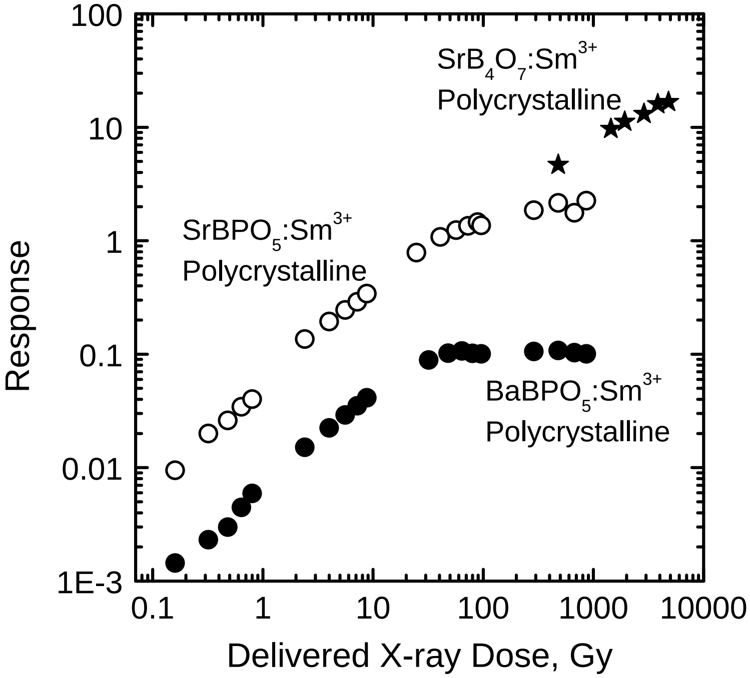

Figure 5.4: Dose-response curves of Sm^{3+}-doped $BaBPO_5$, $SrBPO_5$, and SrB_4O_7 polycrystalline samples.

5.5 Response stability

The proposed dosimetry approach is based on an indirect detection method. It means that a dosimetry detector material is irradiated by X-rays to detect and store the dose information, and then the detector is brought to a readout set-up to read out and digitize the PL signals from the Sm-ions. Therefore, the stability of such stored information, or dose-response value, is an important consideration. A series of PL spectra of $SrBPO_5$ were measured over a period of time after X-ray irradiation (about 1500 Gy) and illustrated in Figure 5.5 (a). Between the measurements, the sample was kept in the dark to prevent any unnecessary fading of Sm^{2+} by exposure to ambient light. The results suggests that the generated Sm^{2+} is quite stable even after several days. It is instructive to note here that a fraction of the slight decrease in the response over several measurements is due to the photobleaching effect by 405-nm excitation beam during the actual PL measurements.

The conversion stability was also tested under high temperature conditions. The

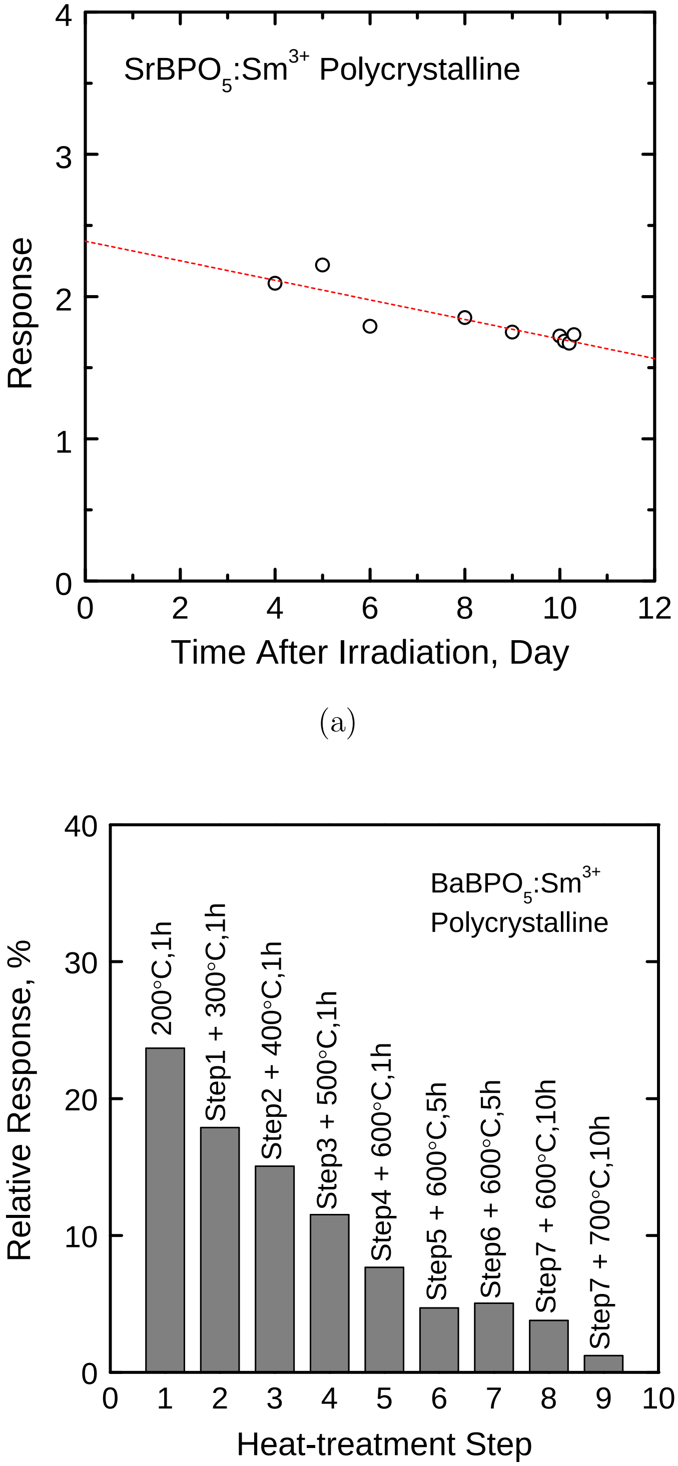

(a)

(b)

Figure 5.5: Stability of generated Sm^{2+} by X-rays. (a) Response of X-ray irradiated SrBPO$_5$ polycrystalline (about 1500 Gy) as a function of time after irradiation. (b) Relative response of X-ray irradiated BaBPO$_5$ polycrystalline compared to that of as-irradiated ($\sim$ 3000 Gy) as a function of heat-treatment histories.

PL spectra of an irradiated piece of sample were measured after every heat treatment while the heat-treatment temperature was elevated up to 700 °C. The relative response value against heat-treatment conditions is illustrated in Figure 5.5 (b). The relative values are those with respect to the as-irradiated value. The response decreased dramatically after heat-treating at 200 °C for 1 h, and it further decreased with increasing temperature as well as time. Eventually, the response value dropped closed to zero after heating the sample at 700 °C for 10 h; as explained above, a zero response represents the absence of Sm^{2+} ions.

Consequently, the X-ray generated Sm^{2+}-ions seem quite sensitive to heat especially at elevated temperatures whereas it is fairly stable at room temperature, and when it is not exposed to excess light. This fact suggests that the materials are erasable by heat-treatment; thus this may open up the possibility for the detector materials to be used multiple times if the response is consistently repeatable. The next section will discuss the reusability of these polycrystalline materials.

5.6 Reusability

In order to test the reusability of Sm^{3+}-doped polycrystalline materials for dosimetry sensing applications, we have, first, measured the dose-response curves, next we attempted to erase the response by heat-treatment, and then the dose-response was measured again after the erasure. Further, the erasure and dose-response measurement were repeated as needed.

Figure 5.6 shows the dose-response curves recorded on an as-prepared sample and heat-treated sample after the previous dose-response measurement for (a) $SrBPO_5$:Sm^{3+} and (b) $BaBPO_5$:Sm^{3+} polycrystalline materials. The heat treatment was performed at 700 °C for 5 hours under the ambient air atmosphere. *The response here refers to the value with respect to that of an as-prepared sample.* Particularly for $SrBPO_5$, the response values of the first plots of the 2nd- and 3rd-time uses are way larger than that corresponding to the 1st-time use. This indicates that the response value was not completely erased by the heat treatment. Despite the difference of ini-

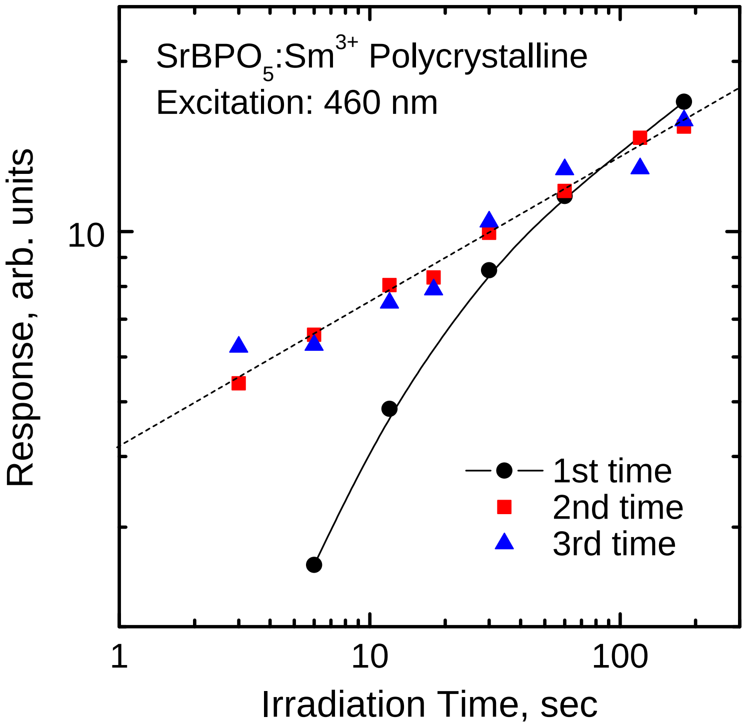

(a) SrBPO$_5$:Sm^{3+} polycrystalline

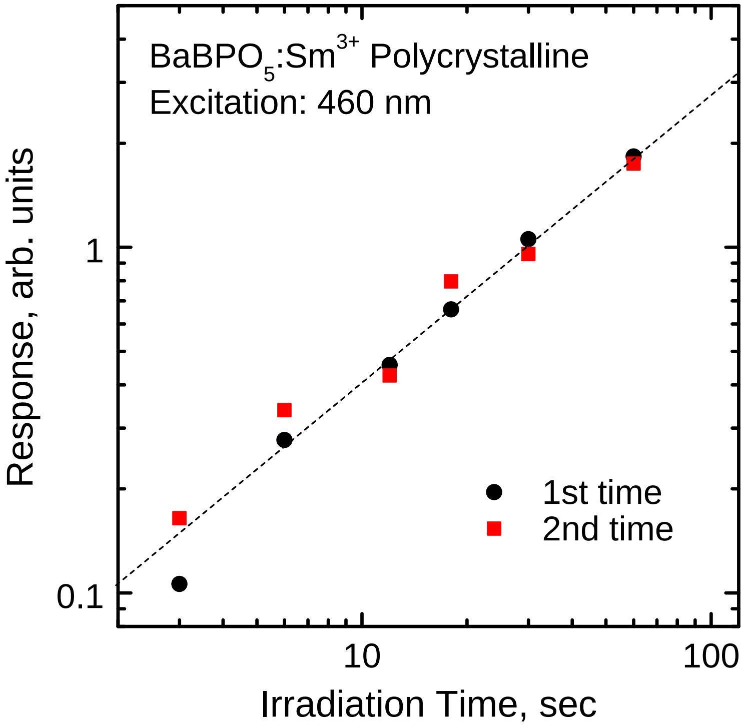

(b) BaBPO$_5$:Sm^{3+} polycrystalline

Figure 5.6: Dose-response curves of as-prepared polycrystalline samples and those after heat-treatment at 700 °C for 5 hours.

tial response values, the curves of 2nd- and 3rd-time uses are very closely correlated. This fact suggests that the material may be still re-usable (as long as the curves are consistent after the 1st-time use). On the other hand, for $BaBPO_5$, most of the response values recorded were erased after the heat-treatment, and Figure 5.6 (b) shows a better agreement between the dose-response curves of the 1st- and 2nd-time uses.

5.7 Homogeneity

Detector material needs to be homogeneous at a submicron scale and over an area of microbeam detection. The MRT dosimetry requires resolving microscale patterns of high-contrast X-ray dose over the area of the microbeam, which may be on a scale of 30 cm^2 (specific protocol has not been determined, yet we assume that the size should be equivalent to a tumour size). As discussed earlier in Section 3.5.3, the host matrix of the detector may be in various forms, for instance single crystal, polycrystalline, or glass. Figure 5.7 compares microscopy images of (a-1) as-prepared polycrystalline material (SrB_4O_7), (b-1) polycrystalline after grain size control (YAG:Ce^{3+}), and (c-1) $BaBPO_5$ glass samples. The signal profiles over the diagonal line drawn in the images are also given in (a-2), (b-2), and (c-2), respectively. The magnification of the images is 10×. The YAG:Ce^{3+} ceramic sample was provided as a courtesy of Professor Tanabe's research group at Kyoto University for the purpose of testing the surface quality of a ceramic material in which the grain size is controlled. The surfaces of SrB_4O_7 polycrystalline and $BaBPO_5$ glass were polished by the same method, and the YAG:Ce^{3+} ceramic was prepared by pressing powder under high pressure and then heating sample at high temperature. The controlled powder grain size is <1 μm. The figure clearly illustrates that the inhomogeneous feature of the polycrystalline surface, which includes grain boundaries and voids between grains and these defects lead to scattering. After grain size control, the homogeneity has improved dramatically; however, it seems that the surface is not as smooth as glass. Therefore, at this magnification and image resolution of our interest, a glass material

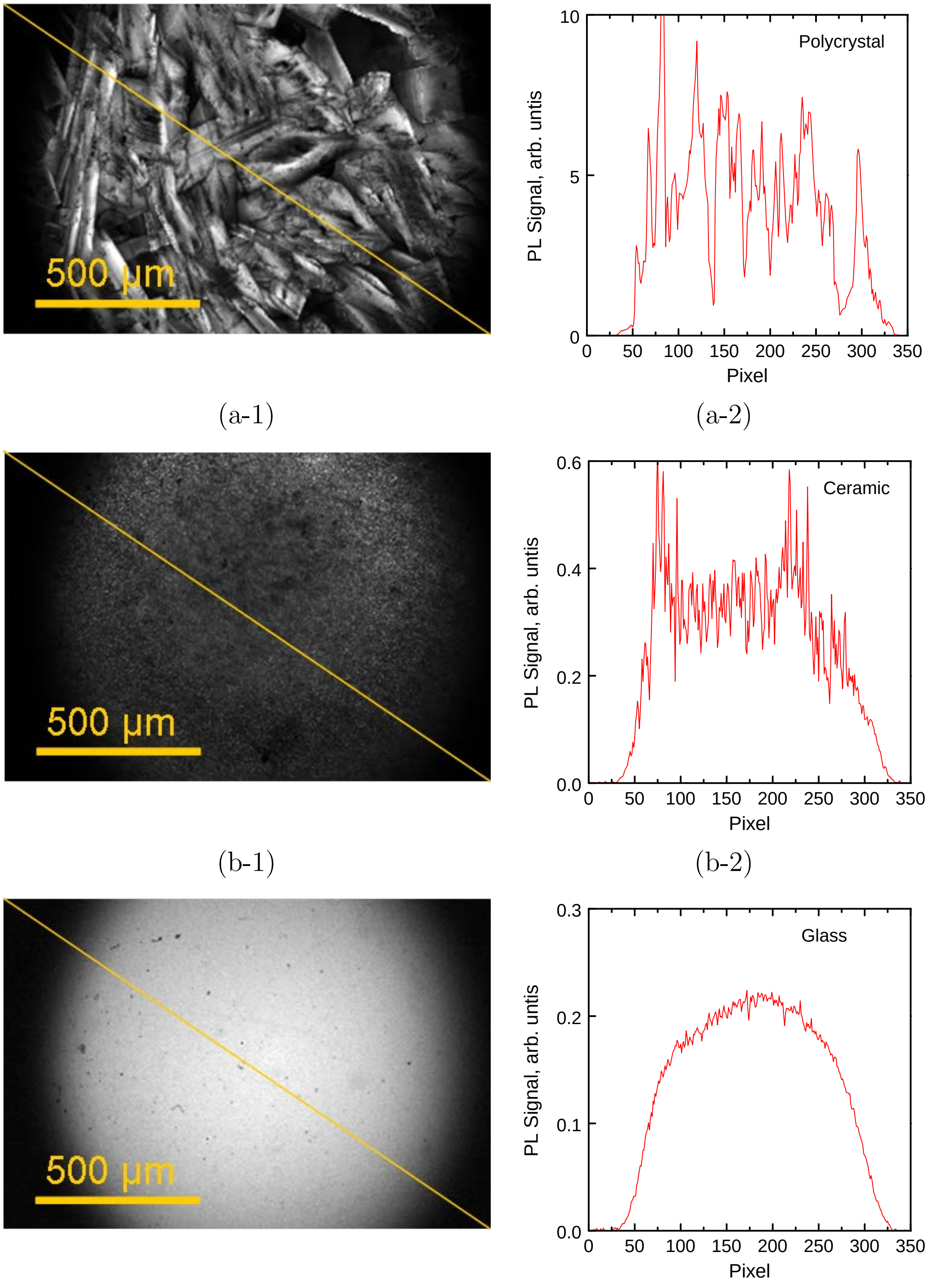

(a-1) (a-2)

(b-1) (b-2)

(c-1) (c-2)

Figure 5.7: Microscopy images of sample surfaces, (a-1) SrB_4O_7 polycrystalline, (b-1) YAG ceramic, and (c-1) $BaBPO_5$ glass. The corresponding PL signals along the diagonal line on each image are plotted on (a-2), (b-2), and (c-2), respectively. The magnification is 10×.

should be the best choice as a host matrix for Sm-ions in terms of the image quality.

5.8 Conclusion

We have examined a number of Sm^{3+}-doped materials in order to search for a potential dosimetry detector materials to be used for MRT. Such a material must allow the $Sm^{3+} \rightarrow Sm^{2+}$ change by X-ray irradiations and the PL signals of Sm^{3+} and Sm^{2+} must be measurable. Since the valence change is used as a measure of radiation dose, the response should be present in a dose range of interest. Further, the detector material needs to be homogeneous over the cross-sectional area of microbeam and also at submicron scale.

The tested material types include polycrystalline, glass, and glass-ceramic samples with different chemical compositions. All the materials showed the typical PL spectrum of Sm^{3+} due to the $4f$-$4f$ transitions. In addition, Sm^{2+} emission due to $4f$-$4f$ transitions was observed in the SrB_4O_7 polycrystalline sample, implying that Sm^{2+} ions are included and optically active in the as-prepared sample.

Among all the samples we tested, any expected conversion of Sm^{3+} ions in glass and glass-ceramic samples was not observed. To our surprise, our glasses reproduced from the earlier works, Li_2O-SrO-B_2O_3 [45] and SrO-BaO-P_2O_5-B_2O_3 [47] which were reported to show the conversion of Sm^{3+} to Sm^{2+}, did not show this conversion. This suggests that the conversion process is likely to be very sensitive to the preparation conditions. However, notable response against delivered X-rays was found in polycrystalline $BaBPO_5$, $SrBPO_5$, and SrB_4O_7. The PL signature of Sm^{2+} suggested that the PL emissions are due to typical $4f$-$4f$ transitions in these materials.

The $Sm^{3+} \rightarrow Sm^{2+}$ conversion induced by X-ray dose strongly depends on the host material. The saturation of response was found to be around several *tens* of grays for BaBPO:Sm^{3+} polycrystalline and several *hundreds* of grays for SrBPO:Sm^{3+}, and we did not observe any saturation up to $\sim$ 5500 Gy for SrB_4O_7 polycrystalline samples (the lower detection limit strongly depends on the instrument specifications such as the sensitivity of spectrometer used and strength of the excitation laser). Therefore, these materials, especially $SrBPO_5$ and SrB_4O_7, have good potential for satisfying the requirement of large dynamic range needed in MRT.

The X-ray generated Sm^{2+} ions are quite stable at room temperature in the dark, and the extent of response was kept stored over several days with little change of signal in converted Sm^{2+} ions. However, the stability of Sm^{2+} ion is dramatically reduced at elevated temperatures, and almost all the Sm^{2+} can be removed (that is converted back to Sm^{3+}) after heating the sample at 700 °C (in the case of BaBPO:Sm^{3+} polycrystalline samples). Since the heat-treated sample after irradiation showed further $Sm^{3+} \rightarrow Sm^{2+}$ conversion under X-rays, and the dose-response curve follows that observed before the heat-treatment, the heating technique can be used to *erase* the recorded dose information and the detector material is reusable multiple times.

Despite these excellent features of polycrystalline samples discussed above, the observation of the sample surfaces suggested that the materials are not suitable for MRT dosimetry. The surface of these polycrystalline samples is coarse even after polish as it contains pores, cracks and other defects due to the nature of the polycrystalline structure. Even with the control of crystalline grain size less than 1 μm, the surface was not homogeneous enough at the microscopic scale of interest. One of the possible ways may be to use a transparent ceramic. The transparent ceramic consists of nanometer sized powders of crystal with the cubic crystalline structure. When the powders were made into a ceramic in such a way that the boundaries of powders are ”fused” to each other, the whole ceramic bulk becomes optically transparent. It is because the crystal boundaries are well arranged that there are no refractive index differences across the powders. Unfortunately, the crystalline materials we tested in this work do not have a cubic structure; thus, further research is needed to explore cubic polycrystalline hosts.

Since the polycrystalline materials (especially $SrBPO_5$:Sm^{3+}) are highly sensitive to X-rays and the signal is stable, the material may also have a potential to substitute for an ordinary digital radiographic film. The commercially available imaging plate uses the PSL effect by crystalline powders such as BaFBr:Eu^{2+} which are distributed uniformly over the plate. The resolution of an imaging plate using the PSL effect is strongly limited by the focused spot size of stimulation light and by the nature of the PSL effect; the stored information is instantly lost after the exposure. In contrast to the PSL based phosphor, our Sm-doped polycrystalline materials have very stable signal as the generated Sm^{2+}-ion even after the PL measurement to extract the information. This is an advantage especially when the digitization is done using a confocal configuration with a pinhole at the detector side. In this configuration, only a selected dot within the excited spot can reflect as a single pixel and the spatial resolution can be dramatically improved compared to conventional medical radiography.

CHAPTER 6

Sm^{3+}-DOPED FLUOROPHOSPHATE AND FLUOROALUMINATE GLASSES

6.1 Introduction

We use the valence change of doped Sm^{3+} ion ($Sm^{3+} \rightarrow Sm^{2+}$) due to interactions with X-rays as a measure of the X-ray dose delivered to the sample [122], [123]. A transparent glass is an ideal candidate as a successful dosimetric imaging material since the transparent matrix significantly reduces unwanted light scattering during readout. In addition, at the microscopic scale of interest (submicrons at finest), the glass structure is uniform and the glass property is homogeneous. Sm^{3+}-doped fluorophosphate (FP) and fluoroaluminate (FA) glasses were the first transparent glass materials (fabricated in collaboration with the Dr. Edgar's group at Victoria University of Wellington, New Zealand) that we found to show the $Sm^{3+} \rightarrow Sm^{2+}$ conversion by X-ray irradiation. One of the easiest techniques to investigate whether or not the doped Sm^{3+} ion has been converted by X-ray irradiation is to measure the photoluminescence (PL) spectra, using a straightforward steady state photoluminescence technique, of a piece of glass sample before and after x-ray irradiation, X-ray irradiation can be done using an ordinary X-ray tube. It is a significant task for us to investigate such a conversion using the synchrotron X-ray source as well as confocal fluorescence microscopy readout. The microbeam radiation therapy (MRT) is typically carried out using high flux and high energy synchrotron X-rays. Since there is a good chance that the dosimeter material has flux and energy dependences, and the flux and energy profile generated by an X-ray tube are very different, it is very important to use synchrotron X-ray in order to accurately evaluate the dosimeter material which is to be used in MRT applications. Furthermore, the degree of conversion may not be the same over the entire volume at a certain level of x-ray exposure; rather it decreases as a function of the X-ray penetration depth inside the sample. Therefore, it is very important for us to readout at a consistent depth in the sample over several measurements with different samples, and this is possible using the confocal microscope readout.

6.2 Methodology

This chapter covers the study of Sm^{3+}-doped FP and FA glasses as high-dose and high-spatial-resolution X-ray detector material for use in Microbeam Radiation Therapy applications. One of the most important properties is the dose-response (that is, response against delivered dose). For dose-response measurements, a bulk glass sample of one kind was cut into pieces (approximately $3 \times 2 \times 0.5$ mm^3), and then the surfaces were polished. X-ray irradiations were carried out at the BMIT (05B1-1) beamline, CLS. A set of samples for each given composition was subject to irradiation by a broad beam with varying doses from ~ 1 Gy to over 1000 Gy, and then the response of each sample piece was read out using a confocal microscopy readout set-up. Hence, plotting the measured response values against the X-ray dose delivered yields a dose-response curve. In addition, the samples were also irradiated by a microbeam to investigate the ability for the glass detectors to store the distribution of X-ray dose in microbeam (i.e. dose-profile) and also to investigate the ability for confocal microscopy set-up to read out the response information recorded on the detector sample.

After the X-ray irradiation, some of the samples were, further, exposed to blue (460 nm) or UV (254 nm) light, and then the response values were measured in the same manner mentioned above. For light exposure, a 3-W LED (OSRAM) and a UV tube lamp (DE-4, UVP)were used, respectively. In the case of the exposure by LED, the samples were exposed inside an integrating sphere in order to ensure a uniform exposure over several pieces of sample, whereas UV exposure did not require such a technique as the intensity was fairly uniform along the tube. Moreover, together with investigations including optical transmittance, thermally stimulated luminescence (TL), and photobleaching techniques, the mechanism of $Sm^{3+} \rightarrow Sm^{2+}$ conversion is discussed in the following sections.

6.3 Experimental Results

6.3.1 Response of Valence Conversion upon X-ray Irradiation

The valence conversion of Sm ($Sm^{3+} \rightarrow Sm^{2+}$) upon X-ray irradiation may be used as a probe of X-ray dose delivered as mentioned previously. After the X-ray irradiations, the appearance of Sm^{2+} emissions in PL was found for both Sm-doped FP and FA samples. Figure 6.1 illustrates the dose-response curves, which present response values as a function of delivered X-ray dose, of FP and FA glasses doped with different concentrations of Sm^{3+}. The response values were normalized to be unity at saturation. It is worth noting that every point on these graphs corresponds to an individual piece of sample. Put differently, we avoided building up cumulative doses on a single sample. This approach allows more flexibility in the experiments since we can then also examine post-treatment effects on individual samples. In addition, the latter approach provides samples for TL measurements, as well. Further, by using an individual sample for each point, i.e. for each dose, we avoid the effects of bleaching that would otherwise occur had we used one sample throughout all dose measurements. In both the host materials, continuous valence conversion was confirmed from a dose of ~ 1 Gy up to over 1000 Gy, where saturation occurs, thus limiting the dynamic range at the upper end. As seen in Figure 6.1, the valence conversion rate as well as the dynamic range seems to vary with the concentration of Sm^{3+}-dopant, and appears to be different for FP and FA host matrices. The samples with the highest concentrations of Sm^{3+} (5.0 % and 10.0 %) are not shown in Figure

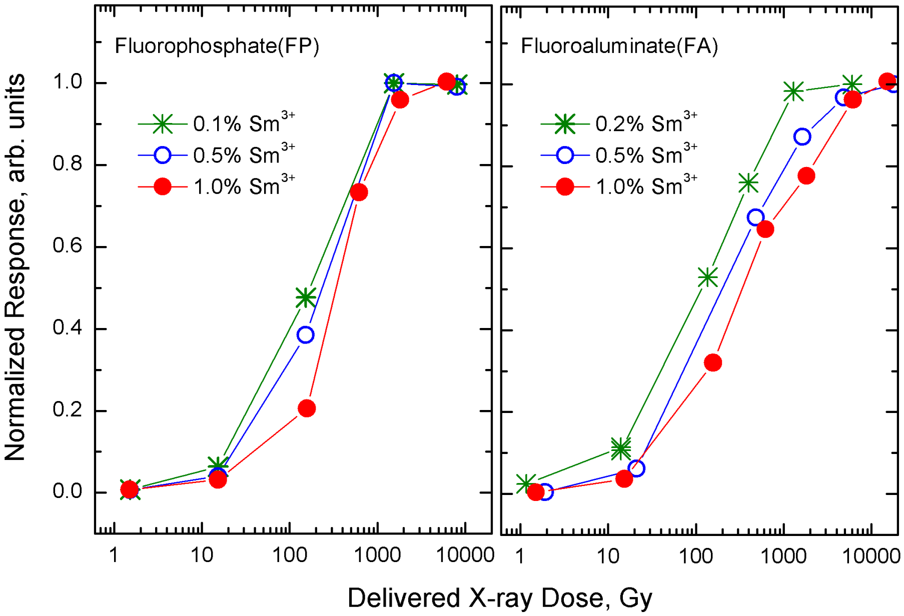

Figure 6.1: Dose-response curves of Sm-doped FP and FA glasses with different dopant concentrations. Every plot corresponds to a response value recorded on an individual sample.

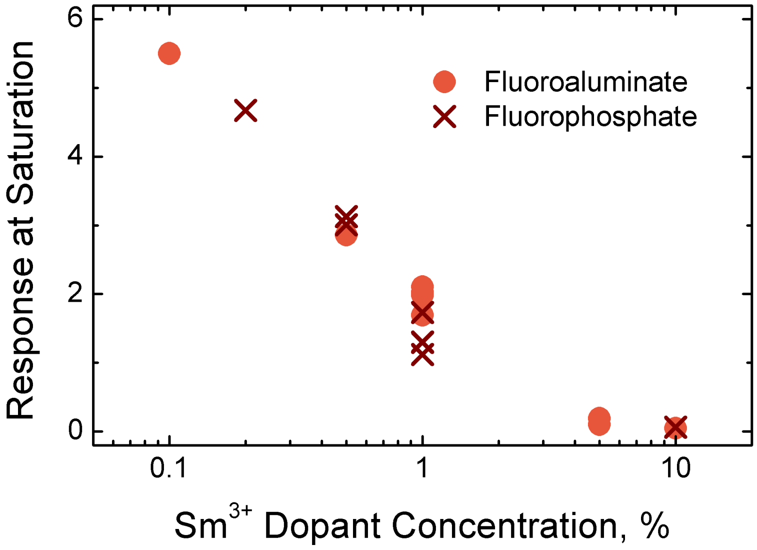

Figure 6.2: Response values at saturation against concentration of Sm dopant.

6.1 because the extent of conversion was so small that the results (or the response) had significant noise. Figure 6.2 illustrates the response values at saturation against the concentration of Sm^{3+} for both FP and FA glasses. It is clear that the response value at saturation decreases with increasing Sm^{3+} dopant concentration. Namely, the conversion rate seems to decrease for larger Sm concentrations, while the dynamic range appears to be larger for FA than FP glasses. Also, the response values at saturation appear to be independent on the host glass matrix.

6.3.2 Stability of Response Signal

After the irradiation, it is important that the dosimetric detector stores the dose information over a long period of time until the stored information is read out and digitized. Figure 6.3 shows the change of response as a function of time after the irradiation. A set of glass pieces of one kind (i.e. of a given composition) was irradiated by 500 Gy of radiation all together, and then the response value of each piece was digitized at varying times after the irradiation. Therefore, each plotted point in the graph represents an individual glass piece.

It seems like that the stability of response depends strongly on the concentration of Sm^{3+} ions added into the detector glass. The lower the concentration, the stronger is the fading after the irradiation. However, eventually the response values are stabilized after 1 day. For those doped with 1 % of Sm^{3+}, it seems that the response value is very stable from just after the irradiation (1 h).

6.3.3 Dose-profile of Microbeam

With a glass detector (0.2 % Sm^{3+}-doped FA glass), we have attempted to measure X-ray dose distribution of microbeam (dose-profile) to show the capability of our approach. Three pieces of glass were irradiated by a microbeam at the CLS at different entrance doses. For these irradiations, a broad X-ray beam of approximately 14, 140, or 1400 Gy was delivered to the MSC, and the produced microbeam was delivered to the sample. The recorded dose-profile by the sample was further digitized

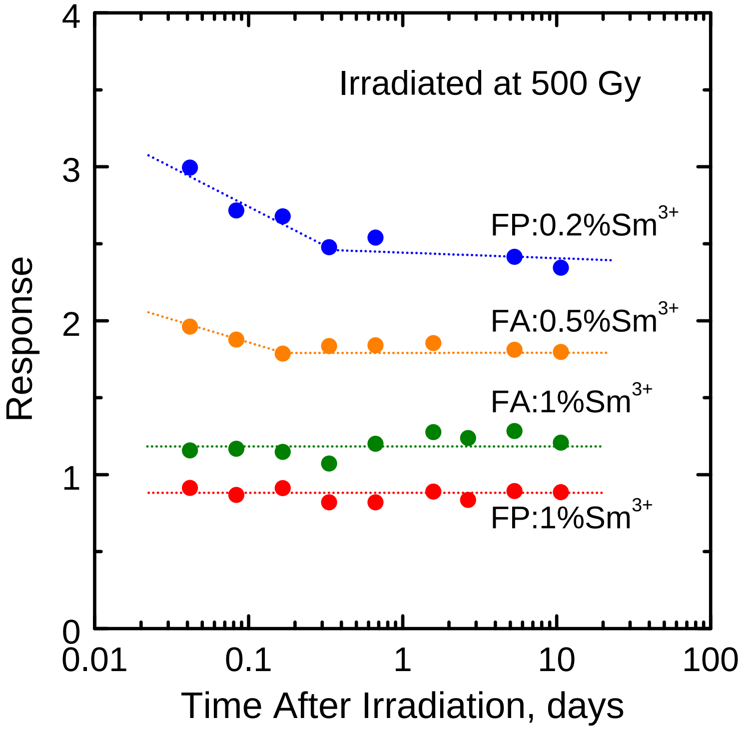

Figure 6.3: Stability of response after X-ray irradiation. Detector samples were irradiated by 500 Gy.

by using a confocal microscopy and the ratio of the PL signal from the Sm^{2+} to that from the Sm^{3+}-ions (i.e. $\mathrm{PL}(\mathrm{Sm}^{2+})/\mathrm{PL}(\mathrm{Sm}^{3+})$). Figure 6.4 shows the as-acquired image by the confocal microscope reader. The two peaks of microbeam have been successfully detected in the two-dimensional space, and it is clearly seen that the peak intensity increases as the entrance dose increases. Further, the response values were averaged along the microplanar beams and the averaged values were calibrated to the *dose* values based on the dose-response curve acquired earlier in Figure 6.1. The results are a one-dimensional representation of dose-profile as illustrated in Figure 6.5. We have successfully detected both valley and peak doses together over a high dose range. Further, our results unveiled that the peak shape is more or less flat at the centre of microplanar beams, while the tail of beam caused by X-ray scattering is well represented. Figure 6.6 compares our experimental observation with Monte Carlo simulation data by Nettelbeck et al. [124]. These two independent works agree very well, thus the result shows that our measurement technique is highly promising.

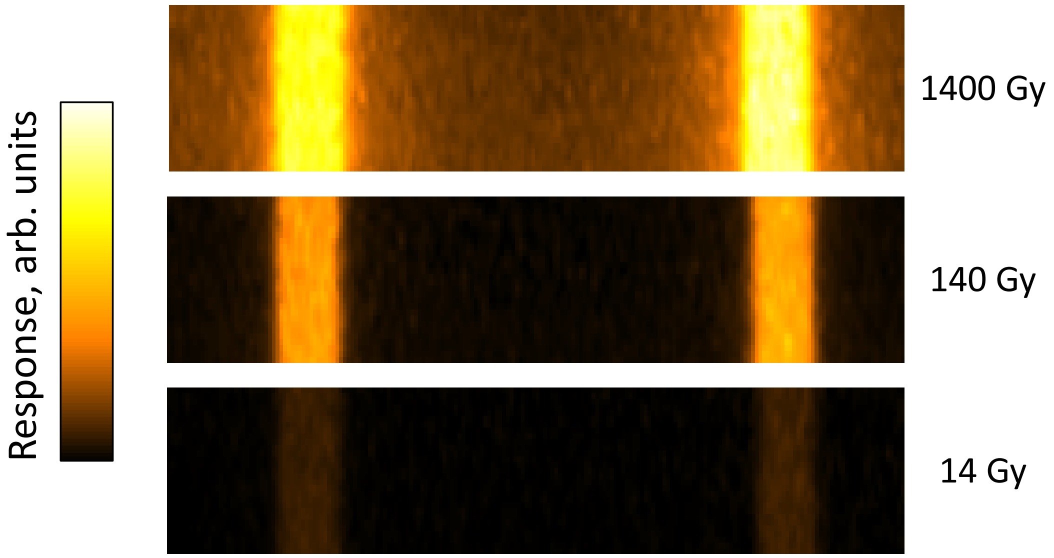

Figure 6.4: The two-dimensional distribution of X-ray in microbeam for varying entrance doses, 14, 140, and 1400 Gy. The measurements were done using 0.2% Sm^{3+}-doped FA glass detector. Note that the pixel values are response as defined in Equation 4.3.

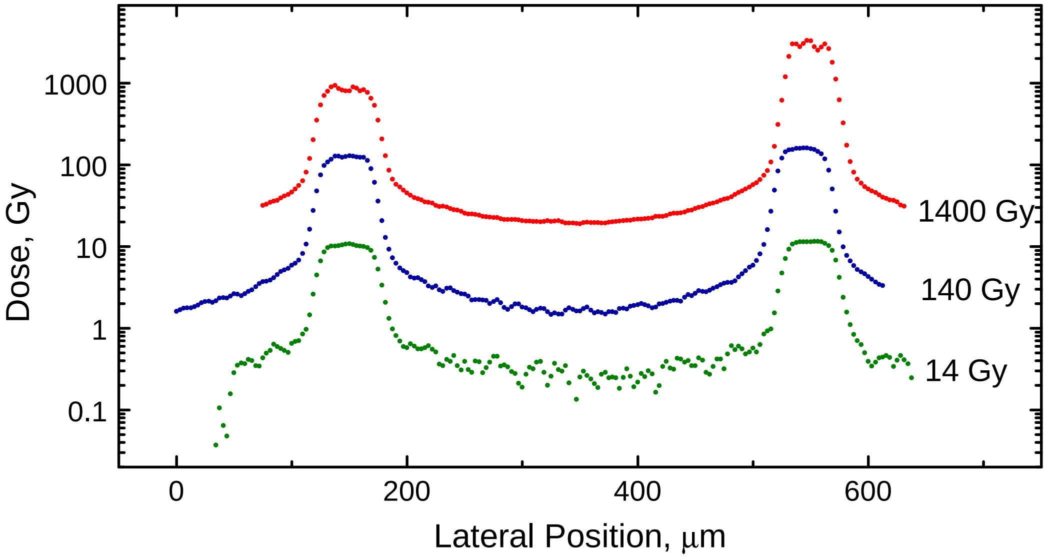

Figure 6.5: Dose-profiles of microbeam measured using 0.2% Sm^{3+}-doped FA glass. The doses, 14, 140, and 1400 Gy are estimated values at the upstream of MSC.

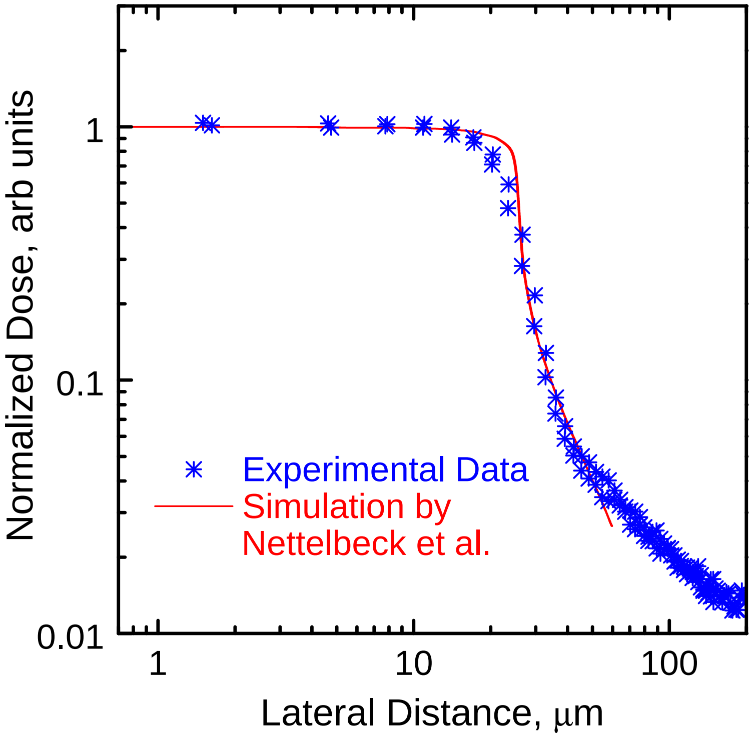

Figure 6.6: Comparison of microbeam peak shapes obtained by our experimental measurement as well as by a Monte Carlo simulation by Nettelbeck [124]. The values are normalized to the peak dose.

6.3.4 Colour Change due to X-ray Irradiation

Both as-prepared FP and FA samples were visually transparent with slight yellowish colouration. However, upon X-ray irradiations, the samples became darker and the darkening was much stronger in the FP than the FA sample. These observations are summarised in Figure 6.7, which compares X-ray induced absorbance spectra of as-irradiated, blue-exposed and UV-exposed Sm-doped FP and FA samples. The light treatments were carried out after the X-ray irradiation. It is clear that the induced absorbance was stronger in the FP glass than that of FA, and blue ($\sim$ 2.7 eV) or UV ($\sim$ 4.9 eV) light treatment reduced the induced absorbance in both the samples. This bleaching effect was more pronounced for the UV light treatment.

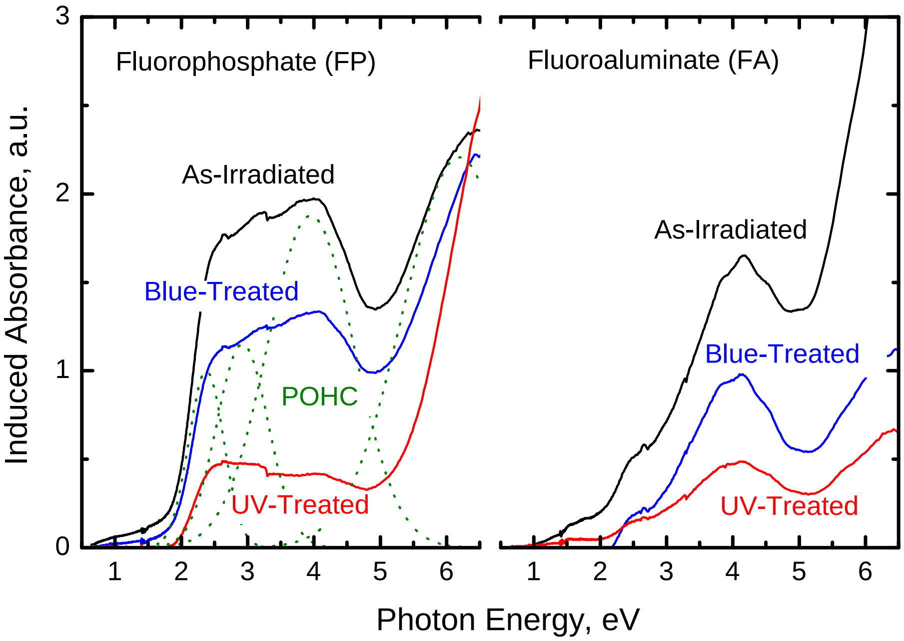

Figure 6.7: X-ray induced absorbance of Sm-doped FP and FA. The concentration of Sm for both the glasses was 1 %. The dotted curves show a presentation of the induced absorbance in an FP glass as a sum of Gaussians. Three of them are tentatively associated with phosphorus-oxide hole centers (POHCs) [125].

6.3.5 Thermally Stimulated Luminescence

In Figure 6.8, TL glow curves of irradiated Sm-doped FP glass and that of FA glass are compared. The concentration of the initial Sm^{3+} dopant was 1.0 %. The dashed lines are Gaussian curve fits. For both FP and FA glasses, the spectra of the TL emission (not shown here) were for the *f*–*f* transitions of Sm^{3+} ions. In both the TL spectra, two major peaks were observed; however, an additional peak was present in the FP glass. This may imply the existence of an additional charge trapping level in the FP glass compared to that in the FA glass. In addition, the two major TL peaks in FA glass appeared to be at higher temperatures by ∼ 60 °C, with respect to those of FP glass.

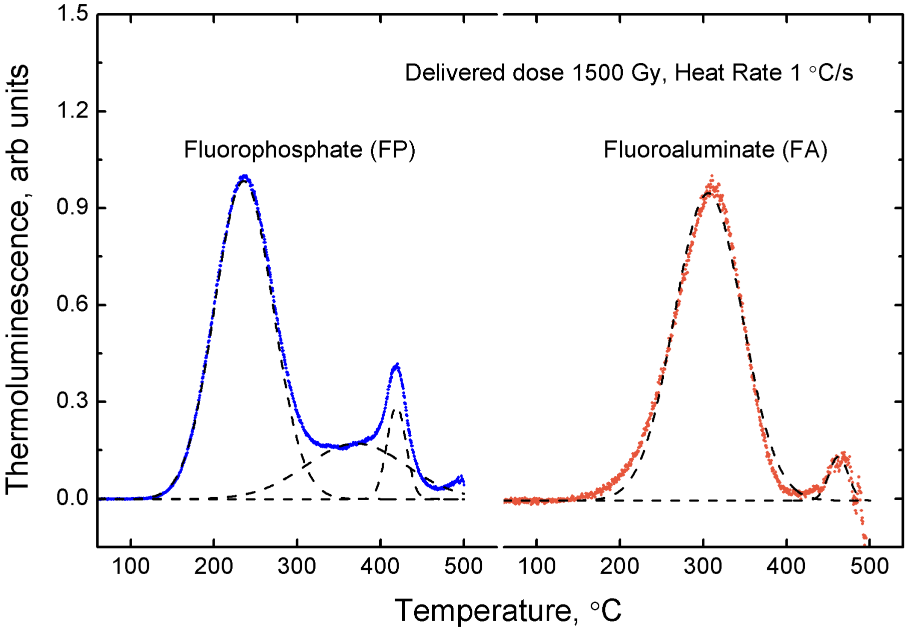

Figure 6.8: TL glow curves of irradiated Sm-doped FP and FA glasses. The delivered X-ray dose was about 1500 Gy. The heating rate was 1 °C/s.

6.3.6 Effect of Dose-Response upon Post-Irradiation Optical Treatment

Figure 6.9 compares the dose-response curves of FP and FA samples with and without optical treatments by blue and UV light. To facilitate the comparison, all the graphs were plotted twice: with absolute response values in the upper part of the figure and with values normalized to that at saturation in the lower part. As can be seen in the upper part of the figure, the absolute values decreased by the optical treatment for both types of host glass. This effect may be attributed to the optically stimulated conversion of $\mathrm{Sm}^{2+} \rightarrow \mathrm{Sm}^{3+}$, or commonly referred as photobleaching of Sm^{2+}. In the case of Sm-doped FA glasses, the effects of blue and UV photobleaching on the response curves were approximately the same. On the other hand, the effects of photobleaching on the normalized dose-response curves of the FP glass, as shown in the lower part of Figure 6.9, depend on whether blue or UV bleaching is used. In particular, the UV treatment of FP glass has led to the disappearance of saturation. But, this comes at the cost of sensitivity.

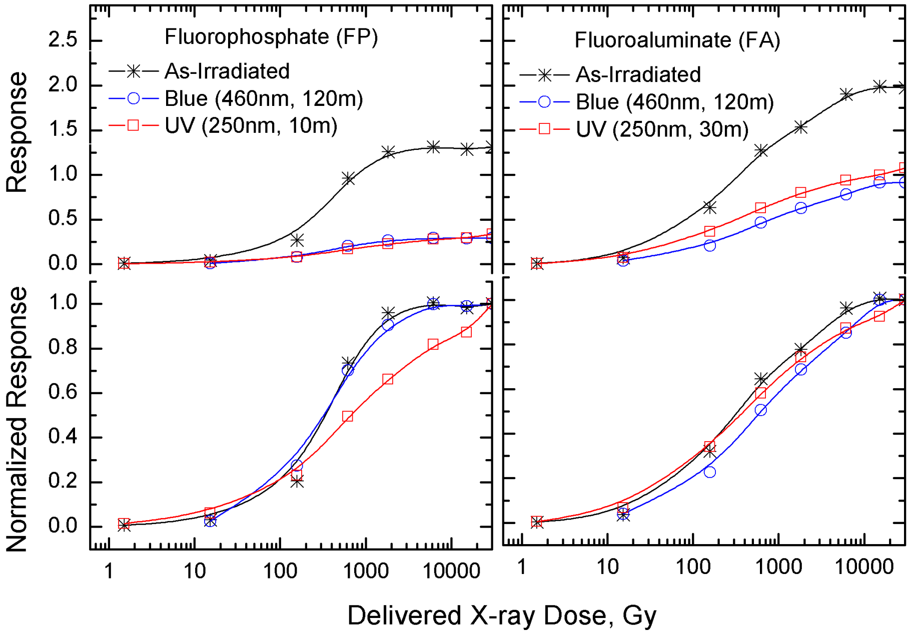

Figure 6.9: Dose-response curves of Sm-doped FP and FA glasses before and after optical treatment. The concentration of Sm was 1 %. To facilitate comparison all the graphs are plotted twice: with absolute response values (upper part) and with normalized values to that at saturation (lower part). Every plot corresponds to a response value recorded on an individual sample.

Figure 6.10 compares measured microbeam dose-profiles with large peak doses. The detector material used was 1 % Sm^{3+}-doped FP glass. Since the as-irradiated FP glass plate does not have an ability to detect above 1000 Gy, the measurement of peak dose could not be achieved as shown in Figure 6.10 (top). However, with a cure of UV treatment, the detection dose range can be expanded, thus peak dose was successfully detected as shown in Figure 6.10 (bottom).

6.4 Discussions

The experiments showed that both Sm-doped FP and FA glasses exhibited effective valence conversion of Sm ions under X-ray irradiation. The dynamic range of conversion, i.e. the irradiation dose necessary to reach saturation, exceeded several thousands of Grays which is very promising for dosimetric detector applications in MRT. The response signal is very stable over a long-time period. The stability seems to depend on the concentration of Sm^{3+} added, and we did not find any fading of

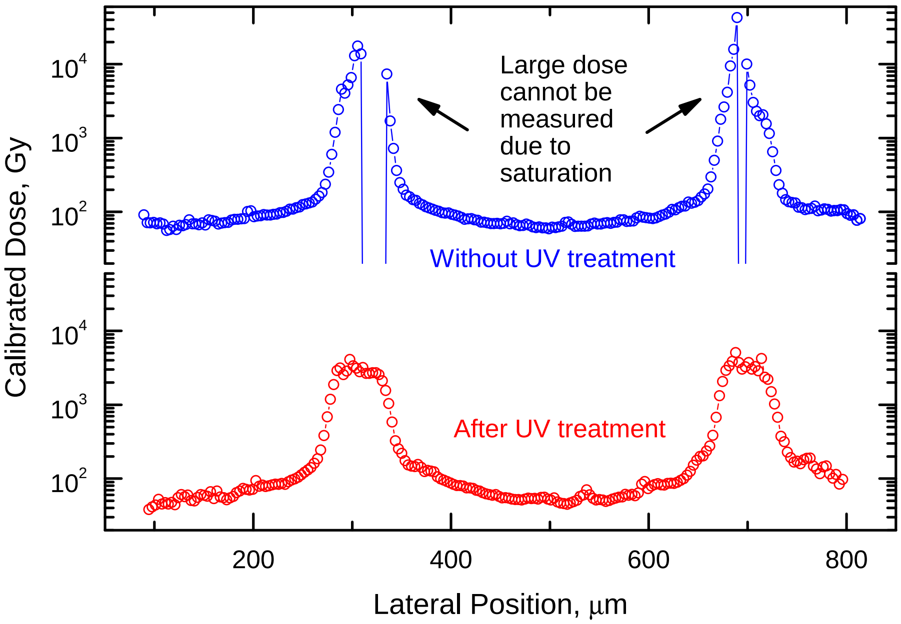

Figure 6.10: An example of microbeam measurement at high-dose using UV treatment technique. The detector plate is 1 % Sm^{3+}-doped FP glass in which the saturation takes place around 1000 Gy and above. The UV treatment technique with an appropriate dose calibration enables to measure large dose. The detected dose at the peaks is approximately 3000 Gy.

signal when the glass detectors (both FP and FA) are doped with 1 % Sm^{3+} ions. However, all the tested materials showed no change of response after 24 hours after the irradiation. As shown in Figure 6.5, we have demonstrated, with the use of confocal microscopy readout, that our approach enables the detection of the dose distribution of the microbeam (dose-profile) which contains very large doses, and the detected profile is in an excellent agreement with the simulation data [124].

The conversion rate seems to depend on the concentration of Sm dopants and on the composition of host matrix. It is worth noting here that a similar dependence on the host environment has also been observed in some crystalline materials [122]. The comparison of Sm-doped FP and FA glasses shows that the conversion reaches saturation at a lower dose in FP than FA glass as seen in Figure 6.1. On the other hand, Figure 6.2 indicates that the total numbers of converted Sm^{2+} ions were the same for the both hosts. These experimental observations imply that FP is a more sensitive dosimetric material. Below, we will discuss this fact using a charge trapping model and a phosphorous-oxygen hole center (POHC), which is present in an FP glass system.

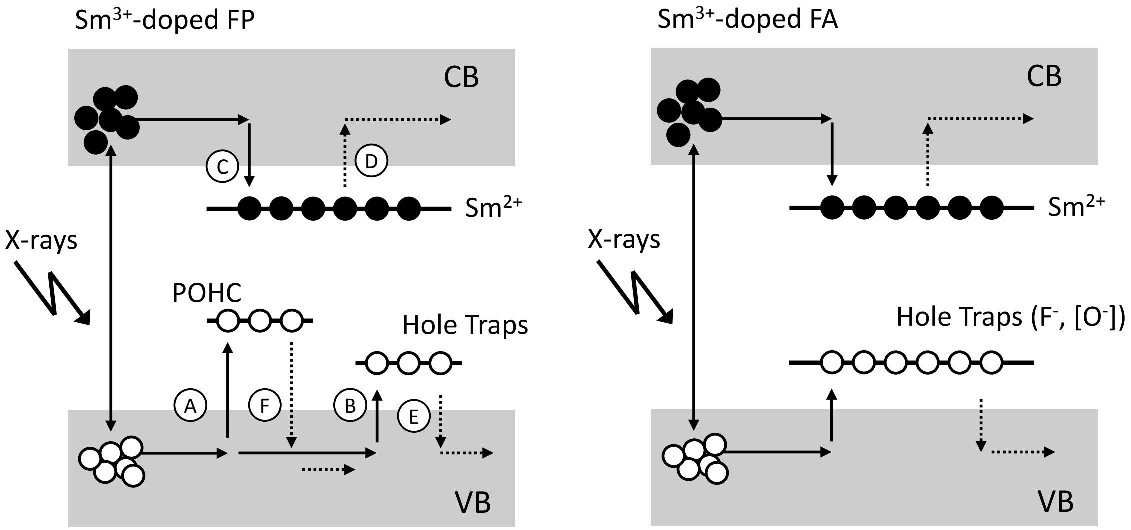

Figure 6.11: Suggested band diagram models of Sm^{3+}-doped FP and FA glass detectors.

The interconversion of Sm-ions may be explained using a band diagram as illustrated in Figure 6.11. Here, we assume that Sm^{3+} ions act as electron-trapping centres in order to become Sm^{2+}. The X-ray irradiation generates numerous electron-hole pairs. Some of the electrons are captured by Sm^{3+} ions (which then become Sm^{2+}) (indicated as Ⓒ) while the corresponding holes must be captured by some hole-trapping centres to ensure persistent $Sm^{3+} \rightarrow Sm^{2+}$ conversion (indicated as Ⓐ (and Ⓑ)). Figure 6.2 indicates that increasing the concentration of electron-trapping centres (Sm^{3+} ions) did not increase the total number of converted Sm^{2+} ions. Moreover, PL measurements indicated that most of the Sm^{3+} ions stayed unconverted at saturation. These facts imply that, when the conversion reaches its saturation, some of the electron-trapping centres, i.e. Sm^{3+}, are still available to capture electrons, while the hole trapping centres are fully occupied. Therefore, it is safe to say that, in our glass systems, the $Sm^{3+} \rightarrow Sm^{2+}$ conversion process is controlled by a hole-trapping process rather than electron trapping.

There are several models of hole-trapping centres in fluoride glasses. One of the models was put forward by Griscom et al. [126]. According to this model, the existence of hole-trapping centres in heavy-metal fluoride glasses is associated with F- and O-ion vacancies. FP glass has O-ions as one of the main compositions, and FA glass may contain O-ions as a foreign impurity. These trapping centres may be illustrated as in Figure 6.11. In addition, Ebeling et al. suggest that in the FP glass some of the phosphorous-oxygen bonds are converted into POHCs by trapping holes (indicated as Ⓐ) [125]. The POHCs give rise to strong optical absorption bands in the UV region and this was indeed observed in our experiments (Figure 6.7). Our TL measurements support this idea as the glow curve in the FP glass showed an additional peak at around 375 °C compared to that of FA. This peak may be associated with the release of holes from POHCs. This conclusion is supported by the effective bleaching of induced absorbance by annealing at the same temperature range.

The same idea of additional hole-trapping center in FP glasses may explain the difference in the dose-response curves of FP glasses between UV- and blue-treatments shown in Figure 6.9. During the X-ray irradiation, multiple types of hole capture centers, including POHCs, operate at different speeds or have different time scales. More particularly, trapping rate of Ⓐ and Ⓑ (indicated in Figure 6.11) may not be the same. Exposure to UV would bleach POHCs more efficiently than the others (indicated as Ⓕ), which would lead to a reduction in the concentration of Sm^{2+} (indicated as Ⓓ). As a result, the dose-response curves after UV-treatment represent the Sm valence conversion rate, in arbitrary units, disregarding the effects of POHCs. Further, the Sm-doped FP samples under UV treatment did not show saturation. This implies, in turn, that the POHCs and corresponding number of Sm^{2+} ions populate at a higher rate, which give higher sensitivity to the Sm-doped FP glass with respect to the Sm-doped FA glass. Thus, if there existed no POHCs in FP glass, the dynamic range would be larger. In other words, with the functionality of hole trapping with phosphorous-oxygen bonds, the dynamic range of FP glass may be smaller, but the detector sensitivity is higher. Moreover, FP glass could be used as a "flexible dynamic range" dosimeter material as the dynamic range of FP glass can be enlarged with UV-treatment, at the cost of sensitivity, if needed. The latter effect was demonstrated and illustrated in Figure 6.10. The large peak dose, which cannot be measured by the as-irradiated sample, was successfully detected using the UV-treatment technique. However, the S/N ratio decreased as significant amount of Sm^{2+} ion was also removed by UV exposure. The signal-to-noise ratio also depends on the performance of the readout instruments, thus the improvement of microscopy set-up should overcome this issue.

6.5 Conclusion

We have studied Sm^{3+}-doped FP and FA glasses with varying concentrations of Sm^{3+} dopants as potential X-ray dosimetric detector materials for high-dose high-resolution applications in MRT. This type of dosimeter employs the degree of Sm^{3+} to Sm^{2+} conversion as a measure of the delivered X-ray dose. The detailed examination of dynamic ranges of the samples have unveiled excellent coverage of the dose range used in MRT, from ~ 1 to over 1000 Gy, followed by saturation. Our demonstration of microbeam measurement, with such a material, showed a remarkable ability to detect the dose distribution of microbeams with a large dose. When the concentration of the Sm^{3+} dopant was higher, the saturation seemed to be reached at a higher dose. In other words, the dynamic range of the detector may be controlled by the doping concentration of Sm^{3+}. Moreover, the saturation dose also seems to depend on the choice of the host glass; the saturation was reached at a higher dose in FA glasses than that in FP. The conversion response was further studied with optical bleaching and TL experiments in order to understand the charge trapping mechanisms. The results indicate that the POHC present in the FP glass plays a major role in increasing the sensitivity of this Sm-doped glass system. On the other hand, the dynamic range of the FP glass can be controlled by UV-treatment, which allows us to achieve over 1000 Gy of dose detection.

In fact, Vahedi [127] and Morrell [128] have shown that the Sm^{2+} ions generated by X-ray irradiation in FP and FA glasses can be reset to the trivalent state by exposing to light a UV lamp, a strong purple laser, or by heating the detector material to a temperature around its glass transition temperature. Furthermore, these ”erased” glasses are reusable multiple times. Therefore, we strongly believe that Sm^{3+}-doped FP and FA glasses are probably the best candidates for the detector material to be used to measure the distribution of high-dose X-rays on the micrometer scale such as in a microbeam.

Chapter 7

Samarium(III)-Doped Oxyfluoride Glass-Ceramic

7.1 Introduction

In Chapter 3, we have proposed a novel X-ray dosimetry technique for large-dynamic-range and high-spatial-resolution to be used in Microbeam Radiation Therapy (MRT). [122, 123]. The technique uses a dosimeter material which is a host material that has been doped with Sm^{3+} ion in which the embedded Sm^{3+} ion is converted to Sm^{2+} ion under X-ray exposure. The extent of this conversion is then used as a measure of the radiation dose delivered, and this conversion is read out, at a submicron of resolution, as photoluminescence (PL) signals using a confocal microscopy readout.

Potential dosimeter materials in our approach are clearly those that allow the $Sm^{3+} \rightarrow Sm^{2+}$ reduction to occur under irradiation; examples of irradiation include X-rays [47, 45, 48], γ-rays [39] and intense infrared femtosecond laser [51]. In Chapter 5, we have studied a number of Sm^{3+}-doped materials. However, the $Sm^{3+} \rightarrow Sm^{2+}$ conversion by X-ray irradiation is not observed in all possible host materials, but only in selected hosts. It seems that the conversion is more commonly found in crystals rather than glasses. Such host crystals include CaF_2, SrF_2, $BaBPO_5$, $SrBPO_5$, SrB_4O_7 and a number of others. These can be easily fabricated into powder and distributed on a film, but during the readout, the excitation as well as the PL signal are scattered by the powderized material, leading to a poor readout resolution (see Figure 5.7). In order to avoid this issue of light scattering, one can use a single crystal; however, the fabrication of specialized large area crystals is challenging and usually expensive. On the other hand, in Chapter 7, we have successfully fabricated Sm^{3+}-doped fluorophosphate (FP) and fluoroaluminate (FA) glasses, both of which are excellent materials showing the desirable $Sm^{3+} \rightarrow Sm^{2+}$ conversion by X-ray exposure. The latter works have been already published in the literature [129], [123], [127]. These glasses are transparent and can be easily fabricated into a sufficiently large area. However, from our investigation, it was found that the converted Sm^{3+} ion in these glasses shows a PL signal which is dominantly due to the radiative transition within the $4f$ orbital shell (the $4f$-$4f$ transition). Such a radiative transition is understood to have a long lifetime (typically on the order of milliseconds in the case of $4f$-$4f$ transitions of rare-earth ions). This means that it takes more than a millisecond to readout one pixel point; thus it requires quite a long time to read out the entire sample.

In addition to crystals and glasses, glass-ceramics are another class of materials that have recently attracted much attention. It typically has a transparent glass matrix which contains nanocrystals uniformly distributed over the volume. Therefore, it may be possible to design a glass-ceramic as a new dosimeter material in such a way that the Sm^{3+}-doped nanocrystals, which are already known to show the $Sm^{3+} \rightarrow Sm^{2+}$ conversion, are included in a glass matrix. A Sm^{3+}-doped oxyfluoride glass is a primary candidate. In this particular glass, it is understood that, doped rare earth ion (in this case Sm^{3+}) acts as a nucleation centre, and then CaF_2 nanocrystals can be grown upon an appropriate heat treatment schedule. As a result, we may obtain a glass-ceramic containing CaF_2 nanocrystals doped including Sm^{3+}. (The Sm^{3+} ions are actually embedded in CaF_2 nanocrystals.) As mentioned above, Sm^{3+} embedded in CaF_2 crystals are known to be reduced to Sm^{2+} by X-ray exposure [79, 130, 131, 59, 132]; while, Sm^{2+} included in CaF_2 is reported to show PL emission which is dominantly, at room temperature, due to the $5d \rightarrow 4f$ transition [133], the lifetime of which is typically on the order of nanoseconds [134, 135]. The PL lifetime is one of the key parameters that limit the readout speed since the detector sample is scanned point-by-point. Many materials that exhibit the $Sm^{3+} \rightarrow Sm^{2+}$ reduction by X-ray irradiation seem to typically show a PL lifetime on the order of milliseconds due to the parity-forbidden f-f transitions. Oxyfluoride glass ceramics containing CaF_2 nanocrystals have been widely studied with various rare-earth dopants for applications such as up-conversion, quantum cutting etc. [74, 75, 76, 136, 137, 138, 139, 140].

7.2 Methodology

The experiments have been planned and carried out as illustrated in Figure 7.1. First, Sm^{3+}-doped oxyfluoride glass ($45SiO_2$-$20Al_2O_3$-$22CaF_2$-$10CaO$-$3SmF_3$ in mol. %) was synthesized by a conventional melt-quenching method. (The detailed descriptions of the synthesis can be found earlier in Section 4.2.) It is instructive to note here that this type of glass-ceramic is obtained by heat-treating an as-prepared glass at an appropriate temperature and for an appropriate duration of time such that nanocrystals is nucleated and grow in the glass matrix, which then becomes a glass-ceramic. Suitable heat treatment temperatures can be obtained by examining DSC measurements. Following the synthesis of a dosimetric glass sample, DSC measurements were carried out to obtain the temperature, at which the nucleation and growth of CaF_2 nanocrystals occur; if such nanocrystals can be grown in the host of interest.

Next, the structural analysis was carried out by XRD and SEM measurements. An as-prepared sample as well as samples after heat-treatment at different temperatures were subject to XRD measurements to investigate whether or not CaF_2 nanocrystals had been formed in the glass matrix as well as estimating the nanocrystal size, if any. The range of heat-treatment temperature was based on the DSC measurement result obtained earlier. Further, observations by an SEM was carried out to find out the 2-dimensional distribution of nanocrystals on a suitably curt surface in addition to the XRD measurements. The nanocrystals need to be uniformly distributed at the nano- or sub-micrometer scale since, ideally, the material is expected to be used to detect X-ray doses distributed on a micrometer scale and the valence change of the Sm-ions embedded in CaF_2 nanocrystals store the dose values.

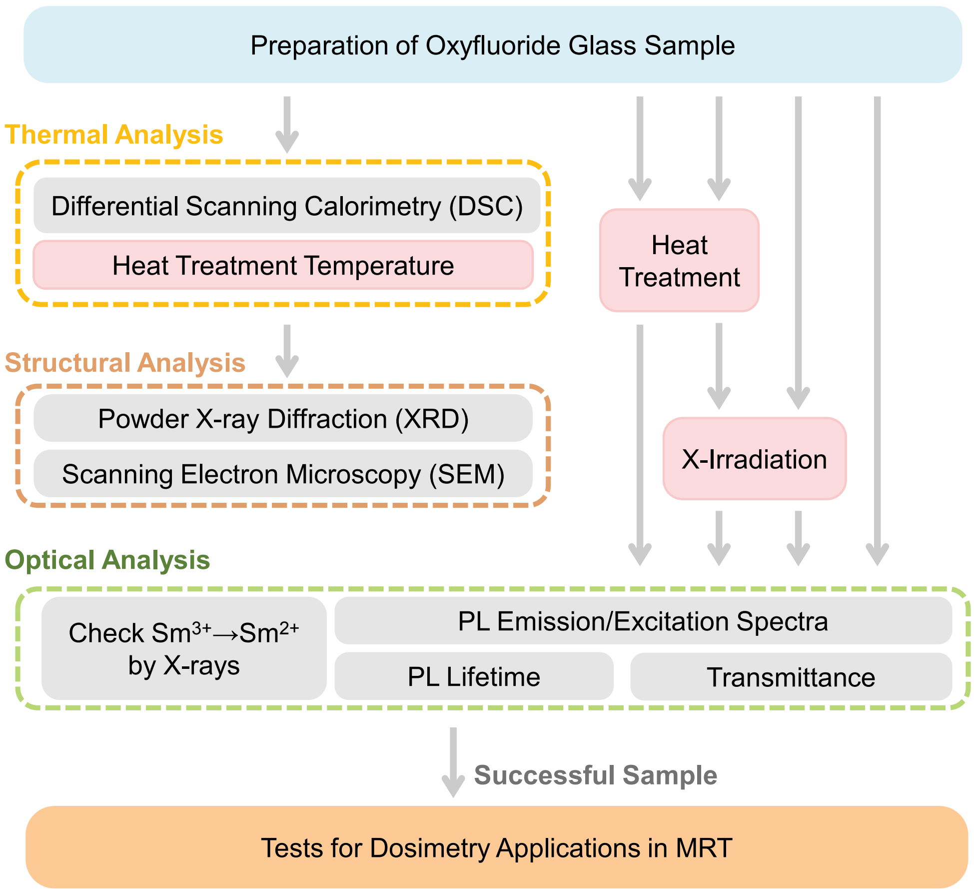

Figure 7.1: Illustration of experimental procedure.

Optical properties were also investigated for the samples with and without heat-treatment and with and without X-ray irradiation. The irradiation was carried out with the FAXITRON X-ray unit. Particularly, measurements of PL spectra before and after irradiation was of primal technique to investigate whether or not the $\mathrm{Sm}^{3+} \rightarrow \mathrm{Sm}^{2+}$ change by X-ray irradiation is present. Moreover, PL excitation, PL lifetime as well as optical transmittance measurements were carried out to study optical properties of the material.

Last, applicability of this new material as a dosimetric detector to be used in MRT has been tested. The study includes the dose-response (i.e. response against delivered X-ray dose), which tells us the dose range over which the material can measure the dose, and dose-profile of the microbeam (i.e. X-ray dose distribution in the cross-sectional area of the microbeam). The irradiation was performed at the BMIT, CLS. In order to obtain the dose-response, several pieces of sample were irradiated with varying doses from ~ 1 Gy to over 10 kGy, and the response values of each piece were measured using a confocal microscopy readout set-up. The samples were polished prior to the irradiations, and the response was, at all times, measured at a depth of 20 μm inside the sample from the surface; a good portion of the incident X-ray photons are absorbed in this region. In addition, the *reusability* of the material was also tested. The tests included the *erasability* of the response measured in the material and the *reproducibility* of the dose-response curve. The erasure was attempted by either heat-treatment or UV exposure. Samples were irradiated in the FAXITRON unit. The response was obtained form PL measurements with a 633-nm excitation.

7.3 Results and Discussion

7.3.1 Thermal and Structural Properties

The DSC curve shown in Figure 7.2 indicates a glass transition (T_g) at 608 °C and two crystallization peak temperatures at 687 °C (T_{p1}) and at 853 °C (T_{p2}) where the crystallization rate is maximum, as marked on the thermogram. These characteristics are typical for a glass which can be transformed into a glass-ceramic by an appropriate heat treatment; the exothermic peak at the lower temperature (about 690 °C) in Figure 7.2 typically corresponds to the nucleation and growth of nanocrystals, while the exotherm at the higher temperature corresponds to the crystallization of the glass matrix as discussed in various papers in the literature; see for example references [6, 37].

The XRD results are illustrated in Figure 7.3 for samples that are (a) as-prepared, (b) heat-treated at 700 °C for 4 h and (c) heat-treated at 750 °C for 30 min. Figure 7.3 (a) shows only a broad halo peak at $2\theta \approx 27°$ for the as-prepared glass sample, the signature of which is typical for an amorphous structure. However, for those samples which have been heat-treated at the temperatures between T_{p1} and T_{p2}, at

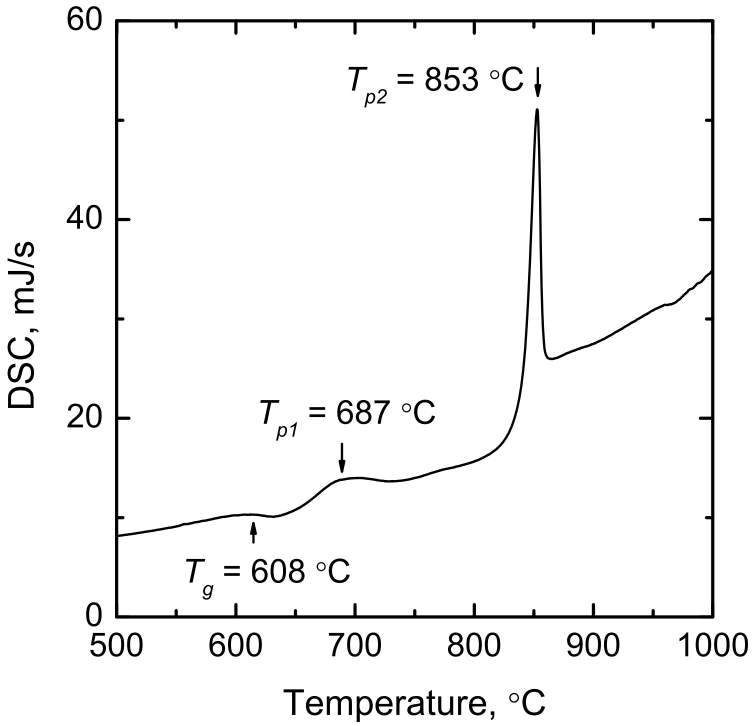

Figure 7.2: DSC curve of as-prepared glass sample $45SiO_2$-$20Al_2O_3$-$22CaF_2$-$10CaO$-$3SmF_3$. Exothermic heat flow is upwards.

700 °C for 4 h and 750 °C for 30 min, additional sharp diffraction peaks were detected as in Figure 7.3 (b) and (c), respectively. The diffraction pattern agrees with the standard card data for the CaF_2 crystal (JCPDS 35-0816), indicated at the bottom of the figure. These peaks are, as expected, attributed to the CaF_2 crystals which are embedded in the glass matrix; we effectively have a glass-ceramic structure. The average linewidths for the (1 1 1), (2 2 0), and (3 1 1) diffraction peaks were used to estimate the mean diameter of crystal grains using the Scherrer relation [141]. (It is important to emphasize that this is only an estimate inasmuch as one should also account for the strain in the nanocrystals as, for example, in the case of $BaBr_2$ nanocrystals in reference [68]. In our case, the instrumental broadening of diffraction peaks has been estimated by measuring the diffraction pattern from a standard Si powder material in which the grain size is known. The estimated average nanocrystal sizes were 37.4 nm and 145.0 nm for the samples heat-treated at 700 °C for 4 h and 750 °C for 30 min, respectively, with the higher heat-treatment temperature resulting in a larger nanocrystal.

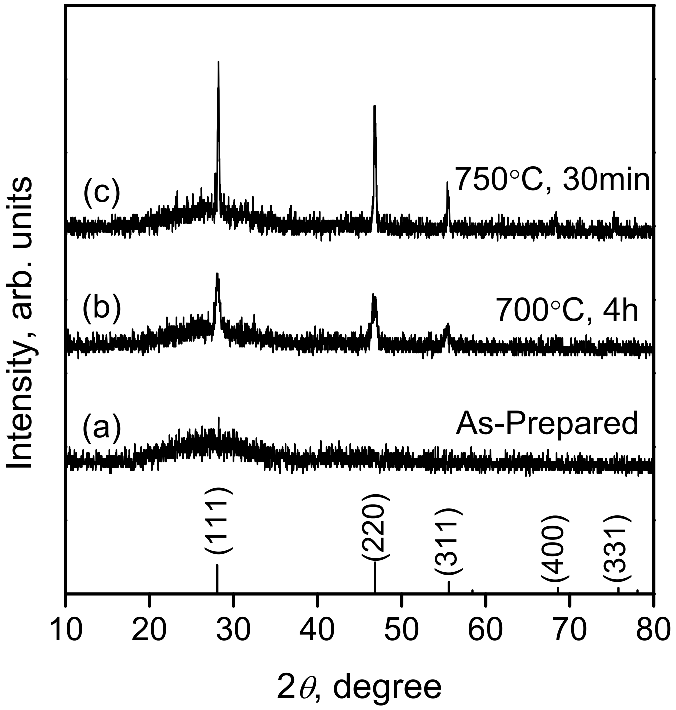

Figure 7.3: XRD curves of samples: (a) as-prepared, (b) annealed at 700 °C for 4 h and (c) annealed at 750 °C for 30 min. The standard card of CaF_2 (JCPDS 35-0816) is shown together in the bottom of the figure as a reference.

Figure 7.4 shows two typical SEM images. In the top image, the dark coloured structures indicated as A are vacancies left behind by nanocrystals (the light coloured particles indicated as B) that had come off the sample. These objects are randomly distributed in the glass matrix, indicated as C, and this is also confirmed in the lower magnification image on the bottom of Figure 7.4. The estimated nanocrystal size above agrees with the SEM observations.

7.3.2 Optical Properties

Figure 7.5 shows the optical transmittance spectra of samples with different treatment histories. The glass-ceramic sample was still transparent (indicated as (b)) when heat-treated at 700 °C for 4 h; however it became milky when heat-treated at 750 °C (not shown in the figure). Upon X-ray irradiation, the irradiated sample became brownish due to the induced strong absorption band in the UV- and visible region as indicated as (c) in Figure 7.5. In our earlier work, we have also observed

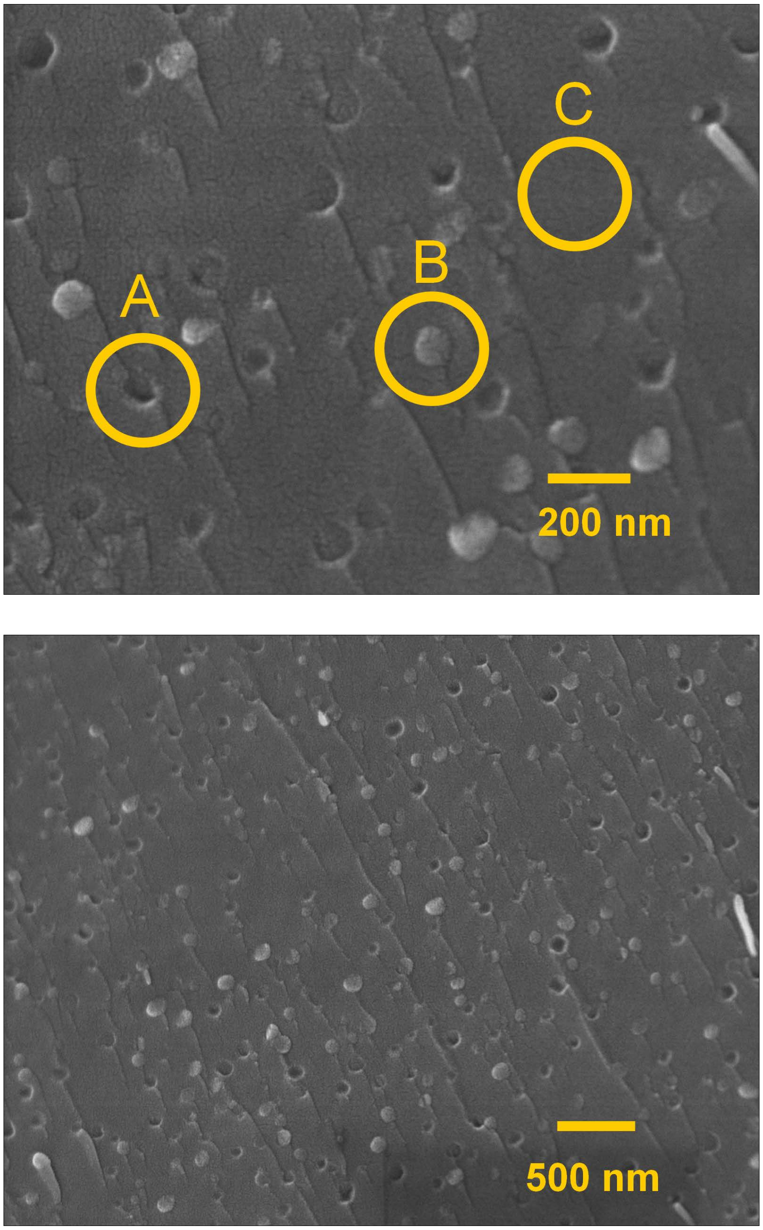

Figure 7.4: SEM image of the sample annealed at 750 °C for 30 min observed at two different magnifications, (top) ×60000 and (bottom) ×25000.

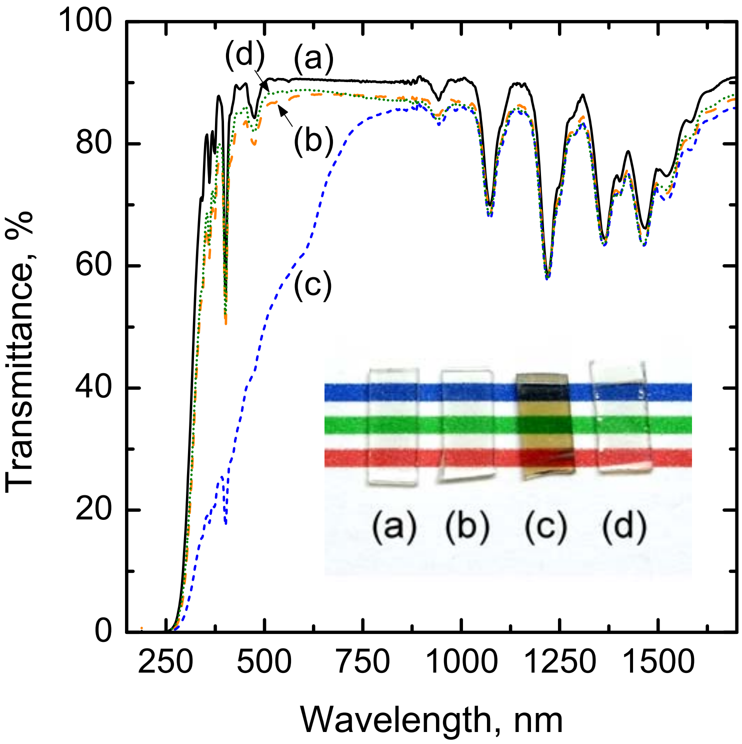

Figure 7.5: Transmittance curves of samples, (a) as-prepared glass, (b) glass-ceramic heat-treated at 700 °C for 4 h, (c) glass-ceramic which was heat-treated (700 °C, 4 h) and then X-irradiated under X-ray tube (1 h, 110 Vp), and (d) glass-ceramic which was first heat-treated (700 °C, 4 h), and next X-irradiated (1 h, 110 Vp), and then heat-treated at 550 °C.

X-ray induced absorbance in Sm-doped fluorophosphate and fluoroaluminate glasses [123, 127]. Despite the colouration in the excitation and, perhaps, emission range, the samples are still suitable as MRT dosimetric plates since we only measure the PL signal very near the surface of the sample by using a confocal microscope; thus, the colouration effect is practically negligible. Figure 7.6 illustrates the absorption coefficients induced by X-ray irradiation in an as-prepared glass and a glass-ceramic heat-treated at 700 °C for 4 h. In addition, the induced absorption due to the Sm^{3+} $\rightarrow$ Sm^{2+} change in a CaF_2 crystal by γ-ray irradiation is plotted in the same figure for comparison. The latter was derived from the work of O'Connor et al. [79]. Due to X-ray irradiation, strong and broad absorption band was observed in the as-prepared glass, whereas the glass-ceramic showed additional weak absorption bands at ~ 2 and 3 eV (indicated as ∇ in the figure). Since the latter spectral positions agree

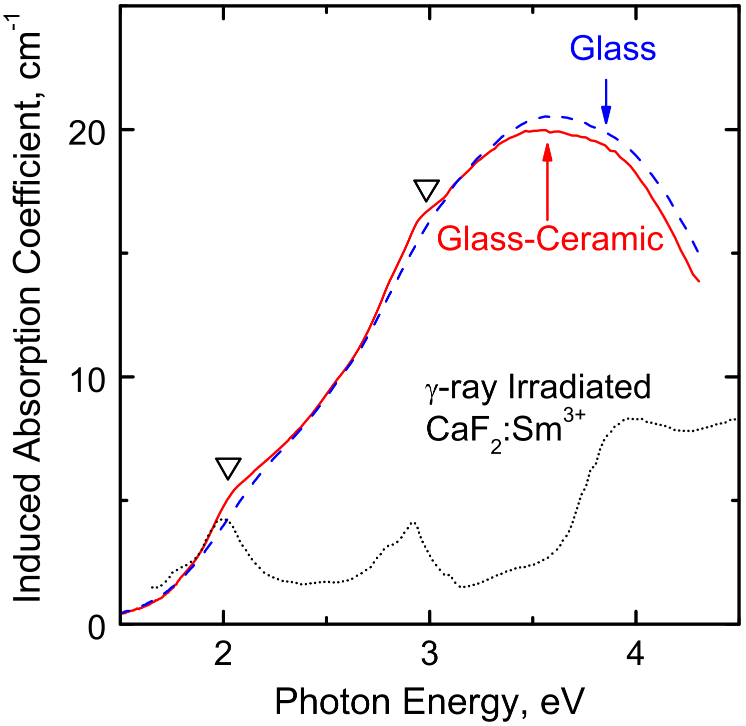

Figure 7.6: X-ray induced absorption coefficients in as-prepared glass sample and that of glass-ceramic sample. The glass-ceramic was heat-treated at 700 °C for 4 h. Weak absorption bands in glass-ceramic is observed on top of broad band in the glass matrix. The origin of the weak bands is attributed to the $Sm^{3+} \rightarrow Sm^{2+}$ change in CaF_2 nanocrystals by X-ray irradiation. The induced absorption by $CaF_2:Sm^{3+} \rightarrow Sm^{2+}$ change by γ-ray irradiation is also plotted as a reference.

with those observed by O'Connor et al., we attribute the origin of these bands to the induced absorption by $Sm^{3+} \rightarrow Sm^{2+}$ conversion in CaF_2 nanocrystals by X-rays. (An additional peak at 4 eV was not clearly pronounced in our measurements. The reason is because its location is near the absorption edge of the glass and the measurement accuracy in this range is limited due to the small signal. The same arguments should also apply to the mismatch in the absorption curves of glass and glass-ceramic samples at the large photon energies. On the other hand, the observed broad absorption in the glass sample is from defect centres generated by X-rays since the sample contains neither CaF_2 nanocrystals nor Sm^{2+} ions (discussed in the next paragraph). The irradiated sample returned to being colorless after a suitable high temperature heat-treatment, shown as (d) in Figure 7.5. The valence reduction is further discussed in detail below.

The excitation and emission spectra of PL were measured for the glass-ceramic samples before and after X-ray irradiation. Heat treatment was done at 700 °C for 4 h and then the sample was irradiated with X-rays for 1 h under an X-ray tube. Before the X-ray irradiation, we only detected typical PL emissions due to the $4f \rightarrow 4f$ transition of Sm^{3+} ions (spectra not shown). However, after the irradiation, additional broadband emission centred at ∼730 nm was observed as shown in Figure 7.7.

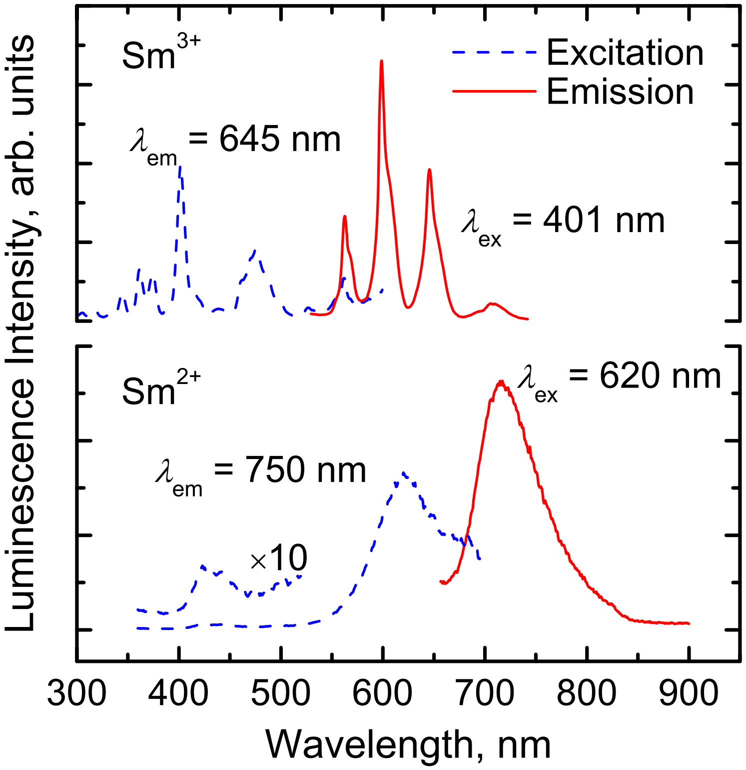

Figure 7.7: Excitation and emission PL spectra of irradiated Sm-doped glass-ceramic sample. Upper spectra for Sm^{3+} and lower spectra for Sm^{2+}. Note that the excitation spectra are for observing PL emission at 645 nm (Sm^{3+}), and PL emission at 750 nm (Sm^{2+}). Further, PL spectrum for Sm^{3+} is excited at 401 nm and that for Sm^{2+} is excited at 620 nm.

We attribute the origin of this broad emission to Sm^{2+} ions embedded in CaF_2 nanocrystals because of the following reasons. (a) First, the appearance of this broad emission was only observed in samples heat-treated above the first crystallization temperature T_{p1}. As-prepared glass and any sample heat-treated below T_{p1} did not

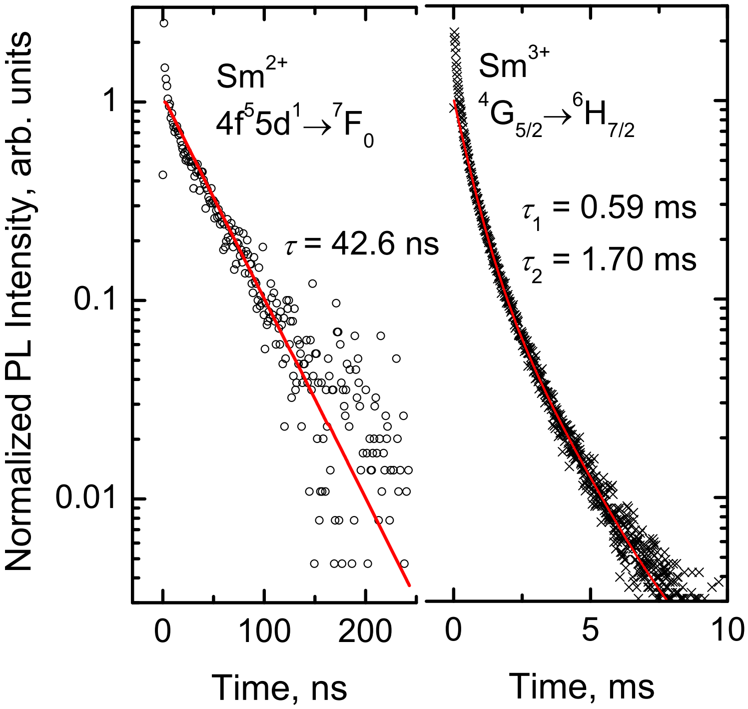

Figure 7.8: PL decay curves: (left) the $4f^5 5d^1 \rightarrow {}^7F_0$ transition by Sm^{2+} ion in X-irradiated glass-ceramic. (right) the ${}^4G_{5/2} \rightarrow {}^6H_{7/2}$ transitions by Sm^{3+} ion in glass-ceramic.

show this emission (not shown in figure). (b) The next argument is the observation of a broadband signature in both emission and excitation spectra. As illustrated in Figure 7.7, the excitation spectrum of the broad emission also has a broad structure. The latter property is typical for the Sm^{2+} ion due to the $4f^5 5d^1 \rightarrow {}^7F_0$ transition in CaF$_2$ crystal, which is an allowed transition by the selection rules. (c) The third reason is the spectral position. Unlike the f-f transition in the trivalent rare earth ions, the $4f^5 5d^1$ excited level in Sm^{2+} is not shielded, thus it is strongly affected by the lattice crystal field. Assuming that the Sm^{2+} ion is located in the CaF$_2$ nanocrystal, the spectral position reasonably agrees with the one reported by Mikhail et al. [133]. (d) The fourth argument is the observed fast lifetime for this ~730 nm emission. Figure 7.8 illustrates PL decay curves of the broadband emission as well as the ${}^4G_{5/2} \rightarrow {}^6H_{7/2}$ transitions by Sm^{3+} ions in the glass-ceramic sample. The decay curves are fitted with double- and single-exponential decay functions, respectively. As a result, the derived time constants are 0.59 ms and 1.70 ms for the former decay curve (Sm^{3+}) and for 42.6 ns for the latter decay curve (Sm^{2+}). Since the f-f transitions are parity forbidden, the $^4G_{5/2} \rightarrow {}^6H_{7/2}$ transitions of Sm^{3+} showed a long lifetime on the millisecond time scale. In contrast, the broad emission showed a much faster lifetime on the order of nanoseconds. This fast lifetime implies that the PL emission is due to transitions which are allowed by the selection rule, i.e. the $4f^5 5d^1 \rightarrow {}^7F_0$ transition of Sm^{2+} ions. This is also supported by the fact that our measurement seems to agree with the reported lifetime in the case of Sm^{2+} doped CaF_2 crystals by Payne et al. [134] and Chase et al. [135]. Consequently, based on our observations above, we attribute this PL broad emission to the $4f^5 5d^1 \rightarrow {}^7F_0$ transition of Sm^{2+} ions which are embedded in CaF_2 nanocrystals, and reduced from the trivalent state by the X-ray irradiation. Further, the lifetime of Sm^{2+} is much faster than that of the f-f transition, which is more commonly found in materials that show $Sm^{3+} \rightarrow Sm^{2+}$ reduction by X-ray irradiation. Therefore, we can expect a much faster readout speed during the readout of PL emissions in laser scanned fluoroscopic microscopy; a distinct advantage. It is worth pointing out here that only a small fraction of Sm^{3+} may have been reduced by X-ray irradiation because of the fact that the optical absorption bands by Sm^{3+} in the 800 - 1000 nm range have only a negligibly small difference before and after irradiation as seen in Figure 7.5. Moreover, weak absorption bands due to the reduction of the Sm^{3+} ion in a CaF_2 nanocrystal seen in Figure 7.6 implies that only a small concentration of nanocrystals are embedded and that the majority of Sm^{3+} ions remain unconverted in the glass matrix. However, due to the large oscillator strength of Sm^{2+}, the total PL intensity is comparable to that of Sm^{3+}. (See the discussions in references [6, 37]).

7.3.3 Response Stability

The stability of the response, or in other words the stability of generated Sm^{2+} by X-ray irradiation was tested at room temperature. Figure 7.9 shows the measured responses against time after the irradiation at 500 Gy. Each plot represents a response value measured from an individual sample piece. It seems like that the response is stable over several days (tested up to 8 days). The material can be used to store the dose information until it is digitized.

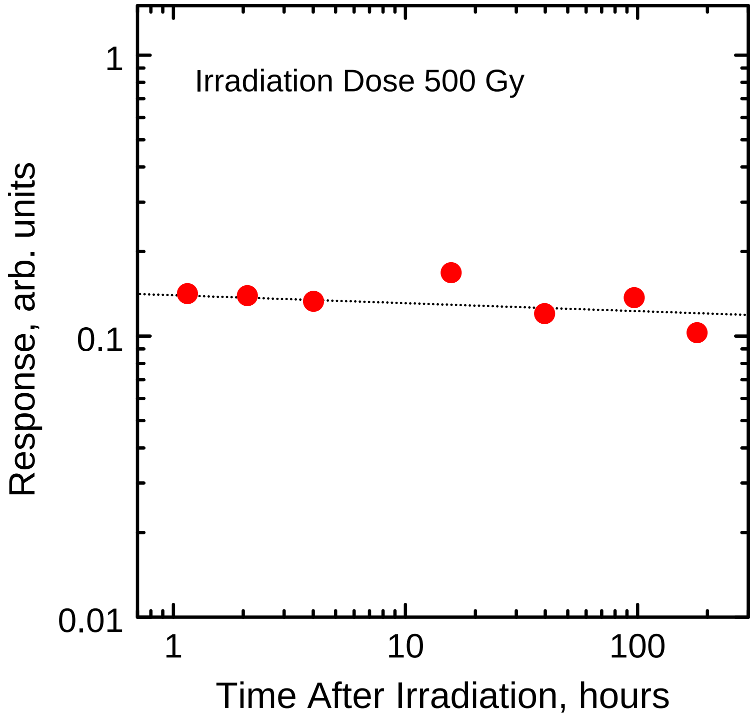

Figure 7.9: Response values after X-ray irradiation (500 Gy). Each plot represents individual piece of detector sample.

7.3.4 Applicability for Large-Dynamic-Range and High-Spatial-Resolution Dosimetry

Figure 7.10 shows a typical dose-response curve of one of our Sm-doped glass-ceramic samples, as measured at the CLS. The heat treatment was done at 700 °C for 4 h in air. The figure shows that our glass-ceramic sample exhibits a sufficiently large response range from ~1 Gy to about 10,000 Gy to detect the X-ray dose at the peaks and valleys of the microbeam in a single measurement, which is essential for monitoring the dose-profile in MRT. It is worth noting here that a commonly used GafChromic® film detector (HD-810) only allows detection from ~10 to several hundreds of grays [22]. Notice that some saturation in the response to the total dose is observable at 10^4 Gy. The inset shows the energy spectrum of the MRT beam. Figure 7.11 demonstrates a dose-profile of a microbeam recorded using the

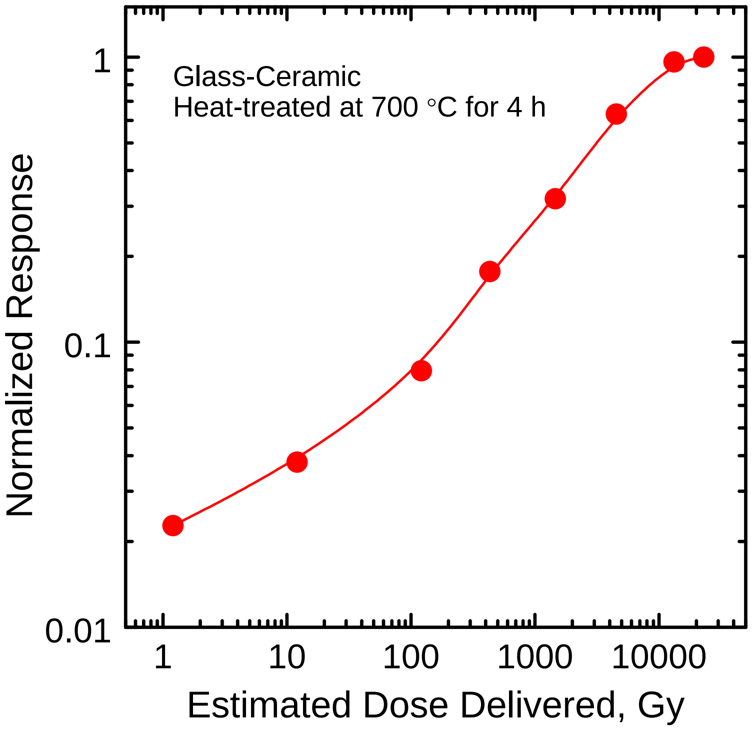

Figure 7.10: Dose-response curve of oxyfluoride glass-ceramic containing $CaF_2:Sm^{3+}$ nanocrystals. The as-prepared glass sample was annealed at 700 °C for 4 h to nucleate the nanocrystals. The dose values are dose in air at the sample surface.

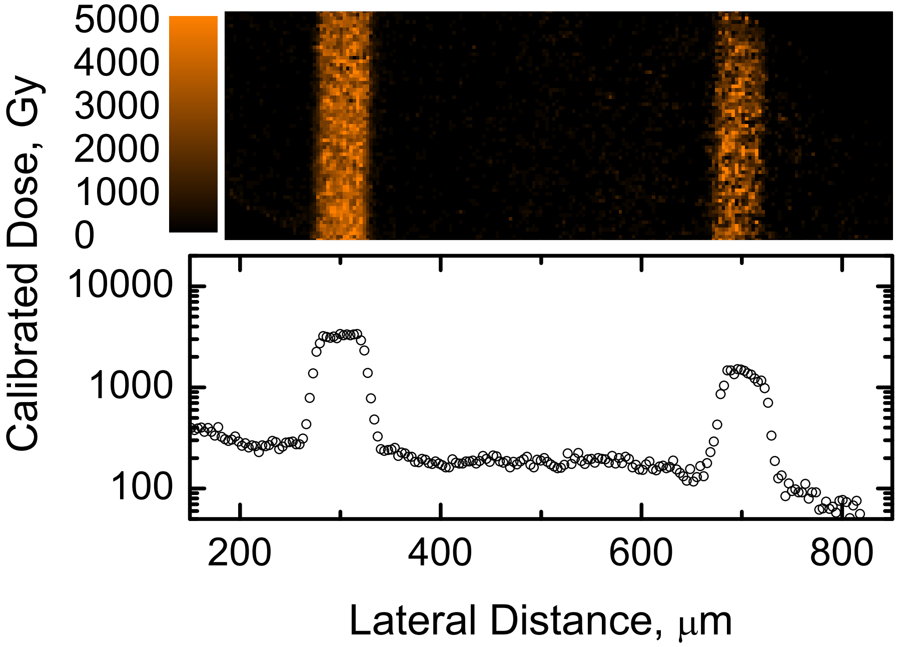

Figure 7.11: Dose distribution of microbeam recorded using an oxyfluoride glass-ceramic containing $CaF_2:Sm^{3+}$ nanocrystals and digitized, using confocal microscopy.

glass-ceramic sample. The dose-response curve displayed in Figure 7.10 was fitted by a mathematical equation and then used for the dose calibration. Although the excitation wavelength was not the best choice, we successfully read and digitized the microbeam pattern and resolved the two peaks which are detected to be separated by 400 μm and the FWHM of the peak is detected to be 50 μm. Both of these values are in agreement with the properties of the microbeam used in this BMIT beamline, and verified by other techniques such as Monte-Carlo simulations.

7.3.5 Reusability

One of the glass-ceramic samples, which was heat-treated at 700 °C for 4 h to nucleate CaF_2 nanocrystals, was used to study the reusability as a dosimeter material.

Figure 7.12 and 7.13 show the change in PL peak intensity by Sm^{2+} while the erasure process was in progress by heating the sample and/or by exposing it to UV light (254 nm) after an irradiation for 1 h under the X-ray tube, respectively. The heating time was fixed to 30 min at all the temperatures. When the sample was heated at lower temperatures, interestingly, the Sm^{2+} PL peak increased despite our intention to erase the sample. When the temperature reached 300 °C, the PL intensity was the highest, and then it decreased at higher temperatures. Ultimately, the PL signal was completely eliminated after heating at 550 °C, at which the X-ray induced absorption was also eliminated and the sample had returned to its transparent state (see Figure 7.5 (d)). An observation of similar behaviour was reported [127] for Sm-doped fluorophosphate glass, in which Sm^{2+} ions were also produced by X-ray irradiation. In contrast, when we attempted erasure by UV exposure, the PL intensity simply decreased, and the PL signal was completely removed after 200 min of exposure.

Figure 7.14 and 7.15 compare the dose-response profile of the PL intensity by Sm^{2+} against X-ray irradiation time (i.e. dose) before and after erasure by heating at 550 °C for 1 h and by UV exposure for 17 h, respectively. For both the erasure methods, the response curves were well reproduced with very good agreement. Therefore, the Sm-doped oxyfluoride glass-ceramic synthesized in this work is

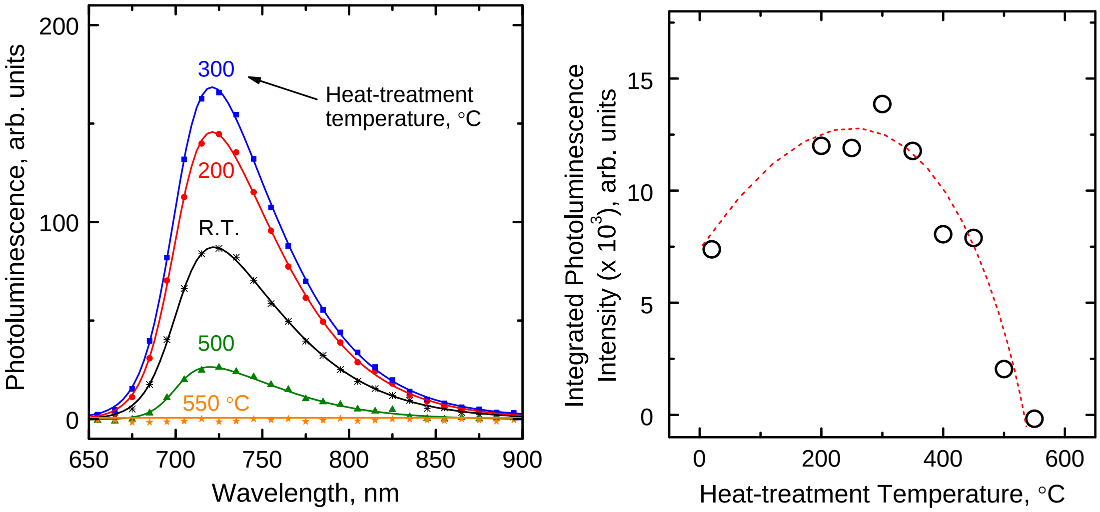

Figure 7.12: Photoluminescence spectra recorded during the heat erasure at varying temperatures (left), and the corresponding integrated photoluminescence intensity (right). The excitation wavelength is 633 nm.

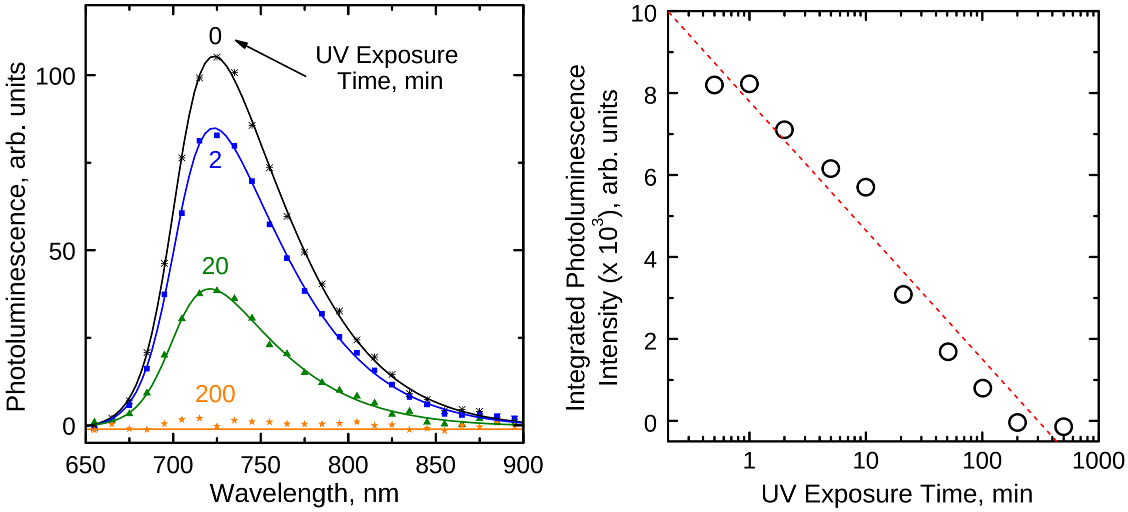

Figure 7.13: Photoluminescence spectra recorded during the erasure by UV exposure at varying exposure times (left), and the corresponding integrated photoluminescence intensity (right). The excitation wavelength is 633 nm.

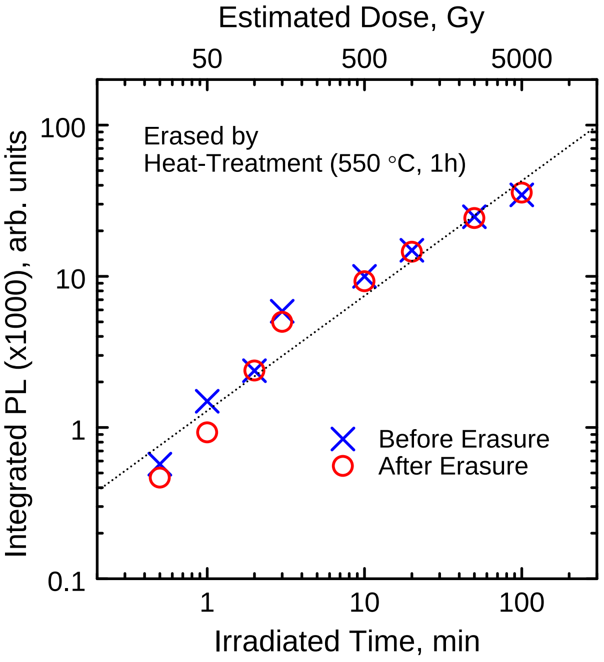

Figure 7.14: PL intensity by Sm^{2+} against X-ray irradiation dose recorded before and after heat-erasure at 550 °C for 1 hour. The dose values are dose in air at the sample surface. The excitation wavelength is 633 nm.

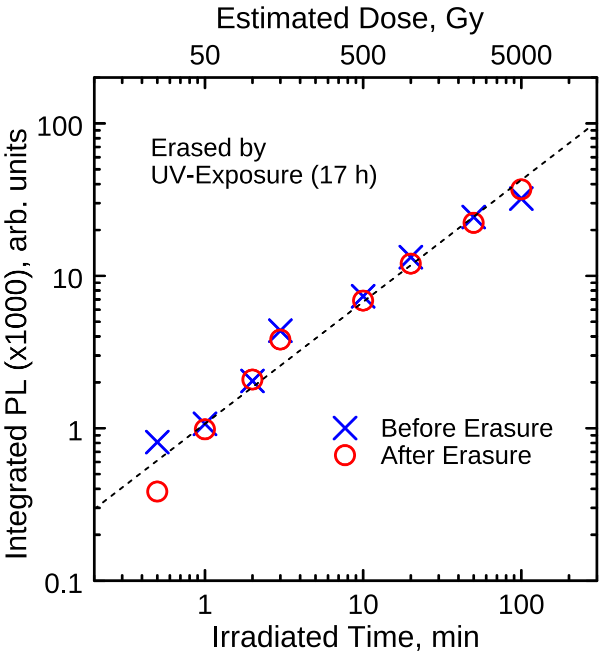

Figure 7.15: PL intensity by Sm^{2+} against X-ray irradiation dose recorded before and after erasure by exposing to UV (254 nm) light for 17 hours. The dose values are dose in air at the sample surface. The excitation wavelength is 633 nm.

reusable as a dosimetric detector material for MRT with both thermal and optical erasure methods. The heat treatment temperature, as apparent from the DSC thermograms in Figure 7.2, is actually below T_g and T_{p1}. At present, we do not have an explanation for the origin of the thermally erasure of Sm^{2+} at 550 °C. However, it seems reasonable to expect some detrapping of holes that result in the reconversion of Sm^{2+} to Sm^{3+}. Holes detrapped in the glass matrix near or around nanocrystals can diffuse to Sm^{2+} ions and convert these to Sm^{3+}.

7.4 Conclusions

A Sm^{3+}-doped oxyfluoride glass-ceramic was synthesized as a new dosimeter material to be used for MRT applications. The new material may be modeled as illustrated in Figure 7.16.

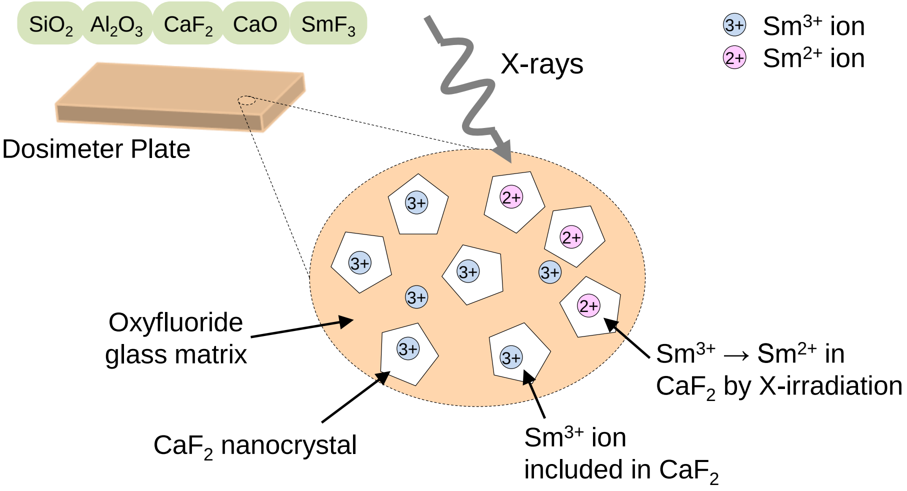

Figure 7.16: Illustration of oxyfluoride glass-ceramic detector which contains CaF_2:Sm^{3+} nanocrystals.

When the as-prepared glass is heat-treated, CaF_2 nanocrystals are nucleated and grown in the oxyfluoride glass matrix. The doped Sm^{3+} ions are reduced to Sm^{2+} during the X-ray irradiation of the glass-ceramic samples, and this valence reduction process takes place only in the CaF_2 crystal environment, that is, within the CaF_2 nanocrystals. As a result, the PL of Sm^{2+} is predominantly due to the parity allowed $4f^55d^1 \rightarrow {}^7F_0$ transition. The lifetime (42.6 ns) for this transition is much faster than that of the f-f transition, which is more commonly found in glasses showing the $Sm^{3+} \rightarrow Sm^{2+}$ reduction by X-ray irradiation. Hence, using our new Sm-doped glass-ceramic material, the recorded dose information can potentially be read out using a laser scanning technique, such as confocal fluorescent microscopy, with a much faster speed than that used for Sm-doped glasses. Further, the potential practical usefulness for MRT has been demonstrated by carrying out measurements under an X-ray microbeam generated at the BMIT beamline at the Canadian Light Source (the Canadian synchrotron). The glass-ceramic is able to detect X-ray doses up to several thousands of grays over a dynamic range suitable for MRT. Further, by making use of the scanning ability of the confocal microscope developed in this work, we were able to obtain the dose distribution profile across the beam cross section, which agreed with the known characteristics of the microbeam. Cross-sectional dose distribution of the microbeam has been successfully detected using our new detector material. Furthermore, the recorded dose information on the detector is erasable either thermally (by suitable heat treatment at a high temperature) or optically (by UV radiation), and the erased detector is reusable. The new Sm-doped oxyfluoride glass-ceramic with CaF_2 nanocrystals reported in this work shows potential for practical use in high-dose and high-resolution dosimetry for MRT.

Chapter 8

Measurements of Microbeam at CLS, ESRF, and SPring-8

8.1 Introduction

Measurement of the characteristics of a microbeam is a challenging task. X-ray dose is spatially modulated over the cross-section of microbeam, in which very large gradient of X-ray dose is distributed on a microscopic scale. Such a dose distribution cannot be accurately measured by any existing technique. Thus, we have been developing a novel dosimetry technique which meets nearly all the dosimetry requirements. Such a dosimetric technique should have the detection ability for large doses in the range of 5 - 1000 Gy and microscopic spatial resolution, both together. The earlier studies of dosimetry for MRT and our original approach were discussed in Chapter 3.

It seems that the dosimetry using a GafChromic® film (HD-810) is the most commonly accepted technique in the field of radiosurgery which involves large radiation doses. The GafChromic® film is primarily used for quality assurance and system calibration in general. In addition, nowadays it is most commonly used for MRT studies. It has excellent stability in ambient temperature and light exposure over a long time period, tissue equivalence, and no energy dependence over a wide photon energy range. Previously, Bräuer-Krisch et al. [22] have reported that the dynamic range is not satisfactory (10 – 400 Gy) for MRT applications, and the image resolution is ∼12.5 μm using a microdensitometer readout technique.

In Chapters 5, 6, and 7, we have characterized various dosimetric detectors towards the high-resolution and high-dose dosimetry applications for MRT. Our demonstrations showed that Sm^{3+}-doped FP and FA glasses and CaF_2:Sm^{3+}-contained glass-ceramic seem to have the ability to detect the dose distribution of the microbeam. In particular, the FA glass has an excellent degree of $Sm^{3+} \rightarrow Sm^{2+}$ conversion and a sufficiently large dynamic range to detect low and large doses in the microbeam. Further, the excellent long-term stability allows us to transfer the samples to the reader without any fading of signal after irradiation. The PL lifetime is much slower than that of CaF_2:Sm^{3+}-contained glass-ceramic detector. However the readout speed is of less importance since our main objective is large-dose detection at microscopic image resolution.

This chapter focuses on the measurement of the microbeam. The measurements were done by two different methods; using Sm^{3+}-doped FA glass and GafChromic® film detectors. The basic dosimetry concepts of these detection techniques are different as the former uses a change in the PL signal induced by X-ray irradiation as a measure of the radiation dose whereas the latter measures a change in the absorption (or transmission)of light. However, for a proper comparison, the readout set-up has been built to measure these detectors under the similar conditions as closely as possible. The details of the instruments were described earlier in the thesis in Sections 4.5 and 4.6. The measurements on the microbeam were carried out at three different synchrotron facilities: CLS (Saskatoon, Canada), ESRF (Grenoble, France), and SPring-8 (Hyogo, Japan). As discussed in Section 4.4, the microbeams are produced by different methods and the irradiations are done by different geometries between these facilities. These differences are summarised in Table 4.5.

Throughout this chapter, we will compare the characteristics of two dosimetry methods: Sm-doped FA glass and GafChromic® film detectors. Further, we will compare the properties of microbeams produced at different synchrotrons.

8.2 Methodology

For microbeam measurements at CLS, ESRF, and SPring-8, we have used 1% Sm^{3+}-doped FA glass as well as GafChromic® film (HD-810) for a reference. The glass sample was cut into pieces each with size approximately 2 mm × 3 mm × 0.5 mm, and one side of each sample piece was polished. The detectors were irradiated by both a broad beam and microbeam at each synchrotron facilities. The main differences of the beamline specifications for our consideration are the X-ray energy (spectrum), the dose rate, and the production of the microbeam. For all the measurements, regardless of the facilities, the FA glass detector and GafChromic® film were irradiated together in a consistent orientation with respect to the beam: the film and glass were held physically attached to each other and the samples are at the up-stream side. Moreover, the FA glass piece was always placed with the polished side facing towards the up-stream of the X-ray beam. Several sets of detectors were irradiated with a broad X-ray beam with varying dose to obtain dose-response curves (response value vs. dose delivered). Some of the other sets of detectors were irradiated by the microbeam with a few different entrance doses. After the irradiations, the film and glass detectors were each covered by an aluminium foil in order to avoid unexpected fading of the signal until the readout stage. The GafChromic® film was digitized using a flatbed scanner (Perfection V700, EPSON) or widefield optical microscope described in Section 4.6, and Sm-doped FA glass detector was digitized using a confocal microscope, which is described in Section 4.5. The response values obtained for each broad beam irradiation were plotted against the corresponding dose delivered (to obtain the dose-response curve), and then fitted by a so-called Hill function:

$$R(D) = R(\infty)\frac{D^n}{k^n + D^n} \tag{8.1}$$

where $R(D)$ is the response value at the irradiation dose D, $R(\infty)$ is response value at saturation, n and k are curve fitting coefficients, which reflects the slope and shoulder of curve, respectively. The fitted curve was used for calibrating dose values obtained from detectors irradiated by the microbeam. We use this function as it accurately fits the dose response curves, particularly at the shoulder of the curve, of both GafChromic® film and Sm-doped FA glass detector.

8.3 Results and Discussion

8.3.1 Dose-response

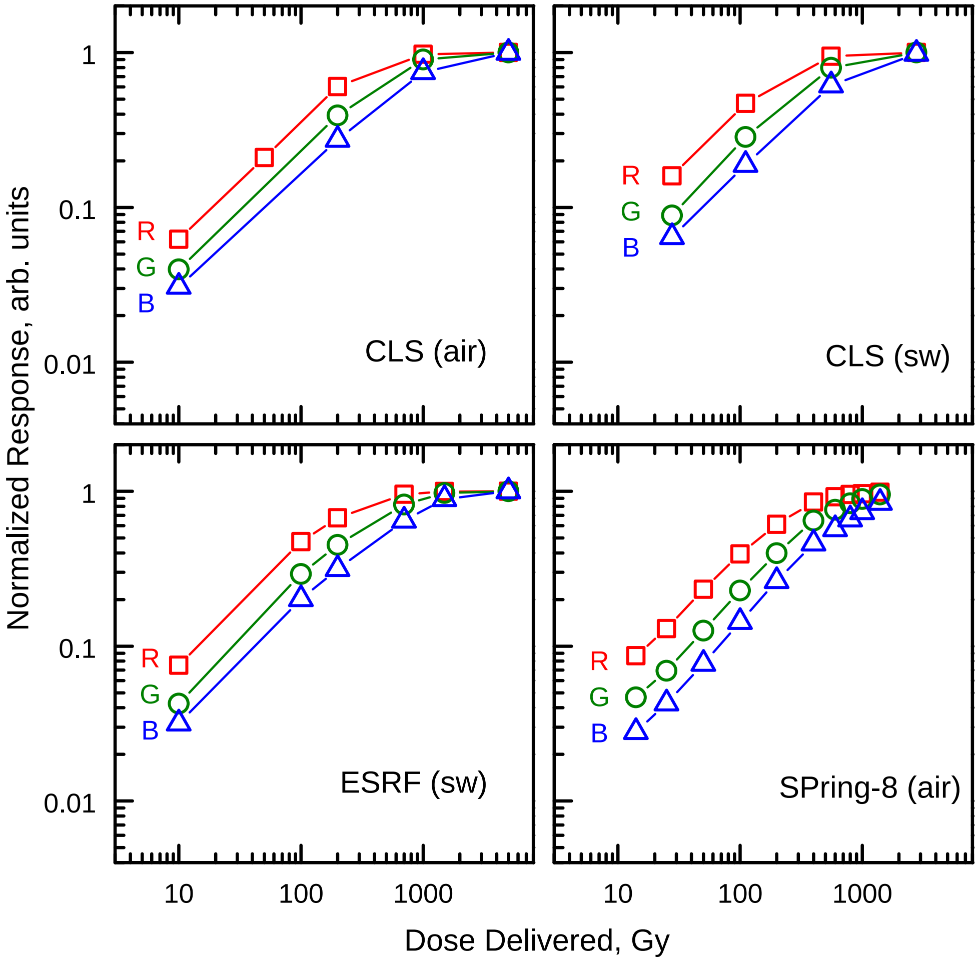

Figure 8.1: Dose-response of GafChromic® film (HD-810) tested at CLS, ESRF, and SPring-8. The films irradiated at varying doses were digitized by the wide-field microscopy and then the acquired colour images were further split into the individual channels. The notations (air) and (sw) are air and SW absorbers, respectively, in which the films were irradiated.

Figure 8.1 shows dose-response curves of GafChromic® film for three colour channels (red, green, and blue) tested at different facilities (CLS, ESRF, and SPring-8). The films were digitized using a wide-field microscopy. Here, the response $R(D)$ for a given dose D is defined as:

$$R(D) = I_t(0) - I_t(D) \tag{8.2}$$

where $I_t(D)$ is the transmitted light signal through a film which is irradiated at a dose of D, and $I_t(0)$ is transmitted light signal through a non-irradiated film.

It seems that there is no significant difference in the increase rate of response regardless of the facilities where the irradiations were carried out. These facilities use different X-ray spectra and dose rate as well as the irradiation geometry varies. Muench et al. [34] have uncovered the energy dependence of GafChromic® film (HD-810) as a 30 % drop of response as the effective photon energy decreases from 1710 keV to 28 keV. Mass attenuation coefficients (μ/ρ) of GafChromic® film against that of water are shown in Figure 8.2. In the high-energy region, coefficients of GafChromic® film and water are close to each other. However, at lower photon energies, the interaction of X-rays with film becomes less than that in water. As a result, the response also decreases.

Since the main optical absorption of GafChromic® film induced by X-ray irradiation takes place in the red region ($\sim$ 610 and 670 nm), the response in the red channel (which is a measure of transmission of red light) is, as expected, the most sensitive. The sensitivity of the green and blue channels follow next, respectively. The dynamic range seems to cover the range from 10 Gy to several hundreds of grays when using the red channel, and up to approximately 2000 Gy for blue channel. As far as we are aware, the microdensitometer used in the earlier studies is equipped with a He-Ne laser. Therefore, the response was read out only for the red colour (633 nm). In contrast, our wide-field optical microscopy reader set-up is equipped with a white light source with a colour image sensor. This allows the detection of large doses, particularly using a blue channel.

Figure 8.3 (top) shows dose-response curves of FA:1%Sm^{3+} glass detector when

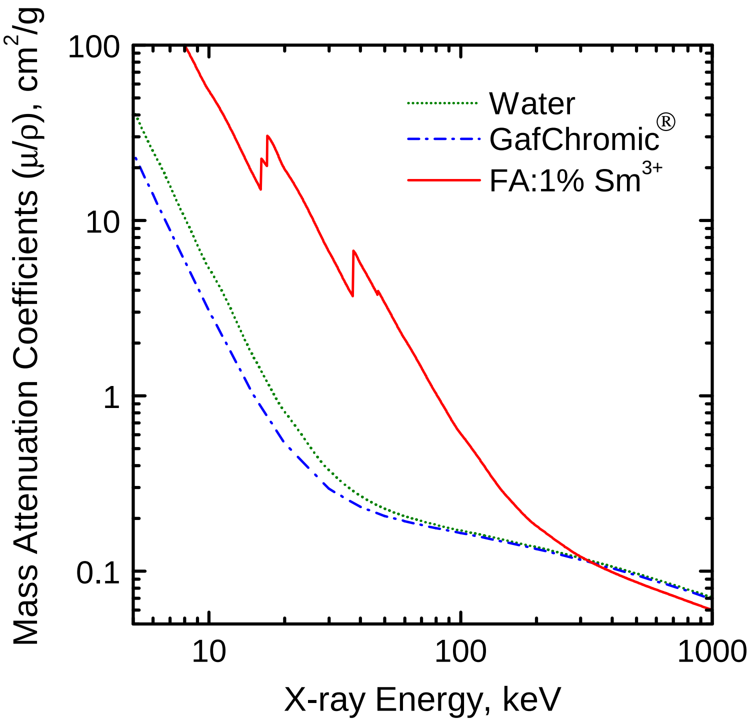

Figure 8.2: Mass attenuation coefficients of water, GafChromic® film, and FA:1%Sm^{3+} glass detector. The coefficients of GafChromic® film and water were reproduced from [3] and those for FA glass were calculated based on Equation 2.6.

irradiated at the CLS, ESRF, and SPring-8. Overall, the detector showed the ability to detect the X-ray dose of range used for MRT (∼1 Gy to over 1000 Gy). The dose-response curves measured at different facilities, the dependence (the shape of the response-dose curve) of response on the dose delivered seems to vary between the synchrotron facilities unlike the GafChromic® film (HD-810). The dose-response curves measured with irradiations at ESRF and SPring-8 are very well-correlated, whereas the measurements at the CLS showed a higher increase in the rate of response values against X-ray dose delivered, which results in the saturation of response taking place at a lower dose. The largest difference between these two groups is in the X-ray photon energies. The peak energies at ESRF and SPring-8 are reasonably close, but the one at the CLS is much lower. In fact, the mass attenuation coefficients (μ/ρ) of 1 % Sm^{3+}-doped FA glass (Figure 8.2) clearly illustrates a much stronger interaction with low energy X-ray photons and, particularly, a significant

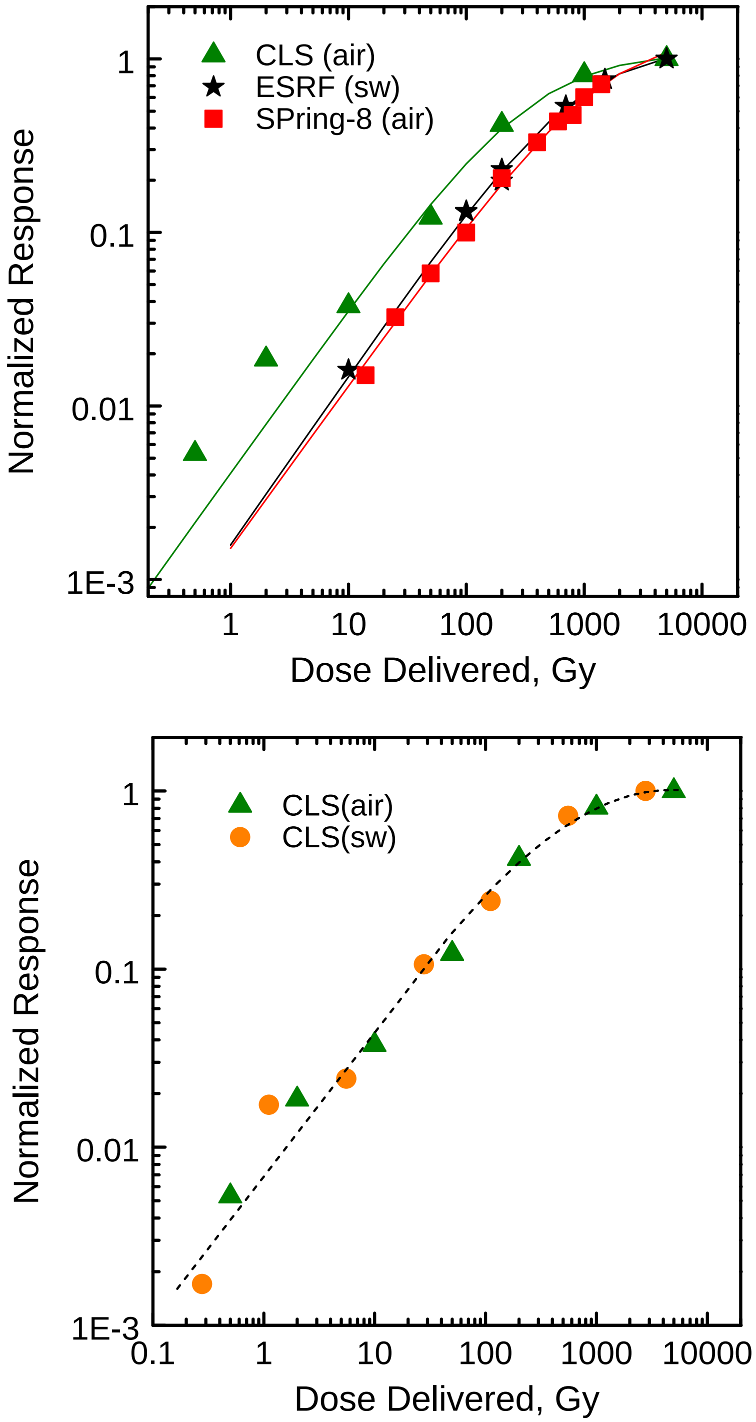

Figure 8.3: Dose-response curves of 1% Sm^{3+}-doped FA glass irradiated at CLS, ESRF, and SPring-8. The bottom figure compares the dose-response curves measured when irradiations were carried out in air and SW phantom with the thickness of 2 cm.

non-linear X-ray interaction with the glass matrix by the *L*-edge of Barium ion, located approximately around 40 keV. Approximately 10 at.% of Ba ions is included in the glass. Furthermore, additional secondary X-rays associated with the *L*-edge are expected to emitted from the detector material itself. Therefore, for the reasons above, there is a good chance that this FA glass detector has an energy-dependent characteristic and the sensitivity is larger for lower energy photons especially ∼40 keV. (See Suggestions for Future Work, in Section 9.5.)

Figure 8.3 (bottom) compares dose-response curves of 1 % Sm^{3+}-doped FA glass, which were measured in the ambient air environment and in the SW phantom. The distance between the entrance of the beam and detector was 2 cm. The measurements were done at the CLS. Inside the phantom, the beam intensity becomes weaker and the X-ray spectrum shifts towards higher energy. However, since these two curves show an excellent agreement, it indicates that the dependence of detector response on the X-ray energy and intensity difference associated with the SW phantom is not significant. This observation may indicate that the hardening of the X-ray spectrum due to the absorption by the phantom and secondary emission of lower X-ray energy were somewhat balanced out because the former effect tends to reduce the response while the latter effect tends to increase the sensitivity.

8.3.2 Dose-profile

Figure 8.4 illustrates example images of films irradiated by a broad beam and microbeam, which were digitized by the flatbed scanner described above and a wide-field microscope. The films were irradiated at the ESRF. Figure 8.4 (a) and (b) are broad beam and microbeam images digitized by the flatbed scanner, respectively. Figure 8.4 (c) is a closed-up image of (b), and (d) is a microbeam image digitized using a wide-field microscope. For its large field of view (FOV), the flatbed scanner is suitable for use in extracting the general characteristics of the microbeam. The designed dimensions of the entire beam cross-section are 2 cm × 2 cm. However, the image resolution is not as good compared to that digitized by the microscope.

The dark regions in the middle of films shown in Figure 8.4 (a) and (b) are where

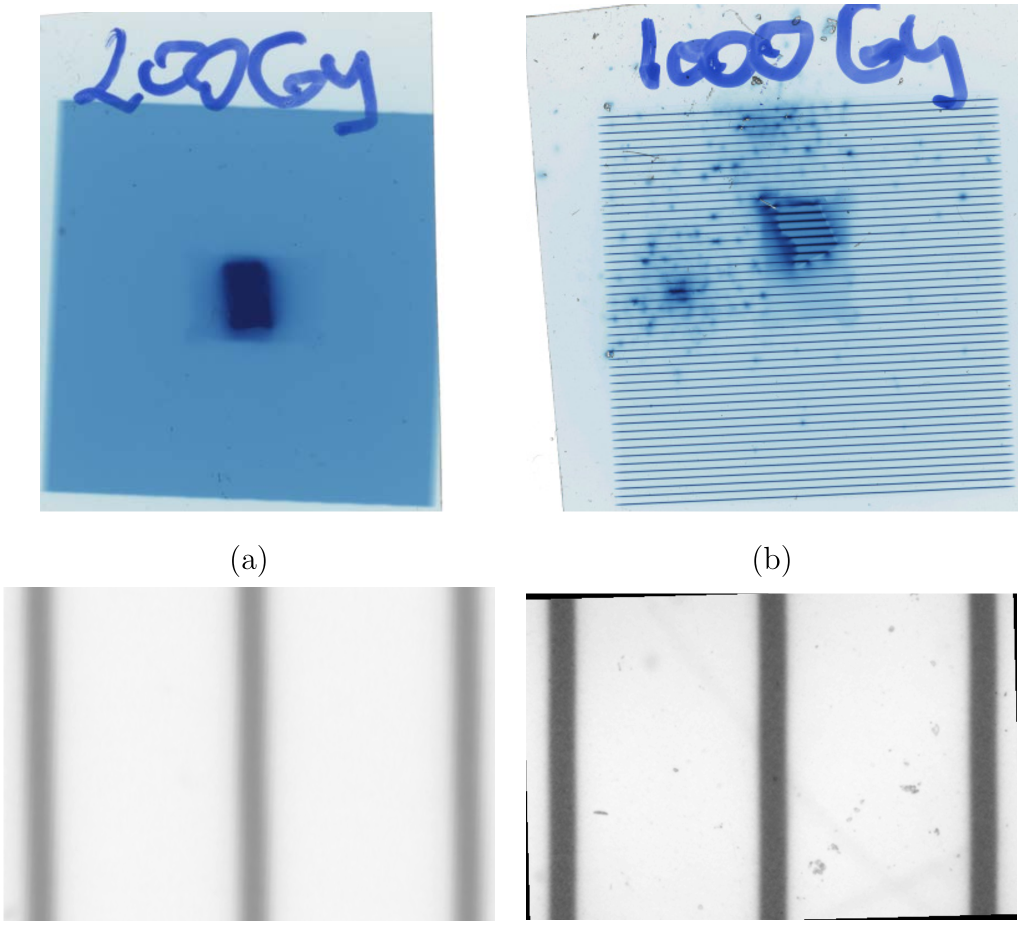

(a) (b)

(c) (d)

Figure 8.4: Example images of GafChromic® films irradiated by a broad beam and microbeam. (a), (b), and (c) were digitized by EPSON flatbed scanner and (c) is a closed-up image of (b). (d) is an image of the same film as (b) and (c) but digitized by a wide-field microscope. (c) and (d) are the images of blue channel. The objective lens used for the microscopy readout was 10×/0.3NA.

the glass detector sample was attached during the irradiations. It indicates that the region where the glass piece was attached suffered a larger dose. The main possible reason is by the build-up of X-ray dose scattered at the glass detector into the film. As X-ray interacts with matter, the incident X-ray photons get scattered, and also secondary X-rays are emitted. Indeed, there is a strong *L*-edge absorption associated with the Ba in the glass (Figure 8.2), which would lead to an *L*-edge fluorescence. These phenomena give rise to an additional dose deposited into the film from the glass. Figure 8.4 (b) was actually irradiated inside a solid-water phantom. The dose build-up effect in the film is apparently stronger in the presence of glass than the phantom since the glass detector has larger mass-attenuation coefficients and density, hence simply more X-rays are scattered.

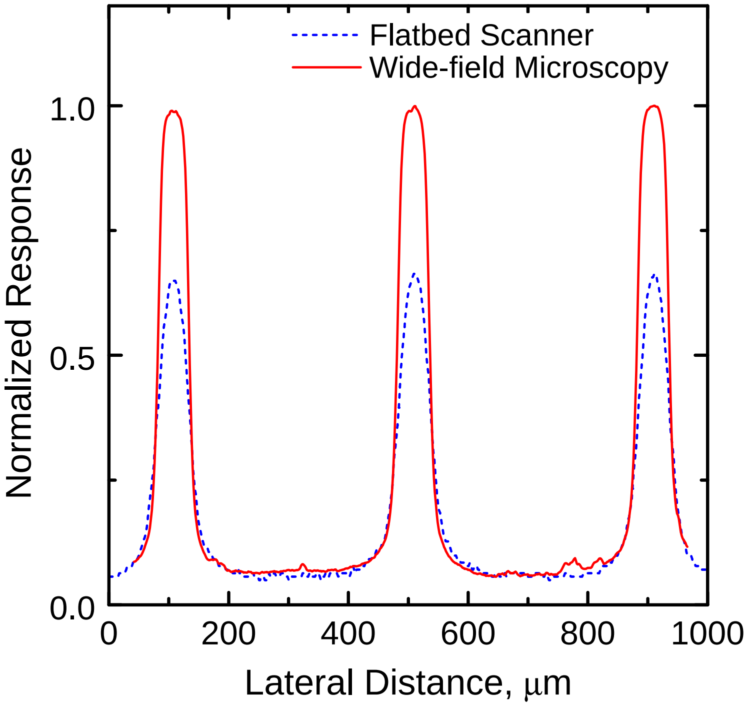

Figure 8.5: Lateral profiles of microbeam detected by GafChromic® film (HD-810) which were digitized using a flatbed optical scanner (blue line) and wide-field optical microscope (red line). The blue channel was used for both the profiles.

Figure 8.5 compares the lateral profiles of images acquired by two digitization methods — flatbed scanner and wide-field microscope. Notice that the vertical axis is not calibrated for dose values but represents a normalized response; it does not necessarily have linear correspondence with the dose value. Nevertheless, it is clearly seen that the dose distribution, especially at the peaks, is more accurately represented by the microscopy readout. The peak values when read out by the flatbed scanner are approximately 60 % of the case for a wide-field microscopy readout. In fact, this peak signal drop is as expected by the difference of in the MTFs of the two digitizing methods (Figure 4.24 and 4.27). The contrast value MTF at 10 lp/mm, which corresponds to a bar width of 50 μm (same as the width of microplanar beam in the microbeam) is also 60 % by the flatbed scanner but almost 100 % with the wide-field microscopy. Moreover, the peak shape by the flatbed scanner readout seems to be more smeared. Despite these differences, the structure around the valley regions (between the peaks) seems to have a good agreement between the two digitization methods. This may suggest that the flatbed scanner still may be able to handle the digitization of the valley dose and perhaps its distribution.

Figure 8.6 illustrates example microbeam profiles obtained using an FA glass detector doped with 1% Sm^{3+} ion. The image was acquired using a 20× objective. The FOV of objective lens is $\sim$1 mm of diameter. The optical power of excitation was 0.5 μW at the detector sample. The excitation intensity was set such that the intensity is sufficiently strong for the microscope to detect signals with a decent S/N ratio, and also such that the intensity is small enough to avoid unwanted photobleaching during the measurement in the mean time. Furthermore, the sampling pitch was 10 μm, which is sufficiently large to prevent the photobleaching of adjacent pixel areas while a measurement of a single pixel is excited. Despite the noise level and coarse sampling distance compared to the images obtained by GafChromic® film with the reader introduced earlier, we have successfully detected two peaks of the microbeam structure. The detailed analyses will be made in the following sections.

The distribution of X-ray dose in the cross-sectional area of the microbeam has been measured by both GafChromic® film and FA:Sm^{3+} glass detectors. The obtained values in the two dimensional space were further processed to average along the lines of micoropanar beams. The results are a representation in the one-dimensional space as shown in Figure 8.7 and 8.8. Figure 8.7 shows the dose-profiles

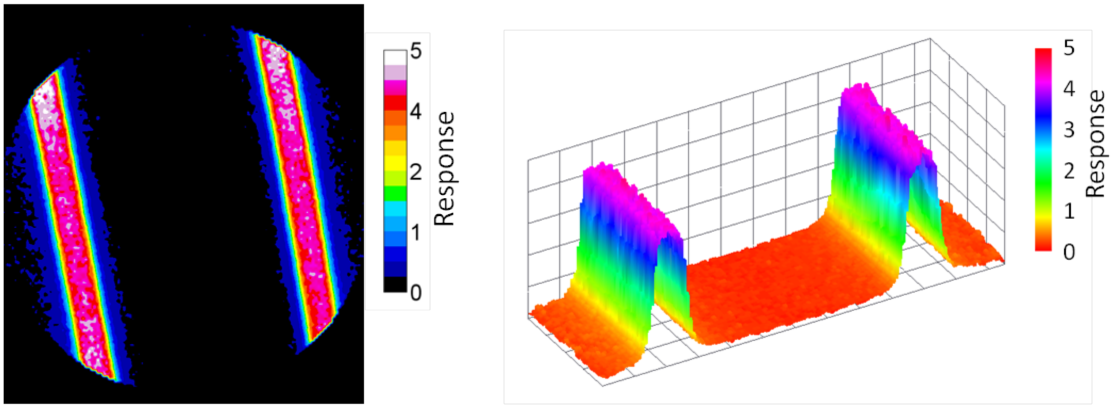

(a) 2D representation (b) 3D representation

Figure 8.6: Microbeam profiles obtained using 1 % Sm^{3+}-doped FA glass detector. The images are represented in the forms of (a) two and (b) three dimensions. Notice the values are response. The entrance dose is 1000 Gy. The objective lens used was 20×/0.75NA

obtained by GafChromic® film (digitization by the wide-field microscope) for the CLS, ESRF, and SPring-8. The red channel was used for low dose range up to 300 Gy and blue channel was used for higher dose than 300 Gy. The bottom figure illustrates the dose-profiles measured using 1 % Sm^{3+}-doped FA glass detector. Interestingly, the peak-to-valley dose ratio (PVDR) seems to vary between the irradiation facilities despite the fact that major beam dimensions and delivered entrance dose expected are the same (beam width = 50 μm, centre-to-centre distance = 400 μm, and entrance dose = 1000 Gy). The PVDRs for the CLS(air) and SPring-8 are the largest (∼50). Further, the valley dose for SPring-8 measured by the GafChromic® film is larger than that measured by the FA glass. We believe that this is because the GafChromic® film does not have sufficient sensitivity to measure low valley doses, which leads to inconsistent results. The discussions will be extended in the following sections with more detailed analyses.

8.3.3 Peak Shape

From the dose-profile obtained, we have further studied the shape of detected microplanar peaks in the microbeam. The shape is studied by examining the normal-

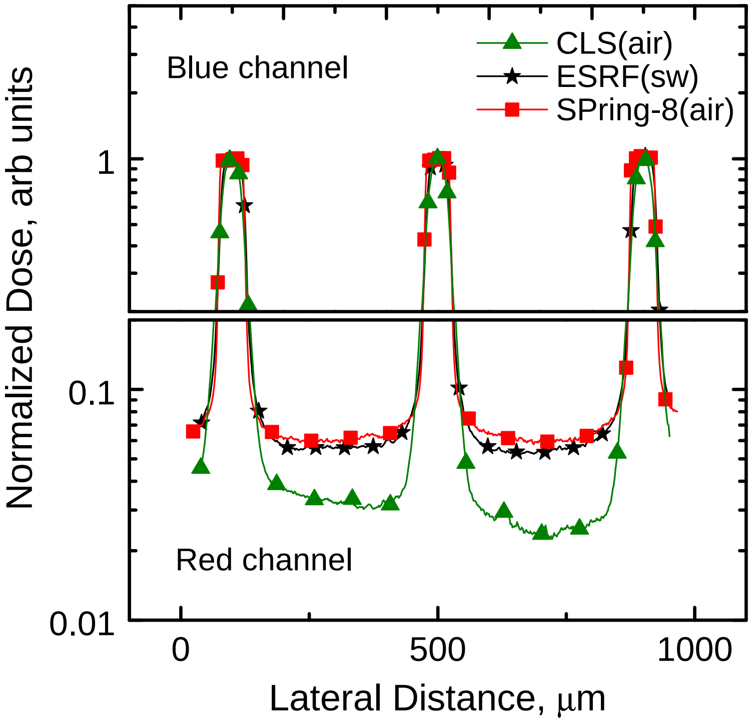

Figure 8.7: Dose-profiles of microbeam measured using GafChromic® film. The top part is by blue channel and the bottom is red channel.

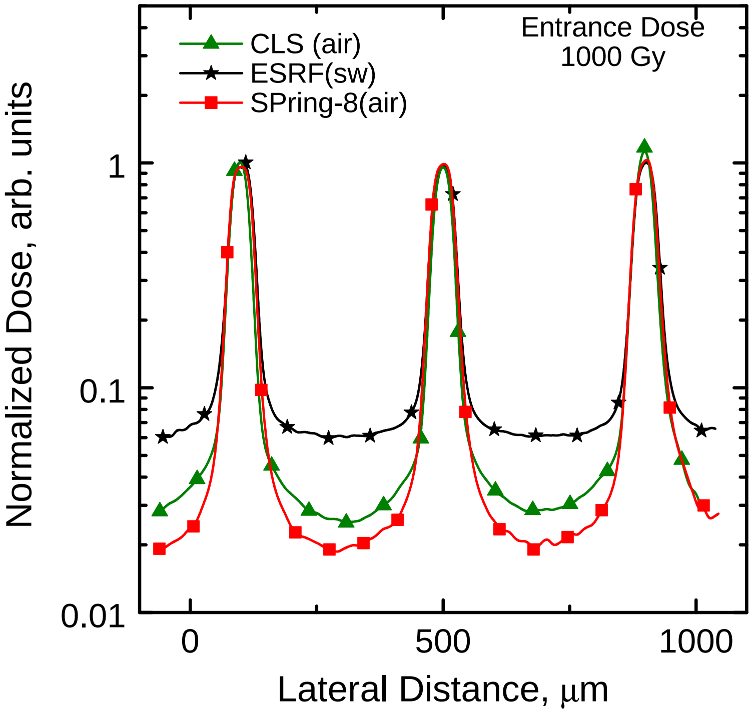

Figure 8.8: Dose-profiles of microbeam measured using 1 % Sm^{3+}-doped FA glass.

ized dose value versus the distance from the centre of microplanar beam. Figure 8.9 compares the peak shapes of the microbeam measured by a GafChromic® film. Together with the experimental data, a simulation results by Nettelbeck et al. [124] are plotted. The simulation was done using a standard Monte Carlo code against the same design of multi-slit collimator (MSC) model. All the entrance doses for these curves are 1000 Gy. The data are from blue channel. Clearly, it has been observed that the dose values are consistent (flat) over the top region of peak, and the dose dramatically drops off farther away from peak. Further, it seems that microbeam at SPring-8 has the sharpest edge among the others and has an excellent agreement with the Monte Carlo simulation. The peak edge of microbeam at the ESRF has the second sharpest structure and is only slightly off the simulation line. The peak shape for the CLS is the most smeared.

Figure 8.10 shows the peak shapes of the microbeams at the CLS, ESRF, and SPring-8, which were measured by using a 1 % Sm^{3+}-doped FA glass detector. As for the GafChromic® film, the flat profile on the top of the peak was clearly observable. However, the edge for SPring-8 measurement was not as sharp as seen by the GafChromic® film, so the measured profile falls off the simulation data. Otherwise, the tendency of the sharpness of the other peaks is consistent, that is, the peak at CLS appeared to be the most smeared structure. In fact, later we discovered that the cause of the smeared peak at the CLS was mainly due to the imperfection in the MSC alignment. In another experimental opportunity, we have attempted to align the MSC more precisely using an online X-ray camera. Figure 8.13 compares the peak shape of the microbeam at SPring-8 with that of CLS after the improvement of the alignment. Both the irradiations were carried out in air. As seen in the graph, the agreement between the two curves has been dramatically improved.

Otherwise, the shapes for CLS and SPring-8 obtained by Sm-doped FA glass detector are in a better agreement with the Monte Carlo simulation by Nettelbeck et al. particularly in the valley region compared to the measurement results by the GafChromic® film. Only the valley dose of the microbeam at ESRF showed much higher values. One possible reason would be due to the X-ray scattering in the phantom. Since the detectors were irradiated through a 2-cm phantom, scattered X-rays as well as the corresponding secondary radiations should also reach the detectors. However, our follow-up experiments did not completely answer this question. The Figure 8.12 compares the peak shapes of the microbeam measured in air and SW (2 cm) absorbers. Irradiation was done at the CLS. Despite the different absorbers, the peak shapes seem to reasonably agree especially at the edge; and, a notable increase in the valley dose has not been confirmed.

We believe that the reason for the sharpest structure seen for the SPring-8 arises mainly from the orientation of irradiation. While the irradiations at CLS and ESRF are made in such a way that the microplanar beam lines lie vertically (perpendicular to the orbital plane of storage ring), the irradiation geometry at the SPring-8 is made so that the microplanar beams are produced horizontally. Since the X-ray photons generated by a bending magnet or wiggler source propagate in a "fan shape", the beam divergence in the horizontal direction is much larger than that in the vertical direction. As a result, the microbeam produced by the irradiation geometry for the SPring-8 has a small divergence towards the valley regions, hence the edge of the peak is sharp. On the other hand, for the microbeam irradiations at CLS and ESRF, the beam divergence is larger in the direction towards the valley regions, which is the horizontal direction with respect to the storage ring orbit. As a result, the edge of the microplanar beam is not as sharp.

8.3.4 Characterization of the microbeam

The peak doses, valley doses, PVDR, and FWHM of microbeams have been measured with varying entrance doses at CLS, ESRF, and SPring-8. Here, the entrance dose is defined as the broad X-ray dose measured at up-stream of MSC. The GafChromic® film was used for the measurements. The measurements were done using Sm^{3+}-doped FA glass and GafChromic® film detectors. Figure 8.11 (left) shows the measured values using GafChromic® films. The film was digitized using a wide-field microscope as described previously. The red channel was used for the valley dose as well as peak dose measurement when the entrance dose was smaller than 300 Gy. For over

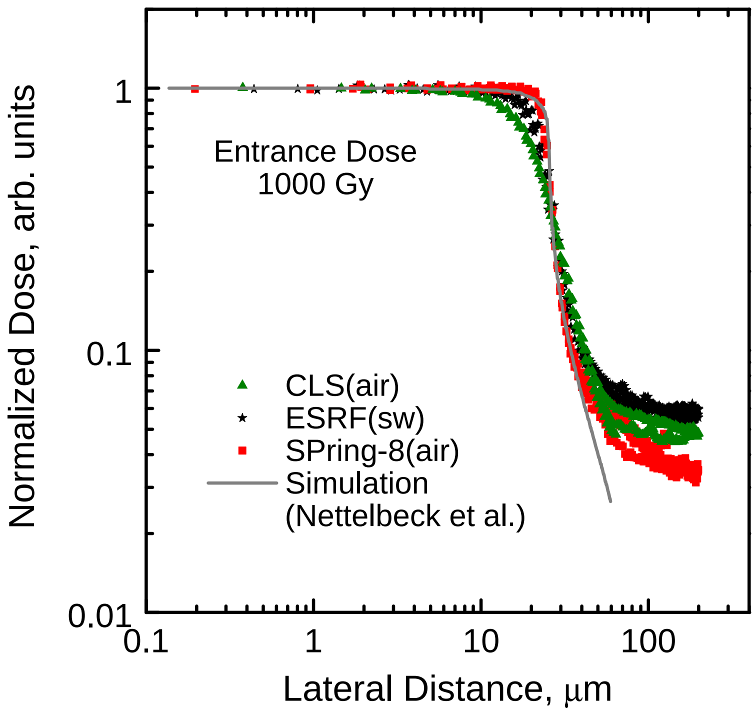

Figure 8.9: Peak shapes of microbeam at CLS, ESRF, and SPring-8 measured using GafChromic® film with a digitization by a wide-field microscopy reader. For comparison, a Monte Carlo simulation result by Nettelbeck et al. [124] is plotted together. The entrance dose was 1000 Gy.

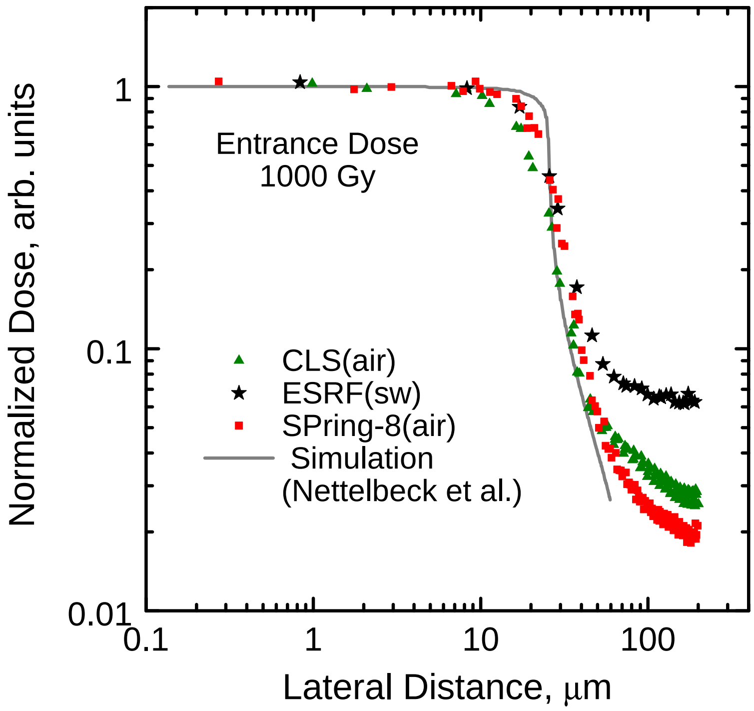

Figure 8.10: Peak shapes of microbeam at CLS, ESRF, and SPring-8 measured using 1 % Sm^{3+}-doped FA glass detector. For comparison, a Monte Carlo simulation result by Nettelbeck et al. [124] is plotted together. The entrance dose was 1000 Gy.

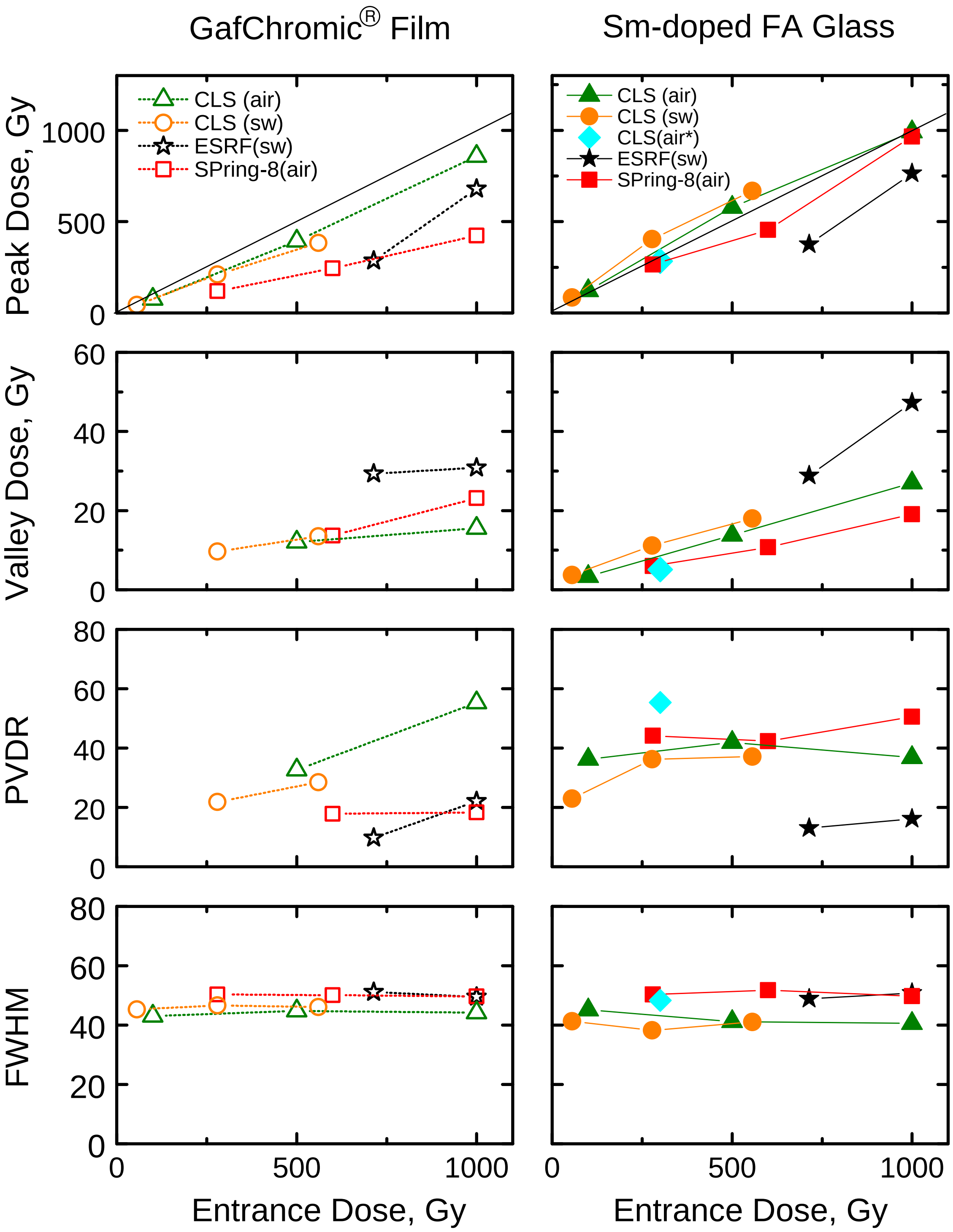

Figure 8.11: Characteristic parameters of microbeam (peak dose, valley dose, PVDR, and FWHM) for varying entrance doses measured using (left) Sm-doped FA glass detector and (right) GafChromic® film. CLS(air*) indicates the data obtained with an improved alignment of MSC than CLS(air) and CLS(sw).

several measurements with different entrance doses, the detected microbeam peak doses appeared to be substantially smaller than the entrance doses. Such a difference is present regardless of the difference of the dose level. Earlier measurements with a flatbed scanner also showed smaller values for the peak dose, but the reason was thought to be due to the insufficient resolution of the scanner, MTF = 0.6 at 10 lp/mm (10 lp/mm corresponds to bar patterns having the width of 50 μm). However, the contrast in the case of the microscope reader is almost 100 % at this spatial frequency. Earlier studies by Nariyama et al. [118] have also shown the smaller detected peak values compared to Monte Carlo simulation. They argued that the cause was due to the small volume of the irradiated region by the microbeam, where electronic equilibrium is not fulfilled. However, the mismatch between the measured dose value and entrance dose they have observed was only less than 15 - 20 %, while our observation showed much greater differences. The valley doses could not be detected when the entrance dose was smaller than 100 Gy and when the peak dose was 280 Gy at SPring-8.

In contrast to the results obtained by the GafChromic® film, Figure 8.11 (right) shows measurement results obtained by the FA:1%Sm^{3+} glass detector. Unlike the measurements by GafChromic® film, the peak doses reasonably agree with the entrance doses. (Here, the entrance dose is defined as the X-ray dose measured at upstream of the MSC). Further, the detected valley doses are well correlated to the entrance dose as well as the irradiation environment. The valley dose increases as a function of entrance dose. The valley dose of the microbeam at the SPring-8 seems to be the lowest, CLS is next, and the values at the ESRF are noticeably higher than the others. It should be emphasized that the irradiations at the CLS and SPring-8 were carried out under an air environment while at the ESRF the detectors were irradiated through a 2-cm SW absorber. It is commonly understood that X-ray scattering as the microbeam is transmitted in a phantom adds to the dose in the valley. The effect is seen clearly when we compare the values obtained at the CLS with and without the SW phantom. However, the difference is not as significant as that observed at the ESRF.

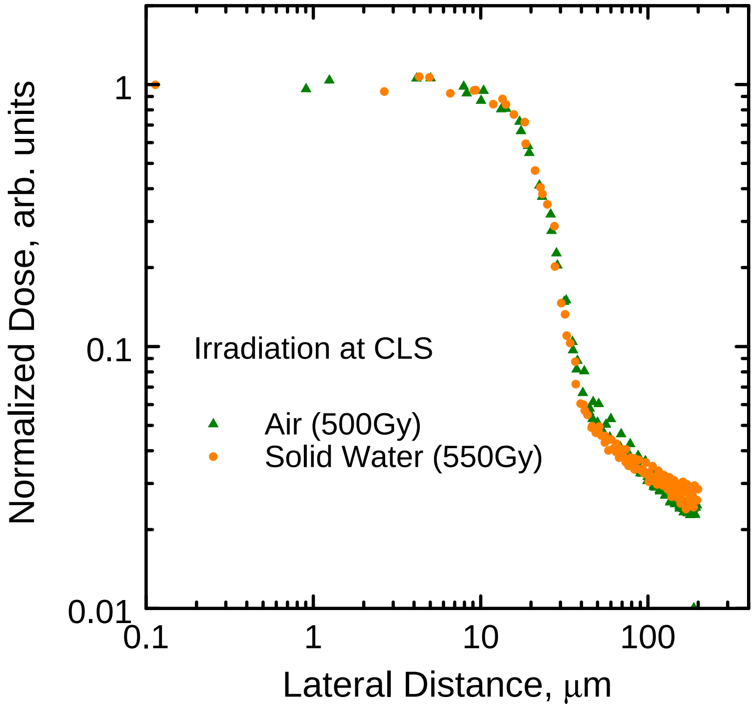

Figure 8.12: Peak shapes of microbeams measured in air and SW phantom (2 cm) at CLS.

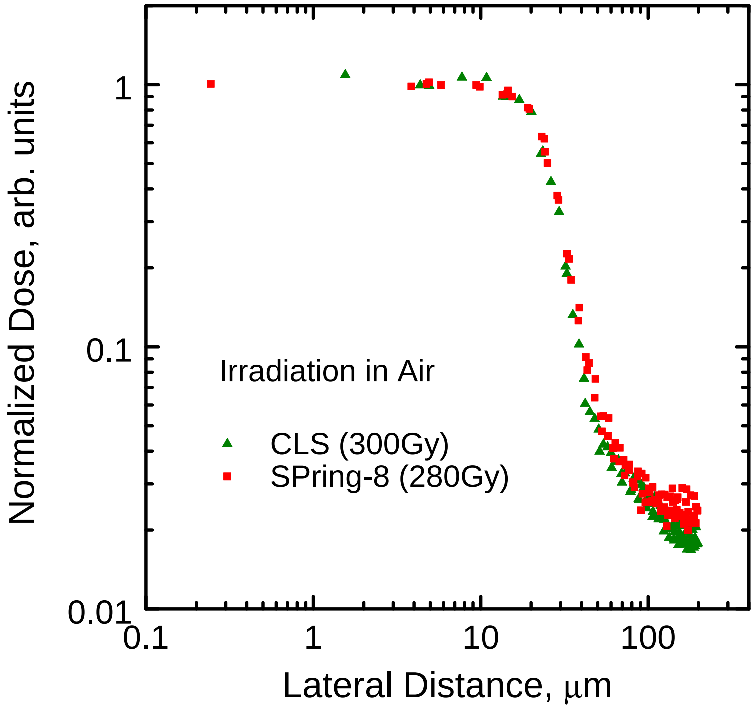

Figure 8.13: Peak shapes of microbeams measured at CLS and SPring-8 in ambient air environment. The alignment of MSC at CLS is improved.

The measured characteristics of microbeam at the ESRF are notably different from those measured at other facilities. The peak dose is significantly lower and valley dose is larger. One may think that the main cause may come from environment in which the microbeams were measured — air or SW phantom. For the measurements at CLS when irradiated through a phantom, the valley doses may be slightly larger by 15 % than in air. However, the increase is not as significant as observed at the ESRF. Further increase of valley dose may be explained by the observation by Siegbahn et al [25]. In our case, they have shown a significant increase of valley dose with increasing microbeam height. The height of microbeam at the ESRF is much larger (20 mm) than the others (CLS is 4.5 mm, and SPring-8 is 14 mm). Furthermore, the 5 μm slit inserted between the MSC and detector, which the CLS and SPring-8 do not have, may cause additional scattering of X-rays.

Another correlation observed is that the valley doses measured at the SPring-8 are lower than those at the the CLS when irradiated in air. The lower valley dose leads to a large PVDR. At both the CLS and SPring-8, the irradiations were carried out in an air environment (unlike ESRF); however, we observed different characteristics in the microbeam. We believe the major reason is that the alignment of the MSC at the CLS was not optimized. The detected FWHMs of microplanar beams for the CLS are approximately 10 μm smaller than the SPring-8 (and ESRF). The latter indicates that the MSC was approximately 0.07 degree off axis. After the improvement of alignment (CLS(air*)), the FWHMs increased to 48.4 μm, the peak dose increased while the valley dose decreased, and as a result the PVDR increased. In fact, it is commonly understood that, for example as discussed in [19], narrower FWHM would lead to a higher PVDR; however our observations conflict with the latter notion. It is, most likely, that PVDR decreases by the misalignment of the MSC by a small angle; however, PVDR increases with greater angle of misalignment where the FWHM becomes sufficiently small that the scattering effects become insufficient, but the contribution by the ratio between peak width and the centre-to-centre distance takes over. Spiga et al. [19] have shown by Monte Carlo simulation that PVDR decreases with increasing width of microplanar beams as 25, 50, and 75 μm with a fixed centre-to-centre distance (400 μm), respectively. Also, our separate observation with the accidentally misaligned MSC showed ~1000 of PVDR, where the detected FWHM of the micoropanar beams were ~5 μm. In the latter case, the estimated angle of misalignment was ~0.3 degree.

8.3.5 Microbeam in Solid Water

Characteristic parameters of a microbeam may vary as it transmitted through a patient's body. The microbeam was measured at varying depths in a SW phantom. The measured values for peak dose, valley dose, PVDR, and FWHM are summarised in Figure 8.14. The measurements were done at the CLS using a Sm-doped FA glass detector. The entrance dose was 300 Gy. At the vicinity of the entrance surface (1 mm), the peak dose, valley dose, and PVDR were found to be the highest. As the beam penetrates deeper and deeper, their magnitudes decrease. The fact that the PVDR decreases with the decreasing peak dose suggests that the build-up effect of X-rays at the close to the entrance surface was more pronounced for peak dose (due to simply larger dose). Despite the decrease in PVDR, a significant change in the FWHM has not been observed.

The fact that the PVDR decreases as a function of X-ray penetration depth means that the decay rate for the peak dose is slower than the valley dose. The reason is perhaps due to the fact that a build-up dose effect of X-rays is more pronounced for peak dose than valley in the region close to the side of beam entrance. Despite the significant decrease in the PVDR, FWHM seems to be consistent. At a depth of 100 mm, the peak dose is approximately 10 % of the entrance dose. It may imply that a healthy tissue in the region closer to the entrance of a patient's body may be significantly damaged more than the affected part. We believe that the main cause arises from the fact that the X-ray energy spectrum used at the CLS includes more of low energy photon than the ESRF or SPring-8. The harder the X-rays (the greater their energy), the more build-up dose effect occurs. Hence, we can expect a larger dose even at the inner part of a patient.

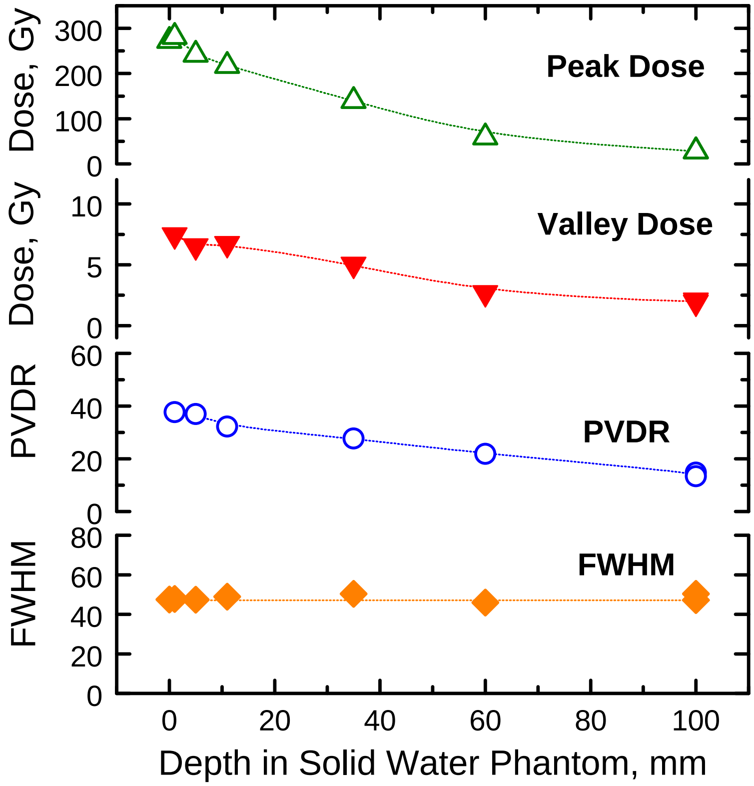

Figure 8.14: Characteristic parameters of microbeam as a function of distance from the entrance surface inside a SW phantom. The measurements were carried out at CLS using 1 % Sm-doped FA glass detector. The entrance dose for all the measurements was fixed to 300 Gy.

8.4 Conclusion

We have studied the microbeam measurement ability of a 1 % Sm^{3+}-doped FA glass detector in comparison with GafChromic® film (HD-810) detector. The GafChromic® film covers approximately the range 10 – 400 Gy when the absorption (or transmission) of red light is used, which agrees with the earlier study. However, with the reader set-up, which is capable of detecting a different colours, the detection of larger doses is possible (particularly up to ∼1000 Gy when the blue channel is used). On the other hand, the Sm-doped FA detector has a dose detection range from ∼1 Gy to over 1000 Gy. When we tested the dose-response of the glass detector at CLS, ESRF, and SPring-8, an energy dependence for the response of the glass detector has been observed. For low energy X-rays, the sensitivity is high whereas the sensitivity is lower at higher energies. The reason is most likely due to the *L*-edge absorption by the Ba-ions contained in the detector material; the *L*-edge is located around 40 keV. With the GafChromic® film, no such strong energy dependence has been observed.

Image resolution of the GafChromic® film has been tested by two different digitization methods. One was a high-resolution flat-bed optical scanner (Perfection V700, EPSON), which is often used to digitize a GafChromic® films. The other technique was a use of a wide-field optical microscope. The flatbed scanner is a useful tool for characterizing the entire dose picture for microbeam due to its large FOV. However, the spatial resolution is not sufficiently high to resolve the dose pattern of microbeam dose distribution with full contrast. Therefore, the peak value drops by approximately 40 % when the width of micoropanar beam is 50 μm. On the other hand, the microscopic reader has sufficient resolving power to be useful in determining the microbeam dose profile, but the FOV is much smaller, depending on which objective lens is used. Nonetheless, the microscopic reader is a particularly useful tool when one needs to measure the peak dose accurately, and also when one needs to study the distribution of the X-ray dose on a microscopic scale. In fact, the shoulder of the microbeam shape seems to be very well represented and agrees with Monte Carlo simulation results [124] especially for the microbeam at the SPring-8. The sensitivity of the GafChromic® film used in this study may not be sufficient to detect valley doses; the detected valley doses appeared to be inconsistent.

When we used a Sm-doped FA glass detector, the microbeam dose-profile was also successfully obtained. The measured peak dose agrees well with the entrance dose, which implies that the resolution is sufficiently high to resolve the 50 μm fine pattern of the microbeam. Also, it is supported by the fact that our demonstration in Figure 4.22 has shown the ability to resolve a 4-μm fluorescent sphere. The valley dose can be also detected together with the peak dose since the detector has a dose detection range of ~1 Gy to over 1000 Gy. Hence, the Sm-doped FA glass plate is an excellent detector to measure both the peak and valley doses together, that is, the PVDR. The peak shape detected using the glass detector may not be as sharp as that obtained by the GafChromic® film especially for the microbeam at SPring-

8, which has the finest edge shape. The possible reason is that the glass matrix itself strongly interacts with the X-rays, so it produces severe scattering of X-rays or secondary radiation. The effect is so strong that it deposits additional dose in the adjacent regions which blurs the edge regions of the micoropanar beam shape as recorded on the film. In order to confirm this hypothesis, we will need to carry out the experiment with a dosimetric detector that has a smaller mass attenuation coefficients and lower density.

The characteristic parameters of the microbeam have been measured at the CLS, ESRF, and SPring-8. It seems that the valley dose at the ESRF is much higher than the CLS and SPring-8. The main cause should arise from the fact that the measurement at the ESRF was done inside a SW phantom, which leads to additional scattering of X-rays, and also the length of the microbeam along the microplanar beams are notably longer than the others. This leads to smaller PVDR values. Furthermore, misalignment of the MSC at the CLS was detected by examining the FWHM of the microplanar beams. The FWHM was approximately 10 μm smaller than expected, in which case the MSC was only 0.07 degree off the axis. In addition, this misalignment caused additional dose in the valley region due to the X-ray scattering at the MSC, leading to a lower PVDR. When the MSC is misaligned at even a greater angle, then the PVDR dramatically increases, e.g. a 0.3 degree of misalignment led to a PVDR of $\sim$1000 in which the FWHM of micoropanar beams was $\sim$5 μm while the centre-to-centre distance was fixed to 400 μm.

The characteristic parameters of a microbeam may vary with the depth inside a patient's body. The measurements at the CLS using a Sm-doped FA glass detector indicated a dramatic decrease of the peak dose over 100 mm from the entrance surface. It indicates that the majority of the X-ray dose may be observed before the microbeam actually reaches to the target tumour. The selection of a high dose at the target tumour would mean more damage would be given to the healthy tissue in the entrance region. Despite the dramatic decrease of peak dose, on the other hand, the decrease rate of the valley dose is smaller; hence the PVDR is highest at the vicinity of the entrance region and decreases gradually as a function of penetration depth. This observation may indicate that the build-up dose effect is strongest close to the entrance region, mainly because the X-rays at the CLS include a number of low energy photons, which tend to be strongly absorbed near the surface due to the photoelectric interaction. The X-ray beams with higher energy, as used at the ESRF or SPring-8, should give a stronger build-up effect in deeper regions of the body and it should allow more efficient treatment. The BMIT at CLS have been developing a new beamline with more preferred design for the MRT, based on a wiggler X-ray source, and it will be available to general users in the near future.

CHAPTER 9

SUMMARY AND CONCLUSIONS

9.1 Introduction

The objective of this Ph.D. work was to develop a prototype of novel dosimetry technique for use in research on Microbeam Radiation Therapy (MRT). A successful dosimetry technique requires having a few micrometer of spatial resolution together with a large dynamic range in a relatively large dose range (∼5 to over 1000 Gy).

In the course of study, we have proposed an original dosimetry technique which is briefly summarised in the next section. The following section (9.3) summarises the works done to characterize potential dosimeter materials tested, and describes the best candidates of material used as a dosimetric detector in our approach. Further, Section 9.4 summarises the works done on actual measurements of microbeam using our dosimetry approach and conventional methods. The microbeams produced at three different synchrotron facilities (CLS, ESRF, and SPring-8) were characterized. The last section (9.5) suggests potential future works to further the research towards commercialization or clinical use.

9.2 Proposed dosimetry technique for large-dynamic-range and high-spatial-resolution

Our approach towards a measurement of microbeam was described in details in Chapter 3, but briefly this section summarises the the principles and how it was successfully implemented, demonstrated and verified. The technique uses a luminescent material to detect an X-ray dose in which the emission spectrum, upon photoexcitation, changes as a function of X-ray dose delivered. Such a detector plate may be a Sm^{3+}-doped material since a number of reports have already shown the reduction of the valence state ($Sm^{3+} \rightarrow Sm^{2+}$) of this ion included in various materials by exposing to various types of radiations, including X-rays. The Sm^{3+} and Sm^{2+} ions exhibit photoluminescence (PL) spectra in different spectral regions, so these two signals can easily be separated and measured individually. Moreover, the extent of $Sm^{3+} \rightarrow Sm^{2+}$ reduction seems to be dependent on the radiation dose; thus, the extent of $Sm^{3+} \rightarrow Sm^{2+}$ reduction may be used as a measure of the X-ray dose delivered. The response as a change in luminescence spectrum, or PL, is further read out and digitized using a confocal fluorescence microscope. The confocal microscopy technique allows us to read out the response signals, in turn X-ray dose, distributed over the area of detector plate on a micrometer scale of resolution.

9.3 Characterization of detector materials

9.3.1 Verification of valence reduction by X-ray irradiation

We have first started the project with a search for suitable detector materials. The materials we have examined include several types of Sm^{3+}-doped polycrystalline, glass and glass-ceramic materials. Although the dosimeter plates in our approach are not limited to Sm-doped materials, it would be one of the most appropriate materials to start the project with since a number of Sm^{3+}-doped materials with the functionality of valence reduction by X-ray irradiation have been already reported elsewhere. In search for a detector material, which is basically material that shows the $Sm^{3+} \rightarrow Sm^{2+}$ reduction by X-ray irradiation, a number of Sm^{3+}-doped materials were synthesized at the university here, and collected from various research groups across the world. The samples were tested by simply comparing the PL spectra before and after X-ray irradiation.

Among the materials we have tested, only few glass samples have shown the reduction effect by X-rays, and the majority of others did not. Very surprisingly, glass materials (Li_2O-SrO-B_2O_3 and SrO-BaO-P_2O_5-B_2O_3), which were reproduced by us by following the synthesis procedures reported in the literature, did not show any reduction, despite the evidence of reduction by earlier studies [45, 47]. On the other hand, polycrystalline materials such as Sm^{3+}-doped $BaBPO_5$ and $SrBPO_5$, as well as SrB_4O_7 co-doped with Sm^{3+} and Sm^{2+} have shown notable reduction effects. However, the glasses made out of these polycrystalline materials did not have the reduction feature at all. After examining many glass samples, it became apparent to us that it is a very challenging task to have the Sm^{3+} ions reduced by X-rays in glasses.

Later, Sm^{3+}-doped fluorophosphate (FP) and fluoroaluminate (FA) glasses, provided by Dr. Andy Edgar's group, have been found to show an excellent extent of the $Sm^{3+} \rightarrow Sm^{2+}$ conversion upon X-ray irradiation. In fact, it turned out these glasses are the best candidates for detector materials for use in our detector technology. The extent of reduction depends on the concentration of Sm^{3+} added. The higher concentration, the smaller degree of conversion, which was a surprising result.

Furthermore, we have designed and synthesized a new type of glass-ceramic material ($45SiO_2$-$20Al_2O_3$-$22CaF_2$-10CaO-$3SmF_3$ in molar %), which contains CaF_2:Sm^{3+} nanocrystals inside the oxyfluoride glass matrix. It is first produced as glass by a conventional melt-quenching technique. Further heat-treatment induces nucleation and growth of the nanocrystals. The DSC measurements suggested that the nucleation of CaF_2 nanocrystals takes place around 690 °C and above, but the heat-treatment temperature should not reach close to 850 °C otherwise the entire glass ceramic crystallizes, that is the entire glass matrix crystallizes. The size of nanocrystals can be controlled by the heat-treatment temperature. When the glass is heated at 700 °C for 4 hours, the average nanocrystal size (”diameter”) was 37.4 nm (estimated by XRD analysis), and the entire glass-ceramic matrix is as transparent as that of glass. On the other hand, when it is heat-treated at 750 °C for 4 hours, the averaged diameter was 145.0 nm (estimated by XRD and SEM). The sample had become milky after the heat-treatment. The valence reduction takes place only for Sm^{3+}

ions which are included inside the CaF_2 nanocrystals, while the Sm^{3+} ions in the glass matrix do not change the valence state by X-ray irradiation. The generated Sm^{2+} ions shows a broad structure of PL emission spectrum due to the $4f^5 5d^1 \rightarrow 7F_0$ transition instead of the $4f$-$4f$ transitions, which is typically observed in most of the materials, especially in Er-ion doped glasses. In fact, among the dosimeter materials we have tested, this glass-ceramic is the only material that shows the PL emission by the $4f^5 5d^1 \rightarrow 7F_0$ transition of Sm^{2+}. Such transitions are allowed by the selection rule of electronic dipole transitions; therefore these transitions are more efficient (intense emission) as well as the lifetime of PL decay for such transitions is very fast. The time constants measured is $\sim$ 43 ns whereas the time constant for the $4f$-$4f$ transitions of Sm^{3+} in a glass host is $\sim$ 0.6 and 1.7 ms (having two time constants because the decay curve is composed of two exponential functions). In our dosimetry technique, the fast PL lifetime allows us to increase the scanning speed, especially when the scanning is based on the point-by-point readout. The fast lifetime allows us minimize the dwell time between the adjacent pixels of readout as the signals from the two adjacent pixels may overlap each other if the scan time between adjacent pixels is short compared with the PL lifetime.

9.3.2 Stability

The stability of the detector's response is very important as our approach relies on an indirect detection method, meaning that the response signal needs to remain in the detector plate until it is read out. All the materials we have tested are sufficiently stable, at room temperature, to be digitized at least a few days after the irradiation.

In particular, the response in polycrystalline $SrBPO_5$:Sm^{3+} is stable over 10 days with some fading of about 30 % (a fraction of the fading is due to the photobleaching effect during the PL measurements).

The stability in Sm^{3+}-doped FP and FA glass detectors seems to strongly depend on the concentration of Sm^{3+} ions added. The smaller the concentration, the more fading occurs. However, the fading of signal is only present within 24 hours after the irradiation, and the response signal seems to be very stable beyond this period. For both FP and FA glasses doped with 1 % of Sm^{3+}, the response signal seems to be very stable immediately after the irradiation, and no fading was observed up to 10 days.

The response of the CaF_2:Sm^{2+} included in an oxyfluoride glass-ceramic detector plate seems to be stable over several days (up to 8 days have been tested).

9.3.3 Dose-response

The response change against the delivered X-ray dose was examined for the materials that had shown the $Sm^{3+} \rightarrow Sm^{2+}$ change by X-ray irradiation.

The dynamic range as well as the valence reduction rate against the X-ray dose deposited vary depending on the host material. Polycrystalline $BaBPO_5$:Sm^{3+} shows a response change from 0.1 Gy to approximately 50 Gy. Above 50 Gy, no change of response was seen, so the reduction process has been saturated. For $SrBPO_5$:Sm^{3+}, the extent of reduction is much larger than $BaBPO_5$:Sm^{3+}, so the signal-to-noise ratio is better. The dynamic range is from 0.1 Gy to approximately 500 Gy, which is followed by saturation. For SrB_4O_7:Sm^{3+},Sm^{2+}, the saturation was not observed over 5500 Gy.

For Sm^{3+}-doped FP and FA glasses, the dynamic range depends on the type of host glass and the concentration of Sm^{3+} added. For a fixed concentration of Sm^{3+} ions, the FA glass seems to have a better detection ability in the higher dose region. In other words, the response saturation takes place at a higher dose for the FA glass whereas FP has better sensitivity for low dose. For the dependence on the doping concentration, the dynamic range shifts towards higher doses with increasing doping concentration of Sm^{3+}. The dynamic range of 1.0 % Sm^{3+}-doped FA glass covers a very wide range from $\sim$ 1 Gy to over 1000 Gy, which matches the dose range used in MRT.

Furthermore, we have found that detectable dose range of Sm^{3+}-doped FP glass detector can be enlarged towards higher dose by UV-exposure treatment after X-ray irradiation. The phenomenon was interpreted as effective photobleaching of hole trapping centres associated with phosphorus-oxygen hole centres (POHCs), which resides in the glass matrix, by UV exposure. The POHCs are created in the FP glass matrix by trapping holes that have been generated by X-ray irradiation; and the corresponding number of electrons is trapped by Sm^{3+} to become Sm^{2+}. However, POHCs are not the only hole traps, so the number of Sm^{2+} created is proportional to the sum of all the hole trapping centres. Since POHCs seem to populate at a high rate against the X-ray dose, this leads to the Sm^{2+} ions to populate at a high rate and the population saturates in a relatively low dose region. However, effective removal of POHCs by the UV exposure after irradiation results in the removal of these Sm^{2+} ions populated at a high rate. Therefore, the number of Sm^{2+} ions that remain are those that correspond to other hole trapping centres, which were populated at a lower rate than POHCs. As a result, the dose-response curve with a post UV exposure has shown larger dynamic range, and the saturation of response in the large dose region has disappeared. Nevertheless, since the UV-treatment removes quite a number of Sm^{2+}, the decrease of the S/N ratio cannot be avoided.

For oxyfluoride glass-ceramics containing CaF_2:Sm^{3+} nanocrystals, the $Sm^{3+} \rightarrow Sm^{2+}$ reduction was confirmed from 1 Gy to 10 kGy, which comfortably covers the dose range used in MRT.

9.3.4 Homogeneity

The detector material must be homogeneous over an area equivalent to the cross-sectional area of microbeam; and also the homogeneity needs to be maintained at a micrometer scale. The observations of sample surface have shown that polycrystalline samples, when the grain size is not controlled, have a surface that seems to be visually very rough even after polishing and the large grains and ores can be observed even with a relatively small magnification (10×). When the grain size is controlled to be smaller than 1 μm, the homogeneity is dramatically improved. However, it is still not as uniform as glass material; glasses are well known to be homogeneous.

For the glass-ceramic samples, the observations by SEM have shown that CaF_2 nanocrystals are uniformly distributed over the sample. Since the $Sm^{3+} \rightarrow Sm^{2+}$ reduction takes place only in the nanocrystals, it is clear that the valence reduction feature is distributed uniformly over the detector plate.

9.3.5 Reusability

When polycrystalline materials are heated at elevated temperatures, the X-ray generated Sm^{2+} seems to become unstable, which leads to $Sm^{2+} \rightarrow Sm^{3+}$ change, hence the response value decreases. This heating technique may be used to "reset" the dosimetry plate for multiple use and may allow us to reuse the detector multiple times. For $BaBPO_5$:Sm^{3+}, the response was almost completely erased after heat-treatment at 700 °C. The detector materials may be reusable after the erasure. In fact, the dose-response curves of $BaBPO_5$:Sm^{3+} polycrystalline detector measured before the heat-treatment (700 °C), or on an as-prepared sample, was in a good agreement with that recorded after the erasure. On the other hand, the response of $SrBPO_5$:Sm^{3+} cannot be erased completely after heating at 700 °C, but the majority of response can be removed. The unerased response signal may affect the dose-response curve. Indeed, the values in the low dose region are higher than those of the as-prepared sample. Hence, the response curve of the erased sample did not agree with the one measured on as-prepared sample. Nevertheless, the response curve measured after further erasure agrees very well with the one measured just after the first erasure. Therefore, $SrBPO_5$:Sm^{3+} may be still be usable multiple times with a heat-treatment erasure technique.

A study on the reusability of Sm^{3+}-doped FP and FA glass detectors is beyond the scope of the thesis. However, Vahedi et al. [127] and Morrell et al. [128] have shown that the response can be erased completely by heating and also by exposing to light, especially UV light. Furthermore, the erased detectors can be used multiple times.

The new glass-ceramic dosimeter material is reusable as well. The recorded dose information on the detector can be erased either by heating at elevated temperatures (550 °C and above) or by exposing to UV light. The dose-response curves measured before and after the erasure agree with each other.

9.3.6 Summary

Throughout the project, we have found a number of materials which show the $\mathrm{Sm}^{3+} \rightarrow \mathrm{Sm}^{2+}$ reduction by X-ray irradiation. Perhaps, the best candidate to date may be 1 % Sm^{3+}-doped FA glass. The dynamic range covers the dose range used in MRT, so it is capable of measuring the peak dose and valley dose together. The detector response as dose information stored on the detector is very stable and no fading was found over 10 days after the irradiation. Furthermore, the glass matrix is homogeneous over a large area, so an accurate measurement of dose distribution is expected. The polycrystalline materials have the severe disadvantage of poor image resolution due to the inhomogeneous surface by crystalline grains even after the grain size was controlled below 1 μm.

The glass-ceramic is another candidate as a dosimetric material. This material system has a distinct advantage because the PL lifetime is so fast that the speed of readout can be dramatically improved. However, the most efficient excitation source is red, which conflicts with the rest of our samples, in which blue excitation is the most efficient. Therefore, the confocal microscope has been built with a blue excitation laser source before the discovery of this material system.

For the reasons above, we have expanded our studies of the applicability of our dosimetry technique for the measurement of microbeam dose profile using a 1 % Sm^{3+}-doped FA glass detector.

9.4 Characterization of microbeams at CLS, ESRF, and SPring-8

The research of microbeam radiation therapy (MRT) has been committed at several synchrotron facilities across the world. The specifications of each beamline as well as the irradiation geometry of microbeam may vary depending on the facility. Therefore, we have measured and characterized the microbeams produced at different synchrotrons (CLS, ESRF, and SPring-8) using our dosimetry approach (with

1 % Sm^{3+}-doped FA glass detector) and one of conventional dosimetry techniques based on using a GafChromic® film.

The GafChromic® film changes, by X-ray irradiation, its optical absorption in the red region (610 and 670 nm). However, as the radiation dose increases, the side-band of absorption overlaps in the green and blue region, in the mean time the increase of absorption in the red region may be saturated. Therefore, the dose-response curve varies depending on the colour channel used. The dose-response of red channel is the most sensitive, which shows detectable response value from ∼10 Gy to 400 Gy. When the blue channel is used, detection of even larger dose is possible up to ∼1000 Gy, whereas the sensitivity of blue channel at low doses is poor. We have observed that the dose-responses obtained at different facilities are consistent.

FA glass detector shows detectable response in a wider dose region (∼1 Gy to over 1000 Gy). However, the results seem to indicate that the response curve depends on the type of X-rays used for the dose-response measurements. The increase in the rate of response (against X-ray dose) seems to be faster with the X-rays at the CLS, whereas the curves obtained at ESRF and SPring-8 are in a good agreement. We think that this is due to the intrinsic property of the energy dependence of the linear attenuation and energy absorption coefficients since the FA glass has a strong non-linearity of X-ray interaction around 40 keV, which is due to the *L*-edge of Ba within the FA glass matrix. Because the peak energy of CLS (50 keV) is the closest to this *L*-edge of Ba than the peak energies at ESRF and SPring-8 (83 and 90 keV, respectively), the mismatch of dose-response curve was more clearly pronounced when measured with the X-rays at CLS.

The image resolution depends on which dosimetric detector has been use and what reader is used to digitize the recorded response values. GafChromic® film detector irradiated with a microbeam was digitized with two different ways: commercial flatbed scanner (Perfection V700, EPSON) and wide-field microscopy (Diaphot-TMD, Nikon) equipped with a digital camera (D3200, Nikon). The flatbed scanner has a large FOV; therefore, it is a strong tool to digitize the entire picture of microbeam. In particular, it enables us to measure the macro-features of a microbeam such as the beam height and number of microplanar beams. In contrast, the microscope readout has much higher spatial resolution, which gives us micro features of microbeam such as width of microplanar beam and shape of dose distribution in the vicinity of microplanar beams. The edge of peak shape was very well represented: the microbeam measured at SPring-8 has the highest gradient at the edge of microplanar beams. The detector film itself may not have sufficient sensitivity to detect the low doses in the valleys of the microbeam, so measurement of PVDR is still a challenge.

FA glass detector also has sufficient image resolution to resolve the dose distribution pattern of a microbeam when a confocal microscope was used for readout and digitization. However, the detected peak shape appeared to be not as sharp as that obtained by GafChromic® film especially for the microbeam at Spring-8, which has the sharpest edge. We believe that the reason is because of the severe scattering of X-rays by the detector matrix. The mass attenuation coefficient is much higher than GafChromic® film, so the intense X-rays are scattered at the peak blur the edge shape. Otherwise, the FA:Sm^{3+} glass detector has sufficient resolution and sensitivity to measure peak and valley doses.

Further, our studies unveiled the characteristic parameters of microbeams produced at different facilities. Particularly, the valley dose measured at ESRF is significantly larger than the others. The main cause should be the long beam height of microbeam (20 mm) at this facility. The valley dose is a product of X-rays scattered in the peak regions, so the longer the height of microplanar beams the more X-rays scattered, hence larger the valley dose. In addition, the irradiation of a SW phantom by a microbeam seems to increase the extent of X-ray scattering, leading to a larger valley dose. However, the effect of solid water phantom seems to be insignificant compared to the effect of beam height.

Imperfections in the collimator alignment was also detected at CLS. The measurements showed that the beam width was $\sim$40 μm instead of $\sim$50 μm. This difference was caused by the misalignment of collimator by only 0.07 degree (estimated) of rotation angle with respect to the beam axis. Such a small angle of misalignment was found to a cause higher value of valley dose, leading to the smaller PVDR. We believe that the cause is the increased extent of X-ray scattering at the MSC. However, further angle of misalignment may increase the PVDR as the peak width is significantly small; when the peak width was $\sim 5\ \mu$m, the PVDR measured was 1000, where the angle of misalignment was 0.3 degree.

Moreover, we have simulated a change of characteristic parameters of microbeam as it penetrates inside the body of patient using a SW phantom. The peak dose is the highest at the vicinity of the entrance surface, and it dramatically decreases over 100 mm of penetration depths. On the other hand, the decrease rate of valley dose is smaller than peak dose. Therefore, the PVDR is highest at the vicinity of an entrance region and decreases gradually as a function of depth. FWHM of the microplanar beams are consistent over the depths we measured up to 100 mm.

9.5 Suggested future works

A fluoroscopic confocal microscope has been constructed and is continuing to be used to demonstrate the proof-of-principle of our proposed dosimetry approach. However, further improvements of the instrument are recommended for further advance of research and practical applications.

1. A variety of wavelengths for the excitation source should be available on the confocal microscope reader. Currently available excitation source is only a 473-nm blue laser. This wavelength is one of the best choices for exciting both Sm^{3+} and Sm^{2+} efficiently, in which the emissions are due to $4f$-$4f$ transitions. However, as we have explained earlier, another type of material may prefer different wavelengths; for example, red light is the best choice for exciting CaF_2:Sm^{2+}. Having a flexibility of excitation source will help us test a variety of potential detector materials and speed up the research.

2. The FOV should be enlarged in order to capture the entire dose distribution across the microbeam. Currently, the scanning is possible only within the FOV

of the objective lens. The use of a motorized translation stage has allowed us to to cover the entire area of the detector plate to scan.

3. Scanning speed should be increased for practical applications, especially when the scanning area becomes larger. The scanning speed is limited by both the PL decay time of detector material and the speed of scanning instrument. Currently, our glass-ceramic containing CaF_2:Sm^{2+} is capable of fast scanning. But the current reader instrument only allows $\sim$30 min per frame.

4. One should examine the dependence of the response on the dose rate and the peak energy. Such a study would provide a deeper understanding of the mechanism involved in the Sm^{3+}-ion reduction. Moreover, the study would open up a discussion on the use of our dosimeter materials for other applications.

Moreover, the search of a new dosimeter material should be continued for better dosimetric performance.

1. Other rare earth ions or transition metals should also be considered as a luminescent centre to be included in the dosimeter plate. So far, only Sm-ion has been of our interest to start off the project and to prove the principle of our approach. However, Sm-ion is not the only choice. Other kinds of luminescent centres may give better results.

2. The dosimeter material should be equivalent to tissue. Such a detector would show a better measurement of the actual dose delivered to the tissue. Moreover, such a detector absorbs less X-rays (or, in other words, is transparent to X-rays); therefore, it may allow us to measure the microbeam, during the actual therapy, at upstream of patient without affecting the microbeam characteristics.

3. A transparent ceramic may be an interesting material to examine. It consists of polycrystallites of cubic crystal structure, in which the adjacent crystallites are closely in contact with each other. As a result, the mismatch of refractive

index at the grain boundary is dramatically improved, and the entire matrix is as transparent as that of single crystal. It would give us further choices for the dosimetric material.

4. The dosimeter may not need to be a bulk plate but a thin film. Generally speaking, the resolution of an imaging plate depends on the thickness of the sensing layer. The thicker the layer, the wider is area for the light to spread; hence spatial resolution decreases. When the detector plate is made in a form of thin film, an area scan camera detector may be used to read out the signal while keeping the image resolution high. Moreover, the use of an area scan camera would dramatically increase the speed of readout over scanning readout.

REFERENCES

[1] S. O. Kasap, "High resolution dosimetric detector for synchrotron microbeam cancer therapy," in *NSERC 2009-2010 Strategic Project Grants*, 2009.

[2] X-RAY DATA BOOKLET, "http://xdb.lbl.gov/."

[3] J. H. Hubbell and S. M. Seltzer, "http://www.nist.gov/pml/data/xraycoef/."

[4] G. S. Belev, "ELECTRICAL PROPERTIES OF AMORPHOUS SELENIUM BASED PHOTOCONDUCTIVE DEVICES FOR APPLICATION IN X-RAY IMAGE DETECTORS," Ph.D. dissertation, 2007.

[5] O. Svelto, S. Longhi, G. Valle, and S. Kuck, *Springer Handbook of Lasers and Optics*, F. Träger, Ed. New York, NY: Springer New York, 2007. [Online]. Available: http://link.springer.com/10.1007/978-0-387-30420-5

[6] C. Koughia, A. Edgar, C. R. Varoy, G. Okada, H. von Seggern, G. Belev, C.-y. Kim, R. Sammynaiken, and S. Kasap, "Samarium-Doped Fluorochlorozirconate Glass-Ceramics as Red-Emitting X-Ray Phosphors," *Journal of the American Ceramic Society*, vol. 94, no. 2, pp. 543–550, Feb. 2011. [Online]. Available: http://doi.wiley.com/10.1111/j.1551-2916.2010.04110.x

[7] N. Miura, "Phosphors for X-ray and ionizing radiation," in *Phosphor Handbook, 2nd ed.*, 2007.

[8] O. E. Berg and H. F. Kaiser, "The X-Ray Storage Properties of the Infra-Red Storage Phosphor and Application to Radiography," *Journal of Applied Physics*, vol. 18, no. 4, p. 343, 1947. [Online]. Available: http://scitation.aip.org/content/aip/journal/jap/18/4/10.1063/1.1697656

[9] J. A. Rowlands, "The physics of computed radiography," *Physics in Medicine and Biology*, vol. 47, no. 23, pp. R123–R166, Dec. 2002. [Online]. Available: http://stacks.iop.org/0031-9155/47/i=23/a=201?key=crossref.1b37704f26a4dda361973134185b6ac9

[10] S. W. McKeever, "Optically stimulated luminescence dosimetry," *Nuclear Instruments and Methods in Physics Research Section B: Beam Interactions with Materials and Atoms*, vol. 184, no. 1-2, pp. 29–54, Sep. 2001. [Online]. Available: http://linkinghub.elsevier.com/retrieve/pii/S0168583X01005882

[11] LANDAUER, "http://www.landauer.co.uk/."

[12] L. Bø tter Jensen, E. Bulur, A. S. Murray, and N. R. J. Poolton, "Enhancements in luminescence measurement techniques." *Radiation protection dosimetry*, vol. 101, no. 1-4, pp. 119–24, Jan. 2002. [Online]. Available: http://www.ncbi.nlm.nih.gov/pubmed/12382719

[13] D. N. Slatkin, "Microbeam radiation therapy," *Medical Physics*, vol. 19, no. 6, p. 1395, 1992. [Online]. Available: http://scitation.aip.org/content/aapm/journal/medphys/19/6/10.1118/1.596771

[14] H. Blattmann, J. Gebbers, E. Bräuer-Krisch, A. Bravin, G. Le Duc, W. Burkard, M. Di Michiel, V. Djonov, D. N. Slatkin, J. Stepanek, and J. A. Laissure, "Applications of synchrotron X-rays to radiotherapy," *Nuclear Instruments and Methods in Physics Research Section A: Accelerators, Spectrometers, Detectors and Associated Equipment*, vol. 548, no. 1-2, pp. 17–22, Aug. 2005. [Online]. Available: http://linkinghub.elsevier.com/retrieve/pii/S0168900205006418

[15] E. A. Siegbahn, J. Stepanek, E. Bräuer-Krisch, and A. Bravin, "Determination of dosimetrical quantities used in microbeam radiation therapy (MRT) with Monte Carlo simulations," *Medical Physics*, vol. 33, no. 9, p. 3248, 2006. [Online]. Available: http://scitation.aip.org/content/aapm/journal/medphys/33/9/10.1118/1.2229422

[16] Z. Bencokova, J. Balosso, and N. Foray, "Radiobiological features of the anti-cancer strategies involving synchrotron X-rays." *Journal of synchrotron radiation*, vol. 15, no. Pt 1, pp. 74–85, Jan. 2008. [Online]. Available: http://www.ncbi.nlm.nih.gov/pubmed/18097081

[17] M. De Felici, R. Felici, M. S. del Rio, C. Ferrero, T. Bacarian, and F. A. Dilmanian, "Dose distribution from x-ray microbeam arrays applied to radiation therapy: An EGS4 Monte Carlo study," *Medical Physics*, vol. 32, no. 8, p. 2455, 2005. [Online]. Available: http://scitation.aip.org/content/aapm/journal/medphys/32/8/10.1118/1.1951043

[18] J. Stepanek, H. Blattmann, J. A. Laissue, N. Lyubimova, M. Di Michiel, and D. N. Slatkin, "Physics study of microbeam radiation therapy with PSI-version of Monte Carlo code GEANT as a new computational tool," *Medical Physics*, vol. 27, no. 7, p. 1664, 2000. [Online]. Available: http://scitation.aip.org/content/aapm/journal/medphys/27/7/10.1118/1.599034

[19] J. Spiga, E. A. Siegbahn, E. Bräuer-Krisch, P. Randaccio, and A. Bravin, "The GEANT4 toolkit for microdosimetry calculations: Application to microbeam radiation therapy (MRT)," *Medical Physics*, vol. 34, no. 11, p. 4322, 2007. [Online]. Available: http://link.aip.org/link/MPHYA6/v34/i11/p4322/s1&Agg=doi

[20] E. Bräuer-Krisch, H. Requardt, P. Régnard, S. Corde, E. Siegbahn, G. LeDuc, T. Brochard, H. Blattmann, J. Laissue, and A. Bravin, "New

irradiation geometry for microbeam radiation therapy." *Physics in medicine and biology*, vol. 50, no. 13, pp. 3103–11, Jul. 2005. [Online]. Available: http://www.ncbi.nlm.nih.gov/pubmed/15972983

[21] E. Bräuer-Krisch, R. Serduc, E. A. Siegbahn, G. Le Duc, Y. Prezado, A. Bravin, H. Blattmann, and J. A. Laissue, "Effects of pulsed, spatially fractionated, microscopic synchrotron X-ray beams on normal and tumoral brain tissue," *Mutation Research/Reviews in Mutation Research*, vol. 704, no. 1-3, pp. 160–166, 2010. [Online]. Available: http://www.ncbi.nlm.nih.gov/pubmed/20034592

[22] E. Bräuer-Krisch, A. Rosenfeld, M. Lerch, M. Petasecca, M. Akselrod, J. Sykora, J. Bartz, M. Ptaszkiewicz, P. Olko, A. Berg, M. Wieland, S. Doran, T. Brochard, A. Kamlowski, G. Cellere, A. Paccagnella, E. A. Siegbahn, Y. Prezado, I. Martinez-Rovira, A. Bravin, L. Dusseau, P. Berkvens, and K. K. W. Siu, "Potential High Resolution Dosimeters For MRT," in *AIP Conference Proceedings, 6th International Conference on Medical Applications of Synchrotron Radiation*, K. K. W. Siu, Ed., vol. 1266, 2010, pp. 89–97. [Online]. Available: http://link.aip.org/link/APCPCS/v1266/i1/p89/s1&Agg=doihttp://scitation.aip.org/content/aip/proceeding/aipcp/10.1063/1.3478205

[23] A. Rosenfeld, G. Kaplan, T. Kron, B. Allen, A. Dilmanian, I. Orion, B. Ren, M. Lerch, and A. Holmes-Siedle, "MOSFET dosimetry of an X-ray microbeam," *IEEE Transactions on Nuclear Science*, vol. 46, no. 6, pp. 1774–1780, 1999. [Online]. Available: http://ieeexplore.ieee.org/lpdocs/epic03/wrapper.htm?arnumber=819153

[24] E. Bräuer-Krisch, A. Bravin, M. Lerch, A. Rosenfeld, J. Stepanek, M. Di Michiel, and J. A. Laissue, "MOSFET dosimetry for microbeam radiation therapy at the European Synchrotron Radiation Facility," *Medical Physics*, vol. 30, no. 4, p. 583, 2003. [Online]. Available: http://scitation.aip.org/content/aapm/journal/medphys/30/4/10.1118/1.1562169

[25] E. A. Siegbahn, E. Bräuer-Krisch, A. Bravin, H. Nettelbeck, M. L. F. Lerch, and A. B. Rosenfeld, "MOSFET dosimetry with high spatial resolution in intense synchrotron-generated x-ray microbeams," *Medical Physics*, vol. 36, no. 4, p. 1128, 2009. [Online]. Available: http://link.aip.org/link/MPHYA6/v36/i4/p1128/s1&Agg=doi

[26] M. Petasecca, A. Cullen, I. Fuduli, A. Espinoza, C. Porumb, C. Stanton, A. H. Aldosari, E. Bräuer-Krisch, H. Requardt, a. Bravin, V. Perevertaylo, A. B. Rosenfeld, and M. L. F. Lerch, "X-Tream: a novel dosimetry system for Synchrotron Microbeam Radiation Therapy," *Journal of Instrumentation*, vol. 7, no. 07, pp. P07 022–P07 022, Jul. 2012. [Online]. Available: http://stacks.iop.org/1748-0221/7/i=07/a=P07022?key=crossref.8d1255d7745abc72cb917ba74e51af5f

[27] H. Johnston, M. Hilts, J. Carrick, and A. Jirasek, “An x-ray CT polymer gel dosimetry prototype: II. Gel characterization and clinical application.” *Physics in medicine and biology*, vol. 57, no. 10, pp. 3155–75, May 2012. [Online]. Available: http://stacks.iop.org/0031-9155/57/i=10/a=3155

[28] A. Jirasek, J. Carrick, and M. Hilts, “An x-ray CT polymer gel dosimetry prototype: I. Remnant artefact removal.” *Physics in medicine and biology*, vol. 57, no. 10, pp. 3137–53, May 2012. [Online]. Available: http://stacks.iop.org/0031-9155/57/i=10/a=3137

[29] J. Bartz, G. Sykora, E. Bräuer-Krisch, and M. Akselrod, “Imaging and dosimetry of synchrotron microbeam with aluminum oxide fluorescent detectors,” *Radiation Measurements*, vol. 46, no. 12, pp. 1936–1939, Dec. 2011. [Online]. Available: http://linkinghub.elsevier.com/retrieve/pii/S1350448711001193

[30] G. Akselrod, M. Akselrod, E. Benton, and N. Yasuda, “A novel Al_2O_3 fluorescent nuclear track detector for heavy charged particles and neutrons,” *Nuclear Instruments and Methods in Physics Research Section B: Beam Interactions with Materials and Atoms*, vol. 247, no. 2, pp. 295–306, Jun. 2006. [Online]. Available: http://linkinghub.elsevier.com/retrieve/pii/S0168583X06001315

[31] M. Ptaszkiewicz, E. Braurer-Kirsch, M. Klosowski, L. Czopyk, and P. Olko, “TLD dosimetry for microbeam radiation therapy at the European Synchrotron Radiation Facility,” *Radiation Measurements*, vol. 43, no. 2-6, pp. 990–993, Feb. 2008. [Online]. Available: http://linkinghub.elsevier.com/retrieve/pii/S1350448707005896

[32] P. Olko, L. Czopyk, M. Kosowski, and M. P. Waligórski, “Thermoluminescence dosimetry using TL-readers equipped with CCD cameras,” *Radiation Measurements*, vol. 43, no. 2-6, pp. 864–869, Feb. 2008. [Online]. Available: http://linkinghub.elsevier.com/retrieve/pii/S1350448707005641

[33] J. C. Crosbie, I. Svalbe, S. M. Midgley, N. Yagi, P. A. W. Rogers, and R. A. Lewis, “A method of dosimetry for synchrotron microbeam radiation therapy using radiochromic films of different sensitivity.” *Physics in medicine and biology*, vol. 53, no. 23, pp. 6861–77, Dec. 2008. [Online]. Available: http://www.ncbi.nlm.nih.gov/pubmed/19001701

[34] P. J. Muench, A. S. Meigooni, R. Nath, and W. L. McLaughlin, “Photon energy dependence of the sensitivity of radiochromic film and comparison with silver halide film and LiF TLDs used for brachytherapy dosimetry,” *Medical Physics*, vol. 18, no. 4, p. 769, 1991. [Online]. Available: http://scitation.aip.org/content/aapm/journal/medphys/18/4/10.1118/1.596630

[35] S. J. Doran, T. Brochard, J. Adamovics, N. Krstajic, and E. Bräuer-Krisch, “An investigation of the potential of optical computed tomography for

imaging of synchrotron-generated x-rays at high spatial resolution." *Physics in medicine and biology*, vol. 55, no. 5, pp. 1531–47, Mar. 2010. [Online]. Available: http://www.ncbi.nlm.nih.gov/pubmed/20157228

[36] M. Lerch, M. Petasecca, A. Cullen, A. Hamad, H. Requardt, E. Bräuer-Krisch, A. Bravin, V. Perevertaylo, and A. Rosenfeld, "Dosimetry of intensive synchrotron microbeams," *Radiation Measurements*, vol. 46, no. 12, pp. 1560–1565, Dec. 2011. [Online]. Available: http://linkinghub.elsevier.com/retrieve/pii/S1350448711004215

[37] A. Edgar, C. Varoy, C. Koughia, D. Tonchev, G. Belev, G. Okada, S. Kasap, H. von Seggern, and M. Ryan, "Optical properties of divalent samarium-doped fluorochlorozirconate glasses and glass ceramics," *Optical Materials*, vol. 31, no. 10, pp. 1459–1466, Aug. 2009. [Online]. Available: http://dx.doi.org/10.1016/j.optmat.2009.02.003http://linkinghub.elsevier.com/retrieve/pii/S0925346709000445

[38] Q. Luo, X. Qiao, X. Fan, S. Liu, H. Yang, and X. Zhang, "Reduction and luminescence of europium ions in glass ceramics containing SrF_2 nanocrystals," *Journal of Non-Crystalline Solids*, vol. 354, no. 40-41, pp. 4691–4694, Oct. 2008. [Online]. Available: http://linkinghub.elsevier.com/retrieve/pii/S0022309308005498

[39] B. H. Babu and V. V. Ravi Kanth Kumar, "Fluorescence properties and electron paramagnetic resonance studies of γ-irradiated Sm^{3+}-doped oxyfluoroborate glasses," *Journal of Applied Physics*, vol. 112, no. 9, p. 093516, 2012. [Online]. Available: http://link.aip.org/link/JAPIAU/v112/i9/p093516/s1&Agg=doi

[40] J. Qiu and K. Hirao, "γ-ray induced reduction of Sm^{3+} to Sm^{2+} in sodium aluminoborate glasses," *Journal of Materials Science Letters*, vol. 20, no. 8, pp. 691–693, 2001.

[41] E. Malchukova, B. Boizot, G. Petite, and D. Ghaleb, "Oxidation of Sm^{2+} in β-irradiated Sm-doped borosilicate glasses under laser illumination," *Journal of Luminescence*, vol. 111, no. 1-2, pp. 53–59, Jan. 2005. [Online]. Available: http://linkinghub.elsevier.com/retrieve/pii/S0022231304002224

[42] S. Fan, C. Yu, D. He, X. Wang, and L. Hu, "Tunable white light emission from γ-irradiated Ag/Eu co-doped phosphate glass phosphor," *Optical Materials Express*, vol. 2, no. 6, p. 765, May 2012. [Online]. Available: http://www.opticsinfobase.org/abstract.cfm?URI=ome-2-6-765

[43] Y. Shimizugawa, N. Umesaki, K. Hanada, I. Sakai, and J. Qiu, "X-ray induced reduction of rare earth ion doped in Na_2O-Al_2O_3-B_2O_3 glasses," *Journal of Synchrotron Radiation*, vol. 8, no. 2, pp. 797–799, Mar. 2001. [Online]. Available: http://scripts.iucr.org/cgi-bin/paper?S0909049500020598

[44] M. Nogami and K. Suzuki, "Formation of Sm^{2+} Ions and Spectral Hole Burning in X-ray Irradiated Glasses," *Society*, vol. 106, no. May, pp. 5395–5399, 2002.

[45] Y. Huang, C. Jiang, K. Jang, H. S. Lee, E. Cho, M. Jayasimhadri, and S.-s. Yi, "Luminescence and microstructure of Sm^{2+} ions reduced by x-ray irradiation in $Li_2OSrOB_2O_3$ glass," *Journal of Applied Physics*, vol. 103, no. 11, p. 113519, 2008.

[46] Y. Li, Y. Huang, and C. Jiang, "The dependence of luminescence on reduction of Sm^{2+} ions doped in lithium barium borate glasses," *Applied Physics*, pp. 663–669, 2009.

[47] Y. Li, J. Wang, Y. Huang, and H. J. Seo, "Temperature-Dependent $^5D_0 \rightarrow {}^7F_0$ Luminescence of Sm^{2+} Ions Doped in Alkaline Earth Borophosphate Glass," *Journal of the American Ceramic Society*, vol. 93, no. 3, pp. 722–726, Mar. 2010. [Online]. Available: http://doi.wiley.com/10.1111/j.1551-2916.2009.03513.x

[48] J. Wang, Y. Huang, Y. Li, and H. J. Seo, "The Reduction and Luminescence Characteristics of Sm^{2+} Doped in $Ba_3BP_3O_{12}$ Crystal," *Journal of the American Ceramic Society*, vol. 94, no. 5, pp. 1454–1459, May 2011. [Online]. Available: http://doi.wiley.com/10.1111/j.1551-2916.2010.04250.x

[49] E. Malchukova, B. Boizot, D. Ghaleb, and G. Petite, "β-Irradiation effects in Gd-doped borosilicate glasses studied by EPR and Raman spectroscopies," *Journal of Non-Crystalline Solids*, vol. 352, no. 4, pp. 297–303, Apr. 2006. [Online]. Available: http://linkinghub.elsevier.com/retrieve/pii/S0022309305007672

[50] E. Malchukova, B. Boizot, G. Petite, and D. Ghaleb, "Optical properties and valence state of Sm ions in aluminoborosilicate glass under β-irradiation," *Journal of Non-Crystalline Solids*, vol. 353, no. 24-25, pp. 2397–2402, Jul. 2007. [Online]. Available: http://linkinghub.elsevier.com/retrieve/pii/S0022309307003961

[51] J. Qiu, K. Miura, T. Suzuki, T. Mitsuyu, and K. Hirao, "Permanent photoreduction of Sm^{3+} to Sm^{2+} inside a sodium aluminoborate glass by an infrared femtosecond pulsed laser," *Applied Physics Letters*, vol. 74, no. 1, p. 10, 1999. [Online]. Available: http://scitation.aip.org/content/aip/journal/apl/74/1/10.1063/1.123117

[52] K. Miura, J. Qiu, S. Fujiwara, S. Sakaguchi, and K. Hirao, "Three-dimensional optical memory with rewriteable and ultrahigh density using the valence-state change of samarium ions," *Applied Physics Letters*, vol. 80, no. 13, p. 2263, 2002. [Online]. Available: http://link.aip.org/link/APPLAB/v80/i13/p2263/s1&Agg=doi

[53] G. J. Park, T. Hayakawa, and M. Nogami, "Formation of Sm^{2+} ions in femtosecond laser excited Al_2O_3-SiO_2 glasses," *Journal of Physics: Condensed Matter*, vol. 15, no. 8, pp. 1259–1265, Mar. 2003. [Online]. Available: http://stacks.iop.org/0953-8984/15/i=8/a=310?key=crossref.12cf8b1e41a53289cdc6ab4723174c7f

[54] M. Nogami, G. Kawamura, G. J. Park, and H. You, "Effect of Al^{3+} and Ti^{4+} ions on the laser reduction of Sm^{3+} ion in glass," *Journal of Luminescence*, vol. 114, pp. 178–186, 2005.

[55] P. Dorenbos, "Systematic behaviour in trivalent lanthanide charge transfer energies," *Journal of Physics: Condensed Matter*, vol. 15, no. 49, pp. 8417–8434, Dec. 2003. [Online]. Available: http://stacks.iop.org/0953-8984/15/i=49/a=018?key=crossref.784ef865e66765618c346caee936a909

[56] G. Blasse and B. C. Grabmaier, *Luminescent Materials.* Berlin, Heidelberg: Springer Berlin Heidelberg, 1994. [Online]. Available: http://link.springer.com/10.1007/978-3-642-79017-1

[57] A. V. Sidorenko, P. Dorenbos, A. J. J. Bos, C. W. E. V. Eijk, and P. A. Rodnyi, "Lanthanide level location and charge carrier trapping in $LiLnSiO_4$:Ce^{3+} ,Sm^{3+}, Ln = Y or Lu," *Journal of Physics: Condensed Matter*, vol. 18, no. 19, pp. 4503–4514, May 2006. [Online]. Available: http://stacks.iop.org/0953-8984/18/i=19/a=006?key=crossref.7368381af024b8962bea2f522ced8a6b

[58] D. Ehrt, T. Kittel, M. Will, S. Nolte, and A. Tünnermann, "Femtosecond-laser-writing in various glasses," *Journal of Non-Crystalline Solids*, vol. 345-346, pp. 332–337, Oct. 2004. [Online]. Available: http://linkinghub.elsevier.com/retrieve/pii/S0022309304005757

[59] J. Merz and P. Pershan, "Charge Conversion of Irradiated Rare-Earth Ions in Calcium Fluoride. I," *Physical Review*, vol. 162, no. 2, pp. 217–235, Oct. 1967. [Online]. Available: http://link.aps.org/doi/10.1103/PhysRev.162.217

[60] N. M. Winch and A. Edgar, "Transparent caesium bromide storage-phosphors for radiation imaging," *Physica Status Solidi (a)*, vol. 209, no. 12, pp. 2427–2432, Dec. 2012. [Online]. Available: http://doi.wiley.com/10.1002/pssa.201200359

[61] A. W. Bett, S. P. Philipps, S. Essig, S. Heckelmann, R. Kellenbenz, V. Klinger, M. Niemeyer, D. Lackner, and F. Dimroth, "OVERVIEW ABOUT TECHNOLOGY PERSPECTIVES FOR HIGH EFFICIENCY SOLAR CELLS FOR SPACE AND TERRESTRIAL APPLICATIONS," *Proceedings of the 28th Europian Photovoltaic Solar Energy Conference and Exhibition*, 2013.

[62] N. Kotera, S. Eguchi, J. Miyahara, S. Matsumoto, and H. Kato, "Method and apparatus for recording and reproducing a radiation image," p. U.S. Patent 4236078, 1980.

[63] M. Sonoda, M. Takano, J. Miyahara, and H. Kato, "Computed radiography utilizing scanning laser stimulated luminescence." *Radiology*, vol. 148, no. 3, pp. 833–8, Sep. 1983. [Online]. Available: http://pubs.rsna.org/doi/abs/10.1148/radiology.148.3.6878707http://www.ncbi.nlm.nih.gov/pubmed/6878707

[64] H. Nanto, A. Nishimura, M. Kuroda, Y. Takei, Y. Nakano, T. Shoji, T. Yanagita, and S. Kasai, "X-ray imaging plate using CsBr:Eu phosphors for computed radiography," *Nuclear Instruments and Methods in Physics Research Section A: Accelerators, Spectrometers, Detectors and Associated Equipment*, vol. 580, no. 1, pp. 278–281, Sep. 2007. [Online]. Available: http://linkinghub.elsevier.com/retrieve/pii/S0168900207010224

[65] S. Kasap, J. B. Frey, G. Belev, O. Tousignant, H. Mani, J. Greenspan, L. Laperriere, O. Bubon, A. Reznik, G. DeCrescenzo, K. S. Karim, and J. A. Rowlands, "Amorphous and polycrystalline photoconductors for direct conversion flat panel x-ray image sensors." *Sensors (Basel, Switzerland)*, vol. 11, no. 5, pp. 5112–57, Jan. 2011. [Online]. Available: http://www.pubmedcentral.nih.gov/articlerender.fcgi?artid=3231396&tool=pmcentrez&rendertype=abstract

[66] C. Koughia, G. Belev, G. Soundararajan, G. Okada, D. Tonchev, A. Edgar, C. R. Varoy, H. V. Seggern, and S. Kasap, "Trivalent Er and Sm ions in fluorochlorozirconate glasses: optical properties and X-ray luminescence," *October*, vol. 4, pp. 1–4, 2011.

[67] A. Edgar, "Photostimulated luminescence in a rare earth-doped fluorobromozirconate glass ceramic," *Applied Physics Letters*, vol. 75, no. 16, pp. 2386–2388, 1999.

[68] A. Edgar, M. Secu, G. V. M. Williams, S. Schweizer, and J.-M. Spaeth, "Structural phase changes in barium bromide nano-crystals in a fluorobromozirconate glass-ceramic x-ray storage phosphor," *Journal of Physics: Condensed Matter*, vol. 13, no. 28, pp. 6259–6269, Jul. 2001. [Online]. Available: http://stacks.iop.org/0953-8984/13/i=28/a=308?key=crossref.60d55c8b5d808412055b755e196324a1

[69] S. Schweizer, L. W. Hobbs, A. Edgar, and G. V. M. Williams, "Photostimulated luminescence in Eu-doped fluorochlorozirconate glass ceramics," *Applied Physics Letters*, vol. 83, no. 3, pp. 449–451, 2003.

[70] M. Secu, S. Schweizer, J.-m. Spaeth, A. Edgar, G. V. M. Williams, and U. Rieser, "Photostimulated luminescence from a fluorobromozirconate glass-ceramic and the effect of crystallite size and phase," *Journal of Physics: Condensed Matter*, vol. 15, no. 7, pp. 1097–1108, Feb. 2003. [Online]. Available: http://stacks.iop.org/0953-8984/15/i=7/a=307?key=crossref.938744bf14eff4fb423743349ac6f0d8

[71] A. Edgar, G. V. M. Williams, M. Secu, S. Schweizer, and J. Spaeth, "Optical properties of a high-efficiency glass ceramic X-ray storage phosphor," *Radiation Measurements*, vol. 38, pp. 413–416, 2004.

[72] S. Schweizer, L. W. Hobbs, A. Edgar, G. V. M. Williams, and J. Hamlin, "Photostimulated luminescence from fluorochlorozirconate glass ceramics and the effect of crystallite size," pp. 1–8, 2005.

[73] G. Chen, "Fluorozirconate-based nanophase glass ceramics for high-resolution medical X-ray imaging," *Journal of Non-Crystalline Solids*, vol. 352, pp. 610–614, 2006.

[74] Y. Kishi, S. Tanabe, S. Tochino, and G. Pezzotti, "Fabrication and Efficient Infrared-to-Visible Upconversion in Transparent Glass Ceramics of Er-Yb Co-Doped CaF_2 Nano-Crystals," *Journal of the American Ceramic Society*, vol. 88, no. 12, pp. 3423–3426, Dec. 2005. [Online]. Available: http://doi.wiley.com/10.1111/j.1551-2916.2005.00614.x

[75] Y. Kishi and S. Tanabe, "Infrared-to-visible upconversion of rare-earth doped glass ceramics containing CaF_2 crystals," *Journal of Alloys and Compounds*, vol. 408-412, pp. 842–844, Feb. 2006. [Online]. Available: http://linkinghub.elsevier.com/retrieve/pii/S0925838805006146

[76] J. Ueda and S. Tanabe, "Visible to near infrared conversion in $Ce^{3+}Yb^{3+}$ Co-doped YAG ceramics," *Journal of Applied Physics*, vol. 106, no. 4, p. 043101, 2009. [Online]. Available: http://link.aip.org/link/JAPIAU/v106/i4/p043101/s1&Agg=doi

[77] A. Edgar, "Optical properties of glasses," in *Optical Properties of Condensed Matter and Applications*, J. Singh, Ed. England: John Wiley & Sons Ltd., 2006.

[78] A. Edgar and G. V. M. Williams, "Spatial resolution of a glass-ceramic X-ray storage phosphor," *Current Applied Physics*, vol. 6, pp. 399–402, 2006.

[79] J. R. O'Connor and H. A. Bostick, "Radiation Effects in CaF_2:Sm," *Journal of Applied Physics*, vol. 33, no. 5, p. 1868, 1962. [Online]. Available: http://scitation.aip.org/content/aip/journal/jap/33/5/10.1063/1.1728848

[80] R. L. Calvert and R. J. Danby, "Thermoluminescence and radiophotoluminescence from Eu-and Sm-doped $CaSO_4$," *Physica Status Solidi (a)*, vol. 83, no. 2, pp. 597–604, Jun. 1984. [Online]. Available: http://doi.wiley.com/10.1002/pssa.2210830222

[81] Y. Huang, K. Jang, W. Zhao, E. Cho, H. S. Lee, X. Wang, D. Qin, Y. Zhang, C. Jiang, and H. J. Seo, "Irradiation-induced reduction and luminescence properties of Sm^{2+} doped in $BaBPO_5$," *Journal of Solid State Chemistry*, vol. 180, no. 12, pp. 3325–3332, Dec. 2007. [Online]. Available: http://linkinghub.elsevier.com/retrieve/pii/S0022459607003970

[82] Z. Liu, M. Stevens-Kalceff, and H. Riesen, "Photoluminescence and Cathodoluminescence Properties of Nanocrystalline BaFCl:Sm^{3+} X-ray Storage Phosphor," *The Journal of Physical Chemistry C*, vol. 116, no. 14, pp. 8322–8331, Apr. 2012. [Online]. Available: http://pubs.acs.org/doi/abs/10.1021/jp301338b

[83] K. Jang, I. Kim, S. Park, Y. Huang, H. J. Seo, and C. Kim, "Reduction effect on the optical properties of Sm^{2+} doped in SrB_4O_7 and SrB_6O_{10} crystals," *Journal of Physics and Chemistry of Solids*, vol. 67, no. 11, pp. 2316–2321, Nov. 2006. [Online]. Available: http://linkinghub.elsevier.com/retrieve/pii/S0022369706003179

[84] S. Park, Y. Chung, K. Jang, H.-G. Liu, Y.-I. Lee, and C. Kim, "Influence of Sm^{3+}-Ions on the Hole-Burning Efficiency of Sm^{2+}-Ions Doped in $Mg_{0.5}Sr_{0.5}FCl_{0.5}Br_{0.5}$ Mixed Crystals," *Japanese Journal of Applied Physics*, vol. 43, no. 12, pp. 8103–8106, Dec. 2004. [Online]. Available: http://jjap.jsap.jp/link?JJAP/43/8103/

[85] J. Wang, Y. Li, Y. Huang, L. Shi, and H. J. Seo, "The luminescence and stabilities of Sm^{2+} ions doped in $LiBaB_9O_{15}$," *Materials Chemistry and Physics*, vol. 120, no. 2-3, pp. 598–602, Apr. 2010. [Online]. Available: http://linkinghub.elsevier.com/retrieve/pii/S025405840900755X

[86] Y. Huang, J. Wang, and H. J. Seo, "The Irradiation Induced Valence Changes and the Luminescence Properties of Samarium Ions in Ba_2SiO_2," *Journal of The Electrochemical Society*, vol. 157, no. 12, p. J429, 2010. [Online]. Available: http://jes.ecsdl.org/cgi/doi/10.1149/1.3497357

[87] D. Chen, H. Miyoshi, T. Akai, and T. Yazawa, "Colorless transparent fluorescence material: Sintered porous glass containing rare-earth and transition-metal ions," *Applied Physics Letters*, vol. 86, no. 23, p. 231908, 2005. [Online]. Available: http://link.aip.org/link/APPLAB/v86/i23/p231908/s1&Agg=doi

[88] A. Edgar, C. Varoy, C. Koughia, G. Okada, G. Belev, and S. Kasap, "High-resolution X-ray imaging with samarium-doped fluoroaluminate and fluorophosphate glass," *Journal of Non-Crystalline Solids*, vol. 377, pp. 124–128, Jan. 2013. [Online]. Available: http://linkinghub.elsevier.com/retrieve/pii/S0022309312007375

[89] L. C. Dixie, A. Edgar, and M. F. Reid, "Sm^{2+} fluorescence and absorption in cubic BaCl2: Strong thermal crossover of fluorescence between $4f^6$ and $4f^5 5d^1$ configurations," *Journal of Luminescence*, vol. 132, no. 10, pp. 2775–2782, Oct. 2012. [Online]. Available: http://linkinghub.elsevier.com/retrieve/pii/S0022231312003080

[90] L. Dixie, A. Edgar, and M. Bartle, "Energy resolved imaging with a stratified phosphor detector," *Radiation Measurements*, vol. 3, pp. 1–5,

Feb. 2013. [Online]. Available: http://linkinghub.elsevier.com/retrieve/pii/S1350448713000553

[91] U. Caldiño, A. Speghini, S. Berneschi, M. Bettinelli, M. Brenci, S. Pelli, and G. Righini, "Optical spectroscopy and waveguide fabrication in Sm^{3+}/Tb^{3+} doped zincsodiumaluminosilicate glasses," *Optical Materials*, vol. 34, no. 7, pp. 1067–1071, May 2012. [Online]. Available: http://linkinghub.elsevier.com/retrieve/pii/S0925346712000110

[92] X. Liu, B. Chen, E. Pun, and H. Lin, "Eu^{3+} and Sm^{3+} co-activated aluminum germanate glass channel waveguide as irradiation source for photodynamic therapy," *Journal of Luminescence*, vol. 137, pp. 77–82, May 2013. [Online]. Available: http://linkinghub.elsevier.com/retrieve/pii/S0022231312007521

[93] K. Hirao, S. Todoroki, D. H. Cho, and N. Soga, "Room-temperature persistent hole burning of Sm^{2+} in oxide glasses," *Optics Letters*, vol. 18, no. 19, pp. 1586–1587, Oct. 1993. [Online]. Available: http://www.ncbi.nlm.nih.gov/pubmed/19823453http://www.opticsinfobase.org/abstract.cfm?URI=ol-18-19-1586

[94] D.-h. Cho, K. Hirao, K. Fujita, and N. Soga, "Photochemical Hole Burning and Local Structural Change in Sm^{2+}-Doped Borate Glasses," *Journal of the American Ceramic Society*, vol. 79, no. 2, pp. 327–332, Feb. 1996. [Online]. Available: http://doi.wiley.com/10.1111/j.1151-2916.1996.tb08124.x

[95] D. Wei, B. Yuan, Y. Huang, T. Tsuboi, and H. J. Seo, "Influence of Crystallization on the Conversion of $Sm^{3+}Sm^{2+}$ in SrO-Bi_2O_3-K_2O-B_2O_3 Glass-Ceramics," *Journal of the American Ceramic Society*, vol. 96, no. 7, pp. 2167–2171, Jul. 2013. [Online]. Available: http://doi.wiley.com/10.1111/jace.12230

[96] Q. Jing, Q. Wu, L. Liu, J.-a. Xu, Y. Bi, Y. Liu, H. Chen, S. Liu, Y. Zhang, L. Xiong, Y. Li, and J. Liu, "An experimental study on SrB_4O_7:Sm^{2+} as a pressure sensor," *Journal of Applied Physics*, vol. 113, no. 2, p. 023507, 2013. [Online]. Available: http://link.aip.org/link/JAPIAU/v113/i2/p023507/s1&Agg=doi

[97] Q. Wei, N. Dubrovinskaia, and L. Dubrovinsky, "Ruby and Sm:YAG fluorescence pressure gauges up to 120 GPa and 700 K," *Journal of Applied Physics*, vol. 110, no. 4, p. 043513, 2011. [Online]. Available: http://link.aip.org/link/JAPIAU/v110/i4/p043513/s1&Agg=doi

[98] H.-Y. Lin, Y.-C. Fang, and S.-Y. Chu, "Energy Transfer $Sm^{3+} \rightarrow Eu^{3+}$ in Potential Red Phosphor $(Ca, Ba)_3(VO_4)_2$:Sm^{3+}, Eu^{3+} for Use in Organic Solar Cells and White Light-Emitting Diodes," *Journal of the American Ceramic Society*, vol. 93, no. 11, pp. 3850–3856, Nov. 2010. [Online]. Available: http://doi.wiley.com/10.1111/j.1551-2916.2010.03957.x

[99] M. S. Kim, L. Krishna Bharat, and J. S. Yu, "White light emission characteristics of Tb^{3+} and Sm^{3+} co-doped $CaYAlO_4$ nanocrystalline phosphors for solid-state lighting," *Journal of Luminescence*, vol. 142, pp. 92–95, Oct. 2013. [Online]. Available: http://linkinghub.elsevier.com/retrieve/pii/S0022231313001841

[100] A. Dhobale, M. Mohapatra, V. Natarajan, and S. Godbole, "Synthesis and photoluminescence investigations of the white light emitting phosphor, vanadate garnet, $Ca_2NaMg_2V_3O_{12}$ co-doped with Dy and Sm," *Journal of Luminescence*, vol. 132, no. 2, pp. 293–298, Feb. 2012. [Online]. Available: http://linkinghub.elsevier.com/retrieve/pii/S0022231311004984

[101] L. Li, Y. Yang, D. Zhou, Z. Yang, X. Xu, and J. Qiu, "Investigation of the role of silver species on spectroscopic features of Sm^{3+}-activated sodiumaluminosilicate glasses via Ag^+-Na^+ ion exchange," *Journal of Applied Physics*, vol. 113, no. 19, p. 193103, 2013. [Online]. Available: http://link.aip.org/link/JAPIAU/v113/i19/p193103/s1&Agg=doi

[102] Q. Li, J. Lin, J. Wu, Z. Lan, Y. Wang, F. Peng, and M. Huang, "Improving photovoltaic performance of dye-sensitized solar cell by downshift luminescence and p-doping effect of Gd_2O_3:Sm^{3+}," *Journal of Luminescence*, vol. 134, pp. 59–62, Feb. 2013. [Online]. Available: http://linkinghub.elsevier.com/retrieve/pii/S0022231312005558

[103] X. Y. Huang, J. X. Wang, D. C. Yu, S. Ye, Q. Y. Zhang, and X. W. Sun, "Spectral conversion for solar cell efficiency enhancement using YVO_4:Bi^{3+},Ln^{3+} (Ln = Dy, Er, Ho, Eu, Sm, and Yb) phosphors," *Journal of Applied Physics*, vol. 109, no. 11, p. 113526, 2011. [Online]. Available: http://link.aip.org/link/JAPIAU/v109/i11/p113526/s1&Agg=doi

[104] D.-h. Cho, K. Hirao, N. Soga, and M. Nogami, "Photochemical hole burning in Sm^{2+}-doped aluminosilicate and borosilicate glasses," *Journal of Non-Crystalline Solids*, vol. 215, no. 2-3, pp. 192–200, Jul. 1997. [Online]. Available: http://linkinghub.elsevier.com/retrieve/pii/S0022309396005959

[105] G. Kawamura, T. Hayakawa, and M. Nogami, "Effect of counter ions on the reduction process of Sm^{3+} ions in $TiO_2ZrO_2Al_2O_3SiO_2$ glasses," *Journal of Alloys and Compounds*, vol. 408-412, pp. 845–847, Feb. 2006. [Online]. Available: http://linkinghub.elsevier.com/retrieve/pii/S0925838805006079

[106] Y. Shimizugawa, N. Sawaguchi, K. Kawamura, and K. Hirao, "X-ray absorption fine structure of samarium-doped borate glasses," *Journal of Applied Physics*, vol. 81, no. 10, p. 6657, 1997. [Online]. Available: http://scitation.aip.org/content/aip/journal/jap/81/10/10.1063/1.365205

[107] D. Cho, K. Hirao, and N. Soga, "Persistent spectral hole burning of Sm^{2+} in borate glasses," *Journal of Non-Crystalline Solids*, vol. 189, no.

1-2, pp. 181–190, Aug. 1995. [Online]. Available: http://www.ncbi.nlm.nih.gov/pubmed/21548614http://www.ncbi.nlm.nih.gov/pubmed/20201534http://linkinghub.elsevier.com/retrieve/pii/0022309395002359

[108] J. Qiu, K. Nouchi, K. Miura, T. Mitsuyu, and K. Hirao, "Room-temperature persistent spectral hole burning of x-ray-irradiated Sm^{3+}-doped glass," *Journal of Physics: Condensed Matter*, vol. 12, no. 23, pp. 5061–5067, Jun. 2000. [Online]. Available: http://stacks.iop.org/0953-8984/12/i=23/a=314?key=crossref.b36346a86c96ec249ea749e00b94b888

[109] M. Minsky, "Microscopy Apparatus," p. 3013467, 1957.

[110] P. M. Conn, *Techniques in Confocal Microscopy.* Elsevier, 2010.

[111] S. O. Kasap, *Optoelectronics and Photonics: Principles and Practices (2nd Edition) Chapter 1.* Prentice Hall, 2012.

[112] SIEMENS, "Simulation of X-ray Spectra." [Online]. Available: https://w9.siemens.com/cms/oemproducts/home/x-raytoolbox/spektrum/pages/default.aspx

[113] J. M. Boone and J. A. Seibert, "An accurate method for computer-generating tungsten anode x-ray spectra from 30 to 140 kV," *Medical Physics*, vol. 24, no. 11, pp. 1661–1670, Nov. 1997. [Online]. Available: http://scitation.aip.org/content/aapm/journal/medphys/24/11/10.1118/1.597953

[114] J. M. Boone, T. R. Fewell, and R. J. Jennings, "Molybdenum, rhodium, and tungsten anode spectral models using interpolating polynomials with application to mammography," *Medical Physics*, vol. 24, no. 12, p. 1863, 1997. [Online]. Available: http://scitation.aip.org/content/aapm/journal/medphys/24/12/10.1118/1.598100

[115] J. M. Boone, "Spectral modeling and compilation of quantum fluence in radiography and mammography," in *Proceedings of the SPIE*, J. T. Dobbins III and J. M. Boone, Eds., vol. 3336, Jul. 1998, pp. 592–601. [Online]. Available: http://proceedings.spiedigitallibrary.org/proceeding.aspx?articleid=942360

[116] D. Anderson, B. Warkentin, E. A. Siegbahn, and B. G. Fallone, "Ionization Chamber Measurements in a Small, Non-Uniform Beam - Applications for Synchrotron Beam Dosimetry," *Medical Physics*, vol. 38, p. 3559, 2011.

[117] N. Nariyama, N. Kishi, and S. Ohnishi, "Development of a portable free-air ionization chamber as an absolute intensity monitor for high-energy synchrotron radiation up to 150keV," *Nuclear Instruments and Methods in Physics Research Section A: Accelerators, Spectrometers, Detectors and Associated Equipment*, vol. 524, no. 1-3, pp. 324–331, May 2004. [Online]. Available: http://linkinghub.elsevier.com/retrieve/pii/S0168900204001329

[118] N. Nariyama, T. Ohigashi, K. Umetani, K. Shinohara, H. Tanaka, A. Maruhashi, G. Kashino, A. Kurihara, T. Kondob, M. Fukumoto, and K. Ono, "Spectromicroscopic film dosimetry for high-energy microbeam from synchrotron radiation." *Applied radiation and isotopes : including data, instrumentation and methods for use in agriculture, industry and medicine*, vol. 67, no. 1, pp. 155–9, Jan. 2009. [Online]. Available: http://www.ncbi.nlm.nih.gov/pubmed/18789708

[119] E. Bräuer-Krisch, H. Requardt, T. Brochard, G. Berruyer, M. Renier, J. A. Laissue, and A. Bravin, "New technology enables high precision multislit collimators for microbeam radiation therapy." *The Review of scientific instruments*, vol. 80, no. 7, p. 074301, Jul. 2009. [Online]. Available: http://www.ncbi.nlm.nih.gov/pubmed/19655968

[120] X. Qiao, X. Fan, J. Wang, and M. Wang, "Luminescence behavior of Er^{3+} ions in glass ceramics containing CaF_2 nanocrystals," *Journal of Non-Crystalline Solids*, vol. 351, pp. 357–363, 2005.

[121] Y. Huang, W. Zhao, L. Shi, and H. J. Seo, "Structural defects and luminescence properties of Sm^{2+} ions doped in $BaBPO_5$ phosphor by X-ray irradiation," *Journal of Alloys and Compounds*, vol. 477, no. 1-2, pp. 936–940, May 2009. [Online]. Available: http://linkinghub.elsevier.com/retrieve/pii/S0925838808019993

[122] G. Belev, G. Okada, D. Tonchev, C. Koughia, C. Varoy, A. Edgar, T. Wysokinski, D. Chapman, and S. Kasap, "Valency conversion of samarium ions under high dose synchrotron generated X-ray radiation," *Physica Status Solidi (C)*, vol. 8, no. 9, pp. 2822–2825, Sep. 2011. [Online]. Available: http://doi.wiley.com/10.1002/pssc.201084103

[123] G. Okada, B. Morrell, C. Koughia, A. Edgar, C. Varoy, G. Belev, T. Wysokinski, D. Chapman, and S. Kasap, "Spatially resolved measurement of high doses in microbeam radiation therapy using samarium doped fluorophosphate glasses," *Applied Physics Letters*, vol. 99, no. 12, p. 121105, 2011. [Online]. Available: http://link.aip.org/link/APPLAB/v99/i12/p121105/s1&Agg=doi

[124] H. Nettelbeck, G. J. Takacs, M. L. F. Lerch, and A. B. Rosenfeld, "Microbeam radiation therapy: A Monte Carlo study of the influence of the source, multislit collimator, and beam divergence on microbeams," *Medical Physics*, vol. 36, no. 2, p. 447, 2009. [Online]. Available: http://link.aip.org/link/MPHYA6/v36/i2/p447/s1&Agg=doi

[125] P. Ebeling, D. Ehrt, and M. Friedrich, "X-ray induced effects in phosphate glasses," *Optical Materials*, vol. 20, no. 2, pp. 101–111, Sep. 2002. [Online]. Available: http://linkinghub.elsevier.com/retrieve/pii/S0925346702000526

[126] D. L. Griscom, "Defect centers in heavy-metal fluoride glasses: a review," *Journal of Non-Crystalline Solids*, vol. 161, no. 2, pp. 45–51, Aug. 1993. [Online]. Available: http://linkinghub.elsevier.com/retrieve/pii/002230939390667M

[127] S. Vahedi, G. Okada, B. Morrell, E. Muzar, C. Koughia, A. Edgar, C. Varoy, G. Belev, T. Wysokinski, D. Chapman, and S. Kasap, "X-ray induced Sm^{3+} to Sm^{2+} conversion in fluorophosphate and fluoroaluminate glasses for the monitoring of high-doses in microbeam radiation therapy," *Journal of Applied Physics*, vol. 112, no. 7, p. 073108, 2012. [Online]. Available: http://link.aip.org/link/JAPIAU/v112/i7/p073108/s1&Agg=doi

[128] B. Morrell, G. Okada, S. Vahedi, C. Koughia, A. Edgar, C. Varoy, G. Belev, T. Wysokinski, D. Chapman, R. Sammynaiken, and S. O. Kasap, "Optically erasable samarium-doped fluorophosphate glasses for high-dose measurements in microbeam radiation therapy," *Journal of Applied Physics*, vol. 115, no. 6, p. 063107, Feb. 2014. [Online]. Available: http://scitation.aip.org/content/aip/journal/jap/115/6/10.1063/1.4864424

[129] G. Okada, S. Vahedi, B. Morrell, C. Koughia, G. Belev, T. Wysokinski, D. Chapman, C. Varoy, A. Edgar, and S. Kasap, "Examination of the dynamic range of Sm-doped glasses for high-dose and high-resolution dosimetric applications in microbeam radiation therapy at the Canadian synchrotron," *Optical Materials*, vol. 35, pp. 1976–1980, 2013. [Online]. Available: http://linkinghub.elsevier.com/retrieve/pii/S0925346712004818

[130] D. S. McClure and Z. Kiss, "Survey of the Spectra of the Divalent Rare-Earth Ions in Cubic Crystals," *The Journal of Chemical Physics*, vol. 39, no. 12, pp. 3251–3257, 1963. [Online]. Available: http://link.aip.org/link/JCPSA6/v39/i12/p3251/s1&Agg=doi

[131] Z. J. Kiss and P. N. Yocom, "Stable Divalent Rare-Earth-Alkaline-Earth Halide Systems," *The Journal of Chemical Physics*, vol. 41, no. 5, pp. 1511–1512, 1964. [Online]. Available: http://link.aip.org/link/JCPSA6/v41/i5/p1511/s1&Agg=doi

[132] J. Merz and P. Pershan, "Charge Conversion of Irradiated Rare-Earth Ions in CaF_2. II. Thermoluminescent Spectra," *Physical Review*, vol. 162, no. 2, pp. 235–247, Oct. 1967. [Online]. Available: http://onlinelibrary.wiley.com/doi/10.1002/cbdv.200490137/abstracthttp://link.aps.org/doi/10.1103/PhysRev.162.235

[133] P. Mikhail, K. Ramseyer, G. Frei, F. Budde, and J. Hulliger, "Bleaching of Sm^{2+} during photoluminescence and cathodoluminescence," *Optics Communications*, vol. 188, no. 1-4, pp. 111–117, Feb. 2001. [Online]. Available: http://linkinghub.elsevier.com/retrieve/pii/S003040180001141X

[134] S. A. Payne and L. L. Chase, "$Sm^{2+} \rightarrow Nd^{3+}$ energy transfer in CaF_2," *Journal of the Optical Society of America B*, vol. 3, no. 9, p. 1181, Sep. 1986. [Online]. Available: http://www.opticsinfobase.org/abstract.cfm?URI=josab-3-9-1181

[135] L. L. Chase, S. A. Payne, and G. D. Wilke, "Optical properties and nonradiative decay of Sm^{2+} in CaF_2-YF_3 and CaF_2 -LaF_3 mixed crystals," *Journal of Physics C: Solid State Physics*, vol. 20, no. 7, pp. 953–965, Mar. 1987. [Online]. Available: http://stacks.iop.org/0022-3719/20/i=7/a=010?key=crossref.54d25b0cb0d9c84c5313d59f3508bb6a

[136] S. Ye, B. Zhu, J. Chen, J. Luo, and J. R. Qiu, "Infrared quantum cutting in Tb^{3+}, Yb^{3+} codoped transparent glass ceramics containing CaF_2 nanocrystals," *Applied Physics Letters*, vol. 92, no. 14, p. 141112, 2008. [Online]. Available: http://link.aip.org/link/APPLAB/v92/i14/p141112/s1&Agg=doi

[137] G. Lakshminarayana, R. Yang, M. Mao, J. Qiu, and I. Kityk, "Photoluminescence of Sm^{3+}, Dy^{3+}, and Tm^{3+}-doped transparent glass ceramics containing CaF_2 nanocrystals," *Journal of Non-Crystalline Solids*, vol. 355, no. 52-54, pp. 2668–2673, Dec. 2009. [Online]. Available: http://linkinghub.elsevier.com/retrieve/pii/S0022309309005936

[138] G. Aldica and M. Secu, "Investigations of the non-isothermal crystallization of CaF_2 nanoparticles in Sm-doped oxy-fluoride glasses," *Journal of Non-Crystalline Solids*, vol. 356, no. 33-34, pp. 1631–1636, Jul. 2010. [Online]. Available: http://linkinghub.elsevier.com/retrieve/pii/S0022309310003492

[139] M. Secu, "Nanoparticles size effects in thermoluminescence of oxyfluoride glass-ceramics containing Sm^{3+}-doped CaF_2 nanocrystals," *Journal of Nanoparticle Research*, vol. 13, no. 7, pp. 2727–2732, Dec. 2010. [Online]. Available: http://www.springerlink.com/index/10.1007/s11051-010-0181-2http://link.springer.com/10.1007/s11051-010-0181-2

[140] M. Kanno, T. Honma, and T. Komatsu, "Two-Dimensional Mapping of Er^{3+} Photoluminescence in CaF_2 Crystal Lines Patterned by Lasers in Oxyfluoride Glass," *Journal of the American Ceramic Society*, vol. 92, no. 4, pp. 825–829, Apr. 2009. [Online]. Available: http://doi.wiley.com/10.1111/j.1551-2916.2009.03010.x

[141] H.P. Klug and L. Alexander, *X-ray Diffraction Procedures: For Polycrystalline and Amorphous Materials*, 2nd ed. New York: Wiley, 1974.

APPENDIX A

PUBLICATIONS

This appendix includes papers published from the Ph.D. work. The list of papers are below followed by a set of publication copies.

1. G. Belev, G. Okada, D. Tonchev, C. Koughia, C. Varoy, A. Edgar, T. Wysokinski, D. Chapman, S. Kasap, "Valency conversion of samarium ions under high dose synchrotron generated X-ray radiation" *Physica Status Solidi C*, Vol. 8, pp. 2822-2825, 2011

2. G. Okada, B. Morrell, C. Koughia, A. Edgar, C. Varoy, G. Belev, T. Wysokinski, D. Chapman, S. Kasap, "Spatially resolved measurement of high doses in microbeam radiation therapy using samarium doped fluorophosphate glasses", *Applied Physics Letters*, Vol. 99, No. 12, 121105, 2011

3. Go Okada, Shahrzad Vahedi, Brian Morrell, Cyril Koughia, George Belev, Tomasz Wysokinski, Dean Chapman, Chris Varoy, Andy Edgar, Safa Kasap , "Examination of the dynamic range of Sm-doped glasses for high-dose and high-resolution dosimetric applications in microbeam radiation therapy at the Canadian synchrotron", *Optical Materials*, Vol. 35, No. 11, 1976-1980, 2013

4. B. Morrell, G. Okada, S. Vahedi, C. Koughia, A. Edgar, C. Varoy, G. Belev, T. Wysokinski, D. Chapman, R. Sammynaiken, S.O. Kasap, "Optically erasable samarium-doped fluorophosphate glasses for high-dose measurements in microbeam radiation therapy", *Journal of Applied Physics*, Vol. 115, No. 6, 063107, 2014

5. Go Okada, Jumpei Ueda, Setsuhisa Tanabe, George Belev, Tomasz Wysokinski, Dean Chapman, Dancho Tonchev, Safa Kasap, "SamariumDoped Oxyfluoride Glass-Ceramic as a New Fast Erasable Dosimetric Detector Material for Microbeam Radiation Cancer Therapy Applications at the Canadian Synchrotron", *Journal of the American Ceramic Society*, Vol. 97, No. 7, pp. 2147-2153, 2014

Phys. Status Solidi C **8**, No. 9, 2822–2825 (2011) / **DOI** 10.1002/pssc.201084103

physica status solidi pss c
www.pss-c.com
current topics in solid state physics

Valency conversion of samarium ions under high dose synchrotron generated X-ray radiation

George Belev[*, 1], **Go Okada**[2], **Dancho Tonchev**[2], **Cyril Koughia**[2], **Chris Varoy**[3], **Andy Edgar**[3], **Tomasz Wysokinski**[1], **Dean Chapman**[4], **and Safa Kasap**[2]

[1] Canadian Light Source, University of Saskatchewan, 101 Perimeter Road, S7N 0X4, Saskatoon, Canada
[2] Department of Electrical and Computer Engineering, University of Saskatchewan, Saskatoon, Canada
[3] School of Chemical and Physical Sciences and MacDiarmid Institute, Victoria University of Wellington, Wellington, New Zealand
[4] Department of Anatomy and Cell Biology, University of Saskatchewan, Saskatoon, Canada

Received 3 October 2010, accepted 4 February 2011

Keywords microbeam, dosimetry, Sm ions, X-ray fluorescence

---

[*] Corresponding author: e-mail George.Belev@lightsource.ca, Phone: +01 306 657 3814, Fax: +01 306 657 3535

Microbeam Radiation Therapy (MRT) is a synchrotron based technique for cancer treatment. During MRT tumours are irradiated with micro-planar arrays of synchrotron-generated X-rays. The quality assurance of such a technique depends on the accurate measurement of very high dose levels (>1000 Gy) together with a precise measurement of the dose distribution over a scale of a few microns. For such applications we need to have a high dynamic range, high-dose detector with very high spatial resolution. As part of the work towards the development of such a detector we have examined the X-ray radiation induced conversion of rare-earth ions, especially Sm^{3+} to Sm^{2+}, embedded in suitable media. We have exposed a variety of Sm^{3+} doped media, from single crystals to glass-ceramics, to a high dose radiation at the Canadian Light Source to examine whether we could convert the rare-earth ion valency. The irradiation was carried out at a bending magnet beamline using filtered white beam with a spectrum peaking at 50 keV. We have used the distinctly different signatures in the photoluminescence emission spectra of the two valency states to identify the rare-earth ions and whether a valency conversion has taken place. We report the results from these experiments, which show that the conversion of Sm^{3+} to Sm^{2+} is not universal and depends very much on the host material. We discuss possible reasons for the presence and lack of radiation induced valency conversion of Sm-ions, and identify the challenges that must be overcome to develop a high-resolution, high-dose detector.

1 Introduction Microbeam Radiation Therapy (MRT) is a synchrotron based cancer treatment radiotherapy technique which uses arrays of 20-100 μm wide planar X-ray beams. Irradiation with such microbeams spares the normal tissue, including the central nervous system, and preferentially damages tumors as described in the literature [1, 2]. During MRT the maximum skin-entrance absorbed dose can reach very high values (1000 Gy and more) without causing tissue necrosis. MRT dosimetry should record not only the total dose delivered to the tissue but also the peak to valley dose ratios, i.e. the ratios between the dose in the centre of the beam and the dose in the center of the region between two adjacent peaks. The valley dose should be as low as possible and should not exceed a certain threshold (~20 Gy) to ensure efficient healthy tissue repair within the irradiated microslices. Since the microbeams vary in thickness from 20-100 μm and the gaps between the latter are in the range 100-400 μm, the standard dosimeters lack the spatial resolution to precisely record the dose distribution typical for MRT. Many dosimetric detectors like Gafchromic film, gel dosimeters, MOSFET detectors, TLD dosimeters have been tested [3]; however the readout spatial resolution for all these detectors is limited to 20-30 μm which does not fully satisfy the requirements for MRT dosimetry. MRT is part of the scientific program of the Biomedical Imaging and Therapy Beamlines at the Canadian Light Source (CLS) in Saskatoon, Canada. We have recently started a comprehensive research program in an attempt to develop a dosimetric technique having an adequate dynamic range and spatial resolution for MRT.

It is well known that in variety of Samarium-doped materials, exposure to soft X-rays can lead to a relatively stable change in the oxidation state of Sm-ions, i.e. $Sm^{3+} \rightarrow Sm^{2+}$ [4]. The concentration of Sm^{2+} ions created in this way should be proportional to the delivered radiation dose and the latter can be used for radiation dose measurement purposes [5]. The conversion $Sm^{3+} \rightarrow Sm^{2+}$ is accompanied by a distinct change in the photoluminescence (PL) spectrum of the material. This localized valency conversion in irradiated regions allows the possibility of a non destructive and completely optical very high spatial resolution (better than 1 μm) fluorescent dose readout method based on confocal microscopy [6].

In the course of our initial work we have exposed a variety of Sm^{3+} doped media, from single crystals to glass-ceramics, to a high dose X-ray radiation to examine the suitability of these materials to act as radiation detector media based on a possible $Sm^{3+} \rightarrow Sm^{2+}$ conversion. The main goals for these initial experiments were to examine the conversion $Sm^{3+} \rightarrow Sm^{2+}$ under high doses of relatively high energy X-rays in different materials, how stable are the Sm^{2+} ions produced by the irradiation, the measurement of the dose response curves of various Sm-doped materials that convert, and the study of some accompanying effects such as the photodarkening that occurs in almost all materials under exposure to high doses of X-rays. We report the results from these investigations at the CLS and discuss the challenges that need to be overcome to develop a high-resolution high-dynamic range dissymmetric detector for use in synchrotron based radiation therapy techniques.

2 Materials and methods For the needs of this initial work we have used Sm-doped materials that were already prepared for various other research projects. The tested materials include: fluorochlorozirconate glasses and glass-ceramics, SiO_2-NaO-Al_2O_2-LaF_3-PbF_2-SmO_3 glasses, LaO_3-B_2O_3-GeO_2-SmO_3 glasses, and SrB_4O_7 polycrystalline material. We have also specially fabricated a few materials for which $Sm^{3+} \rightarrow Sm^{2+}$ conversion under X-rays have been reported in literature. We have fabricated Sm-doped Li_2O–SrO–B_2O_3 glasses following closely the composition and the preparation conditions published in [4]. We have prepared $SrBPO_5$:Sm^{3+} and $BaBPO_5$:Sm^{3+} polycrystalline materials following very closely the solid state reactions and preparation conditions in [7]. We have also prepared glasses from the $SrBPO_5$ and $BaBPO_5$ polycrystalline materials using conventional melt quench techniques. The irradiated samples had an effective thickness for the incident X-rays in the range 0.5-4 mm.

The sample irradiation was performed on the Biomedical Imaging and Therapy Beamline (05B1-1) at Canadian Light Source, Saskatoon, Canada. The X-ray beam was filtered with Cu filters having an effective thickness of 0.94 mm. The resulting spectrum shape is shown in inset of Fig. 1. The irradiation was done 26 m away from the source. At the point of irradiation the dose rate was estimated to be around 4 Gy/min for an air absorber.

The luminescence spectra were recorded with a fiber optics spectrophotometer (Stellar-Net Inc) having a 200 μm entrance slit and covering the range 230-1100 nm. The spectrophotometer resolution is about 8 nm as stated by the manufacturer. It was possible to record both PL and X-ray (XL) excited luminescence from the samples. All the spectra were measured at room temperature (23 °C). In the case of photoluminescence measurements we used a 408 nm laser diode as an excitation source. The spectra were recorded through a 550 nm long-pass filter to eliminate the influence of the scattered excitation light.

3 Results and discussion Almost all samples before the irradiation showed PL and XL spectra that are typical for Sm^{3+} ions. The only exception were the SrB_4O_7 polycrystalline samples in which both Sm^{3+} and Sm^{2+} ions were present in the non-irradiated sample. None of the glass and glass-ceramic samples irradiated by us showed any measurable $Sm^{3+} \rightarrow Sm^{2+}$ conversion even after irradiation to very high doses (60 min of irradiation time). Oxidation state changes occurred for the Sm-ions in all polycrystalline samples. The changes in the PL spectrum observed for $SrBPO_5$:Sm^{3+} and $BaBPO_5$:Sm^{3+} polycrystalline materials are illustrated in Fig. 1. After ~1 min of irradiation the PL spectrum is dominated by Sm^{2+} ions produced by the irradiation. Changes in the PL spectrum were clearly detectable after irradiation with duration of only 0.1 s (~0.7 mGy for an air absorber). Figure 1 clearly illustrates that the integrated intensity of the spectrum in the range 670-830 nm can be used as a measure of the Sm^{2+}

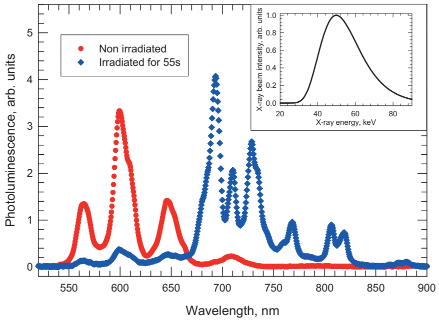

Figure 1 PL spectra for a $SrBPO_5$:Sm^3 polycrystalline sample before and after X-ray irradiation. The duration of the irradiation was 55 s. The shape of the X-ray spectrum is illustrated in the insert. In the irradiated sample, the spectrum is dominated by characteristic features arising from Sm^{2+} ions.

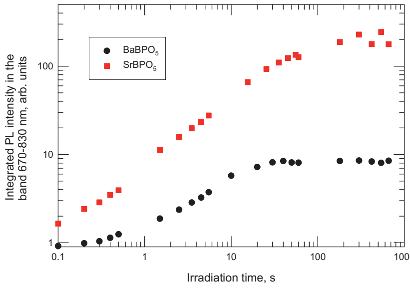

Figure 2 Dose-response curves for $SrBPO_5:Sm^{3+}$ and $BaBPO_5:Sm^{3+}$. The integrated intensity in the band 670-830 nm is used as a measure for the Sm^{2+} ion concentration. The signal is also normalized to the intensity of the Sm^{3+} peak around 600 nm to account for small changes in the excitation and light collection conditions due to the gradual photodarkening of the samples during the irradiation.

ion concentration in the material. The small band around 710 nm due to Sm^{3+} ions causes only a little offset in the signal and can be corrected for if necessary. The dose response curves shown in Fig. 2 use this approach to estimate the Sm^{2+} ion concentration. It is very encouraging that the dose response curves measured for the $SrBPO_5$ sample cover more than 2 orders of magnitude which comes close to the dynamic range required for MRT dosimetry.

For the SrB_4O_7 polycrystalline material (not shown) we were unable to observe saturation in the dose response curve even after two hours of irradiation (total dose to air 240 Gy) which shows that the conversion rate in this material is such that a dosimeter with a very high dynamic range is possible. However, practical applications of this material will be difficult because Sm^{2+} ions in significant concentration are present in the non-irradiated material due to the preparation technique.

All samples without exception have shown "photodarkening" or "discoloration" as result of the X-ray exposure. This effect is most likely due to the formation of colour centres under the influence of the radiation. The photodarkening effect is varies in magnitude and appearance in the materials we have examined. For example, it is much less pronounced in $SrBPO_5$ than in $BaBPO_5$. The darkening is an undesired effect because it changes the excitation and light collection conditions during the measurement; the detector readout and calibration would be adversely affected by the darkening effect. For example, the observed saturation in the dose response curves in Fig. 2 can be due to changes in the excitation and light collection conditions and not necessarily due to the saturation of the $Sm^{3+} \rightarrow Sm^{2+}$ conversion reaction. Some of the colour centres formed by the radiation are obviously related to the reduction of the Sm^{3+} ions to Sm^{2+} ions and the electron exchange with a defect centre in the process while others

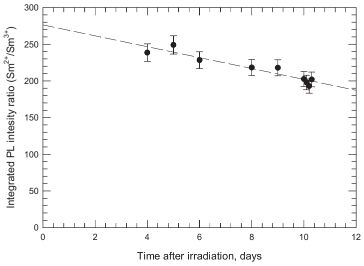

Figure 3 Decay of the Sm^{2+} ion concentration with time after the X-ray irradiation. Some of the observed decay is due to the excitation light during the measurements. The dashed line is only guide for the eyes.

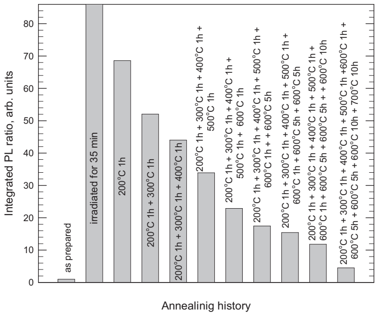

Figure 4 Effects of different annealing conditions on the concentration of the Sm^{2+} ions formed by the X-ray irradiation. It is possible to convert almost all Sm^{2+} ions to their initial 3+ state by choosing suitable annealing temperature and annealing time (duration).

are formed independently of the latter process. In many samples we were able to almost completely bleach the photodarkening by annealing the sample at low temperatures (200 °C) without affecting too much the concentration of Sm^{2+} ions (see Fig. 4).

To further check the stability of Sm^{2+} ions we have measured the decrease in their concentration with time after the X-ray irradiation. The samples were kept in the dark between the measurements. The results are presented in Fig. 3. Only a slight decrease in the Sm^{2+} concentration over time is evident. At least part of this decrease is caused by the excitation light during the PL measurements.

Finally we have tried to convert the Sm^{2+} ions back to their starting Sm^{3+} state by annealing the irradiated sample at different temperatures and for different durations. As illustrated in Fig. 4 we have succeeded to almost completely "erase" the Sm^{2+} ions created by the X-ray irradiation, which opens the possibilities for the creation of an erasable detector media for multiple use. This idea is further supported by the fact that when irradiated again the "erased" samples showed dose response curves very similar to those shown in Fig. 2 for the as-prepared samples.

The glass materials are a natural choice for the fabrication of a dosimetric detector plate for MRT for a number of reasons. The glasses are easy to work with and most importantly, have uniform properties to a very fine spatial scale. Compared with a polycrystalline medium, glasses exhibit very little light scattering, and so they would allow a very high resolution fluorescent microscopic readout. Thus, it is disappointing that we were not able to observe the desired $Sm^{3+} \rightarrow Sm^{2+}$ conversion in any of the glass materials investigated in this work so far.

The Li_2O–SrO–B_2O_3 glasses produced by us following the conditions described in [4] showed no detectable presence of Sm^{2+} ions even after a very high dose of X-ray irradiation. The failure of conversion in this particular glass can be due to small differences in the purity of the starting materials, preparation conditions, and glass post-treatment. Another significant difference is the spectrum of the X-rays used to irradiate the samples. The authors of [4] have used X-ray tube with Cu anode to irradiate the sample. The spectrum in this case is dominated by the Cu-K line (8.9 keV). These X-rays are very soft and are absorbed completely at the surface of the samples. In the case of our work the X-rays were much harder and they deposited their energy in the volume of the sample. Thus, it is also very difficult to compare the doses delivered to the samples in [4] and in our work.

We were also unable to observe any $Sm^{3+} \rightarrow Sm^{2+}$ in the borophosphate glasses prepared in this work in spite of the fact that the starting polycrystalline material shows very clear radiation induced conversion as described above. X-ray induced reduction of Sm^{3+} ions in very similar glasses prepared with very similar technique has been described in [8]. The reasons for the lack of radiation induced conversion in the oxidation state of Sm ions can be the same as that described above for the Li_2O–SrO–B_2O_3 glass. Additionally, it is known that $BaBPO_5$ is an incongruently melting compound [9] and for the latter reason the properties of the borophosphate glass can be strongly affected by the conditions under which the starting polycrystalline material was melted and the melt was quenched.

4 Conclusions We examined various materials for the presence of $Sm^{3+} \rightarrow Sm^{2+}$ conversion under the influence of X-ray irradiation for developing a medium for use in a high-dose high-resolution dosimetric detector for radiation therapy applications such as MRT. Among all the materials examined by us so far we have found the Sm^{3+} to Sm^{2+} conversion only in polycrystalline $BaBPO_5$, $SrBPO_5$, and SrB_4O_7. No changes in the Sm ion oxidation state under X-ray irradiation were observed for any of the glasses studied in this work; our results for some of the glass compositions do not agree with previously published results. Our studies suggest that the conversion of Sm^{3+} to Sm^{2+} under X-ray irradiation is not universal. It depends very much on the host material and on the preparation conditions.

The measured dose response curves for $SrBPO_5$ polycrystalline samples cover more than 2 orders of magnitude and come close to meeting the requirements for MRT dosimetry applications. The Sm^{2+} ions created by the X-ray irradiation are relatively stable and their concentration shows little change with time after the irradiation. On the other hand, by suitable annealing, it seems possible to almost completely erase the effects of the irradiation induced $Sm^{3+} \rightarrow Sm^{2+}$ conversion, which creates the possibility for creating a detector plate for multiple use.

One undesired effect of high-dose irradiation is the discoloration of the sample induced by the irradiation itself that might interfere with the proposed optical readout technique.

Nonetheless, based on our initial findings we think that it is possible to create a practical high resolution high dose dosimetric detector for MRT applications using the $Sm^{3+} \rightarrow Sm^{2+}$ conversion as the radiation detection mechanism and we will continue our search for suitable host materials for the latter purpose.

Acknowledgements Research described in this paper was performed at the Canadian Light Source, which is supported by NSERC (Canada), NRC (Canada), the Canadian Institutes of Health Research, the Province of Saskatchewan, Western Economic Diversification Canada, and the University of Saskatchewan. We thank Prof. Animesh Jha, University of Leeds (UK), and Prof. Marin Gospodinov, Bulgarian Academy of Sciences, Institute of Solid State Physics, Sofia, Bulgaria, for supplying some of the materials used in this research. This work was supported by an NSERC Strategic Grant Sponsored by DALSA Inc.

References

[1] D. N. Slatkin, P. Spanne, F. A. Dilmanian, and M. Sandborg, Med. Phys. **19**, 1395 (1992).
[2] H. Blattmann, J. O. Gebbers, E. Bräuer-Krisch, A. Bravin, G. Le Duc, W. Burkard, M. Di Michiel, V. Djonov, D. N. Slatkin, J. Stepanek, and J. A. Laissue, Nucl. Instrum. Methods Phys. Res. A **548**, 17 (2005).
[3] M. Ptaszkiewicza, E. Braurer-Kirschb, M. Klosowskia, L. Czopyka, and P. Olkoa, Rad. Meas. **43**, 990 (2008).
[4] Y. Huang, Ch. Jiang, K. Jang, H. S. Lee, E. Cho, M. Jayasimhadri, and S. Yi, J. Appl. Phys. **103**, 113519 (2008).
[5] H. Riesen and W. Kaczmarek, Inorg. Chem. **46**, 7235 (2007).
[6] M. Akselrod, R. C. Yoder, and G. M. Akselrod, Radiat. Protect. Dosim. **119**, 357 (2006).
[7] Y. Huanga, W. Zhaoa, L. Shib, and H. J. Seob, J. Alloys Compd. **477**, 936 (2009).
[8] Y. Li, J. Wang, and Y. Huang, J. Am. Ceram. Soc. **93,** 722 (2010).
[9] Sh. Pan, Y. Wu, P. Fu, X. Wang, G. Zhang, and Ch. Chen, J. Opt. Soc. Am. B **21,** 761 (2004).

APPLIED PHYSICS LETTERS **99**, 121105 (2011)

Spatially resolved measurement of high doses in microbeam radiation therapy using samarium doped fluorophosphate glasses

Go Okada,[1] Brian Morrell,[1] Cyril Koughia,[1,a)] Andy Edgar,[2] Chris Varoy,[2] George Belev,[3] Tomasz Wysokinski,[3] Dean Chapman,[4] and Safa Kasap[1]
[1]*Department of Electrical and Computer Engineering, University of Saskatchewan, Saskatoon, SK S7N 5A9, Canada*
[2]*School of Chemical and Physical Sciences and MacDiarmid Institute, Victoria University of Wellington, Kelburn Parade, New Zealand*
[3]*Canadian Light Source Inc., University of Saskatchewan, Saskatoon, SK S7N 0X4, Canada*
[4]*Department of Anatomy and Cell Biology, University of Saskatchewan, Saskatoon, SK S7N 5E5, Canada*

(Received 31 May 2011; accepted 11 August 2011; published online 20 September 2011)

The measurement of spatially resolved high doses in microbeam radiation therapy has always been a challenging task, where a combination of high dose response and high spatial resolution (microns) is required for synchrotron radiation peaked around 50 keV. The x-ray induced $Sm^{3+} \rightarrow Sm^{2+}$ valence conversion in Sm^{3+} doped fluorophosphates glasses has been tested for use in x-ray dosimetry for microbeam radiation therapy. The conversion efficiency depends almost linearly on the dose of irradiation up to ∼5 Gy and saturates at doses exceeding ∼80 Gy. The conversion shows strong correlation with x-ray induced absorbance of the glass which is related to the formation of phosphorus-oxygen hole centers. When irradiated through a microslit collimator, a good spatial resolution and high "peak-to-valley" contrast have been observed by means of confocal photoluminescence microscopy. © *2011 American Institute of Physics*. [doi:10.1063/1.3633102]

Microbeam radiation therapy (MRT) is an experimental form of radiation treatment which has the potential to improve the treatment of many types of cancer compared to customary broad-beam radiation treatment.[1,2] It is based on the markedly different response of tumor and normal cells to this form of treatment.[3] A potentially interesting approach for MRT dosimetry is the effect of valence conversion of rare earth ions embedded in a suitable host material as discussed by the present group.[4] Various papers have demonstrated the possibility of valence conversion of different rare earth ions in a variety of host materials under different forms of excitation such as x-rays, γ-, and β-irradiation as well as near-infrared (NIR) optical excitation.[5–10] Among the rare earth ions, Sm^{3+} to Sm^{2+} conversion is of particular interest because the dominant emission bands of Sm^{3+} and Sm^{2+} ions are very easy to distinguish, all dominant bands are situated in a red region of the spectrum and make a good match to silicon based detectors used in optical measurement. It should be stressed immediately that $Sm^{3+} \rightarrow Sm^{2+}$ conversion may provide submicron spatial resolution with respect to optical storage of information as was recently demonstrated.[7,8]

We present data on Sm-doped fluorophosphate (FP) glasses as a potential dosimeter material to measure both the dose and the peak-to-valley dose ratio (PVDR), a critical parameter for efficient MRT therapy. We demonstrate the efficiency of $Sm^{3+} \rightarrow Sm^{2+}$ conversion in these glasses, measure the dynamic range of the effect, and illustrate the feasibility of a spatially resolving dosimetric sensor based on the confocal detection of photoluminescence (PL).

FP glasses used in this paper have been already described.[11] The x-ray irradiation was performed using synchrotron radiation at the Biomedical Imaging and Therapy 05B1-1 bend magnet beamline, Canadian Light Source, Saskatoon, Canada. The spectrum of filtered x-ray radiation had a maximum around 50 keV and is shown in the inset of Figure 1(a). The intensity of x-ray irradiation corresponded to an approximate dose of 4 Gy/min. The steady-state PL spectra were measured using an ASEQ Fiber input Mini-spectrometer with spectral resolution better than 1 nm within the 200–1200 nm range. The excitation source for all the photoluminescence spectra was a laser diode with an emission wavelength at 405 nm.

Figure 1 shows the transformation of PL spectra due to $Sm^{3+} \rightarrow Sm^{2+}$ valence reduction appearing under x-ray irradiation. Chemically, this process may be presented as a sum of two reactions $Sm^{3+} + e^- \rightarrow Sm^{2+}$ and $PO + h^+ \rightarrow POHC$, where e^- and h^+ are the electron and hole appearing under x-ray irradiation, PO represents a phosphate group and POHC stands for phosphorus-oxygen hole centre. The possible atomic models of POHCs are discussed by Griscom.[5] Figure 2(a) shows the spectrum of optical absorption induced by x-ray irradiation, and Figure 2(b) demonstrates that this spectrum may be presented as a sum of several overlapping Gaussians. Three of them marked as G1, G2, and G3 are of particular interest and their average parameters are presented in Table I.

It is widely accepted that the radiation induced absorption is related to atomic scale defects appearing in a glass structure and in some glasses these defects have been identified by comparing the induced optical absorption with EPR spectra, e.g., Refs. 5, 12–14 show an example of such an identification in fluorophosphate glass. It has been proven that the POHCs in phosphate glasses form several absorption bands in the visible and near UV parts of spectrum.[13] Table I lists their typical properties and compares them with our results in this work. The agreement of the results implies that x-ray induced absorption in our glasses is related to POHCs.

[a)] Electronic mail: cyril.koughia@usask.ca.

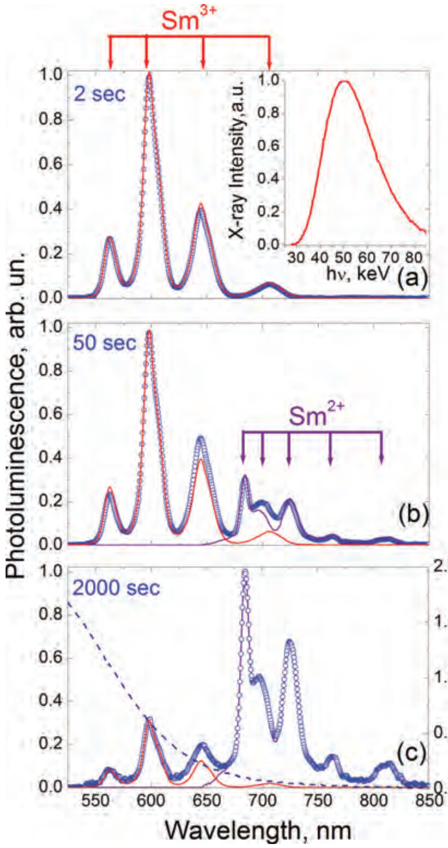

FIG. 1. (Color online) The evolution of PL spectra under synchrotron x-ray irradiation. The irradiations times are (a) 2 s, (b) 50 s, and (c) 2000 s, respectively. Experimental data are shown by symbols. Emissions of Sm^{3+} and Sm^{2+} ions are shown by thin (red and purple) solid lines. The inset in (a) shows the spectrum of the x-ray irradiation. Broken line in (c) represents the x-ray induced absorbance.

Further, the excellent match between the G1, G2, and G3 bands with those reported by Ehrt *et al.* would deem the absorption arising from Sm^{2+} to be a minor effect.

Figure 1 suggests that the Sm^{2+} appearance during x-ray irradiation may be characterized by the ratio $R(t) = \int_{676}^{713} \mathrm{PL}(\mathrm{Sm}^{2+})d\lambda / \int_{676}^{713} \mathrm{PL}(\mathrm{Sm}^{3+})d\lambda$, where $\mathrm{PL}(\mathrm{Sm}^{2+})$ and $\mathrm{PL}(\mathrm{Sm}^{3+})$ are the PL spectra of Sm^{2+} and Sm^{3+}, respectively. The time t in $R(t)$ is simply the duration of exposure in which 1 min corresponds to a dose of 4 Gy. The choice of integration range from 676 to 713 nm is based on two factors. First, there are PL bands of both Sm^{2+} and Sm^{3+} in this spectral region. Second, the influence of x-ray induced darkening (which occurs invariably under intense x-ray irradiation) is not as important in this spectral range as at shorter wavelengths, as illustrated by the x-ray induced absorption data depicted in Figure 1(c).

Figure 3 shows that for a large variety of Sm-concentrations, the time dependence of $R(t)$ may be universally approximated by $R(t) = R_0[1 - \exp(-t/\tau)]$, with $\tau \approx 270$ s where the parameters R_0 and τ do not depend on the concentration of Sm. These results demonstrate that the present material, as it is, may be used as a quasi-linear dose recording sensor in a wide dynamic range covering about three orders of magnitude up to ~5 Gy and as a non-linear sensor up to ~80 Gy where the saturation is reached. Figure 3 also shows that $R(t)$ seems to be practically independent of the Sm concentration over a wide range of concentrations. This fact implies that the rate of Sm^{3+} to Sm^{2+} conversion and the subsequent saturation of the Sm^{2+} concentration are controlled and limited by some dominant process which is independent of the Sm concentration. The limiting process is likely to be the formation of POHC. The results in Figure 3 support this hypothesis by showing a good correlation between $R(t)$ and the amplitude of POHC related absorption bands.

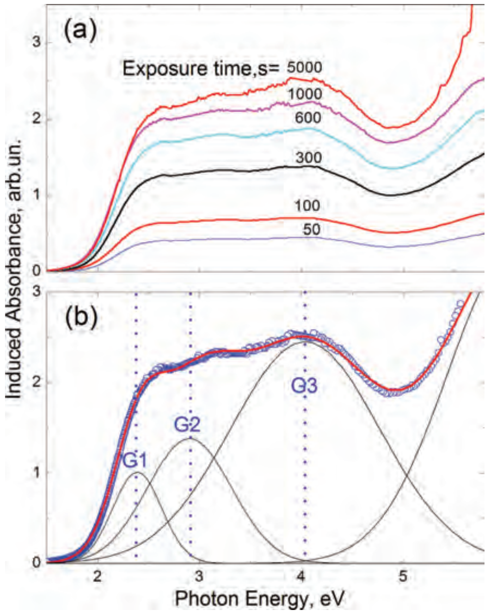

FIG. 2. (Color online) (a) The evolution of an induced absorbance under synchrotron x-ray irradiation. The thickness of samples is 3 mm. (b) Tentative presentation of induced absorbance after 5000 s of irradiation in the same sample as a sum of Gaussians associated with x-ray induced defects.

Figure 4 shows a typical result from laser scanning confocal photoluminescence microscopy measurements on an irradiated sample. It is clear that $Sm^{3+} \rightarrow Sm^{2+}$ x-ray induced conversion in fluorophosphate glass can be used for x-ray

TABLE I. The comparison of central wavelengths (λ), central energies (E), and widths (W) of Gaussian absorption bands (G1-G3) observed in the present paper with POHC data from Ebeling *et al.* (Ref. 13) The widths (W) of Gaussian bands refer to the full widths at half maxima.

	Present paper			Values by Ebeling *et al.*		
Bands	λ (nm)	E (eV)	W (eV)	λ (nm)	E (eV)	W (eV)
G1	321 ± 10	3.86 ± 0.12	1.33	325	3.82 ± 0.04	1.12
G2	430 ± 4	2.88 ± 0.03	0.97	430	2.89 ± 0.04	1.00
G3	521 ± 3	2.38 ± 0.01	0.56	540	2.30 ± 0.02	0.50

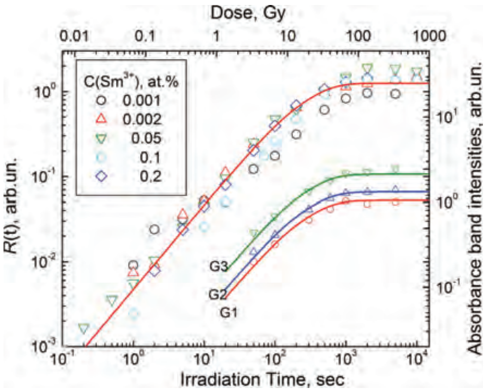

FIG. 3. (Color online) The ratio $R(t)$ for glasses with varying concentration of Sm and the intensity of x-ray induced Gaussians absorbance bands (G1-G3) vs. irradiation time/dose. The lines are based on an exponential rise with $\tau \approx 270$ s and varying values of R_0.

dose measurements at high spatial resolution. Figure 4 represents the dose distribution in a FP10 glass sample irradiated through an 8 mm thick tungsten/air microslit collimator (MSC) manufactured by Usinage et Nouvelles Technologies, Morbier, France. The microbeams are 50 μm wide and have centre-to-centre distance of 400 μm. The simplified construction of the MSC is shown in the inset of Figure 4. The irradiation time was chosen to be 5 min corresponding to a peak dose ~20 Gy which is close to the upper limit of the linear response region. The dose distribution was evaluated by using a modified CLSM (confocal laser scanning microscope) manufactured by Molecular Dynamics with custom-designed software. The PL excitation was done by a high-brightness LED with maximum emission peaked around 460 nm. In this experiment, the integrated PL of Sm^{2+} and PL of Sm^{3+} were measured simultaneously and independently by two photomultipliers supplied with different optical filters covering the spectral ranges 560-670 nm and 650-850 nm, respectively. The ratio $R(300\ \text{s}) = \text{PL}(\text{Sm}^{2+})/\text{PL}(\text{Sm}^{3+})$ was computed numerically. Figure 4 demonstrates the good spatial resolution of the detector. The measured values for FWHM of the peaks and the PVDR are comparable to those recently published for FDTNs, which have the potential to be a prime candidate as a dose verification tool in MRT.[15]

Initial experiments indicate that the current Sm-doped detector plate is reusable after uv bleaching. On the speed of measurement, Figure 3 shows that a significant transformation of the PL spectra at the peak occurs in a few seconds, but allowing for a peak to valley ratio of ~100, this suggests that an irradiation time of approximately a few minutes is required for a satisfactory measurement. The 4f-4f transitions of the Sm ions used here have lifetimes in the ms region, which necessitates scanning times of a few minutes in a scanning confocal microscope to achieve an adequate signal to noise ratio.

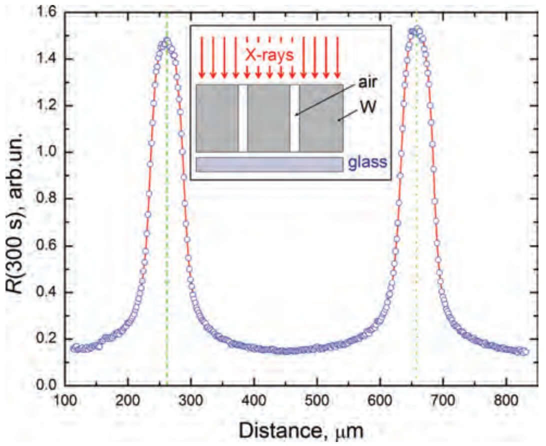

FIG. 4. (Color online) The Sm^{3+} → Sm^{2+} conversion pattern induced by x-rays through a microslit collimator and readout by luminescence confocal microscope as the ratio $R(300\text{s}) = \text{PL}(\text{Sm}^{2+})/\text{PL}(\text{Sm}^{3+})$. The line is a guide to eye. The inset shows the geometry of the experiment. The irradiation time is 5 min which corresponds to ~20 Gy.

Research described in this paper was performed at the Canadian Light Source, which is supported by NSERC, NRC, the Canadian Institutes of Health Research, the Province of Saskatchewan, Western Economic Diversification Canada, and the University of Saskatchewan. We thank NSERC and the New Zealand Ministry for Science and Innovation for financial support and Teledyne-DALSA for sponsoring the project through NSERC.

[1] D. N. Slatkin, F. A. Dilmanian, P. Spanne, and M. Sandborg, Med. Phys. **19**, 1395 (1992).

[2] F. Avraham Dilmanian, P. Romanelli, Z. Zhonge, R. Wang, M. E. Wagshul, J. Kalef-Ezra, M. J. Maryanski, E. M. Rosen, and D. J. Anschel, Eur. J. Radiol. **68S**, S129 (2008).

[3] J. C. Crosbie, R. L. Anderson, K. Rothkamm, C. M. Restall, L. Cann, S. Ruwanpura, S. Meachem, N. Yagi, I. Svalbe, R. A. Lewis, B. R. G. Williams, and P. A. W. Rogers, Int. J. Radiat. Oncol. Biol. Phys. **77**, 886 (2010).

[4] G. Belev, G. Okada, D. Tonchev, C. Koughia, C. Varoy, A. Edgar, T. Wysokinski, D. Chapman, and S. Kasap, Physica Status Solidi C **8**, 2822 (2011).

[5] D. L. Griscom, E. J. Friebele, K. J. Long, and J. W. Fleming, J. Appl. Phys. **54**, 3743 (1983).

[6] K. Miura, J. Qiu, S. Fujiwara, S. Sakaguchi, and K. Hirao, Appl. Phys.Lett. **80**, 2263 (2002).

[7] J. Lim, M. Lee, and E. Kim, Appl. Phys. Lett. **86**, 191105 (2005).

[8] E. Malchukova, B. Boizot, G. Petite, and D. Ghaleb, J. Non-Cryst. Solids **353**, 2397 (2007).

[9] Y. Huang, C. Jiang, K. Jang, H. Sueb, E. Cho, M. Jayasimhadri, and S.-S. Yi, J. Appl. Phys. **103**, 113519 (2008).

[10] C. A. G. Kalnins, H. Ebendorff-Heidepriem, N. A. Spooner, and T. M. Monro, J. Am. Ceram. Soc. **94**, 474 (2011).

[11] H. Ebendorff-Heidepriem and D. Ehrt, Opt. Mater. **18**, 419 (2002).

[12] D. Ehrt, P. Ebeling, and U. Natura, J. Non-Cryst. Solids **263&264**, 240 (2000).

[13] P. Ebeling, D. Ehrt, and M. Friedrich, Opt. Mater. **20**, 101 (2002).

[14] D. Möncke and D. Ehrt, Opt. Mater. **25**, 425 (2004).

[15] J. A. Bartz, G. J. Sykora, E. Bräuer-Krisch, and M. S. Akselrod, Radiat. Meas. (in press).

Optical Materials 35 (2013) 1976–1980

Contents lists available at SciVerse ScienceDirect

Optical Materials

journal homepage: www.elsevier.com/locate/optmat

Examination of the dynamic range of Sm-doped glasses for high-dose and high-resolution dosimetric applications in microbeam radiation therapy at the Canadian synchrotron

Go Okada [a], Shahrzad Vahedi [a], Brian Morrell [a], Cyril Koughia [a], George Belev [b], Tomasz Wysokinski [b], Dean Chapman [c], Chris Varoy [d], Andy Edgar [d], Safa Kasap [a,*]

[a] *Department of Electrical and Computer Engineering, University of Saskatchewan, 57 Campus Dr., Saskatoon, SK, Canada*
[b] *Canadian Light Source Inc., 101 Perimeter Road, Saskatoon, SK, Canada*
[c] *Department of Anatomy and Cell Biology, University of Saskatchewan, Saskatoon, SK, Canada*
[d] *School of Chemical and Physical Sciences and MacDiarmid Institute, Victoria University of Wellington, New Zealand*

ARTICLE INFO

Article history:
Available online 13 December 2012

Keywords:
Samarium-doped glass
Fluorophosphate glass
Fluoroaluminate glass
Valency conversion
Dosimetry
Microbeam Radiation Therapy (MRT)

ABSTRACT

Microbeam Radiation Therapy (MRT) is a promising cancer treatment technique. During the treatment, a micro-planar lattice of narrow X-ray beams called a microbeam (each narrow X-ray beam is typically 20–100 μm wide separated by 100–400 μm) delivers a very large dose (>1000 Gy) onto a tumor. Sm^{3+}-doped glasses that involve the reduction of the Sm-valency ($Sm^{3+} \rightarrow Sm^{2+}$) upon X-ray irradiation are one of the potential dosimetric detectors for this particular application. With this class of detectors, we use the extent of valency reduction as a measure of the delivered X-ray dose, and the response read out using a confocal microscopic technique via the Sm^{2+}/Sm^{3+} photoluminescence. This method enables us to measure the dose distribution of the microbeam. In this paper, we show that both Sm^{3+}-doped fluorophosphate and fluoroaluminate glasses exhibit a dynamic range for the conversion response from 1 to over 1000 Gy, which satisfies the dose range for MRT applications. The dynamic range depends on the concentration of Sm^{3+} dopants as well as the detector glass composition. Moreover, X-ray induced absorbance, photobleaching and thermally-stimulated luminescence (TL) measurements suggest that the hole trapping process during X-ray irradiation is a dominant factor for the valency conversion, and the accommodation of precursor POHCs in fluorophosphate glasses gives rise to an acceleration of the conversion process.

1. Introduction

Microbeam Radiation Therapy (MRT) is a promising cancer treatment technique, and it has been intensively studied with a view to clinical applications since the 1990s [1]. During the treatment, a micro-structured, high energy and large dose X-ray beam (called a "microbeam") is directly aimed at a tumor from a sequence of directions, all with a common focus on the tumor; as a result, the tumor undergoes necrosis from the intense irradiation which strikes all parts of it. Such a microbeam is produced by inserting a multi-slit collimator (MSC; slit width = 20–100 μm, slit separation = 100–400 μm) in a well-collimated X-ray beam such as that from synchrotron radiation with the energy range of 50–150 keV, and a wide range of X-ray dose (a few Grays to more than 1000 Gy) is distributed over the cross-sectional area of the microbeam.

In order to advance MRT research and bring it to the clinical application stage, it is a fundamental requirement to accurately measure and understand the dose distribution profile of microbeam. Successful detectors must have a large dynamic range (1–1000 Gy or larger) and have a resolving power of a few microns. To the best of our knowledge, no existing detectors have successfully measured the distribution of microbeams for MRT with satisfactory resolution and dynamic range.

In the past few years, we have been developing a dosimetry technique especially for MRT applications. It is well known that trivalent rare-earth ions (such as Eu^{3+} and Sm^{3+}) included in some host glasses exhibit a valency change from the trivalent to divalent state when irradiated with ionizing radiation, such as X- and γ-rays [2–4]. In our approach, we use Sm^{3+}-doped glasses as a dosimeter and use the X-ray induced Sm^{3+} to Sm^{2+} valence reduction as a measure of the dose delivered. This effect is easily quantified using photoluminescence (PL) of Sm^{3+} and Sm^{2+} ions; in addition, scanning confocal microscopy can be used to achieve dose distribution mapping with a high spatial resolution of a few microns. We initially proposed this approach for MRT dosimetry

---

* Corresponding author.
E-mail address: safa.kasap@usask.ca (S. Kasap).

0925-3467/$ - see front matter © 2012 Elsevier B.V. All rights reserved.
http://dx.doi.org/10.1016/j.optmat.2012.10.049

in order to overcome the detector limitations (dynamic range and spatial resolution) [5]. Subsequently we have demonstrated successful readout of the Sm valence states, and measurements of the delivered dose distributed over the microbeam cross section, justifying its potential for MRT dosimetry [6].

In this paper, we report studies of the dynamic range, optical absorbance, photobleaching and thermally-stimulated luminescence (TL) of Sm^{3+}-doped fluorophosphate (FP) and fluoroaluminate (FA) glasses with different dopant concentrations. Also, we discuss physical models explaining the experimental observations concerning $Sm^{3+} \leftrightarrow Sm^{2+}$ inter-conversion. Sm-doped glasses have currently received much interest for various applications, such as X-ray imaging, dosimetry and solar cells [7–9].

2. Experimental procedure

Sm^{3+}-doped FP and FA glasses were synthesized by a conventional melt-quenching method as described in [10]. The compositions of samples are: for FP glasses, $10MgF_2$-(34.4-x) AlF_3-$30.4CaF_2$-$15.2SrF_2$-$10Sr(PO_3)_2$-$x$$SmF_3$ (x = 0.2, 0.5, 1.0, and 10.0 mol%) (x = 0.2, 0.5, 1.0, and 10.0 mol%); and for FA glasses $10MgF_2$-$35AlF_3$-$20CaF_2$-$10SrF_2$-(15-x)YF_3-$10BaF_2$-$x$$SmF_3$ (x = 0.1, 0.5, 1.0, 5.0 and 10.0 mol%). Sythesized bulk samples were cut in smaller pieces and polished for the following experiments.

The polished samples were irradiated with X-rays at Canada's synchrotron facility, Canadian Light Source Inc. An X-ray beam with the peak energy of 50 keV, which is a common choice of energy used in MRT, was realized by filtering the soft X-ray component from the bend magnet synchrotron source (05B1-1 beamline, Biomedical Imaging and Therapy) using copper filters with an effective thickness of 0.94 mm. The dose rate was experimentally estimated to be 1.6 Gy/s at 250 mA of the storage ring current. Several pieces of each sample type were irradiated for different times (0.5–20,000 s) in the dark. After the irradiations, samples were wrapped in an aluminum foil and stored until the following experiments were carried out.

Some of the irradiated samples were bleached optically. They were exposed to a 3-W 460-nm LED (OSRAM) or a 254-nm UV tube lamp (DE-4, UVP) for a defined duration of time. In the case of the LED exposure, samples were exposed inside an integrating sphere in order to ensure a uniform exposure over several pieces of sample.

The extent of $Sm^{3+} \rightarrow Sm^{2+}$ conversion upon X-ray irradiation before and after the optical bleaching was read out using a confocal microscopy technique. Details of the readout setup may be found in our prospective papers, but briefly: the excitation light from a 473-nm DPSS laser was guided to the sample with mirrors and an objective lens (20×, 0.75 NA, Plan Apo, Nikon), then the beam was focused to a point at 20 μm depth inside the samples. The resulting PL emissions from the Sm^{3+} and Sm^{2+} ions were guided back through the objective lens, optical filters and a pinhole towards two individual photomultiplier tubes (PMT; R1477-06, Hamamatsu). Optical filters were selected such that one of the PMTs measures the PL emission from Sm^{3+} ions in the range of 570–660 nm ($I_{PMT(3+)}$) and the other measures the PL emission of Sm^{2+} ions in the range of 670–800 nm ($I_{PMT(2+)}$). These two separate signals were measured simultaneously. The intensity at the focal spot of the objective lens was estimated to be ~10 W/cm². Here, the *Response* was defined as follows and used throughout our experiments:

$$Response \equiv \left.\frac{I_{PMT(2+)}}{I_{PMT(3+)}}\right|_{irradiated} - \left.\frac{I_{PMT(2+)}}{I_{PMT(3+)}}\right|_{non\text{-}irradiated} \tag{1}$$

where $I_{PMT(2+)}$ and $I_{PMT(3+)}$ are measured signal intensities from the two photomultipliers, which measure PL emissions from Sm^{2+} and Sm^{3+}, respectively. As indicated in the equation, the first term takes into account the signals from irradiated samples; whereas, the second term is for non-irradiated samples, which subtracts the contribution of typical $^4G_{5/2} \rightarrow {}^6H_{11/2}$ emission peak of Sm^{3+} overlapping the $^5D_0 \rightarrow {}^7F_{0,1}$ emissions by Sm^{2+}. As a result, the response value without irradiation is, indeed, zero.

X-ray induced optical absorbance was computed using optical transmittance measurement data of non-irradiated, as-irradiated and photobleached samples recorded on a spectrophotometer (Lambda 900, Perkin Elmer).

TL spectra of irradiated samples were measured using a laboratory-constructed set-up based on an earlier work by Quilty et al. [11]. Two platinum resistive elements (F3101, Omega) were coupled using thermally conductive cement in which one served to heat the sample while the other measured the temperature. The luminescent signal was collected by an objective lens (10×, 0.30 NA, Meopta) and detected by a PMT (R1477-06, Hamamatsu). A data acquisition interface (USB-6009, National Instruments) with a custom Labview® program was used for the PID (Proportional–Integral–Derivative) feedback temperature control and recording data. The contribution of infrared emissions in the TL glow curves, which originates from the heating element above 400 °C, was measured separately and numerically subtracted. The heating rate was selected to be 1 °C/s. The sample size was approximately $1 \times 2 \times 3$ mm³.

3. Results

The valency conversion of Sm ($Sm^{3+} \rightarrow Sm^{2+}$) upon X-ray irradiation may be used as a probe of X-ray dose delivered. After irradiations, the appearance of Sm^{2+} emissions in PL was found for both Sm-doped FP and FA samples. Fig. 1 illustrates the dose response curves, which present response values as a function of delivered X-ray dose, of FP and FA glasses doped with different concentrations of Sm^{3+}. The response values were normalized to be unity at saturation. It is worth noting that every point on these graphs corresponds to an individual piece of sample. Put differently, we avoided building up cumulative doses on a single sample. This approach allows more flexibility in the experiments since we can then also examine post-treatment effects on individual samples. In addition, the latter approach provides samples for TL measurements, as well. Further, by using an individual sample for each point, i.e. for each dose, we avoid the effects of bleaching that would otherwise occur had we used one sample through all dose measurements. In both the host materials, continuous valency conversion was confirmed from a dose of ~1 Gy up to over 1000 Gy, where saturation occurs, thus limiting the dynamic range at the upper end. As seen in Fig. 1, the valence conversion rate as well as the dynamic range seems to vary with the concentration of Sm^{3+} dopant, and appears to be different between FP and FA host matrices. The samples with the highest concentrations of Sm^{3+} (5.0% and 10.0%) are not shown in Fig. 1 because the extent of conversion was so small that the results (or the response) had significant noise. Fig. 2 illustrates response values at saturation against the concentration of Sm^{3+} for both FP and FA glasses. It is clear that the response value at saturation decreases with increasing Sm^{3+} dopant concentration. Namely, the conversion rate seems to decrease for larger Sm concentrations, while the dynamic range appears to be larger for FA than FP glasses. Also, the response values at saturation appear to be independent on the host glass matrix.

Both as-prepared FP and FA samples were visually transparent with slight yellowish coloration. However, upon X-ray irradiations, the samples became darker and the darkening was much stronger in the FP than the FA sample. These observations are summarized

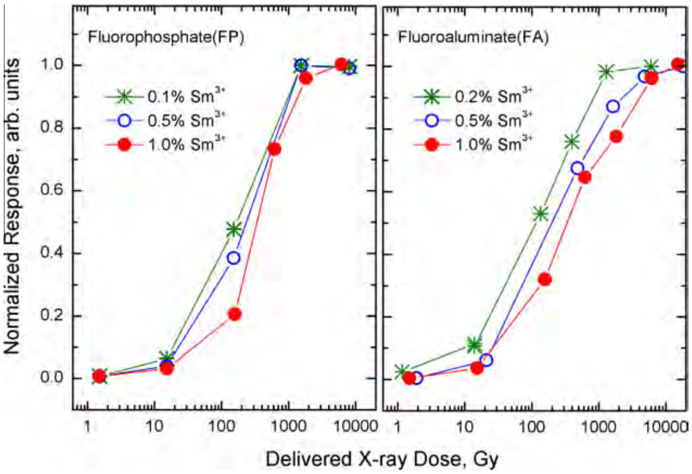

Fig. 1. Dose–response curves of Sm-doped FP and FA glasses with different dopant concentrations. Every plot corresponds to a response value recorded on an individual sample.

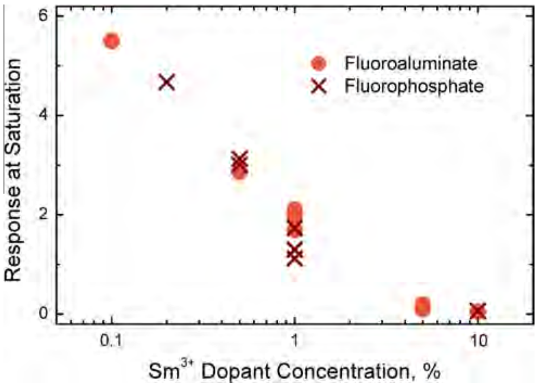

Fig. 2. Response values at saturation against concentration of Sm dopant.

in Fig. 3, which compares X-ray induced absorbance spectra of as-irradiated, blue-exposed and UV-exposed Sm-doped FP and FA samples. The light treatments were carried out after the X-ray irradiation. It is clear that the induced absorbance was stronger in FP glass than that of FA, and blue (~2.7 eV) or UV (~4.9 eV) light treatment reduced the induced absorbance in both the samples. This bleaching effect was more pronounced for UV light treatment.

In Fig. 4, TL glow curves of irradiated Sm-doped FP glass and that of FA glass are compared. The concentration of the initial Sm^{3+} dopant was 1.0%. The dashed lines are Gaussian curve fits. For both FP and FA glasses, the spectra of the TL emission (not shown here) were for the f–f transitions of Sm^{3+} ions. In both the TL spectra, two major peaks were observed; however, an additional number of peaks was present in the FP glass. This may imply the existence of an additional number of charge trapping level in the FP glass compared to that in the FA glass. In addition, the two major TL peaks in FA glass appeared to be at higher temperatures by ~60 °C, with respect to those of FP glass.

Fig. 5 compares the dose response curves of FP and FA samples with and without optical treatments by blue and UV light. To facilitate the comparison, all the graphs were plotted twice: with

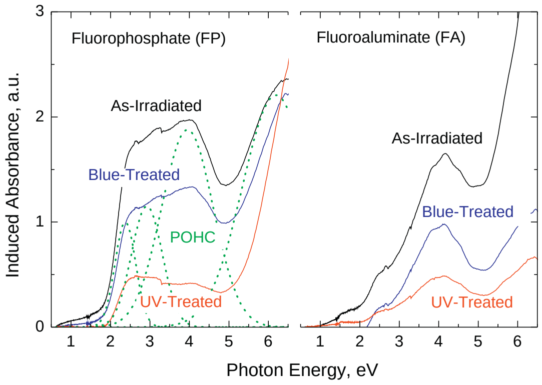

Fig. 3. X-ray induced absorbance of Sm-doped FP and FA. The concentration of Sm for both the glasses was 1%. The dotted curves show a presentation of induced absorbance in FP glass as a sum of Gaussians. Three of them are tentatively associated with phosphorus–oxide hole centers (POHCs) [13].

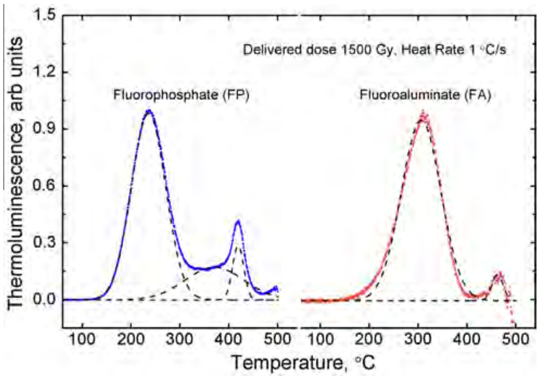

Fig. 4. TL glow curves of irradiated Sm-doped FP and FA glasses. The delivered X-ray dose was about 1500 Gy. The heating rate was 1 °C/s.

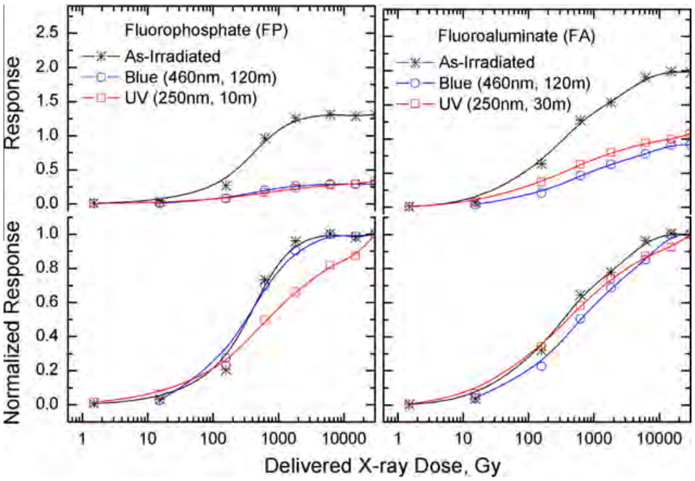

Fig. 5. Dose–response curves of Sm-doped FP and FA glasses before and after optical treatment. The concentration of Sm was 1%. To facilitate comparison all the graphs are plotted twice: with absolute response values (upper part) and with normalized values to that at saturation (lower part). Every plot corresponds to a response value recorded on an individual sample.

absolute response values in the upper part of the figure and with values normalized to that at saturation in the lower part. As can be seen in the upper part of the figure, the absolute values decreased by the optical treatment for the both types of host glass. This effect may be attributed to the optically stimulated conversion of $Sm^{2+} \rightarrow Sm^{3+}$, or commonly referred as photobleaching of Sm^{2+}. In the case of Sm-doped FA glasses, the effects of blue and UV photobleaching on the response curves were approximately the same. On the other hand, the effects of photobleaching on the normalized dose response curves of the FP glass, as shown in the lower part of Fig. 5, depend on whether blue or UV bleaching is used. In particular, the UV treatment of FP glass has led to the disappearance of saturation. But, this comes at the cost of sensitivity.

4. Discussion

The experiments showed that both Sm-doped FP and FA glasses exhibited effective valence conversion of Sm ions under X-ray irradiation. The dynamic range of conversion, i.e. the irradiation dose necessary to reach saturation, exceeded several thousands of Grays which is very promising for dosimetric detector applications in MRT. The conversion *rate* seems to depend on the concentration of Sm dopants and on the composition of host matrix. It is worth noting here that similar dependence on the host environment has also been observed in some crystalline materials [5]. The comparison of Sm-doped FP and FA glasses shows that the conversion reaches saturation at a lower dose in FP than FA glass as seen in Fig. 1. On the other hand, Fig. 2 indicates that the total numbers of converted Sm^{2+} ions were the same for the both hosts. These experimental observations imply that FP is a more sensitive dosimetric material. Below, we will discuss this fact using a charge trapping model and a phosphorous–oxygen hole center (POHC), which is present in an FP glass system.

We assume that Sm^{3+} ions act as electron-trapping centers in order to become Sm^{2+}. X-ray irradiation generates numerous electron–hole pairs. Some of the electrons are captured by Sm^{3+} ions (which then become Sm^{2+}) while the corresponding holes must be captured by some hole-trapping centers to ensure persistent $Sm^{3+} \rightarrow Sm^{2+}$ conversion. Fig. 2 indicates that increasing the concentration of electron-trapping centers (Sm^{3+} ions) did not increase the total number of converted Sm^{2+} ions. Moreover, PL measurements indicated that most of the Sm^{3+} ions stayed unconverted at saturation. These facts imply that, when the conversion reaches its saturation, some of the electron-trapping centers, i.e. Sm^{3+}, are still available to capture electrons, while the hole trapping centers are fully occupied. Therefore, it is safe to say that, in our glass systems, the $Sm^{3+} \rightarrow Sm^{2+}$ conversion process is controlled by a hole-trapping process rather than electron trapping.

There are several models of hole-trapping centers in fluoride glasses. One of them is put forward by Griscom et al. [12]. According to this model, the existence of hole-trapping centers in heavy-metal fluoride glasses is associated with F- and O-ion vacancies. FP glass has O-ions as one of the main compositions, and FA glass may contain O-ions as a foreign impurity. In addition, Ebeling et al. suggest that in FP glass some of the phosphorous–oxygen bonds are converted into POHCs by trapping holes [13]. The POHCs give rise to strong optical absorption bands in the UV region and this was indeed observed in our experiments (Fig. 3). Our TL measurements support this idea as the glow curve in the FP glass showed an additional peak at around 375 °C compared to that of FA. This peak may be associated with the release of holes from POHCs. This conclusion is supported by effective bleaching of induced absorbance by annealing at the same temperature range. A more detailed TL investigation is currently under way.

The same idea of additional hole-trapping center in FP glass may explain the difference in dose–response curves of FP glasses between UV- and blue-treatments shown in Fig. 5. During X-ray irradiation, multiple types of hole capture centers, including POHCs, operate at different speeds or have different time scales. Exposure to UV would bleach POHCs more efficiently than the others, which would lead to a reduction in the concentration of Sm^{2+}. As a result, the dose response curves after UV-treatment represent the Sm valency conversion rate, in arbitrary units, disregarding the effects of POHCs. Further, the Sm-doped FP samples under UV treatment did not show saturation. This implies, in turn, that the POHCs and corresponding number of Sm^{2+} ions populate at a higher rate, which give higher sensitivity to the Sm-doped FP glass with respect to the Sm-doped FA glass. Thus, if there existed no POHCs in FP glass, the dynamic range would be larger. In other words, with the functionality of hole trapping with phosphorous–oxygen bonds, the dynamic range of FP glass may be smaller, but the detector sensitivity is higher. Moreover, FP glass could be used as a "flexible dynamic range" dosimeter material as the dynamic range of FP glass can be enlarged with UV-treatment, at the cost of sensitivity, if needed.

5. Conclusion

We have studied Sm^{3+}-doped FP and FA glasses with varying concentrations of Sm^{3+} dopants as potential X-ray dosimetric detector materials for high-dose high-resolution applications in MRT. This class of dosimeter employs the degree of Sm^{3+} to Sm^{2+} conversion as a measure of delivered X-ray dose. The examination of dynamic ranges of the samples have unveiled excellent coverage of the dose range used in MRT, from $\sim$1 to over 1000 Gy, followed by saturation. When the concentration of Sm^{3+} dopant was higher, the saturation seemed to be reached at a higher dose. In other words, the dynamic range of the detector may be controlled by the doping concentration of Sm^{3+}. Moreover, the saturation dose also seems to depend on the choice of host glass; saturation was reached at a higher dose in FA glass than that in FP. The conversion response was further studied with optical bleaching and TL experiments in order to understand the charge trapping mechanisms. The results indicate that POHC present in FP glass plays a major role in increasing the sensitivity of this Sm-doped glass system.

Acknowledgements

The present research has been performed at the Canadian Light Source, which is supported by NSERC, NRC, the Canadian Institutes of Health Research, the Province of Saskatchewan, Western Economic Diversification Canada, and the University of Saskatchewan. We express our gratitude to NSERC and the New Zealand Ministry for Science and Innovation for financial support, and Teledyne-DALSA for sponsoring the project through an NSERC Strategic Grant.

References

[1] D. Slatkin, P. Spanne, F. Dilmanian, M. Sandborg, Med. Phys. 19 (1992) 1395.
[2] J. Qiu, K. Hirao, J. Mater. Sci. Lett. 20 (2001) 691.
[3] Y. Huang, C. Jiang, K. Jang, H. Lee, E. Cho, M. Jayasimhadri, S. Yi, J. Appl. Phys. 103 (2008) 113519.
[4] S. Fan, C. Yu, D. He, X. Wang, L. Hu, Opt. Mater. Express 2 (2012) 765.
[5] G. Belev, G. Okada, D. Tonchev, C. Koughia, C. Varoy, A. Edgar, T. Wysokinski, D. Chapman, S. Kasap, Phys. Status Solidi C 8 (2011) 2822.
[6] G. Okada, B. Morrell, C. Koughia, A. Edgar, C. Varoy, G. Belev, T. Wysokinski, D. Chapman, S. Kasap, Appl. Phys. Lett. 99 (2011) 121105.
[7] A. Edgar, C.R. Varoy, C. Koughia, D. Tonchev, G. Belev, G. Okada, S.O. Kasap, H. von Seggern, M. Ryan, Opt. Mater. 31 (2009) 1459.
[8] C. Koughia, A. Edgar, C.R. Varoy, G. Okada, H. von Seggern, G. Belev, C.Y. Kim, R. Sammynaiken, S. Kasap, J. Am. Ceram. Soc. 94 (2011) 543.
[9] K. Kawano, B.C. Hong, K. Sakamoto, T. Tsuboi, H.J. Seo, Opt. Mater. 31 (2009) 1353.
[10] H. Ebendorff-Heidepriem, D. Ehrt, Opt. Mater. 18 (2002) 419.
[11] J.W. Quilty, J. Robinson, G.A. Appleby, A. Edgar, Rev. Sci. Instrum. 78 (2007) 083905.
[12] D. Griscom, J. Non-Cryst. Solids 161 (1993) 45.
[13] P. Ebeling, D. Ehrt, M. Friedrich, Opt. Mater. 20 (2002) 101.

JOURNAL OF APPLIED PHYSICS **115**, 063107 (2014)

Optically erasable samarium-doped fluorophosphate glasses for high-dose measurements in microbeam radiation therapy

B. Morrell,[1] G. Okada,[1] S. Vahedi,[1] C. Koughia,[1,a)] A. Edgar,[2] C. Varoy,[2] G. Belev,[3]
T. Wysokinski,[3] D. Chapman,[3] R. Sammynaiken,[4] and S. O. Kasap[1]
[1]*Department of Electrical and Computer Engineering, University of Saskatchewan, Saskatoon, Saskatchewan S7N 5C9, Canada*
[2]*School of Chemical and Physical Sciences and MacDiarmid Institute, Victoria University of Wellington, Wellington 6140, New Zealand*
[3]*Canadian Light Source, Inc., University of Saskatchewan, Saskatoon, Saskatchewan S7N 5C9, Canada*
[4]*Saskatchewan Structural Sciences Centre, University of Saskatchewan, 110 Science Place, Saskatoon, Saskatchewan S7N 5C9, Canada*

(Received 13 October 2013; accepted 25 January 2014; published online 13 February 2014)

Previous work has demonstrated that fluorophosphate (FP) glasses doped with trivalent samarium (Sm^{3+}) can be used as a dosimetric detector in microbeam radiation therapy (MRT) to measure high radiation doses and large dose variations with a resolution in the micrometer range. The present work addresses the use of intense optical radiation at 405 nm to erase the recorded dose information in Sm^{3+}-doped FP glass plates and examines the underlying physics. We have evaluated both the conversion and optical erasure of Sm^{3+}-doped FP glasses using synchrotron-generated high-dose x-rays at the Canadian Light Source. The Sm-ion valency conversion is accompanied by the appearance of x-ray induced optical absorbance due to the trapping of holes and electrons into phosphorus-oxygen hole (POHC) and electron (POEC) capture centers. Nearly complete Sm^{2+} to Sm^{3+} reconversion (erasure) may be achieved by intense optical illumination. Combined analysis of absorbance and electron spin resonance measurements indicates that the optical illumination causes partial disappearance of the POHC and the appearance of new POEC. The suggested model for the observed phenomena is based on the release of electrons during the Sm^{2+} to Sm^{3+} reconversion process, the capture of these electrons by POHC (and hence their disappearance), or by PO groups, with the appearance of new and/or additional POEC. Optical erasure may be used as a practical means to erase the recorded data and permits the reuse of these Sm-doped FP glasses in monitoring dose in MRT. *© 2014 AIP Publishing LLC*.
[http://dx.doi.org/10.1063/1.4864424]

I. INTRODUCTION

Radiation induced valency conversion of rare earth ions in various solids is of great scientific and practical interest. Numerous researches have demonstrated the possibility of valence conversion of different ions in a variety of host materials under different forms of excitation, such as x-ray, γ- and β-irradiation as well as optical excitation.[1–6] Among the rare earth ions, Sm^{3+} to Sm^{2+} conversion is of particular interest because the dominant emission bands of Sm^{3+} and Sm^{2+} ions are readily distinguishable. In addition, all dominant bands are situated in the red region of the spectrum. There is therefore a good match to silicon-based detectors used in optical measurements. Recent work has also demonstrated that Sm^{3+} to Sm^{2+} conversion may provide submicron spatial resolution with respect to optical storage of information.[1,2] Samarium, of course, is not the only rare-earth element that can possess multivalency states, depending on the host medium. Europium is another good example of a multivalent ion whose valence changes can be optically detected.[7,8]

Recently, we have investigated the Sm^{3+} to Sm^{2+} valency conversion in Sm-doped fluorophosphate (FP) and fluoroaluminate glasses for potential use as dosimetric plates with high spatial resolution for Microbeam Radiation Therapy (MRT).[9,10] This is an experimental form of radiation treatment that has the potential to improve the treatment of many types of cancer compared with customary broad-beam radiation treatment; the microbeam that is used in this form of therapy is normally generated at a synchrotron facility.[11–15] The MRT is based on the markedly different responses of tumor and normal cells to this form of treatment at the cell level as recently discussed in a paper by Crosbie *et al*.[16] In practice, the radiation is applied in the form of a grid by passing the highly collimated x-ray beam from a synchrotron through a microplane collimator, which is a stack of parallel plates of two materials with dramatically different x-ray transparencies.[17,18]

The accurate, simultaneous recording of peak and valley doses that differ by hundreds of grays, and the large dose gradients (hundreds of grays over several microns) in the whole x-ray energy range of interest for MRT (50–250 keV) are an extremely challenging task. No current detector can satisfactorily meet all these requirements. The research and

---

[a)]e-mail: cyril.koughia@usask.ca

0021-8979/2014/115(6)/063107/8/$30.00

development of detectors suitable for MRT has therefore become an important goal if MRT is to advance further. Detectors, such as ionization chambers, alanine dosimeters, MOSFET detectors, Gafchromic® films, radiochromic polymers, Thermoluminescence Detectors (TLDs), polymer gels, Fluorescent Nuclear Track Detectors (FNTDs, based on Al_2O_3:C, Mg single crystal detectors), optically stimulated luminescence detectors, and floating gate-based dosimeters have been reviewed with respect to their potential applications in MRT.[19] The latest attempts to solve the problem are based on using damage caused by x-ray irradiation to biological objects,[20] aluminum oxide fluorescent detectors,[21] high resolution optical calorimetry,[22] confocal laser microscopy of the radiophotoluminescence (PL) of silver activated phosphate glass,[23] thermoluminescence of Ge-doped silica fibers,[24] silicon strip detector,[25] and spectromicroscopic film dosimetry.[26] Another novel approach is the valence conversion of rare earth ions embedded in a suitable host material upon irradiation as discussed by the present group.[27]

In an earlier work, we showed the applicability of Sm-doped FP glasses as a potential dosimetric material to measure both the dose and the peak-to-valley dose ratio (PVDR), a critical parameter for successful MRT. We demonstrated the efficiency of $Sm^{3+} \rightarrow Sm^{2+}$ conversion in these glasses and illustrated the feasibility of a spatially resolving dosimetric sensor based on the confocal detection of photoluminescence.[9] We also demonstrated that the effects of irradiation may be erased by annealing at temperatures exceeding the glass transition temperature T_g (= 450–470 °C for these glasses).[10] Meanwhile, annealing at lower temperatures leads to a "thermal enhancement" effect, which was also discussed in detail in Ref. 10. It seems obvious that the use of thermal annealing at temperatures exceeding T_g for the erasure of previously collected information is not a particularly convenient procedure that can be quickly implemented in field, and allow the reuse of the detector soon after it had been irradiated. Therefore, in the present paper, we discuss the possibility of erasure by using intense UV light and discuss the related problems associated with this type of erasure.

Our choice of a fluorophosphate glass as a host for Sm^{3+} is based on three important factors. First, fluorophosphate glasses are known to be good hosts for rare-earth ions and have been of recent scientific interest.[28,29] Secondly, there is considerable published work on Sm^{3+}-doped fluorophosphate glasses, in particular, on their optical properties.[30–32] Thirdly, and most importantly, comparatively few glasses show x-ray induced conversion of Sm^{3+} to Sm^{2+}, as we have reported in previous papers,[10,27] but Sm-doped fluorophosphate glasses show good conversion, even under low dose exposure that can be easily detected by photoluminescence experiments. The latter interesting observation is connected with the formation of hole and electron centers as discussed below. Another relevant observation is the fact that Sm^{3+} ions embedded in various types of polycrystalline samples do seem to convert relative easily to Sm^{2+} when exposed to x-rays.[27] However, polycrystalline samples are not suitable for MRT dosimetery as they do not allow high resolution confocal fluorescence readout from converted Sm^{2+} ions inasmuch as light scattering broadens the detected signal, reducing the effective spatial resolution.

II. EXPERIMENTAL

FP glasses can be thought as a combination of fluoride and phosphate glasses with a variety of possible cationic species. The composition and preparation are based on the FP10 composition published by Ebendorff-Heidepriem.[30] The FP10 batch composition, given in mol. %, is $10.0Sr(PO_3)_2$-$34.4AlF_3$-$10MgF_2$-$30.4CaF_2$-$15.2SrF_2$. The FP10 glasses were doped with Sm^{3+} by adding the SmF_3 in amounts from 0.001 to 0.5 mol. %. The quenched glass samples were cut and polished flat for x-ray and optical measurements.

The x-ray irradiation was performed by two different methods. The first method used a synchrotron radiation at the Biomedical Imaging and Therapy 05B1-1 bend magnet beamline at the Canadian Light Source (CLS), Saskatoon, Canada. The spectrum of filtered x-ray radiation had a maximum around 50 keV.[9] The intensity of synchrotron x-ray irradiation corresponded to an approximate dose rate of 2 Gy/s (±20%). The second irradiation method, which was more convenient, simply used the emission produced by a commercial FAXITRON x-ray tube with a tungsten anode operating at 110 kVp (3 mA filament current) with an approximate dose rate of 0.8 Gy/s. The x-ray tube has a 0.76 mm Be window through which the radiation passed onto the sample, approximately 5 cm from the anode. The mean photon energy was 45.2 keV. The quoted dose rates represent dose in air at the surface of the sample, which is the usual manner in which dose is reported for MRT.

We have also exposed the samples to an x-ray microbeam at the CLS of the type that would be used in MRT. The microbeam was produced by passing a highly collimated x-ray beam through an 8 mm thick Tungsten/Air multislit collimator (MSC) manufactured by Usinage et Nouvelles Technologies, Morbier, France. The microbeams are 50 μm wide and have centre-to-centre distance of 400 μm (which is the spatial periodicity). Further details may be found elsewhere.[9]

The steady-state PL spectra were measured from 200 nm to either 1100 or 1200 nm. For 200–1100 nm measurements, we used a Stellar Net EPP2000 fiber input mini-spectrometer, with a spectral resolution around 4 nm. For 200–1200 nm measurements, we used an ASEQ fiber input mini-spectrometer with spectral resolution better than 1 nm. The excitation source for the photoluminescence spectra was typically a laser diode with an emission wavelength at 405 nm and power 15 mW, which can be used to excite both the Sm^{3+} and Sm^{2+} ions.[33] The intensity of excitation was kept as low as possible to minimize the effect of $Sm^{2+} \rightarrow Sm^{3+}$ reconversion during the measurements. The transmittance spectra were measured using a Perkin-Elmer Lambda 900 spectrophotometer. Electron Spin Resonance (ESR) spectroscopy experiments were conducted on a standard Bruker EMX 10/2.7 instrument.

The erasure illumination was typically carried out by using a violet LED operating at 405 nm with power density of ~100 mW/cm² on the sample. In one set of experiments (Figure 1) a laser diode emitting at 405 nm was used, which gave a power density ~30 mW/cm² on the sample.

III. RESULTS AND DISCUSSION

Figure 1 summarizes the essence of the problem that is being addressed. The x-ray microbeam exiting a multislit collimator is made incident on a Sm-doped FP glass plate, and induces Sm^{3+} to Sm^{2+} conversion. The spatial variation of this conversion on the Sm-doped FP glass is recorded and digitized by examining the PL of Sm^{2+} and Sm^{3+} ions, excited by a low power laser diode operating at 470 nm through a confocal scanning fluoroscopic microscope. Numerically, the degree of Sm^{3+} to Sm^{2+} conversion may be characterized by a response ratio function $R(t)$, or simply called "response," defined by

$$R(t) = PL_{Sm^{2+}}(t)/PL_{Sm^{3+}}(t),$$

where $PL_{Sm^{2+}}(t)$ and $PL_{Sm^{3+}}(t)$ are the integrated photoluminescence of Sm^{2+} and Sm^{3+} bands, respectively, which depend on the time (duration) of irradiation t; note that the total dose is proportional to this time t, given that the dose rate is constant. The exact method of calculating the response $R(t)$ is discussed in detail in our previous work.[10,34] Figure 1 shows the spatial distribution of response R after ~5 kGy dose delivered through the multislit collimator as measured by a confocal fluoroscopic microscope. After the dose distribution has been measured, the specimen must be re-initialized for a second measurement. In other words, the results of previous irradiation should be erased so that the glass plate can be reused. We have already shown that the full erasure may be achieved by annealing at temperatures above the glass transition, which is typically around 450–470 °C for FP glasses.[10] An alternative to erasure by annealing is an erasure by an intense optical illumination. Figure 1 shows the general effect of optical erasure by intense illumination at 405 nm for different durations of illumination. Figure 2(a) highlights the effect of erasure by showing the evolution of the PL spectra from an FP10 glass doped with Sm^{3+}. The initial spectrum of "as-prepared" non-irradiated glass contains only emission bands associated with Sm^{3+} ions. X-ray irradiation induces additional bands, typical for Sm^{2+} ions, which are an indication of the partial conversion of Sm^{3+} into Sm^{2+}. The subsequent erasure reduces and, within 20 min, nearly erases all Sm^{2+} emission bands, which suggests the successful reconversion of Sm^{2+} back into Sm^{3+}. Figure 3(a) shows that the process of Sm^{2+} to Sm^{3+} reconversion is relatively fast and, at the given intensity within 50 min, optical illumination reduces the response by a factor of 100, which corresponds to a nearly full erasure.

Figure 4 addresses the issue of reproducibility of response $R(t)$ after erasure. Figure 4 compares the responses $R(t)$ before and after two consecutive cycles of optical erasure. The time of erasure was chosen intentionally short to avoid a complete recovery. It is worth noting that within a given dose range, $R(t)$ vs. dose behavior seems to be a linear function with a unique slope which is unaffected by erasure. This is a very promising result in that it appears as though optical erasure may be a convenient method of reconversion

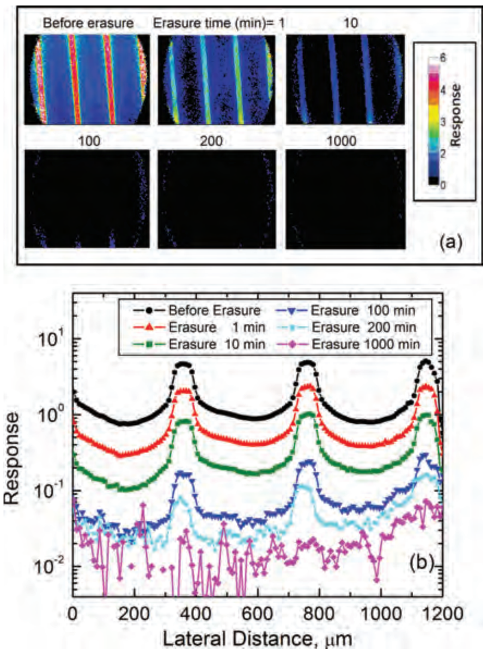

FIG. 1. X-ray irradiation dose profile images (a) two dimensional and (b) one dimensional before and after optical erasure for different durations of erasure illumination. The peak dose was ~5 kGy. PL excitation wavelength was 470 nm. The optical erasure source was a laser diode emitting at a wavelength of 405 nm. The average erasure illumination power density was ~30 mW/cm^2 on the sample.

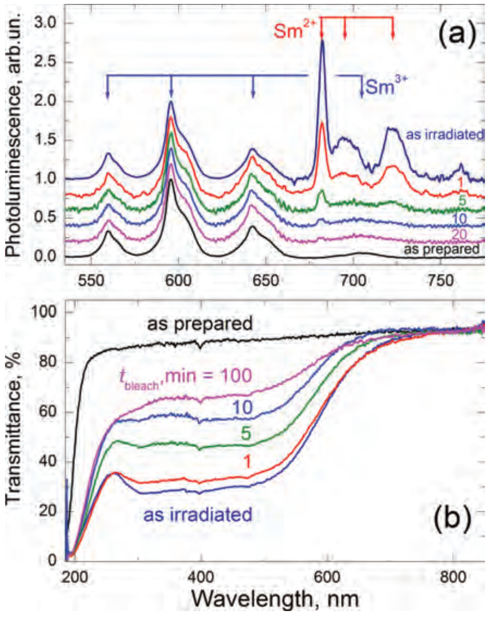

FIG. 2. The effect of intense 405 nm illumination (erasure) on (a) the photoluminescence and (b) optical transmittance of FP10 glass doped with Sm^{3+}, and previously x-ray irradiated for 2 h (total dose delivered was ~14 kGy). The "as-prepared" trace was measured on the same glass prior to x-ray irradiation. "As irradiated" traces refer to the glass prior to any erasure. The times (durations) of erasure are values in minutes indicated above the corresponding curves. The spectra in (a) are shifted vertically to facilitate the comparison. The erasure illumination was at 405 nm (from an LED) with a power density of ~100 mW/cm^2 on the sample.

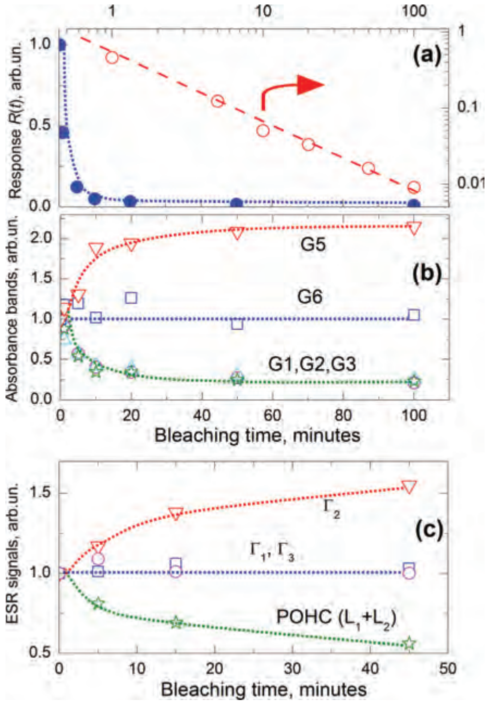

FIG. 3. The effects of intense (~100 mW/cm^2 on the sample) 405 nm illumination (erasure) from an LED (a) on the response $R(t) = \mathrm{PL}(\mathrm{Sm}^{2+})/\mathrm{PL}(\mathrm{Sm}^{3+})$; (b) x-ray induced transmittance; (c) ESR signals in FP10 glasses doped with 0.5% of Sm^{3+} and previously x-ray irradiated for 2 h. All values are shown with respect to their initial values measured in "as irradiated" samples prior to any erasure. (a) Displays the PL twice: in linear and log-log scales. The labeling of Gaussians in (b) is done in accordance with Figure 5 and Table I. The labeling of ESR lines in (c) is done in accordance with Figure 6 and Table II. All lines are guides to the eye.

of Sm^{2+} to Sm^{3+}. However, further experiments, and deeper insight reveal some hidden potential obstacles connected with the creation and transformation of so-called "color centers."

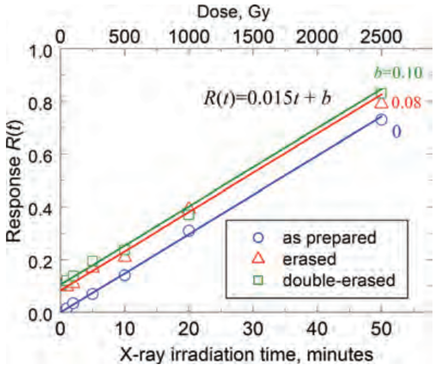

FIG. 4. Response vs. dose behavior, and the influence of x-ray irradiation before and after two consecutive cycles of optical erasure. The values above the curves in the figure show adjustable parameters giving the best fit to experimental data. Notice that the slope of $R(t)$ vs dose is the same in all three cases. (The erasure illumination was at 405 nm from an LED with a power density ~100 mW/cm^2 on the sample)

It is widely known that changes of ion valency due to irradiation are usually accompanied by the formation of ESR and/or optically active defect centers.[35–45] The nature of these centers strongly depends on the nature of the glass itself. As an example, in germanium doped silica, they are usually associated with electrons trapped on germanium or/and silicon at the site of an oxygen vacancy.[46,47] Meanwhile, in heavy metal fluoride glasses, they are usually connected with the presence of neutral fluorine vacancies or interstitial atomic fluorine or impurities (e.g., oxygen).[48] In fluorophosphate glasses of this work, these centers are commonly associated with holes and electrons captured by phosphorous-oxygen complexes.[9,10,30,35,38]

Figure 2(b) shows the effect of x-ray irradiation and subsequent optical erasure on the optical transmittance. It can be clearly seen that the x-ray irradiation significantly reduces the transmittance, while the subsequent erasure partially restores the "status quo." However, even after 100 min of erasure, one can still detect substantial induced absorption. Figure 5 reformulates this effect in terms of induced absorbance and presents a so-called *band separation analysis*, which allows us to quantify the processes of erasure. The technique of band separation presents the induced absorbance as a sum of Gaussians, which may be assigned to different electrons and hole centers.[38,40,49]

Figure 5 shows that in FP glasses, x-ray induced absorbance may be simulated using six overlapping Gaussians. The arrows in Figures 5(b)–5(d) show the evolution of four of the Gaussians under erasure, (b), (c); and annealing, (d). It should be noted that in our earlier work, we used only four Gaussians.[9] There is no contradiction here because the absorbance curve of "as-irradiated" sample alone may be fitted with the same level of accuracy using only four bands (this is shown by a dashed curve in Figure 5(a)). However, the absorbance curves collected during erasure require the additional band marked as G5. Furthermore, it should be emphasized that the band G5 appears also in a band separation analysis of absorbance in the undoped FP sample (with no Sm-doping) that had been just irradiated as shown in Figure 5(e). Meanwhile, the band G4 seems to appear only after thermal annealing as shown in Figure 5(d).

It seems appropriate to mention here that Sm-ions may also contribute to absorption within the 200–600 nm spectral range.[50] However, in our particular case, this contribution seems to be negligible. Indeed, Sm^{3+} is known to have a prominent absorption peak at 400 nm, which may be seen as a tiny feature (a very small dip at 400 nm) in the transmittance spectra in Figure 2(b). Similarly, Sm^{2+} has a peak absorption at around 360–380 nm,[50] but this feature is again negligibly small. The contribution of absorbance from the excitation of Sm-ions has been therefore neglected in the analysis of the absorbance spectra and their evolution during irradiation and bleaching. The inclusion of absorption by Sm-ions does not change the analysis within the margins of error.

Table I compares our results of band separation with published data and shows a very reasonable agreement.[38,40] The only disagreement is the position of the band G6. The disagreement can be explained by the fact that the G6 band could only be captured partially in our experiments, being

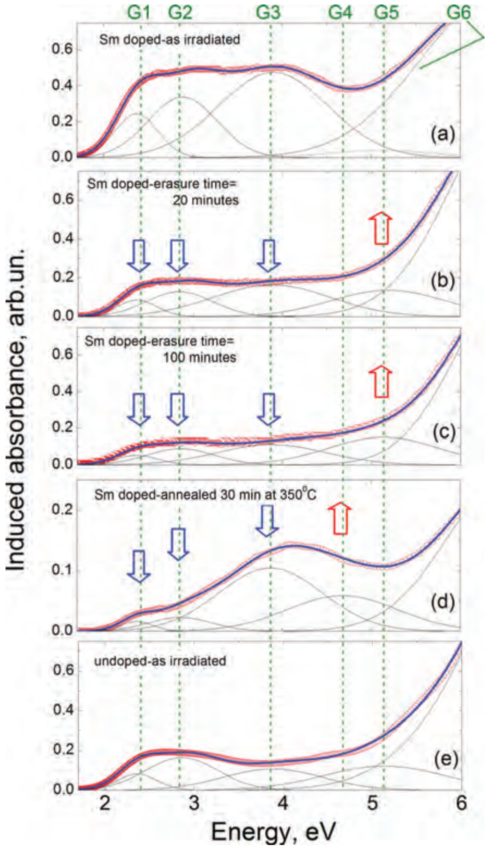

FIG. 5. X-ray induced absorbance in FP10 glass doped with 0.5% of Sm^{3+} and initially x-ray irradiated for 2 h (total dose of ~14 kGy) (a)–(d) and nominally undoped FP10 glass irradiated for 30 min (e). Note that (a)–(c) show the evolution of x-ray induced absorbance under intense 405 nm illumination (erasure). (d) demonstrates the effect of annealing at 350 °C for 30 min. The experimental data (symbols) are approximated by a sum of Gaussians (thick solid lines). The individual Gaussians from G1 to G6 are shown by thin (solid and broken) lines. All Gaussians but G6 are marked at their centers. The center of G6 lies outside of the present figure. The broken line in (a) shows that the presence of the band G5 is not necessary prior to erasure in Sm-doped samples.

TABLE I. The comparison of central wavelengths (λ), central energies (E), and widths (W) of Gaussian absorption bands (G1–G6) observed in the present paper with earlier data by Ebeling *et al.*[40] The widths (W) of Gaussian bands refer to the full width at half maximum (FWHM).

	Present paper			Ebeling *et al.*			
Bands	λ, nm	E, eV	W, eV	λ, nm	E, eV	W, eV	Structural unit
G1	525	2.36 ± 0.03	0.47	540	2.30 ± 0.02	0.50	POHC
G2	433	2.86 ± 0.02	0.74	430	2.89 ± 0.04	1.00	POHC
G3	320	3.88 ± 0.12	1.27	325	3.82 ± 0.04	1.12	POHC
G4	265	4.68 ± 0.09	1.10	265	4.68 ± 0.08	1.00	PO_2
G5	242	5.13 ± 0.02	1.22	240	5.12 ± 0.06	1.00	PO_4
G6	190	6.53 ± 0.08	1.47	210	5.90 ± 0.06	1.00	PO_3

centered outside our spectroscopic range of measurement. In FP glasses, the absorption bands are usually associated with electron and hole capture within phosphorous-oxygen molecular ions or units.[38,40] Table I shows an example of such associations, reproduced from papers published elsewhere.[38,40] Thus, the bands in the visible region (G1–G3) are associated with so-called POHC (phosphorous-oxygen hole centers), while the bands G4, G5, and G6 are supposedly related to PO_2, PO_4, and PO_3 electron centers (POEC), respectively.[40] Figure 3(b) shows the effect of optical illumination (erasure) on the intensities of the Gaussian G1–G6 bands. It shows that the erasure effectively reduces POHC related absorption bands G1–G3, while seemingly leaving the POEC related G6 band unchanged, and surprisingly increases the band G5, seemingly associated with POEC. This is a somewhat discouraging result, because it shows that although an intense optical illumination can successfully reconvert Sm^{2+} back to Sm^{3+}, it leads to the *appearance of new color centers* in the host glass. The new color centers, however, are in the UV range and thus do not prevent the recording of Sm^{3+} and Sm^{2+} PL signals.

Figures 6(a)–6(c) present the ESR signal from our FP10 glass doped with 0.5% of Sm^{3+} and x-ray irradiated for 2 h. It is appropriate to emphasize here that the there was no detectable ESR signal prior to irradiation, and the ESR signal appeared only after x-ray irradiation. For the following interpretation, the experimental data have been approximated by a sum of the first derivatives of four Lorentzians (shown in Figure 6(b)) and six Gaussians (shown in Figures 6(a) and 6(c)). We assume that these ten individual lines belong to five doublets whose spin-Hamiltonian parameters are summarized in Table II. The identification or association of ESR lines was reported previously by Ebeling *et al.*[40] The comparison of present data with the results by Ebeling *et al.*[40] allows us to identify the doublets L_1 and L_2 as belonging to POHC, while the doublets Γ_1, Γ_2, and Γ_3 may be tentatively associated with PO_2, PO_3, and PO_4 complexes, respectively. Figure 3(c) summarizes the influence of optical erasure on the ESR components. It shows that POHC related Lorentzian doublets L_1 and L_2 decrease with erasure, while the POEC related Gaussian doublet Γ_2 increases and Gaussian doublets Γ_1 and Γ_3, also related to POEC, remain seemingly unaffected. Overall, based on the ESR data, the effects of erasure are the same as those based on the band separation analysis above; in other words, optical erasure seems to reduce the POHC while inducing some additional POEC. Note that the lines in Tabel II were used for all ESR spectra that were recorded after each step of bleaching, and only the intensities of the lines change with erasure time (see Figure 3(c)).

From a chemical point of view, we can summarize the effect of optical erasure by a set of chemical reactions in which $h\nu$ represents optical excitation

$$Sm^{2+} + h\nu \rightarrow Sm^{3+} + e^{-}, \tag{1}$$

$$\text{POHC} + e^{-} \rightarrow \text{PO}, \tag{2}$$

$$\text{PO} + e^{-} \rightarrow \text{POEC}, \tag{3}$$

where e^{-} stands for an electron released by Sm^{2+} under optical illumination, PO represents a phosphorus-oxygen based defect

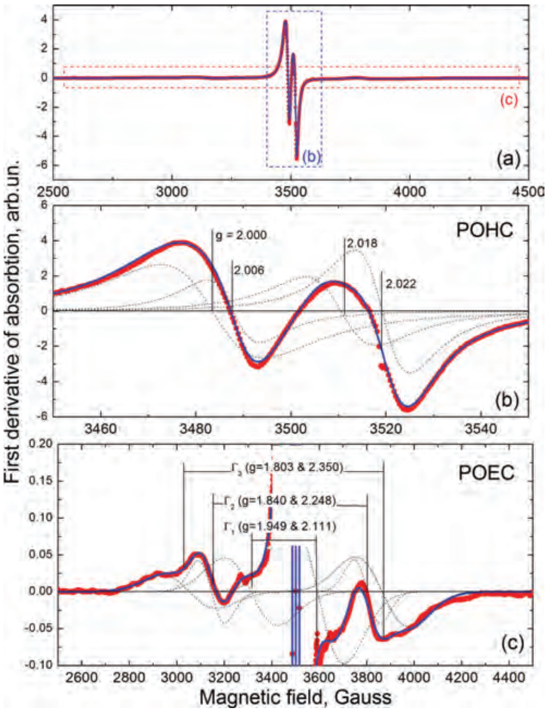

FIG. 6. The ESR signal of FP10 glass doped with 0.5% of Sm^{3+} and x-ray irradiated for 2 h (total dose of ~6 kGy). (a) is an overview of a spectrum where the two rectangles (b) and (c) show the regions which are presented in (b) and (c), respectively. (b) shows strong and narrow lines in the central part of the spectrum, while (c) shows the weak wings of a spectrum. Experimental data (symbols) are approximated by a model (thick solid line) which is a sum of Lorentzians in (b) and Gaussians in (c), shown by thin broken lines. The Lorentzians in (b) are usually associated with phosphorous-oxygen hole centers (POHC), while the Gaussians in (c) represent three doublets (Γ_1-Γ_3) which are normally associated with POEC. The effective g-values shown in the figure correspond to the centers of corresponding Lorentzian and Gaussian components.

precursor, and POHC (POEC) stands for a phosphorus-oxygen center with a captured hole (captured electron for POEC). In other words, Sm^{2+} ions become optically excited and relax to Sm^{3+} with the emission of electrons which are captured by PO precursors, producing POEC with an outcome that depends on the nature of precursor and/or by POHC reconverting to PO groups. We should also emphasize that the above three sets of equations represent an oversimplification of the optical erasure process, because the optical illumination itself may erase and create several types of POHC and POEC.

TABLE II. The lines used for approximating the ESR signals of FP10 glass doped with 0.5% of Sm^{3+} and x-ray irradiated for 2 h. The total dose delivered is ~6 kGy. Three doublets have Gaussian (Γ) and two have Lorentzian (L) lineshapes. $g^{(1)}$ and $g^{(2)}$ are the effective *g*-values for each line of a doublet. g_{average} is the average of $g^{(1)}$ and $g^{(2)}$. *A* is a splitting of two lines of a doublet. *W* is the full width of each line at half maximum. *W* and *A* are defined for a nominal frequency of 9.8 GHz. Possible interpretation of structures related to appropriate doublet is based on comparison with Ebeling *et al.*[40]

Doublets	Γ_1	Γ_2	Γ_3	L_1	L_2
g_{average}	2.030	2.044	2.076	2.014	2.009
A, Gauss	276	695	908	28	31
W, Gauss	251	123	173	28	21
$g^{(1)}$	2.111	2.248	2.350	2.022	2.018
$g^{(2)}$	1.949	1.840	1.803	2.006	2.000
Nature	POEC	POEC	POEC	POHC	POHC

Applying the same rationale to the effect of x-ray irradiation, we can write another set of chemical reactions of the form

$$PO + h^+ \rightarrow POHC, \tag{4}$$

$$Sm^{3+} + e^- \rightarrow Sm^{2+}, \tag{5}$$

$$PO + e^- \rightarrow POEC, \tag{6}$$

where e^- and h^+ stand for electrons and holes generated under x-ray irradiation. In the case of x-ray irradiation, the absorbed x-ray ejects a primary projectile electron, from an inner shell, that ionizes the medium and generates electrons and holes. Equation (6) is a new addition to our previous approach.[9,10] It is worth noting that Eqs. (3) and (6) are identical, which means that certain types of POEC may appear under different types of excitation, in particular, x-ray irradiation and/or optical erasure.

Naturally, Eqs. (1)–(3) and (4)–(6) should be supplemented by a charge conservation condition that can be written as

$$C_{\text{POHC}}(t) = C_{Sm^{2+}}(t) + C_{\text{POEC}}(t), \tag{7}$$

where $C_{\text{POHC}}(t)$, $C_{Sm^{2+}}(t)$, and $C_{\text{POEC}}(t)$ are the concentrations of the species POHC, Sm^{2+}, and POEC, respectively, at any given instant of time *t*. The above equations clearly show that under x-ray irradiation, the electrons are shared between two competing processes: Sm^{3+} to Sm^{2+} conversion and POEC formation.

We still need to answer the question, "What is the maximum Sm^{3+} concentration for a good conversion efficiency?" Figure 7 tries to answer this question. It shows the response *R* as a function of concentration of trivalent samarium $C_{Sm^{3+}}$ for several x-ray doses (*D*) corresponding to different irradiation times. The response is plotted as a function of *D* and $C_{Sm^{3+}}$. Figure 7 shows that there are two distinctive regions in the $R(D,C_{Sm^{3+}})$ vs. $C_{Sm^{3+}}$ dependence. At low concentrations, $R(D,C_{Sm^{3+}}) \approx \text{const}(D)$, which depends on the dose *D*. At higher concentrations, $R(D,C_{Sm^{3+}})$ seems to be inversely proportional to $C_{Sm^{3+}}$, i.e., $R(D,C_{Sm^{3+}}) \propto (C_{Sm^{3+}})^{-1}$. For further interpretation, it seems reasonable to assume that the relative intensity of the PL is approximately proportional to the ratio of the ionic concentrations, i.e., $R(D,C_{Sm^{3+}}) \propto C_{Sm^{2+}}(D)/C_{Sm^{3+}}$, where the constant of proportionality, among other factors, would include the optical oscillator strengths of the PL transitions in Sm^{3+} and Sm^{2+}. Therefore, $R(D,C_{Sm^{3+}}) \approx \text{const}(D)$ means simply that $C_{Sm^{2+}}(D) \propto C_{Sm^{3+}}$. In other words, the more Sm^{3+} we add, the more Sm^{2+} conversion takes place within a given irradiation time, that is, at a given dose rate. Meanwhile, $R(D,C_{Sm^{3+}}) \propto (C_{Sm^{3+}})^{-1}$ should be interpreted as $C_{Sm^{2+}}(D) \approx \text{const}(D)$. The

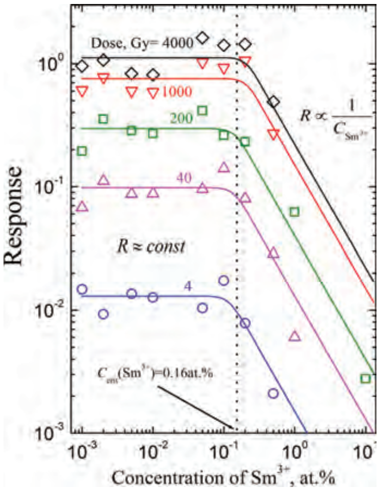

FIG. 7. Response $R = PL(Sm^{2+})/PL(Sm^{3+})$ of FP 10 glass at different delivered doses versus doping (Sm^{3+}) concentration. The PL excitation wavelength was 470 nm.

latter constant depends only on the dose D and does not depend on $C_{Sm^{3+}}$. From a practical view, this result means that the addition of Sm^{3+} over a critical concentration, $C_{crit}(Sm^{3+})$, does not create additional converted Sm^{2+}, and further doping may be considered ineffectual.

The above observation may be explained by the concentration quenching effect, which typically starts to set in at around the concentration where the graph in Figure 7 has a "knee" (begins rolling off), i.e., 0.5–5%, where one rare earth ion has a good chance of being sufficiently close to another rare earth ion to be able to affect the radiative transition. This effect would be dose independent, as observed. We would expect that for "high" concentrations of Sm^{3+}, the Sm^{2+} could relax from its excited states through a Forster-Dexter type mechanism,[51] giving its energy to a nearby Sm^{3+}, assisted by the overlap between a broad 5*d* band and the sharp 4*f* lines. This would certainly reduce the PL intensity ratio for Sm^{2+}/Sm^{3+} through both the numerator and denominator. Alternatively, the luminescence saturation effect may be connected with the host glass itself where the number of sites for Sm^{3+} to Sm^{2+} conversion may be limited by the organization of the host glass ionic network. In any case, further experiments are needed to shed light on the possible origins of "the concentration quenching" effect.

IV. CONCLUSIONS

X-ray induced Sm^{3+} to Sm^{2+} valence conversion in Sm^{3+}-doped FP glasses, and subsequent reconversion of Sm^{2+} to Sm^{3+} under intense optical illumination, has been investigated for potential use in a re-useable dosimetric detector for MRT. It was shown that x-ray irradiated Sm-doped FP glasses can be optically erased by illumination under 405 nm light so that they can be reused in measuring the dose in microbeam radiation therapy. The Sm^{3+} to Sm^{2+} valence conversion is accompanied by the formation of POHC and POEC responsible for x-ray induced optical absorbance. The use of intense optical illumination seemingly achieves near-complete Sm^{2+} to Sm^{3+} reconversion. However, the examination of optical transmission spectra shows that optical illumination only partially erases existing x-ray induced bands, and, at the same time, induces new absorbance bands. We have used a band-separation analysis to interpret the induced absorbance, based on reported possible defect structures in the literature. Combined analysis of absorbance and ESR measurements indicates the optically stimulated erasure of POHC related defects and the development of new POEC related defects. The suggested model for the observed phenomena is based on the release of electrons during Sm^{2+} to Sm^{3+} reconversion, the capture of these electrons by POHC (and hence their disappearance) or by PO groups (with the appearance of additional EC defects). The latter conclusion shows that the direct x-ray induced Sm^{3+} to Sm^{2+} conversion seems to be directly competing with POEC formation. The conversion ratio (the response of the detector) does not depend on the initial concentration of Sm^{3+} in the glass up to a certain critical concentration $C_{crit}(Sm^{3+}) \approx 0.16$ at. %. Beyond this critical concentration, it monotonically decreases with the Sm^{3+} concentration. The latter observation may be connected with the concentration quenching effect, which usually occurs at similar concentrations or with the host glass itself where the number of possible sites for the Sm^{3+} to Sm^{2+} conversion may be limited by the organization of the host glass ionic network.

ACKNOWLEDGMENTS

We thank NSERC and the New Zealand Ministry of Business, Innovation and Employment for financial support and Teledyne-DALSA for sponsoring the project through NSERC. (Irradiation experiments described in this paper were performed at the Canadian Light Source, which is supported by NSERC, NRC, the Canadian Institutes of Health Research, the Province of Saskatchewan, Western Economic Diversification, Canada, and the University of Saskatchewan.)

[1] K. Miura, J. Qiu, S. Fujiwara, S. Sakaguchi, and K. Hirao, Appl. Phys. Lett. **80**, 2263 (2002).
[2] J. Lim, M. Lee, and E. Kim, Appl. Phys. Lett. **86**, 191105 (2005).
[3] A. Z. M. S. Rahman, X. Cao, L. Wei, B. Wang, R. Yu, Z. Chen, G. An, and A. Sidike, Appl. Phys. A **111**, 587 (2013).
[4] E. Malchukova, B. Boizot, G. Petite, and D. Ghaleb, J. Non-Cryst. Solids **353**, 2397 (2007).
[5] Y. Huang, C. Jiang, K. Jang, H. Sueb, E. Cho, M. Jayasimhadri, and S.-S. Yi, J. Appl. Phys. **103**, 113519 (2008).
[6] C. A. G. Kalnins, H. Ebendorff-Heidepriem, N. A. Spooner, and T. M. Monro, J. Am. Ceram. Soc. **94**, 474–477 (2011).
[7] C. Passlick, O. Muller, D. Lutzenkirchen-Hecht, R. Frahm, J. A. Johnson, and S. Schweizer, J. Appl. Phys. **110**, 113527 (2011) and references therein, as an example.
[8] B. Henke, C. Passlick, P. Keil, J. A. Johnson, and S. Schweizer, J. Appl. Phys. **106**, 113501 (2009).
[9] G. Okada, B. Morrell, C. Koughia, A. Edgar, C. Varoy, G. Belev, T. Wysokinski, D. Chapman, and S. Kasap, Appl. Phys. Lett. **99**, 121105 (2011).
[10] S. Vahedi, G. Okada, B. Morrell, E. Muzar, C. Koughia, A. Edgar, C. Varoy, G. Belev, T. Wysokinski, D. Chapman, and S. Kasap, J. Appl. Phys. **112**, 073108 (2012).

[11] D. N. Slatkin, F. A. Dilmanian, P. Spanne, and M. Sandborg, Med. Phys. **19**, 1395 (1992).

[12] F. A. Dilmanian, P. Romanelli, Z. Zhonge, R. Wang, M. E. Wagshul, J. Kalef-Ezra, M. J. Maryanski, E. M. Rosen, and D. J. Anschel, Eur. J. Radiol. **68**, S129 (2008).

[13] P. Deman, M. Vautrin, M. Edouard, V. Stupar, L. Bobyk, R. Farion, H. Elleaume, C. Remy, E. L. Barbier, F. Esteve, and J.-F. Adam, Int. J. Radiat. Oncol., Biol., Phys. **82**, e693 (2012).

[14] A. Bouchet, A. Boumendjel, E. Khalil, R. Serduc, E. Brauer, E. A. Siegbahn, J. A. Laissueg, and J. Boutonnath, J. Synchrotron Radiat. **19**, 478 (2012).

[15] E. Brauer-Krisch, R. Serduc, E. A. Siegbahn, G. Le Duc, Y. Prezado, A. Bravin, H. Blattmann, and J. A. Laissue, Mutat. Res. **704**, 160 (2010).

[16] J. C. Crosbie, R. L. Anderson, K. Rothkamm, C. M. Restall, L. Cann, S. Ruwanpura, S. Meachem, N. Yagi, I. Svalbe, R. A. Lewis, B. R. G. Williams, and P. A. W. Rogers, Int. J. Radiat. Oncol., Biol., Phys. **77**, 886 (2010).

[17] M. Torikoshi, Y. Ohno, N. Yagi, K. Umetani, and Y. Furusawa, Eur. J. Radiol. **68**, S114 (2008).

[18] E. Bräuer-Krisch, H. Requardt, T. Brochard, G. Berruyer, M. Renier, J. A. Laissue, and A. Bravin, Rev. Sci. Instrum. **80**, 074301 (2009).

[19] E. Bräuer-Krisch, A. Rosenfeld, M. Lerch, M. Petasecca, M. Akselrod, J. Sykora, J. Bartz, M. Ptaszkiewicz, P. Olko, A. Berg, M. Wieland, S. Doran, T. Brochard, A. Kamlowski, G. Cellere, A. Paccagnella, E. A. Siegbahn, Y. Prezado, I. Martinez-Rovira, A. Bravin, L. Dusseau, and P. Berkvens, AIP Conf. Proc. **1266**, 89 (2010).

[20] K. Rothkamm, J. C. Crosbie, F. Daley, S. Bourne, P. R. Barber, B. Vojnovic, L. Cann, and P. A. W. Rogers, PLoS One **7**(1), e29853 (2012).

[21] J. A. Bartz, G. J. Sykora, E. Bräuer-Krisch, and M. S. Akselrod, Radiat. Meas. **46**, 1936 (2011).

[22] T. Ackerly, J. C. Crosbie, A. Fouras, G. J. Sheard, S. Higgins, and R. A. Lewise, J. Instrum. **6**, P03003 (2011).

[23] D. Maki, T. Ishii, F. Sato, Y. Kato, T. Yamamoto, and T. Iida, Radiat. Prot. Dosim. **144**, 222 (2011).

[24] A. T. AbdulRahman, D. A. Bradley, S. J. Doran, B. Thierry, E. Bräuer-Krisch, and A. Bravin, Nucl. Instrum. Methods Phys. Res., Sect. A **619**, 167 (2010).

[25] M. Petasecca, A. Cullen, I. Fuduli, A. Espinoza, C. Porumb, C. Stanton, A. H. Aldosari, E. Bräuer-Krisch, H. Requardt, A. Bravin, V. Perevertaylo, A. B. Rosenfeld, and M. L. F. Lerch, J. Instrum. **7**, P07022 (2012).

[26] N. Nariyama, T. Ohigashi, K. Umetani, K. Shinohara, H. Tanaka, A. Maruhashi, G. Kashino, A. Kurihara, T. Kondob, M. Fukumoto, and K. Ono, Appl. Radiat. Isot. **67**, 155 (2009).

[27] G. Belev, G. Okada, D. Tonchev, C. Koughia, C. Varoy, A. Edgar, T. Wysokinski, D. Chapman, and S. Kasap, Phys. Status Solidi C **8**, 2822 (2011).

[28] Y. Tian, R. Xu, L. Hu, and J. Zhang, J. Appl. Phys. **111**, 073503 (2012).

[29] L. Zhang, Z. Yang, Y. Tian, J. Zhang, and L. Hu, J. Appl. Phys. **110**, 093106 (2011).

[30] H. Ebendorff-Heidepriem and D. Ehrt, Opt. Mater. **18**, 419 (2002).

[31] V. Venkatramu, P. Babu, C. K. Jayasankar, Th. Troster, W. Sievers, and G. Wortmann, Opt. Mater. **29**, 1429 (2007).

[32] C. R. Kesavulu and C. K. Jayasankar, J. Lumin. **132**, 2802 (2012).

[33] A. Edgar, C. R. Varoy, C. Koughia, G. Okada, G. Belev, and S. Kasap, J. Non-Cryst. Solids **377**, 124 (2013).

[34] G. Okada, S. Vahedi, B. Morrell, C. Koughia, G. Belev, T. Wysokinski, D. Chapman, C. Varoy, A. Edgar, and S. Kasap, Opt. Mater. **35**, 1976 (2013).

[35] D. L. Griscom, E. J. Friebele, K. J. Long, and J. W. Fleming, J. Appl. Phys. **54**, 3743 (1983).

[36] L. D. Bogomolova, Yu. G. Teplyakov, V. A. Jachkin, V. L. Bogdanov, V. D. Khalilev, F. Caccavale, and S. Lo Russo, J. Non-Cryst. Solids **202**, 178 (1996).

[37] T. V. Bocharova, G. O. Karapetyan, A. M. Mironov, N. M. Mishchenkov, and N. O. Tagil'tseva, Inorg. Mater. **42**(6), 671–680 (2006).

[38] D. Ehrt, P. Ebeling, and U. Natura, J. Non-Cryst. Solids **263–264**, 240–250 (2000).

[39] K. Tanimura, W. A. Sibley, M. Suscavage, and M. Drexhage, J. Appl. Phys. **58**, 4544 (1985).

[40] P. Ebeling, D. Ehrt, and M. Friedrich, Opt. Mater. **20**, 101 (2002).

[41] J. Qiu, Y. Shimizugawa, Y. Iwabuchi, and K. Hirao, Appl. Phys. Lett. **71**, 759 (1997).

[42] N. Ollier, B. Boizot, P. L'henoret, S. Guillous, and G. Petite, J. Appl. Phys. **105**, 113515 (2009).

[43] T. V. Bocharova, G. O. Karapetyan, A. M. Mironov, N. O. Tagil'tseva, and V. D. Khalilev, Glass Phys. Chem. **29**, 7 (2003).

[44] L. Yang, N. Da, D. Chen, Q. Zhao, X. Jiang, C. Zhu, and J. Qiu, J. Non-Cryst. Solids **354**, 1353 (2008).

[45] J. Qiu, K. Nouchi, K. Miura, T. Mitsuyu, and K. Hirao, J. Phys.: Condens. Matter **12**, 5061 (2000).

[46] E. J. Friebele, D. L. Griscom, and G. H. Sigel, Jr., J. Appl. Phys. **45**, 3424 (1974).

[47] J. X. Wen, W. Y. Luo, Z. Y. Xiao, T. Y. Wang, Z. Y. Chen, and X. L. Zeng, J. Appl. Phys. **107**, 044904 (2010).

[48] D. L. Griscom, J. Non-Cryst. Solids **161**, 45 (1993).

[49] P. W. Levy, J. Am. Ceram. Soc. **43**, 389 (1960).

[50] A. Edgar, C. R. Varoy, C. Koughia, D. Tonchev, G. Belev, G. Okada, S. O. Kasap, H. von Seggern, and M. Ryan, Opt. Mater. **32**, 266 (2009).

[51] *Luminescent Materials*, edited by G. Blasse and B. C. Grabmaier (Springer-Verlag, Berlin, New York, 1994), Chap. 5, pp. 90–107.

journal

J. Am. Ceram. Soc., **97** [7] 2147–2153 (2014)
DOI: 10.1111/jace.12938

Samarium-Doped Oxyfluoride Glass-Ceramic as a New Fast Erasable Dosimetric Detector Material for Microbeam Radiation Cancer Therapy Applications at the Canadian Synchrotron

Go Okada,[‡] Jumpei Ueda,[§,¶] Setsuhisa Tanabe,[§] George Belev,[‖] Tomasz Wysokinski,[‖] Dean Chapman,[††]
Dancho Tonchev,[‡] and Safa Kasap[‡,†]

[‡]Department of Electrical and Computer Engineering, University of Saskatchewan, Saskatoon, SK, Canada

[§]Graduate School of Human and Environmental Studies, Kyoto University, Kyoto, Japan

[¶]Graduate School of Global Environmental Studies, Kyoto University, Kyoto, Japan

[‖]Canadian Light Source Inc., Saskatoon, SK, Canada

[††]Department of Anatomy and Cell Biology, University of Saskatchewan, Saskatoon, SK, Canada

There is a special need to develop a dosimetry technique with a large-dynamic range and high-spatial resolution to characterize the microstructured X-ray beams used in microbeam radiation therapy (MRT) for cancer. We report the synthesis and characterization of oxyfluoride glass-ceramic (SiO_2–Al_2O_3–CaF_2–CaO–SmF_3) plates, which contain trivalent-samarium-doped calcium fluoride (CaF_2:Sm^{3+}) nanocrystals, for use as a dosimetric detector material, particularly for MRT applications. Our approach utilizes the extent of $Sm^{3+}\rightarrow Sm^{2+}$ valence reduction caused by X-ray irradiation as a probe of the X-ray dose delivered; and confocal fluorescent microscopy is used to read out the distribution of valence reduction through the photoluminescence (PL) signal. Our study showed that the $Sm^{3+}\rightarrow Sm^{2+}$ valence reduction takes place in CaF_2 nanocrystals, but not in the glass matrix. The Sm^{2+} shows PL emission predominantly due to the fast $4f^55d^1\rightarrow{}^7F_0$ transition, which allows us to read out the detector plate at a high scanning speed. Further, our experiments showed that the detection dose range reaches several thousands of grays, and X-ray dose distribution is detected at a micrometer scale. In addition, the Sm^{2+} signal can be erased either by heating the irradiated sample at a suitable high temperature or by exposing it to UV light; and the erased glass-ceramic plate is reusable. The new Sm-doped oxyfluoride glass-ceramic with CaF_2 nanocrystals reported in this work shows potential for practical use in high-dose and high-resolution dosimetry for MRT.

I. Introduction

MICROBEAM radiation therapy (MRT)[1–5] has recently attracted much attention as a promising new technique for cancer therapy. A specialized X-ray dosimetry technique that is capable of measuring high doses with a high spatial resolution is required for monitoring the dose profile in MRT to advance it to the clinical trial stage. The MRT utilizes an intense and microstructured X-ray beam (known as a microbeam), which requires the dosimetry technique to have submicrometer of X-ray image resolving power and a wide range of dose detection capability (a large dynamic response) at least from 5 to 1000 Gy.[6] In the past few years, we have proposed and demonstrated an approach based on monitoring the samarium (Sm)-valence reduction.[7–12] Our dosimetry technique mainly consists of two parts: (1) confocal fluorescence microscopy for high-resolution image readout; and (2) Sm^{3+}-doped material as a dosimetric detector, which undergoes $Sm^{3+}\rightarrow Sm^{2+}$ reduction as a result of X-ray irradiation. Here, the dose profile of the X-ray beam is recorded on the detector plate as an extent of Sm-valence reduction, and then the recorded dose information is read out by confocal microscopy via the photoluminescence (PL) signal of Sm ions. Potential dosimeter materials are clearly those that allow the $Sm^{3+}\rightarrow Sm^{2+}$ reduction to occur under irradiation; examples of irradiation include X-rays,[13–15] gamma-rays[16], and intense infrared femtosecond laser.[17] Among those materials, we have tested several Sm-doped crystals, glass-ceramics, and glasses including Sm-doped fluorophosphate (FP) and fluoroaluminate (FA) glasses.[7–12] Among the glasses, the Sm-doped FP and FA glasses have been found to be successful dosimetric materials for this particular application. The valence reduction in Sm^{3+} by X-ray irradiation was confirmed, and the dose measurement range was demonstrated to cover doses over a thousand of grays. Moreover, the fine X-ray pattern used in MRT was successfully recorded and read out by confocal fluoroscopic microscopy.

Oxyfluoride glass-ceramics containing CaF_2 nanocrystals have been widely studied with various rare-earth dopants for applications such as up-conversion, quantum cutting, etc.[18–25] The CaF_2 crystal is of particular interest as a host for the Sm^{3+} ion because earlier studies have reported that Sm^{3+}-doped CaF_2 crystals show the $Sm^{3+}\rightarrow Sm^{2+}$ reduction by X-ray irradiation,[26–30] as well as Sm^{2+} ions in the CaF_2 crystal is known to show PL due to the parity-allowed $5d\rightarrow 4f$ transition,[31] the lifetime of which is typically on the order of nanoseconds.[32,33] The PL lifetime is one of the key parameters that limit the readout speed as the detector sample is scanned point-by-point. Many materials that exhibit the $Sm^{3+}\rightarrow Sm^{2+}$ reduction by X-ray irradiation seem to typically show a PL lifetime on the order of milliseconds due to the parity-forbidden *f–f* transitions.

The aim of this work was the synthesis, characterization, and dosimetric testing of an oxyfluoride glass-ceramic containing CaF_2:Sm^{3+} nanocrystals as a new potential dosimeter material to be used for MRT applications. It should be emphasized that Sm-doped glasses and glass-ceramics in this

---

J. McKittrick—contributing editor

Manuscript No. 34020. Received October 25, 2013; approved March 3, 2014.

[†]Author to whom correspondence should be addressed. e-mail: safa.kasap@usask.ca

work are not necessarily limited to applications in MRT, inasmuch as Sm-doped materials have, in recent years, been widely studied for a variety of optoelectronic applications such as X-ray imaging phosphors,[34–37] optical waveguides,[38,39] three-dimensional optical memories,[40–42] pressure sensors,[43,44] white LEDs,[45–48] and solar cells.[45,49,50]

II. Experimental Procedure

An oxyfluoride glass was prepared by a conventional melt-quenching method as described elsewhere.[18,19] The starting materials ($45SiO_2–20Al_2O_3–22CaF_2–10CaCO_3–3SmF_3$, in mol.%) were melted in an alumina crucible at 1400°C for 1 h and then quenched on a preheated stainless plate at 200°C to create an oxyfluoride glass. The quenched glass product was then annealed at 500°C for 1 h to relieve the internal strains arising from quenching.

The thermal properties of the prepared glass sample was studied by differential scanning calorimetry (DSC) (DSC8270; Rigaku, Tokyo, Japan) at a heating rate of 10°C/min. As-prepared samples were subsequently heat-treated to nucleate and grow CaF_2 nanocrystals. The heat-treatment temperature was determined based upon the result of DSC measurement and described in the following section. The structural studies involved scanning electron microscopy (SEM) (JSM-890; JEOL, Peabody, MA) and X-ray diffraction (XRD) (XRD-6000; Shimadzu, Kyoto, Japan) measurements to examine whether the heat-treated glass samples contain nanocrystals and to determine the crystal type and estimate the average crystal size. For XRD analysis, we used $CuK_{\alpha1}$ X-ray characteristic emission, and the scan rate was 2.0°/min.

To investigate the valence reduction in Sm ions by X-irradiation, we exposed as-prepared and heat-treated samples under an X-ray tube (43855D; Faxitron X-Ray LLC, Lincolnshire, IL) set to 110 kVp with the filament current of 3 mA. The air kerma dose was experimentally measured to be ~50 Gy/min using an ionization chamber (Model 96030; Keithley, Cleveland, OH). We measured the optical transmittance using a spectrophotometer (Lambda 900 spectrophotometer; Perkin Elmer, Waltham, MA), and PL emission and excitation spectra using a Shimadzu photospectrometer (RF5000; Shimadzu). Furthermore, the lifetime of the PL emission was measured using a fluorescence lifetime spectrometer (Quantaurus-Tau C11367; Hamamatsu Photonics, Hamamatsu, Japan).

Selected samples were further studied to demonstrate the ability of the present material system as a dosimeter material for MRT application at the Canadian Light Source (CLS), that is, the Canadian synchrotron in Saskatoon. High-dose X-ray irradiations were performed at the Biomedical Imaging and Therapy (BMIT; 05B1-1) beamline at the CLS. The dose rate as air kerma was experimentally estimated to be ~1.7-1.9 Gy/s at 250 mA of the storage ring current using an ionization chamber,[51] and the dose rate was used for our total dose estimation delivered to the sample during irradiation experiments. Note that the term *dose*, here, refers to the total dose, that is, accumulated dose, as the sample exposure time is prolonged to accumulate more dose. Further, the quoted dose value are for dose in air at the surface of the sample The X-ray beam was filtered by a series of Cu filters with an effective thickness of 0.94 mm, which results in the spectrum with a peak energy of 50 keV and a full width at half maximum (FWHM) is approximately 25 keV (see the inset of Fig. 8). Heat-treated samples were cut in several pieces and polished, and then each sample was irradiated by a broad X-ray beam at various dose-values for dose–response measurements. Another set of samples was irradiated by a microbeam (of the type used in MRT) for a dose profile measurement. The microbeam was created by inserting a multislit collimator (a block of tungsten with 75 slits of 50 μm width and 400 μm of center-to-center distance, manufactured by Usinage et Nouvelles Technologies, Morbier, France) in the broad X-ray beam. The distance between the multislit collimator and sample was 1.0 m. After the irradiation, each sample was wrapped in an aluminum foil to avoid exposure to light until readout. The response ($Sm^{3+} \rightarrow Sm^{2+}$ upon irradiation) of each irradiated sample was measured by a confocal microscopy readout setup as two PL signals, one from Sm^{3+} and the other from Sm^{2+}. The brief description of the readout setup can be found elsewhere,[8,10] and the detailed description will be reported in a future paper. A 470-nm diode-pumped solid-state laser was used as the excitation source in these measurements. The confocal microscope setting was such that the signal originated from a spot at the fixed depth of about 20 μm from the surface of sample.

Furthermore, the reusability of the Sm-doped glass-ceramic material as a dosimetric detector was also tested. A reusable dosimetric material requires having the ability to reconvert the reduced Sm^{2+} ions to Sm^{3+} ions as well as the ability to have, after the erasure, the same response behavior as before. In this research, the erasure was tested by two methods: thermal and optical treatments. We have used an electric furnace (CFM1100; MTI Corporation, Richmond, CA) to heat the sample, in which the sample was placed in a crucible to prevent radiative heat exposure. For the optical erasure, an UV fluorescent lamp from an erasable programmable read only memory eraser (DE-4; UVP, Upland, CA) was used. The UV light source has the main emission at 254 nm, and the optical irradiance incident on the sample was ~ 10 mW/cm^2. PL spectrum was measured with a CCD spectrometer (EPP2000; StellarNet Inc, Tampa, FL) to observe the change in PL upon X-ray irradiation and erasure. He–Ne laser (31-2082-000; Coherent Inc., Santa Clara, CA) operating at 633 nm was used as an excitation source to excite Sm^{2+} ions (Sm^{3+} is not excited by this excitation wavelength).

III. Results and Discussion

(1) Thermal and Structural Properties

The DSC curve shown in Fig. 1 indicates a glass-transition (T_g) at 608°C and two crystallization peak temperatures at 687°C (T_{p1}) and at 853°C (T_{p2}) where the crystallization rate is maximum, as marked on the thermogram. These characteristics are typical for a glass which can be transformed into a glass-ceramic by an appropriate heat treatment; the exothermic peak at the lower temperature in Fig. 1 typically corresponds to the nucleation and growth of nanocrystals, whereas the one at the higher temperature corresponds to the crystallization of the glass matrix as discussed in various papers in the literature; see for example Refs. [37,52].

The XRD results are illustrated in Fig. 2 for samples that are (a) as-prepared, (b) heat-treated at 700°C for 4 h and (c) heat-treated at 750°C for 30 min. Figure 2(a) shows only a broad halo peak at $2\theta \approx 27°$ for the as-prepared glass sample, the signature of which is typical for an amorphous structure. However, for those samples which have been heat-treated at the temperatures between T_{p1} and T_{p2}, at 700°C for 4 h and 750°C for 30 min, additional sharp diffraction peaks were detected as in Figs. 2(b) and (c), respectively. The diffraction pattern agrees with the standard card data for the CaF_2 crystal (JCPDS 35-0816), indicated at the bottom of the figure. These peaks are, as expected, attributed to the CaF_2 crystals which are embedded in the glass matrix; we effectively have a glass-ceramic structure. The average linewidths for the (1 1 1), (2 2 0), and (3 1 1) diffraction peaks were used to estimate the mean diameter of crystal grains using the Scherrer relation.[53] It is important to emphasize that this is only an estimate inasmuch as one should also account for the strain in the nanocrystals as, for example, in the case of $BaBr_2$ nanocrystals in Ref. [54]. In our case, the instrumental broadening of diffraction peaks has been estimated by measuring the diffraction pattern from a standard Si powder material in which the grain size is known. The estimated average nanocrystal sizes were 37.4 and 145.0 nm

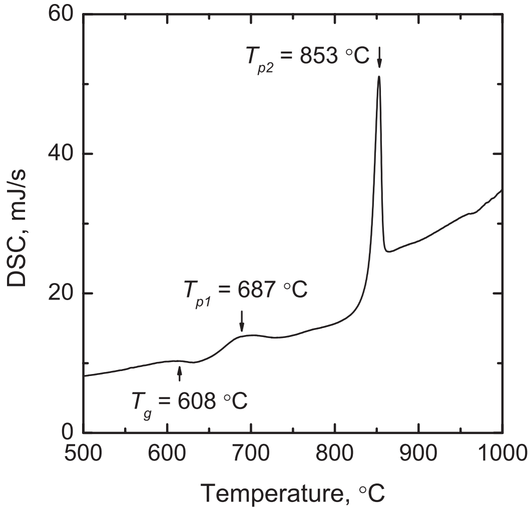

Fig. 1. Differential scanning calorimetry curve of as-prepared glass sample $45SiO_2–20Al_2O_3–22CaF_2–10CaO–3SmF_3$. Exothermic heat flow is upwards.

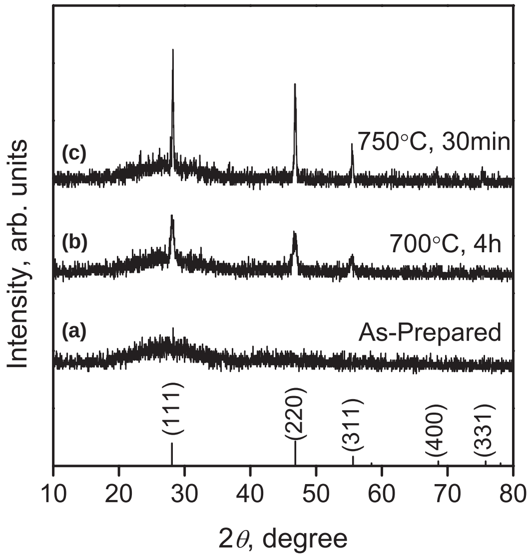

Fig. 2. X-ray diffraction curves of samples: (a) as-prepared, (b) heat-treated at 700°C for 4 h, and (c) heat-treated at 750°C for 30 min. The standard card of CaF_2 (JCPDS 35-0816) is shown together in the bottom of the figure as a reference.

for the samples heat-treated at 700°C for 4 h and 750°C for 30 min, respectively, with the higher heat-treatment temperature resulting in a larger nanocrystal. Figure 3 shows two typical SEM images. In the top image, the dark-colored structures indicated as A are vacancies left behind by nanocrystals (the light-colored particles indicated as B) that had come off the sample. These objects are randomly distributed in the glass matrix, indicated as C, and this is also confirmed in the lower magnification image on the bottom of Fig. 3. The estimated nanocrystal size above agrees with the SEM observations.

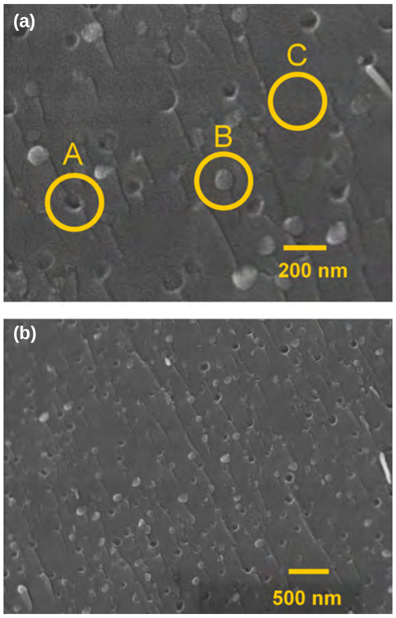

Fig. 3. SEM image of the sample heat-treated at 750°C for 30 min observed at two different magnifications, (top) ×60000 and (bottom) ×25000.

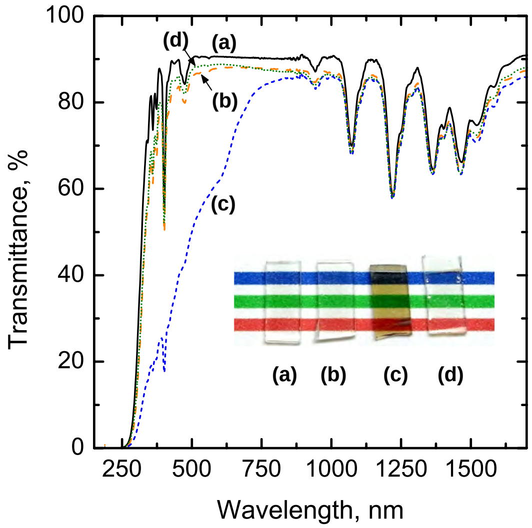

Fig. 4. Transmittance curves of samples, (a) as-prepared glass, (b) glass-ceramic heat-treated at 700°C for 4 h, (c) glass-ceramic which was heat-treated (700°C, 4 h) and then X-irradiated under X-ray tube (1 h, 110 Vp), and (d) glass-ceramic which was first heat-treated (700°C, 4 h), and next X-irradiated (1 h, 110 Vp), and then heat-treated at 550°C.

(2) Optical Properties

Figure 4 shows the optical transmittance spectra of samples with different treatment histories. The glass-ceramic sample (b) was still as transparent as that of as-prepared glass (a) when heat-treated at 700°C for 4 h; however, it became milky when heat-treated at 750°C (not shown in the figure). Upon X-ray irradiation, the irradiated sample became brownish due to the induced strong absorption band in the UV- and visible region as indicated as (c) in Fig. 4. In our earlier work, we have also observed X-ray-induced absorbance in Sm-doped FP and FA glasses.[8,9,10,12] Despite the coloration in the excitation and, perhaps, emission wavelength range, the samples are still suitable as MRT dosimetric plates as we only measure the PL signal at the surface of the sample by using a confocal microscope; thus, the coloration effect is practically negligible. Figure 5 illustrates absorption coefficients induced by X-ray irradiation in as-prepared glass and glass-ceramic heat-treated at 700°C for 4 h. In addition, induced absorption due to $Sm^{3+} \rightarrow Sm^{2+}$ change in a CaF_2 crystal by γ-ray irradiation is plotted in the same figure for comparison. The latter was derived from the work of O'Connor *et al.*[26] Due to X-ray irradiation, strong and broad absorption band was observed in as-prepared glass, whereas the glass-ceramic showed additional weak absorption bands at photon energies ~2 and 3 eV (indicated with ▽ in the figure). As the latter spectral positions agree with those observed by O'Connor *et al.*, we attribute the origin of these bands to the induced absorption by $Sm^{3+} \rightarrow Sm^{2+}$ conversion taken place inside the CaF_2 nanocrystals by X-rays. (An additional peak at 4 eV was not clearly pronounced in our measurements. The reason is because its location is near the absorption edge of the glass and the measurement accuracy in this range is limited due to the small signal. The same reason should also apply to the mismatch of curve by glass and glass-ceramic at high photon energies. On the other hand, the observed broad absorption in the glass is from defect centers generated by X-rays as it contains neither CaF_2 nanocrystals nor Sm^{2+} ions (discussed in the next paragraph). The irradiated sample returned to being colorless after a suitable heat-treatment, shown as (d) in Fig. 4. The valence reduction is further discussed in detail below.

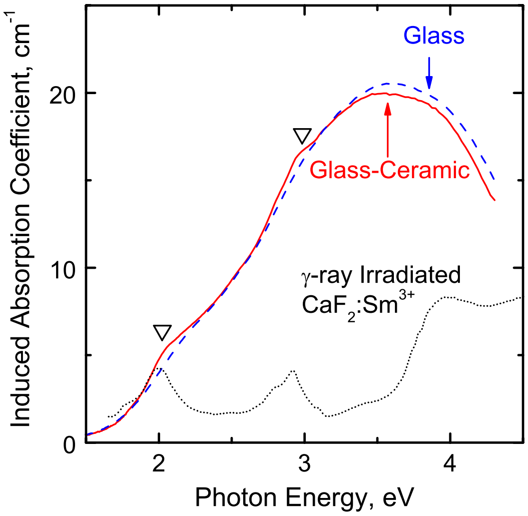

Fig. 5. X-ray induced absorption coefficient in as-prepared glass sample and that of glass-ceramic sample. The glass-ceramic was heat-treated at 700°C for 4 h. Weak absorption bands in glass-ceramic is observed on top of broad band in the glass matrix. The origin of the weak bands is attributed to the $Sm^{3+} \rightarrow Sm^{2+}$ change in CaF_2 nanocrystals by X-ray irradiation. The induced absorption by CaF_2:$Sm^{3+} \rightarrow Sm^{2+}$ change by γ-ray irradiation is also plotted as a reference [26].

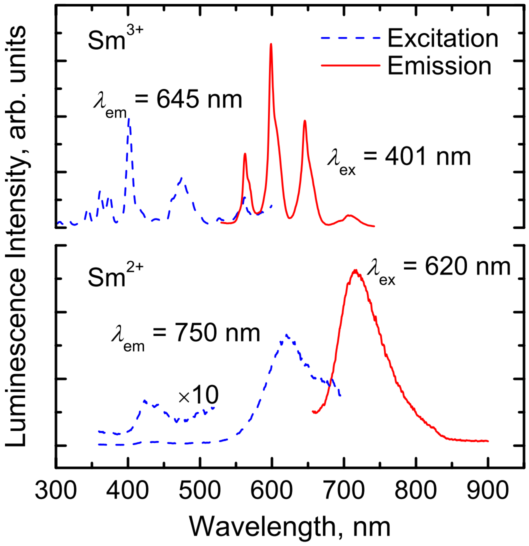

Fig. 6. Excitation and emission PL spectra of irradiated Sm-doped glass-ceramic sample. Upper spectra for Sm^{3+} and lower spectra for Sm^{2+}. Note that the excitation spectra are for observing PL emission at 645 nm (Sm^{3+}), and PL emission at 750 nm (Sm^{2+}). Further, PL spectrum for Sm^{3+} is excited at 401 nm and that for Sm^{2+} is excited at 620 nm.

The excitation and emission spectra of PL were measured for the glass-ceramic samples before and after X-ray irradiation. Heat treatment was done at 700°C for 4 h and then the sample was irradiated with X-rays for 1 h under an X-ray tube. Before the X-ray irradiation, we only detected typical PL emissions due to the 4*f*–4*f* transition of Sm^{3+} ions (spectra not shown). However, after the irradiation, additional broadband emission centered at ~730 nm was observed as shown in Fig. 6. We attribute the origin of this broad emission to Sm^{2+} ions embedded in CaF_2 nanocrystals because of the following reasons. (a) First, the appearance of this broad emission was only observed in samples heat-treated above the first crystallization temperature T_{p1}. As-prepared glass and any sample heat-treated below T_{p1} did not show this emission (not shown in figure). (b) The next argument is the observation of a broadband signature in both emission and excitation spectra. As illustrated in Fig. 6, the excitation spectrum of the broad emission also has a broad structure. The latter property is typical for the Sm^{2+} ion due to the $4f^5 5d^1 \rightarrow {}^7F_0$ transition in CaF_2 crystal, which is an allowed transition by the selection rules. (c) The third reason is the spectral position. Unlike the *f*–*f* transition in the trivalent rare earth ions, the $4f^5 5d^1$ excited level in Sm^{2+} is not

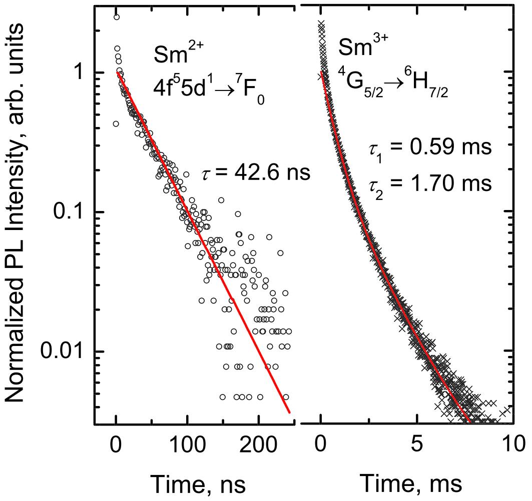

Fig. 7. PL decay curves: (left) the $4f^5 5d^1 \rightarrow {}^7F_0$ transition by Sm^{2+} ion in X-irradiated glass-ceramic. (right) the ${}^4G_{5/2} \rightarrow {}^6H_{7/2}$ transitions by Sm^{3+} ion in glass-ceramic.

shielded, thus it is strongly affected by the lattice crystal field. Assuming that the Sm^{2+} ion is located in the CaF_2 nanocrystal, the spectral position reasonably agrees with the one reported by Mikhail *et al.*[31] (d) The fourth argument is the observed fast lifetime for this ~730 nm emission. Figure 7 illustrates PL decay curves of the broadband emission as well as the ${}^4G_{5/2}\rightarrow{}^6H_{7/2}$ transitions by Sm^{3+} ions in the glass-ceramic sample. The decay curves are fitted with double- and single-exponential decay functions, respectively. As a result, the derived time constants are 0.59 and 1.70 ms for the former decay curve (Sm^{3+}) and for 42.6 ns for the latter decay curve (Sm^{2+}). As the *f–f* transitions are parity forbidden, the ${}^4G_{5/2}\rightarrow{}^6H_{7/2}$ transitions of Sm^{3+} showed long lifetime on the millisecond timescale. In contrast, the broad emission showed a much faster lifetime on the order of nanoseconds. This fast lifetime implies that the PL emission is due to transitions which are allowed by the selection rule, that is, the $4f^55d^1\rightarrow{}^7F_0$ transition of Sm^{2+} ions. This is also supported by the fact that our measurement seems to agree with the reported lifetime in the case of Sm^{2+}-doped CaF_2 crystals by Payne *et al.*[32] and Chase *et al.*[33] Consequently, based on our observations above, we attribute this PL broad emission to the $4f^55d^1\rightarrow{}^7F_0$ transition of Sm^{2+} ions which are embedded in CaF_2 nanocrystals, and reduced from the trivalent state by the X-ray irradiation. Further, the lifetime of Sm^{2+} is much faster than that of the *f–f* transition, which is more commonly found in materials that show $Sm^{3+}\rightarrow Sm^{2+}$ reduction by X-ray irradiation. Therefore, we can expect a much faster readout speed during the readout of PL emissions during laser scanned fluoroscopic microscopy of converted Sm^{2+}

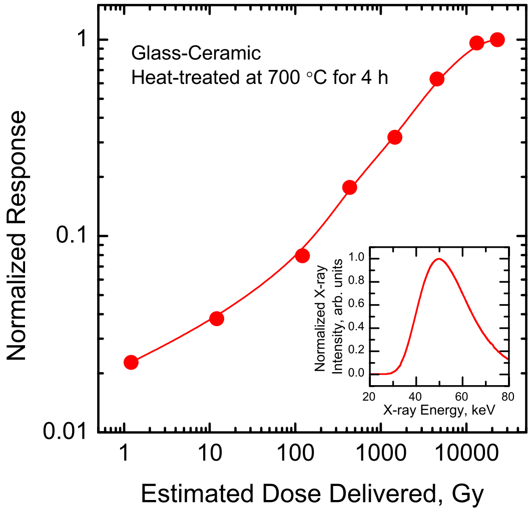

Fig. 8. Dose-response curve of oxyfluoride glass-ceramic containing $CaF_2:Sm^{3+}$ nanocrystals. The as-prepared glass sample was heat-treated at 700°C for 4 h to nucleate the nanocrystals. The dose values are dose in air at the sample surface. The inset is the X-ray spectrum used for irradiation.

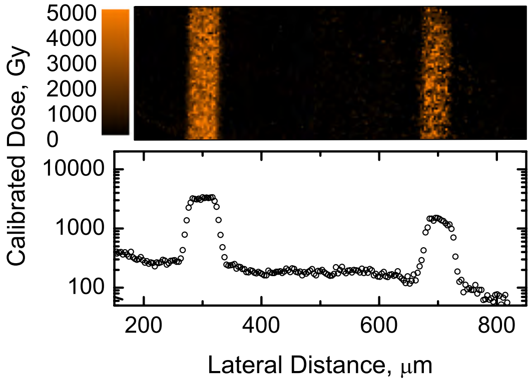

Fig. 9. Dose distribution of microbeam recorded using an oxyfluoride glass-ceramic containing $CaF_2:Sm^{3+}$ nanocrystals and digitized, using confocal PL microscopy.

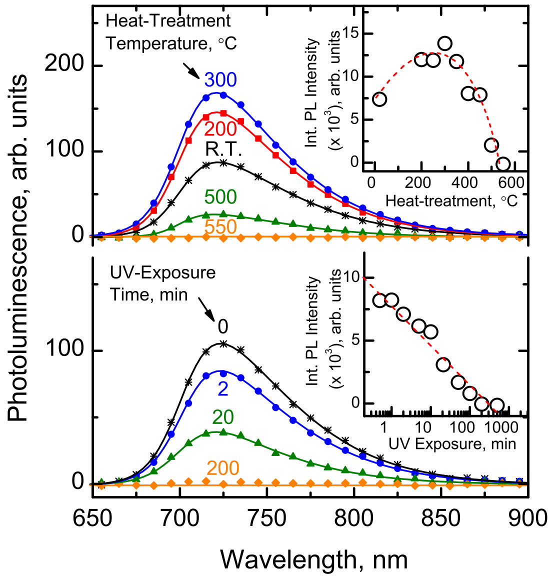

Fig. 10. PL spectra recorded during the erasure process: (top) heat erasure and (bottom) optical erasure. The integrated PL intensity is plotted in the insets. The excitation wavelength is 633 nm.

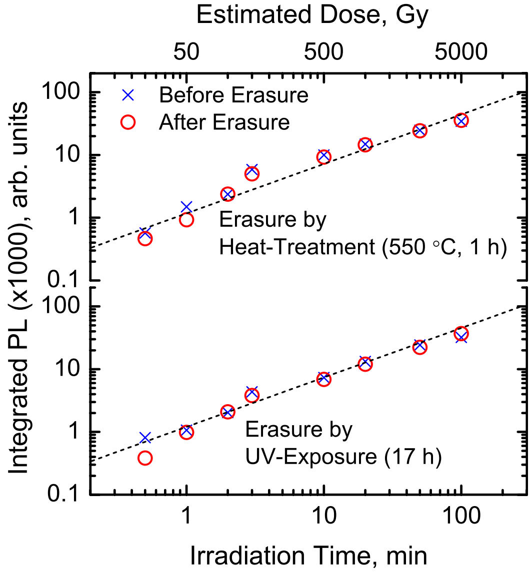

Fig. 11. PL intensity by Sm^{2+} against X-ray irradiation dose recorded before and after erasure (top) by heating at 550°C for 1 h and (bottom) by exposing to UV (254 nm) light with ~10 mW/cm² incident on the sample. The dose values are dose in air at the sample surface. The excitation wavelength is 633 nm.

ions; a distinct advantage. It is worth pointing out here that only a small fraction of Sm^{3+} may have been reduced by X-ray irradiation because of the fact that the optical absorption bands by Sm^{3+} in the 800–1000 nm range have only a negligibly small difference before and after irradiation as seen in Fig. 4. Moreover, weak absorption bands due to the reduction in the Sm^{3+} ion in a CaF$_2$ nanocrystal seen in Fig. 5 implies that only a small concentration of nanocrystals are embedded and that the majority of Sm^{3+} ions remain unconverted in the glass matrix. However, due to the large oscillator strength of Sm^{2+}, the total PL intensity is comparable to that of Sm^{3+}. [See the discussions in Refs. (37,52)]

(3) Applicability for Large-Dynamic-Range and High-Spatial-Resolution Dosimetry

Figure 8 shows a typical dose-response curve of one of our Sm-doped glass-ceramic samples, as measured at the CLS. The heat treatment was done at 700°C for 4 h in air. The figure shows that our glass-ceramic sample exhibits a sufficiently large response range from ~1 Gy to about 10 000 Gy to detect the X-ray dose at the peaks and valleys of the microbeam in a single measurement, which is essential for monitoring the dose profile in MRT. It is worth noting here that a commonly used GafChromic® film detector (HD-810; Ashland Inc, Covington, KY) only allows detection from ~10 to several hundreds of grays.[6] Notice that some saturation in the response to the total dose is observable at ~10^4 Gy. The inset shows the energy spectrum of the MRT beam. Figure 9 demonstrates a dose profile of a microbeam recorded using the glass-ceramic sample. The dose-response curve displayed in Fig. 8 was fitted by a mathematical equation and then used for the dose calibration. Although the excitation wavelength was not the best choice, we successfully read and digitized the microbeam pattern and resolved the two peaks which are detected to be separated by 400 μm and the FWHM of the peak is detected to be 50 μm. Both of these values are in agreement with the properties of the microbeam used in this BMIT beamline, and verified by other techniques such as Monte–Carlo simulations.

(4) Reusability

One of the glass-ceramic samples, which was heat-treated at 700°C for 4 h to nucleate CaF$_2$ nanocrystals, was used to study the reusability as a dosimeter material. Figure 10 shows the change in PL peak intensity by Sm^{2+} while the erasure process was in progress by heating (top) and by exposing to UV light (254 nm) (bottom) after an irradiation for 1 h under the X-ray tube. The heating time was fixed to 30 min at all the temperatures. When the sample was heated at lower temperatures, interestingly, the Sm^{2+} PL peak increased despite our intention to erase the sample. When the temperature reached to 300°C, the PL intensity was the highest, and then it was followed by decrease at higher temperatures. Ultimately, the PL signal was completely eliminated after heating at 550°C, at which the X-ray-induced absorption was also eliminated and the sample had returned to being transparent [see Fig. 4(d)]. An observation of similar behavior was reported[9] for Sm-doped FP glass, in which Sm^{2+} ions were also produced by X-ray irradiation. In contrast, when we attempted erasure by UV exposure, the PL intensity simply decreased, and the PL signal was completely removed after 200 min of exposure.

Figure 11 compares the response profile of the PL intensity by Sm^{2+} against X-ray irradiation time (dose) before and after erasures by heating at 550°C for 1 h (top) and by UV exposure for 17 h (bottom). For both the erasure methods, the response curves were well reproduced with very good agreement. Therefore, the Sm-doped oxyfluoride glass-ceramic synthesized in this work is reusable as a dosimetric detector material for MRT with both thermal and optical erasure methods.

IV. Conclusions

A Sm^{3+}-doped oxyfluoride glass-ceramic was synthesized as a new dosimeter material to be used for MRT applications. When the as-prepared glass is heat-treated, CaF$_2$ nanocrystals are nucleated and grown in the glass matrix. The doped Sm^{3+} ions are reduced to Sm^{2+} during the X-ray irradiation of the glass-ceramic samples, and this valence reduction process takes place only in the CaF$_2$ crystal environment, that is, within the CaF$_2$ nanocrystals. As a result, the PL of Sm^{2+} is predominantly due to the parity allowed $4f^5 5d^1 \rightarrow {}^7F_0$ transition. The lifetime (42.6 ns) for this transition is much faster than that of the *f–f* transition, which is more commonly found in glasses showing the Sm^{3+}→Sm^{2+} reduction by X-ray irradiation. Hence, using our new Sm-doped glass-ceramic material, the recorded dose information can potentially be read out using a laser scanning technique, such as confocal fluorescent microscopy, with a much faster speed than that used for Sm-doped glasses. Further, the potential practical usefulness for MRT has been demonstrated by carrying out measurements under an X-ray microbeam generated at the BMIT beamline at the CLS (the Canadian synchrotron). The glass-ceramic is able to detect X-ray doses from ~1 Gy up to several thousands of grays over a dynamic range suitable for MRT. Furthermore, by making use of the scanning ability of the confocal microscope, we were able to obtain the dose distribution profile across the beam cross section, which agreed with the known characteristics of the microbeam. Cross-sectional dose distribution of the microbeam has been successfully detected using our new detector material. Furthermore, the recorded dose information on the detector is erasable either thermally (by suitable heat treatment at a high temperature) or optically (by UV exposure), and the erased detector is reusable. The new Sm-doped oxyfluoride glass-ceramic with CaF$_2$ nanocrystals reported in this work shows potential for practical use in high-dose and high-resolution dosimetry for MRT.

Acknowledgments

The research described in this study was supported by an NSERC Strategic Grant sponsored by Teledyne-DALSA Inc. and was performed at the CLS, which is supported by NSERC (Canada), NRC (Canada), the Canadian Institute of Health Research, the Province of Saskatchewan, Western Economic Diversification Canada, and the University of Saskatchewan.

References

[1] D. N. Slatkin, P. Spanne, F. A. Dilmanian, and M. Sandborg, "Microbeam Radiation Therapy," *Med. Phys.*, **19** [6] 1395–400 (1992).

[2] H. Blattmann, J. Gebbers, E. Bräuer-Krisch, A. Bravin, G. Le Duc, W. Burkard, M. Di Michiel, V. Djonov, D. N. Slatkin, J. Stepanek, and J. A. Laissure, "Applications of Synchrotron X-Rays to Radiotherapy," *Nucl. Instrum. Methods Phys. Res., Sect. A*, **548** [1–2] 17–22 (2005).

[3] F. A. Dilmanian, Z. Zhong, T. Bacarian, H. Benveniste, P. Romanelli, R. Wang, J. Welwart, T. Yuasa, E. M. Rosen, and D. J. Anschel, "Interlaced X-ray Microplanar Beams: A Radiosurgery Approach with Clinical Potential," *Proc. Natl. Acad. Sci. U.S.A.*, **103** [25] 9709–14 (2006).

[4] J. C. Crosbie, R. L. Anderson, K. Rothkamm, C. M. Restall, L. Cann, S. Ruwanpura, S. Meachem, N. Yagi, I. Svalbe, R. A. Lewis, B. R. G. Williams, and P. A. W. Rogers, "Tumor Cell Response to Synchrotron Microbeam Radiation Therapy Differs Markedly From Cells in Normal Tissues.," *Int. J. Radiat. Oncol. Biol. Phys.*, **77** [3] 886–94 (2010).

[5] E. Bräuer-Krisch, R. Serduc, E. A. Siegbahn, G. Le Duc, Y. Prezado, A. Bravin, H. Blattmann, and J. A. Laissue, "Effects of Pulsed, Spatially Fractionated, Microscopic Synchrotron X-ray Beams on Normal and Tumoral Brain Tissue," *Mutat. Res. Mutat. Res.*, **704** [1–3] 160–6 (2010).

[6] E. Bräuer-Krisch, A. Rosenfeld, M. Lerch, M. Petasecca, M. Akselrod, J. Sykora, J. Bartz, M. Ptaszkiewicz, P. Olko, A. Berg, M. Wieland, S. Doran, T. Brochard, A. Kamlowski, G. Cellere, A. Paccagnella, E. A. Siegbahn, Y. Prezado, I. Martinez-Rovira, A. Bravin, L. Dusseau, P. Berkvens, and K. K. W. Siu, "Potential High Resolution Dosimeters For MRT," pp. 89–97 in AIP Conf. Proceedings, 6th Int. Conf. Med. Appl. Synchrotron Radiat., Vol. 1266, Edited by K. K. W. Siu. American Institute of Physics, Melville, NY, 2010.

[7] G. Belev, G. Okada, D. Tonchev, C. Koughia, C. Varoy, A. Edgar, T. Wysokinski, D. Chapman, and S. Kasap, "Valency Conversion of Samarium Ions Under High Dose Synchrotron Generated X-ray Radiation," *Phys. Status Solidi*, **8** [9] 2822–5 (2011).

[8] G. Okada, B. Morrell, C. Koughia, A. Edgar, C. Varoy, G. Belev, T. Wysokinski, D. Chapman, and S. Kasap, "Spatially Resolved Measurement of High Doses in Microbeam Radiation Therapy Using Samarium Doped Fluorophosphate Glasses," *Appl. Phys. Lett.*, **99** [12] 121105, 3pp (2011).

[9] S. Vahedi, G. Okada, B. Morrell, E. Muzar, C. Koughia, A. Edgar, C. Varoy, G. Belev, T. Wysokinski, D. Chapman, and S. Kasap, "X-ray Induced Sm^{3+} to Sm^{2+} Conversion in Fluorophosphate and Fluoroaluminate Glasses for the Monitoring of High-Doses in Microbeam Radiation Therapy," *J. Appl. Phys.*, **112** [7] 073108, 10pp (2012).

[10] G. Okada, S. Vahedi, B. Morrell, C. Koughia, G. Belev, T. Wysokinski, D. Chapman, C. Varoy, A. Edgar, and S. Kasap, "Examination of the Dynamic Range of Sm-Doped Glasses for High-Dose and High-Resolution Dosimetric Applications in Microbeam Radiation Therapy at the Canadian Synchrotron," *Opt. Mater. (Amst)*, **35**, 1976–80 (2013).

[11] V. Martin, G. Okada, D. Tonchev, G. Belev, T. Wysokinski, D. Chapman, and S. Kasap, "Samarium-Doped Oxyfluoride Borophosphate Glasses for x-ray Dosimetry in Microbeam Radiation Therapy," *J. Non-Cryst. Solids*, **377**, 137–41 (2013).

[12] B. Morrell, G. Okada, S. Vahedi, C. Koughia, A. Edgar, C. Varoy, G. Belev, T. Wysokinski, D. Chapman, R. Sammynaiken, and S. Kasap, "Optically Erasable Samarium-Doped Fluorophosphate Glasses for High-Dose Measurement in Microbeam Radiation Therapy," *J. Appl. Phys.*, **115** [6] 063107, 8pp (2014).

[13] Y. Li, J. Wang, Y. Huang, and H. J. Seo, "Temperature-Dependent $^5D_0 \rightarrow {}^7F_0$ Luminescence of Sm^{2+} Ions Doped in Alkaline Earth Borophosphate Glass," *J. Am. Ceram. Soc.*, **93** [3] 722–6 (2010).

[14] Y. Huang, C. Jiang, K. Jang, H. S. Lee, E. Cho, M. Jayasimhadri, and S. Yi, "Luminescence and Microstructure of Sm^{2+} Ions Reduced by x-ray Irradiation in Li_2O–SrO–B_2O_3 Glass," *J. Appl. Phys.*, **103** [11] 113519, 7pp (2008).

[15] J. Wang, Y. Huang, Y. Li, and H. J. Seo, "The Reduction and Luminescence Characteristics of Sm^{2+} Doped in $Ba_3BP_3O_{12}$ Crystal," *J. Am. Ceram. Soc.*, **94** [5] 1454–9 (2011).

[16] B. H. Babu and V. V. Ravi Kanth Kumar, "Fluorescence Properties and Electron Paramagnetic Resonance Studies of γ-Irradiated Sm^{3+}-Doped Oxyfluoroborate Glasses," *J. Appl. Phys.*, **112** [9] 093516, 9pp (2012).

[17] J. Qiu, K. Miura, T. Suzuki, T. Mitsuyu, and K. Hirao, "Permanent Photoreduction of Sm^{3+} to Sm^{2+} Inside a Sodium Aluminoborate Glass by an Infrared Femtosecond Pulsed Laser," *Appl. Phys. Lett.*, **74** [1] 10–2 (1999).

[18] Y. Kishi, S. Tanabe, S. Tochino, and G. Pezzotti, "Fabrication and Efficient Infrared-to-Visible Upconversion in Transparent Glass Ceramics of Er-Yb Co-Doped CaF_2 Nano-Crystals," *J. Am. Ceram. Soc.*, **88** [12] 3423–6 (2005).

[19] Y. Kishi and S. Tanabe, "Infrared-to-Visible Upconversion of Rare-Earth Doped Glass Ceramics Containing CaF_2 Crystals," *J. Alloy. Compd.*, **408–412**, 842–4 (2006).

[20] J. Ueda, S. Tanabe, and A. Ishida, "Surface Plasmon Excited Infrared-to-Visible Upconversion in Er^{3+}-Doped Transparent Glass Ceramics," *J. Non-Cryst. Solids*, **355** [37–42] 1912–5 (2009).

[21] S. Ye, B. Zhu, J. Chen, J. Luo, and J. R. Qiu, "Infrared Quantum Cutting in Tb^{3+}, Yb^{3+} Codoped Transparent Glass Ceramics Containing CaF_2 Nanocrystals," *Appl. Phys. Lett.*, **92** [14] 141112, 3pp (2008).

[22] G. Lakshminarayana, R. Yang, M. Mao, J. Qiu, and I. V. Kityk, "Photoluminescence of Sm^{3+}, Dy^{3+}, and Tm^{3+}-Doped Transparent Glass Ceramics Containing CaF_2 Nanocrystals," *J. Non-Cryst. Solids*, **355** [52–54] 2668–73 (2009).

[23] G. Aldica and M. Secu, "Investigations of the non-Isothermal Crystallization of CaF_2 Nanoparticles in Sm-Doped oxy-Fluoride Glasses," *J. Non-Cryst. Solids*, **356** [33–34] 1631–6 (2010).

[24] M. Secu, "Nanoparticles Size Effects in Thermoluminescence of Oxyfluoride Glass-Ceramics Containing Sm^{3+}-Doped CaF_2 Nanocrystals," *J. Nanopart. Res.*, **13** [7] 2727–32 (2010).

[25] M. Kanno, T. Honma, and T. Komatsu, "Two-Dimensional Mapping of Er^{3+} Photoluminescence in CaF_2 Crystal Lines Patterned by Lasers in Oxyfluoride Glass," *J. Am. Ceram. Soc.*, **92** [4] 825–9 (2009).

[26] J. R. O'Connor and H. A. Bostick, "Radiation Effects in CaF_2:Sm," *J. Appl. Phys.*, **33** [5] 1868–70 (1962).

[27] D. S. McClure and Z. Kiss, "Survey of the Spectra of the Divalent Rare-Earth Ions in Cubic Crystals," *J. Chem. Phys.*, **39** [12] 3251–7 (1963).

[28] Z. J. Kiss and P. N. Yocom, "Stable Divalent Rare-Earth-Alkaline-Earth Halide Systems," *J. Chem. Phys.*, **41** [5] 1511–2 (1964).

[29] J. L. Merz and P. S. Pershan, "Charge Conversion of Irradiated Rare-Earth Ions in Calcium Fluoride. I," *Phys. Rev.*, **162** [2] 217–35 (1967).

[30] J. L. Merz and P. S. Pershan, "Charge Conversion of Irradiated Rare-Earth Ions in CaF_2. II. Thermoluminescent Spectra," *Phys. Rev.*, **162** [2] 235–47 (1967).

[31] P. Mikhail, K. Ramseyer, G. Frei, F. Budde, and J. Hulliger, "Bleaching of Sm^{2+} During Photoluminescence and Cathodoluminescence," *Opt. Commun.*, **188** [1–4] 111–7 (2001).

[32] S. A. Payne and L. L. Chase, "Sm^{2+}→Nd^{3+} Energy Transfer in CaF_2," *J. Opt. Soc. Am. B*, **3** [9] 1181–8 (1986).

[33] L. L. Chase, S. A. Payne, and G. D. Wilke, "Optical Properties and Nonradiative Decay of Sm^{2+} in CaF_2-YF_3 and CaF_2 -LaF_3 Mixed Crystals," *J. Phys. C: Solid State Phys.*, **20** [7] 953–65 (1987).

[34] A. Edgar, C. R. Varoy, C. Koughia, G. Okada, G. Belev, and S. Kasap, "High-Resolution X-ray Imaging With Samarium-Doped Fluoroaluminate and Fluorophosphate Glass," *J. Non-Cryst. Solids*, **377**, 124–8 (2013).

[35] L. C. Dixie, A. Edgar, and M. F. Reid, "Sm^{2+} Fluorescence and Absorption in Cubic $BaCl_2$: Strong Thermal Crossover of Fluorescence Between $4f^6$ and $4f^55d^1$ Configurations," *J. Lumin.*, **132** [10] 2775–82 (2012).

[36] L. Dixie, A. Edgar, and M. Bartle, "Energy Resolved Imaging With a Stratified Phosphor Detector," *Radiat. Meas.*, **3**, 1–5 (2013).

[37] C. Koughia, A. Edgar, C. R. Varoy, G. Okada, H. von Seggern, G. Belev, C. Kim, R. Sammynaiken, and S. Kasap, "Samarium-Doped Fluorochlorozirconate Glass-Ceramics as Red-Emitting X-Ray Phosphors," *J. Am. Ceram. Soc.*, **94** [2] 543–50 (2011).

[38] U. Caldiño, A. Speghini, S. Berneschi, M. Bettinelli, M. Brenci, S. Pelli, and G. C. Righini, "Optical Spectroscopy and Waveguide Fabrication in Sm^{3+}/Tb^{3+} Doped Zinc–Sodium–Aluminosilicate Glasses," *Opt. Mater. (Amst)*, **34** [7] 1067–71 (2012).

[39] X. Liu, B. J. Chen, E. Y. B. Pun, and H. Lin, "Eu^{3+} and Sm^{3+} co-Activated Aluminum Germanate Glass Channel Waveguide as Irradiation Source for Photodynamic Therapy," *J. Lumin.*, **137**, 77–82 (2013).

[40] K. Hirao, S. Todoroki, D. H. Cho, and N. Soga, "Room-Temperature Persistent Hole Burning of Sm^{2+} in Oxide Glasses," *Opt. Lett.*, **18** [19] 1586–7 (1993).

[41] D. Cho, K. Hirao, K. Fujita, and N. Soga, "Photochemical Hole Burning and Local Structural Change in Sm^{2+}-Doped Borate Glasses," *J. Am. Ceram. Soc.*, **79** [2] 327–32 (1996).

[42] D. Wei, B. Yuan, Y. Huang, T. Tsuboi, and H. J. Seo, "Influence of Crystallization on the Conversion of Sm^{3+}→Sm^{2+} in SrO–Bi_2O_3–K_2O–B_2O_3 Glass-Ceramics," *J. Am. Ceram. Soc.*, **96** [7] 2167–71 (2013).

[43] Q. Jing, Q. Wu, L. Liu, J. Xu, Y. Bi, Y. Liu, H. Chen, S. Liu, Y. Zhang, L. Xiong, Y. Li, and J. Liu, "An Experimental Study on SrB_4O_7:Sm^{2+} as a Pressure Sensor," *J. Appl. Phys.*, **113** [2] 023507, 5pp (2013).

[44] Q. Wei, N. Dubrovinskaia, and L. Dubrovinsky, "Ruby and Sm:YAG Fluorescence Pressure Gauges up to 120 GPa and 700 K," *J. Appl. Phys.*, **110** [4] 043513, 4pp (2011).

[45] H.-Y. Lin, Y.-C. Fang, and S.-Y. Chu, "Energy Transfer Sm^{3+}→Eu^{3+} in Potential Red Phosphor $(Ca, Ba)_3(VO_4)_2$:Sm^{3+}, Eu^{3+} for Use in Organic Solar Cells and White Light-Emitting Diodes," *J. Am. Ceram. Soc.*, **93** [11] 3850–6 (2010).

[46] M. S. Kim, L. Krishna Bharat, and J. S. Yu, "White Light Emission Characteristics of Tb^{3+} and Sm^{3+} co-Doped $CaYAlO_4$ Nanocrystalline Phosphors for Solid-State Lighting," *J. Lumin.*, **142**, 92–5 (2013).

[47] A. R. Dhobale, M. Mohapatra, V. Natarajan, and S. V. Godbole, "Synthesis and Photoluminescence Investigations of the White Light Emitting Phosphor, Vanadate Garnet, $Ca_2NaMg_2V_3O_{12}$ co-Doped With Dy and Sm," *J. Lumin.*, **132** [2] 293–8 (2012).

[48] L. Li, Y. Yang, D. Zhou, Z. Yang, X. Xu, and J. Qiu, "Investigation of the Role of Silver Species on Spectroscopic Features of Sm^{3+}-Activated Sodium–Aluminosilicate Glasses via Ag$^+$-Na$^+$ ion Exchange," *J. Appl. Phys.*, **113** [19] 193103, 5pp (2013).

[49] Q. Li, J. Lin, J. Wu, Z. Lan, Y. Wang, F. Peng, and M. Huang, "Improving Photovoltaic Performance of dye-Sensitized Solar Cell by Downshift Luminescence and p-Doping Effect of Gd_2O_3:Sm^{3+}," *J. Lumin.*, **134**, 59–62 (2013).

[50] X. Y. Huang, J. X. Wang, D. C. Yu, S. Ye, Q. Y. Zhang, and X. W. Sun, "Spectral Conversion for Solar Cell Efficiency Enhancement Using YVO_4: Bi^{3+},Ln^{3+} (Ln = Dy, Er, Ho, Eu, Sm, and Yb) Phosphors," *J. Appl. Phys.*, **109** [11] 113526, 7pp (2011).

[51] D. Anderson, B. Warkentin, E. A. Siegbahn, and B. G. Fallone, "Ionization Chamber Measurements in a Small, Non-Uniform Beam—Applications for Synchrotron Beam Dosimetry," *Med. Phys.*, **38**, 3559 (2011).

[52] A. Edgar, C. R. Varoy, C. Koughia, D. Tonchev, G. Belev, G. Okada, S. O. Kasap, H. von Seggern, and M. Ryan, "Optical Properties of Divalent Samarium-Doped Fluorochlorozirconate Glasses and Glass Ceramics," *Opt. Mater. (Amst)*, **31** [10] 1459–66 (2009).

[53] H. P. Klug and L. E. Alexander, *X-ray Diffraction Procedures*. Wiley, New York, NY, 1974.

[54] A. Edgar, M. Secu, G. V. M. Williams, S. Schweizer, and J.-M. Spaeth, "Structural Phase Changes in Barium Bromide Nano-Crystals in a Fluorobromozirconate Glass-Ceramic X-Ray Storage Phosphor," *J. Phys.: Condens. Matter*, **13** [28] 6259–69 (2001). □